UNIVERSIDAD DEL PAÍS VASCO – EUSKAL HERRIKO UNIBERTSITATEA (UPV/EHU)

STUDY OF MARTIAN DUST AEROSOL WITH MARS SCIENCE LABORATORY ROVER ENGINEERING CAMERAS

Hao CHEN CHEN

Supervisors:

Prof Agustín SÁNCHEZ LAVEGA

Dr Santiago PÉREZ HOYOS

MAY 2019

UNIVERSIDAD DEL PAÍS VASCO – EUSKAL HERRIKO UNIBERTSITATEA (UPV/EHU)

Departamento de Física Aplicada I - Escuela de Ingeniería de Bilbao

Grupo de Ciencias Planetarias

STUDY OF MARTIAN DUST AEROSOL WITH MARS SCIENCE LABORATORY ROVER ENGINEERING CAMERAS

A dissertation submitted in partial fulfilment of the requirements for the degree of Doctor of Philosophy

by

Hao CHEN CHEN

Supervisors:

Prof Agustín SÁNCHEZ LAVEGA

Dr Santiago PÉREZ HOYOS

MAY 2019

Abstract

Planetary atmospheres other than that of Earth provide natural laboratories to test our theories and models for climate studies and can help to identify the physical processes involved in the behaviour and evolution of a planet's climate. Mars has always played a predominant role in comparative studies with Earth: the existing similarities allows to apply our terrestrial models, whereas the differences can provide us a better understanding of present atmospheric processes and characterise its past climate, in order to study why the two planets have followed different evolutionary paths, and even shedding light whether Mars could once have supported life. Extensive exploration efforts in the robotic exploration of Mars have retrieved large amount of data of Mars' atmosphere. Dust aerosol is the main driver of Mars' atmospheric variability, and the determination of the particles' properties is of high relevance for estimating its climate forcing. In particular, the angular distribution of sky brightness can be evaluated to retrieve valuable information regarding the physical properties of the aerosol particles and atmospheric dust loading. In this study we show that images retrieved by the Mars Science Laboratory (MSL) engineering cameras (Navcam and Hazcam) can be used to constrain the size and shape of dust aerosol particles, and to derive the column dust optical depth. A radiative transfer based iterative retrieval method was implemented in order to determine the aerosol modelling parameters that best reproduce the sky radiance as a function of the scattering angle observed by MSL engineering cameras. Dust aerosol particles' size were derived from measurements of the intensity decay within the solar aureole region (scattering angles < 30º), whereas the sky radiance at intermediate and large scattering angles were evaluated to derive the single scattering phase function. Particle's shape was characterised then by comparing the retrieved phase functions with Double Henyey-Greenstein (DHG) analytical phase functions, T-matrix calculations of light scattering properties by randomly oriented non-spherical particles and experimental phase function retrievals of different Martian dust analogue samples. Dust size results show a seasonal behaviour with a positive correlation between dust column opacity and particle's size, with effective radius r_{eff} ranging 0.75 to 2.00 μm. Best fitting DHG parameters generated a phase function with asymmetry parameter g ~ 0.65. Differences in the backscattering region were observed in the retrieved phase functions during the non-dusty season; however, no clear evidences of seasonal or interannual variability were detected. T-matrix results describe particles with diameter-to-length (D/L) ratios of 0.7 and 1.9 for cylinders, and D/L = 2.0 for spheroids ("disk shaped"); and the best fitting Martian dust analogue corresponded to the basalt sample. Results show an overall good agreement with previous studies and have contributed to extend the available observational data and to parameterise dust phase functions. The tools and procedures developed during this research can be implemented for the analysis of retrievals from future Mars exploration missions.

Keywords: Martian atmosphere, dust aerosol, MSL engineering cameras, Navcam, Hazcam, radiative transfer.

UNESCO codes: 2104.03, 2104.07, 2202.07, 2209.14, 2209.20, 2209.23, 2501.23

Acknowledgements

En las siguientes líneas quiero mostrar mi más sincero agradecimiento a las diferentes personas que me han apoyado a lo largo de estos años de doctorado.

En primer lugar, a mis directores de tesis Santiago Pérez Hoyos y Agustín Sánchez Lavega. Gracias haberme dado la oportunidad de investigar y trabajar en el estudio de la atmósfera de Marte durante todo este tiempo. Vuestros útiles y sabios consejos han sido siempre una constante. Extiendo este agradecimiento a todas las personas del Grupo de Ciencias Planetarias. Gracias por haberme transmitido la pasión y dedicación que ponéis día a día en vuestra labor de investigación, además del excelente ambiente de compañerismos y colaboración. Muchísimas gracias también a Scot Rafkin, por recibirme y darme la fantástica oportunidad de realizar parte de mis tareas en Southwest Research Institute en Boulder, Colorado (USA). Ha sido todo un privilegio para mí el haber podido compartir este tiempo con todos vosotros.

También quiero dar gracias a todas las personas del Departamento Física Aplicada I de la Escuela de Ingenieros de Bilbao. Gracias por haberme acogido como uno más. Del día a día en el departamento, tampoco podría olvidarme de toda la gente con los que he compartido despacho, cafés, congresos, comidas y debates de la más diversa y variada naturaleza durante este tiempo. Gracias Iñaki, Jon, Ander, Arrate, Macarena, Itsaso, Itziar, Naiara, Jorge, Peio, Aritz, Laura y Mateu.

Quiero acordarme también de todas las personas que a lo largo de estos años me han ayudado y han hecho todo lo posible para que yo esté escribiendo estas líneas ahora mismo. Gracias de corazón.

Por último, quiero expresar mi gratitud a mi familia y amigos, que siempre han estado ahí conmigo y nunca han dejado de apoyarme. Infinitas gracias.

Hao CHEN CHEN,

Donostia-San Sebastián,

Mayo 2019

Index

List of figures

List of tables

Acronyms and abbreviations

AU	Astronomical Units
CAHVOR	Center, Axis, Horizontal, Vertical, Optical, Radial (camera model)
CAHVORE	Center, Axis, Horizontal, Vertical, Optical, Radial, Entrance (camera model)
CCD	Charged Coupled Device
ChemCam	Chemistry Camera (MSL instrument)
CRISM	Compact Reconnaissance Imaging Spectrometer (MRO instrument)
DHG	Double Henyey-Greenstein
DISORT	Discrete Ordinates Radiative Transfer
D/L	Diameter-to-length
DN	Digital Number
ECAM	Engineering Camera(s)
EECAM	Enhanced Engineering Camera(s) (Mars 2020 mission engineering cameras)
EDR	Experiment Data Record
ERP	Reference Pixel file
FLA	Front Left Hazcam RCE-A (MSL Hazcam)
FLB	Front Left Hazcam RCE-B (MSL Hazcam)
FOV	Field of view
FRA	Front Right Hazcam RCE-A (MSL Hazcam)
FRB	Front Right Hazcam RCE-B (MSL Hazcam)
Hazcam	Hazard avoidance camera
I/F	Radiance factor
IMP	Imager for Mars Pathfinder (Pathfinder instrument)
IR	Infrared
IRIS	Infrared Imaging Spectrometer (Mariner 9 instrument)
IRTM	Infrared Thermal Mapper (Viking Orbiter instrument)
JPL	Jet Propulsion Laboratory
LTST	Local True Solar Time
LUT	Look-up Table
MARCI	Mars Color Imager (MRO instrument)
Mastcam	Mast Cameras (MSL instrument)
MCD	Mars Climate Database
MCS	Mars Climate Sounder (MRO instrument)
MEDA	Mars Environmental Dynamics Analyzer (suite of instrument)
MER	Mars Exploration Rover (mission)
MEx	Mars Express (mission)
MGS	Mars Global Surveyor (mission)
Mini-TES	Miniature Thermal Emission Spectrometer (MER instrument)
MRO	Mars Reconnaissance Orbiter (mission)
MOC	Mars Orbiter Camera (MGS instrument)

MSL	Mars Science Laboratory (mission)
MY	Martian Year
NASA	National Aeronautics and Space Administration
Navcam	Navigation camera
NLA	Navcam Left imager RCE-A (MSL Navcam)
NLB	Navcam Left imager RCE-B (MSL Navcam)
NRA	Navcam Right imager RCE-A (MSL Navcam)
NRB	Navcam Right imager RCE-B (MSL Navcam)
OMEGA	Observatoire pour la Minéralogie, l'Eau, les Glaces et l'Activité (MEx instr.)
Pancam	Panoramic Camera (instrument/MER)
PDS	Planetary Data System (NASA)
PFS	Planetary Fourier Spectrometer (MEx instrument)
PSD	Particle size distribution
RCE	Rover Computer Element
RDR	Reduced Data Record
RDS	Radiation and Dust Sensor (MEDA suite instrument)
REMS	Rover Environmental Monitoring Station (MSL instrument)
RLA	Rear Left Hazcam RCE-A (MSL Hazcam)
RLB	Rear Left Hazcam RCE-B (MSL Hazcam)
RRA	Rear Right Hazcam RCE-A (MSL Hazcam)
RRB	Rear Right Hazcam RCE-B (MSL Hazcam)
RSM	Remote Sensing Mast (MSL)
SAPP	Surface Attitude, Pointing and Positioning
SCLK	Spacecraft Clock
SPICAM	Spectroscopy for Investigation of Characteristics of the Atmosphere of Mars
TES	Thermal Emission Spectrometer (MGS instrument)
THEMIS	Thermal Emission Imaging System (Mars Odyssey instrument)
TOA	Top of atmosphere
UV	Ultraviolet
VIS	Visible (spectrum range)

1. INTRODUCTION

One of the main goals in the solar system exploration is to understand the main processes driving planetary formation and evolution, thus understanding their current behaviour from a geophysical point of view. Answers to some basic questions coming up along this road may be found through comparison, by studying how analogous phenomena of diverse nature take place under the different conditions found in each planet.

This concept is known as *comparative planetology* and could help to identify and evaluate the physical processes involved in the nature and evolution of the planets and their atmospheres (Kahn, 1989; Greeley, 1995; Lowman, 2002). Within this approach, planetary atmospheres other than Earth's can serve as natural laboratories where to test theories and gain more understanding in the mechanisms and interactions driving the climate system when observed under a different environment, with different forcing and boundary conditions (Sánchez-Lavega, 2011; Haberle et al., 2017).

Atmospheric data derived from telescopes, in-orbit spacecraft remote sensing instruments, and surface landing probes can be evaluated and interpreted with adaptations of state-of-the-art Earth computational models to simulate those planetary atmospheres. Occasionally, due to the special preservation or unique conditions, the retrieved data have comparable or higher quality and science value potential than the terrestrial ones (e.g., early solar system records). In such case, the study of planetary data contributes to our knowledge of the terrestrial atmosphere; findings of such investigations can be used to design more specific experiments and remote sensing instruments for probing Earth's environment, and to improve our numerical models (Kahn, 1989). In the long-term, the details of Earth's past, present and future climate can be best addressed by analysing the circumstances that have led to the extreme environments we currently find on other places, such as our neighbouring planets: Venus and Mars (Pollack, 1979; Toon et al., 1982; Bougher, 1995; Taylor, 2011; Ehlmann, 2016).

Mars has always played a special role in the comparative studies with Earth. On Table 1.1 the main physical and orbital parameters of both planets are provided. Although Mars' radius is about half that of the Earth and gravity acceleration is around 40%, the two planets share fundamental properties such as similar rotation periods and orbit inclinations; their relatively thin atmospheres are both heated by radiative and convective exchange with the surface. These conditions generate diurnal variations and seasonal changes of both planets' climate. There are also crucial differences: the higher eccentricity of the Martian orbit leads to larger variations in annual solar insolation, the absence of liquid water on the surface of the planet (no oceans, lakes or rivers) is translated into a smaller surface thermal inertia; and the atmospheric mass is controlled by the heating balance of the polar regions in contrast with the almost constant atmospheric mass on Earth. As a result, Mars' atmosphere presents a fast response to solar

insolation, thus generating more intense diurnal and seasonal cycles when compared to Earth's. In addition, airborne dust particles are always present in the Martian atmosphere, presenting both seasonal and inter-annual variations, and they significantly modify the thermal structure of the atmosphere and are a major driver of atmospheric circulations at all spatial scales.

The fundamental similarities indicate that our terrestrial models should be applicable to Mars, while the existing differences can be used to test our theories and evaluate the numerical modelling capabilities, thus improving our understanding of the climate processes (Haberle et al., 2017).

The study of Mars' atmosphere and its components is of high interest to characterise their present status and main processes, as well as to reconstruct its past climate. On the fundamental science end, atmospheric studies play a key role in astrobiology as they help to understand the origins of life and its development from simple to complex organisms. NASA's astrobiology roadmap (Des Marais et al., 2008) defines the concept of *habitable zone* or *habitability* as the measure of a planet's (or natural satellite) potential to develop and maintain environments hospitable to life as we know it. Such environments depend on the presence of an atmosphere, its properties, and the availability of "extended regions of liquid water, conditions favourable for the assembly of complex organic molecules and energy sources to sustain metabolism". Although present observations retrieved from telescopes, in-orbit and surface imaging show a dusty-red sphere and desolate arid landscapes, research outcomes from multiple missions in the last decade have revealed that early in Martian history liquid water environments were widespread over the surface and sustained by both atmospheric precipitation and outflows from aquifers (Des Marais et al., 2008; Grotzinger et al., 2012; James et al., 2017).

Parameters	Mars	Earth	Mars to Earth ratio (%)
Mass (kg)	0.64×10^{24}	5.97×10^{24}	10.7
Radius of planet (km)	3,396	6,378	53.2
Gravity at surface (m s^{-2})	3.71	9.80	37.9
Length of solar day (seconds)	88,775	86,400	103.0
Length of year (solar days)	669	365	183.0
Spin-axis inclination (º)	25.19	23.44	107.0
Orbit eccentricity	0.0935	0.0167	560.0
Orbit semimajor axis (AU)	1.52	1.00	152.0
Orbit perihelion (AU)	1.38	0.98	141.0
Orbit aphelion (AU)	1.67	1.02	164.0
Solar radiation (W m^{-2})	586.2	1,361.0	43.1
Pressure at surface (mbar, average)	7	1,013	0.7
Temperature at surface (average)	210 K (-63ºC)	288 K (15ºC)	73.0

Table 1.1. Comparison of physical and orbital parameters of Mars and Earth. Source: NASA GSFC Planetary Fact Sheet (https://nssdc.gsfc.nasa.gov/planetary/factsheet/)

On a more practical sense, a thorough understanding of present Martian atmospheric processes is required for improving our models and developing accurate meteorological predictions, in order to plan and design future exploration missions involving surface landers and exploration vehicles and, eventually, the journey of humans to Mars (e.g., Levine, 2018).

The advances made in our understanding of Martian atmosphere properties have been founded in extensive efforts made in the exploration missions during the last decades. The principal atmospheric quantities of interest in the characterisation of current Martian atmosphere are surface pressure, temperatures, wind velocity, aerosol optical depth and physical properties and the abundance of atmospheric species. This research work is focused in the study of dust aerosol in the Martian atmosphere and the retrieval of the airborne dust particle properties.

The study of the optical and physical properties of aerosol particles is important for assessment of their effect on climate. On Earth, the aerosol abundance is considered as one of the major uncertainties in global climate changes (e.g., Hansen and Lacis, 1990; Kaufman et al., 1994). On Mars, they play a critical role in the atmosphere and climate system, in many ways similar to the role of water on Earth (Heavens et al., 2011a, b; Medvedev et al., 2011). The ubiquitous dust particles suspended in the Martian atmosphere affect the thermal structure of the atmosphere and its dynamics by absorbing and scattering the incoming solar radiation. Such variations modify at the same time the distribution and atmospheric loading of dust itself, thus creating a complex feedback mechanism and affecting Mars overall climate system (Newman et al., 2002). In contrast to Earth, where airborne dust particles remain for long periods, dust aerosol particles of similar size on Mars stay for much shorter times. However, while on Earth the dust particles are efficiently trapped or removed from the atmosphere due to the water cycle, the lack of such cleaning mechanisms on Mars cause that these particles, once they reach the surface, may be injected again into the atmosphere. For instance, Martian global dust storms are a unique phenomena in the solar system. They can obscure almost all the surface of the planet in a seasonal timescale and affect the atmospheric temperature and circulation patterns on a global scale. In particular, observations retrieved from surface-based spacecraft operating during the Martian global dust storms in 1977, 2007 and 2018 show dust opacity values exceeding 5 and almost reaching 10 (e.g., Arvidson et al., 1983; Cantor, 2001; Lemmon et al., 2015; Montabone et al., 2015; Guzewich et al., 2019).

In this first Chapter, a summary of the main components of the Martian atmosphere is provided; with emphasis on the effects produced by airborne dust particles on the climate system. Next, a brief overview of the history of Mars' exploration missions is performed. As a conclusion of this Chapter, the motivation behind the performed research work is discussed, and the aim and objectives of this dissertation are stated; and finally, the structure of this thesis is described.

1.1. Dust in the Martian atmosphere

1.1.1. Timekeeping on Mars

Prior to any further definitions, some brief notes regarding timekeeping on Mars are provided on the following lines, covering the concepts of solar longitude (L_S), Martian seasons, Martian solar day ("sol") and Mars Year (MY).

The areocentric or solar longitude L_S (pronounced as "*L sub s*" or "*L s*") is the position of Mars relative to the Sun, measured in degrees (º) from the vernal equinox, which is the start of spring in the northern hemisphere of Mars (Figure 1.1). This number is used as a measure of the Martian seasons: the northern spring/southern autumn begins at L_S = 0º, next the northern summer/southern winter start at L_S = 90º, then the northern autumn/southern spring start at L_S = 180º, the orbit perihelion is reached around L_S = 251º, and finally northern winter/southern summer start at L_S = 270º (Allison, 1997; Lewis, 2003).

The solar day on Mars is referred with the term "sol" (from the Latin word for "Sun"), adopted by the Viking Mission Team in order to avoid confusions with an Earth's day (Snyder, 1979), and has a duration of 24 hours, 39 minutes and 35.244 seconds (Allison, 1997).

Mars or Martian Years (MY) are numbered following the convention by Clancy et al. (2000), defining April 11, 1955 (L_S = 0º) as the beginning of Martian Year 1 (MY 1).

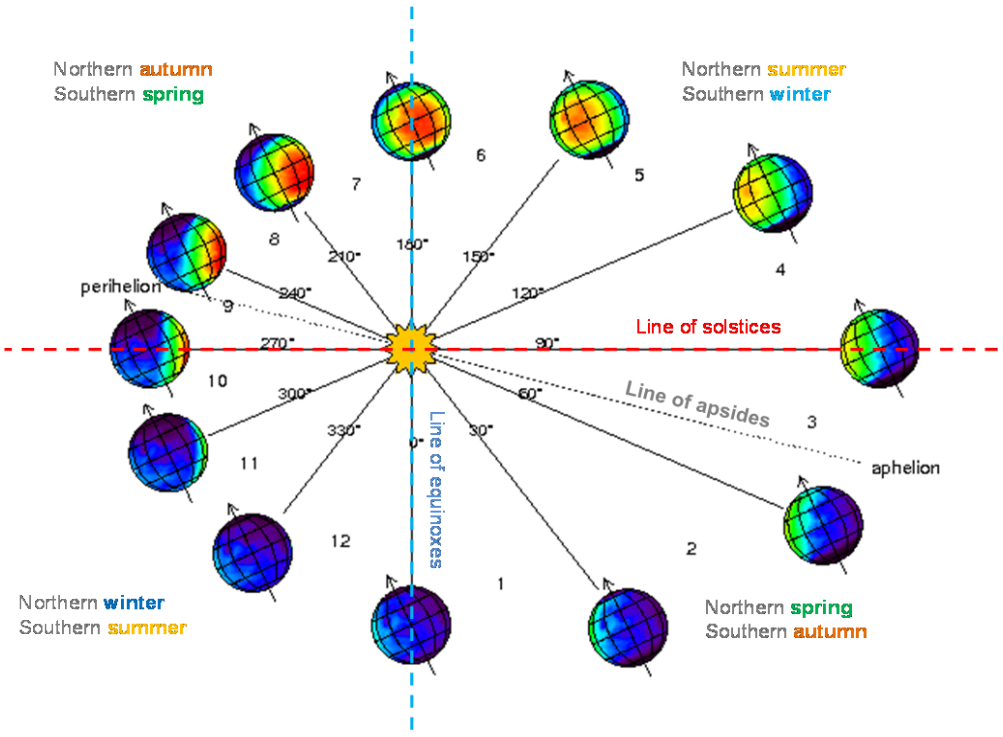

Figure 1.1. Martian solar longitude and seasons. The perihelion solar longitude position is LS = 251º, numbers 1 to 12 indicate the Mars month number given by the Mars Climate Database (MCD) (Forget et al., 1999; Millour et al., 2015). Colour shades indicate the surface temperature derived by MCD at each orbit position, ranging from 140 K (purple) to 315 K (red) (Lewis, 2003). Source: Adapted from Lewis (2003).

1.1.2. The atmosphere of Mars

The Martian atmosphere is very thin, with a pressure on the surface of about 7 mbar (on Earth is ~ 1,013 mbar) and average surface temperature of 210 K (-63ºC), and it is mostly composed of CO_2 (95.3%) with other important constituents being N_2 (2.7%), Ar (1.6%), O_2 (0.15%) and H_2O (0.03%) (Owen, 1982; Mahaffy et al., 2013). Since the rotation period and orbit inclination of Mars are similar to those of Earth, diurnal and seasonal variations are also present on the planet. However, the very thin Martian atmosphere prevents the retention of solar radiation, causing significantly larger temperature differences between day and night; with variations of more than 50 K being commonly observed, and maximums of up to 100 K. In addition to this, the higher orbital eccentricity when compared to Earth's generates a more intense seasonal cycle, as the solar insolation at its perihelion (when the planet is closest to the Sun) is about 40% larger than it is at aphelion (farthest point); for example, minimum surface temperatures of near to 150 K may occur in the polar region during winter nights, while maximum temperatures of around 300 K may be reached in Mars' southern hemisphere near the orbit perihelion (Read et al., 2015)

Based on the composition and temperature of the atmospheric gases, the Martian atmosphere is typically divided into three layers: "low", "middle" and "upper" atmosphere. This structure has been revealed by a variety of observations using both surface-based and in-orbit instrumentation. In Figure 1.2, the temperature profiles retrieved by Mars' lander missions as they descended through the atmosphere are shown.

The lower atmosphere (troposphere) of Mars usually extends from the surface up to altitudes of about 50 km. The temperatures in this region decrease with altitude and the energy transport is dominated by convection. The density of the lower atmosphere is mainly driven by the condensation and sublimation of the atmospheric CO_2 in the polar regions. The atmospheric dust aerosol is confined within this lower atmosphere region and it is the main contributor to the heating of the lower atmosphere (Smith et al., 2017). The middle atmosphere is commonly defined as the region that covers from 50 to about 100 km above Mars' surface. The temperatures show considerable variations, depending on time and season, being such variations influenced by the absorption and emission of solar radiation by CO_2, and by atmospheric waves initiated in the lower atmosphere and enhanced by thermal tides between day-night sides (Schofield et al., 1997). The Martian upper atmosphere (or thermosphere) extends approximately from 100 to 200 km. This region is strongly influenced by coupling from the lower atmosphere via gravity waves, tides, and dust storms; and from the incoming solar radiation (Bougher, 1995). The temperatures suffer large variations above the homopause (~115-130 km), as it is controlled by the absorption of solar extreme ultraviolet radiation, depending on the distance to the Sun and the solar activity cycle. The region above 130 km is the ionosphere, where the solar radiation ionizes atmospheric gases and the combination of high temperatures with low densities enhances the escape of particles (hydrogen, oxygen, carbon, nitrogen) from the planet (Barlow, 2008; Bougher, 1995).

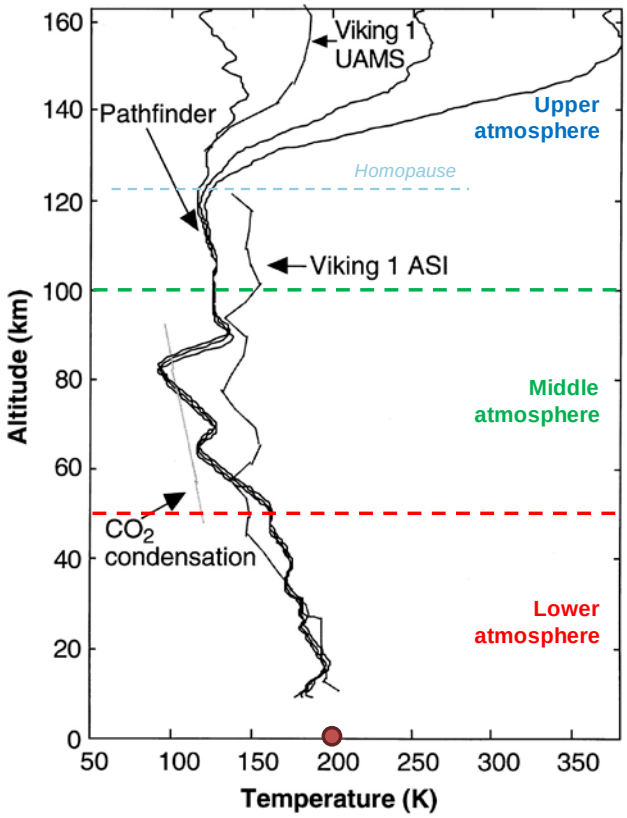

Figure 1.2. Atmospheric temperature profile structure. Overview of Mars atmosphere thermal structure, defining the "lower", "middle", and "upper" atmosphere. The temperature profiles shown are inferred from Viking Lander 1 and Pathfinder missions accelerometer measurements during the descent through the atmosphere. The CO_2 condensation profile and the surface temperature retrieved by Pathfinder (red circle) are also shown for comparison (Schofield et al., 1997; Smith et al., 2017). Source: Adapted from Schofield et al. (1997).

The main components of the general circulation are a zonally symmetric mean circulation, stationary and propagating planetary waves, thermal tides and the flow of atmospheric mass associated with the seasonal cycle of CO_2 into and out of the polar regions; being the latter an unique feature of Mars' meteorology (Haberle, 2003). The mean meridional circulation (i.e., in the north-south direction) dominates at low latitudes and is characterised with a seasonally variable Hadley circulation. In particular, at equinoxes (L_S = 0º, 180º) two symmetric Hadley cells develop sharing a common rising branch centred on the equator, similarly to the terrestrial case for the complete year. However, at solstices (L_S = 90º, 270º) the two Hadleys cells merge into a single cross-equatorial circulation. The mean circulation during the northern winter (L_S = 270º to 360º) is much stronger than that during southern winter (L_S = 90º to 180º) due to the stronger forcing resulting from perihelion (L_S ~ 250º), the existing north-south hemispheric dichotomy in Mars' topography and the global atmospheric dust loading during northern winter season (Barnes et al., 2017).

The climate system of Mars is characterised by three main seasonal cycles: the CO_2, water and dust cycles. Each of these cycles involved the exchange of the material between the surface and atmosphere.

The seasonal cycle of carbon dioxide is greatly affected by the variations in the distribution of incoming solar radiation. With an orbit inclination similar to that of Earth, Martian polar regions experience long periods of zero insolation during which temperatures below CO_2 condensation (~150K) are reached; when the insolation returns to these regions, the process is reverted and the CO_2 ice stored in polar caps sublimates (Figure 1.3). This seasonal condensation and sublimation cycle of the CO_2 in the polar regions produces variations of approximately 25 to 30% of the mass of the atmosphere (Tillman et al., 1993) and generates substantial meridional transports of heat, momentum and constituents, thus controlling the atmospheric circulation on a global scale (e.g., Titus et al., 2017; and references therein)

The existence of a water-cycle was deduced by the Viking mission, revealing a repeating seasonal and spatial pattern, with water variations controlled by exchanges between several reservoirs (Jakosky and Farmer, 1982). The reservoirs of water are found as layers of ice covering the surface or mixed with the regolith, and contain approximately 10^6 to 10^7 times more water than the atmosphere. Among these reservoirs, the north polar cap plays a pivotal role due to the large extension of its exposed area, whereas the southern counterpart has a permanent layer of CO_2 ice that prevents the underlying water-ice from regularly interacting with the atmosphere (Figure 1.3). Thus, the water cycle is predominantly controlled by the seasonal climate variations at the northern pole region. In essence: vast and exposed reservoirs of ice communicate with the atmosphere, whose circulation is vigorous enough to transport the water from pole to pole (meridional transport), thereby closing the atmospheric budget of water on an annual basis (e.g., Montmessin et al., 2017b; and references therein)

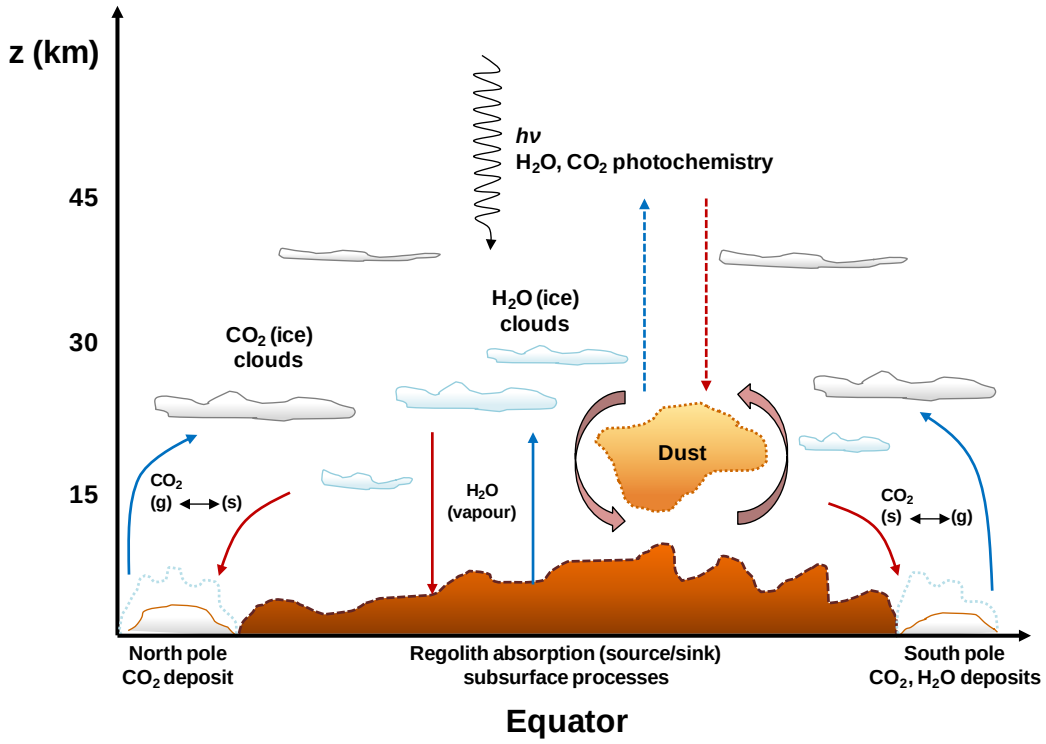

Figure 1.3. Scheme of the Martian cycles and their interaction. Source: Adapted from Sánchez-Lavega et al. (2011).

1.1.3. The dust cycle and its effects

Airborne dust particles affect the atmospheric structure and dynamics at different scales, giving origin to the term “dust cycle” on Mars, in which dust particles are lifted from the surface, transported, and sedimented back to reservoirs. The dust cycle is currently considered a key process controlling the variability of Martian climate at seasonal and interannual scales.

Gierasch and Goody (1972) first indicated that the retrieved vertical temperature profiles could not be reproduced in a radiative-convective model without taking into account the absorption of solar radiation by dust. Figure 1.4 compares the calculated temperature profiles for a carbon dioxide atmosphere model under Martian conditions for two local times, assuming an atmosphere with and without dust, with the range of measured temperature profiles obtained by Mariner 9. Such a simple experiment reveals the need to include airborne dust as a radiatively active in order to accurately model the thermal structure of the atmosphere.

Remote sensing observations of dust opacity have been a scientific focus within the history of Mars exploration. Large temporal records of atmospheric dust loading show that dust is present throughout the year with seasonal abundance variations, being the main feature of the annual cycle the intermittent occurrence of regional- or planetary-scale dust storms (e.g., Cantor et al., 2001). Although interannual variability exists at those particular seasons, some aspects of the behaviour of dust are repeated year-to-year, defining a clear seasonal pattern (e.g., Montabone et al., 2015; Lemmon et al., 2015).

The seasonal behaviour of dust may be characterised by: the non-dusty season, a period characterised by the absence of enhanced dust activity or dust storms, with low column dust optical depth or opacity (τ) values during the northern spring and summer (L_S ~ 0º to 135º); and the dusty season, with higher atmospheric dust opacity levels during the southern hemispheres spring and summer (L_S ~ 135º to 360º) (Figure 1.5).

The first rise in the atmospheric dust loading occurs within the seasonal range of L_S ~ 135º to 180º, when dust storm activity is detected, generally in the southern hemisphere. The second and more significant rise in the atmospheric column dust optical depth takes place before the perihelion (L_S = 251º), and the southern hemisphere’s summer solstice (L_S = 270º), generally around L_S 180º to 235º. This increase is related to the presence of dust storm activity in the northern hemisphere associated with travelling weather systems, which may also trigger dust storms in the southern hemisphere when conditions are favourable. There is a final annual peak in the dust opacity after the southern hemisphere’s solstice, ranging from about L_S 300º to 330º. In a similar manner to the pre-solstice season peak, this rise is related to cross-equatorial and southern hemisphere dust storms, with a significant variability in the strength of the activity from year to year (Lemmon et al., 2015; Montabone et al., 2015; Kahre et al., 2017).

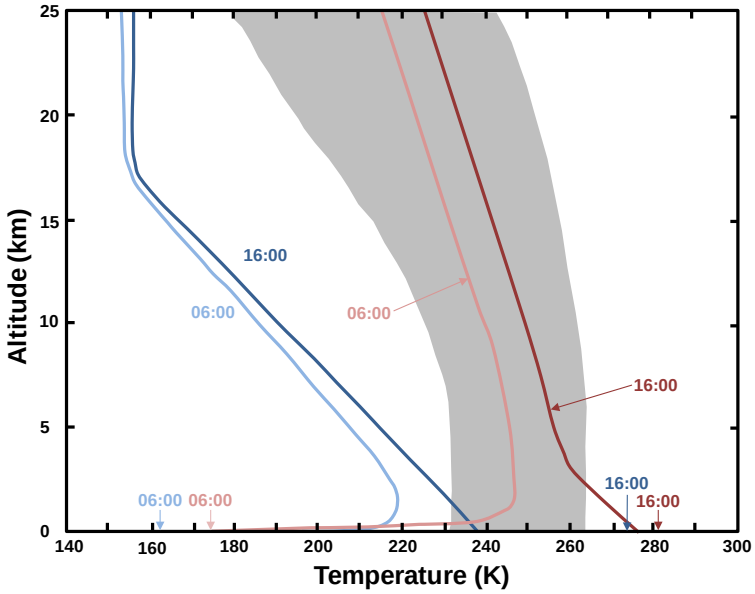

Figure 1.4. Martian temperature profile models by Gierasch and Goody (1972). Calculated temperature profiles for the atmosphere of Mars at 06:00 (morning) and 16:00 (evening) LTST. Blue profiles (left pair) were calculated for a pure CO_2 atmosphere, without suspended dust; red curves (right pair) include the radiative effects of atmospheric dust, evenly mixed at all levels with optical depth of 0.10 at all wavelengths. The shaded area encloses the range of temperature measurements retrieved by Mariner 9. Both models and observations are referred to mid-latitude summer conditions. Source: Adapted from Gierasch and Goody (1972).

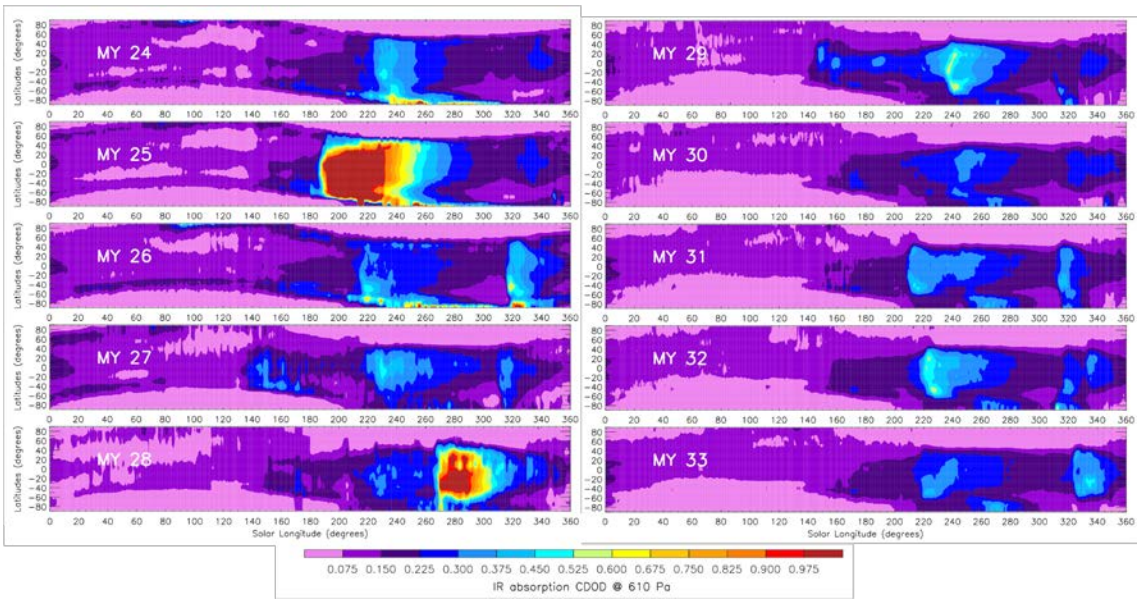

Figure 1.5. Seasonal and latitudinal distribution of column dust optical depth. Zonal mean dust absorption at 9.3 μm as a function of solar longitude and latitude for MY 24 to 33, showing the seasonal and latitudinal distribution of column dust optical depth. For a detailed description of methodology and data, see Montabone et al. (2015). Source: Adapted from Montalbone et al. (2015) and http://www-mars.lmd.jussieu.fr/mars/dust_climatology/

The lifting of dust from the surface of Mars into the atmosphere is associated with the exchange of momentum and heat between the atmosphere and the surface. Two major processes are believed to be the main mechanisms of dust lifting on Mars: wind stress (saltation and direct suspension; Greeley and Iversen, 1985), and convective vortices ("dust devils"; e.g., Neakrase and Greeley, 2010). Because of the low density of the atmosphere, dust-raising winds must be strong. For instance, gust winds of up to 30 m s^{-1} were retrieved by Viking Lander 1, being this value an apparent threshold required to initiate lifting. However, variations may be found depending on surface properties and atmospheric stability. In the case of dust devils, they are typically tens of meters in diameter and several kilometres in height, generally formed over smooth terrain and within several hours around local noon (Haberle, 2003).

Dust lifting events generate clouds and hazes which can show different ranges in both spatial and time scales; varying from local (order of 10^3 km^2) to global (planet encircling, > 10^6 km^2) events, and with a duration of hours to seasonal timescales. Dust storms are common on Mars and lead to heating in the upper atmosphere, due to the absorption and scattering of solar radiation by dust particles, and cooling in the lower atmospheric layers as they prevent radiation from reaching the surface. The extent of a dust storm modification to the atmospheric temperature is shown in Figure 1.6, where it is displayed a cross-section of the zonal-mean daytime temperature (graph of height-latitude) retrieved by MGS-TES for MY 24 and MY 25, when a global dust storm occurred. As a result, temperature increases of about 40 K at altitudes of 15 to 25 km were retrieved over the equator, and more than 60 K over the Sun-lit south pole (Gurwell et al., 2005). On the contrary, the blockage of the incoming solar radiation by atmospheric dust generates drops of about 10 K in the near-surface temperatures (Medvedev et al., 2011).

The interactions of the dust cycle with CO_2 and water cycles are of high relevance for Mars' climate. The dust and CO_2 cycles are coupled through the radiative effects of dust aerosol located in the polar regions. The presence of airborne dust in the poles during its seasonal formation affects the thermal properties of the CO_2 ice cap, modifying its condensation and sublimation rates, and thus affecting the total atmospheric mass. The influence of dust on the CO_2 cycle is then fed back to the dust cycle, as the atmosphere-surface exchange of momentum (surface wind stress) that drives dust lifting processes is directly related to the atmospheric mass (Newman et al., 2002).

Dust and water cycles are coupled through water-ice cloud condensation processes, as the airborne dust may act as condensation nuclei. The ice-covered dust particles have different sedimentation speeds when compared to isolated dust particles (Kahre et al., 2017, Rossow, 1978), thus the cloud formation may modify the vertical distribution of dust and water in the atmosphere. Furthermore, the mixed dust and water ice particles also show radiative properties different to the dust particle alone, causing affections to the atmospheric thermal and dynamical state, and resulting into modifications of the dust lifting and sedimentation process (Montmessin et al., 2002).

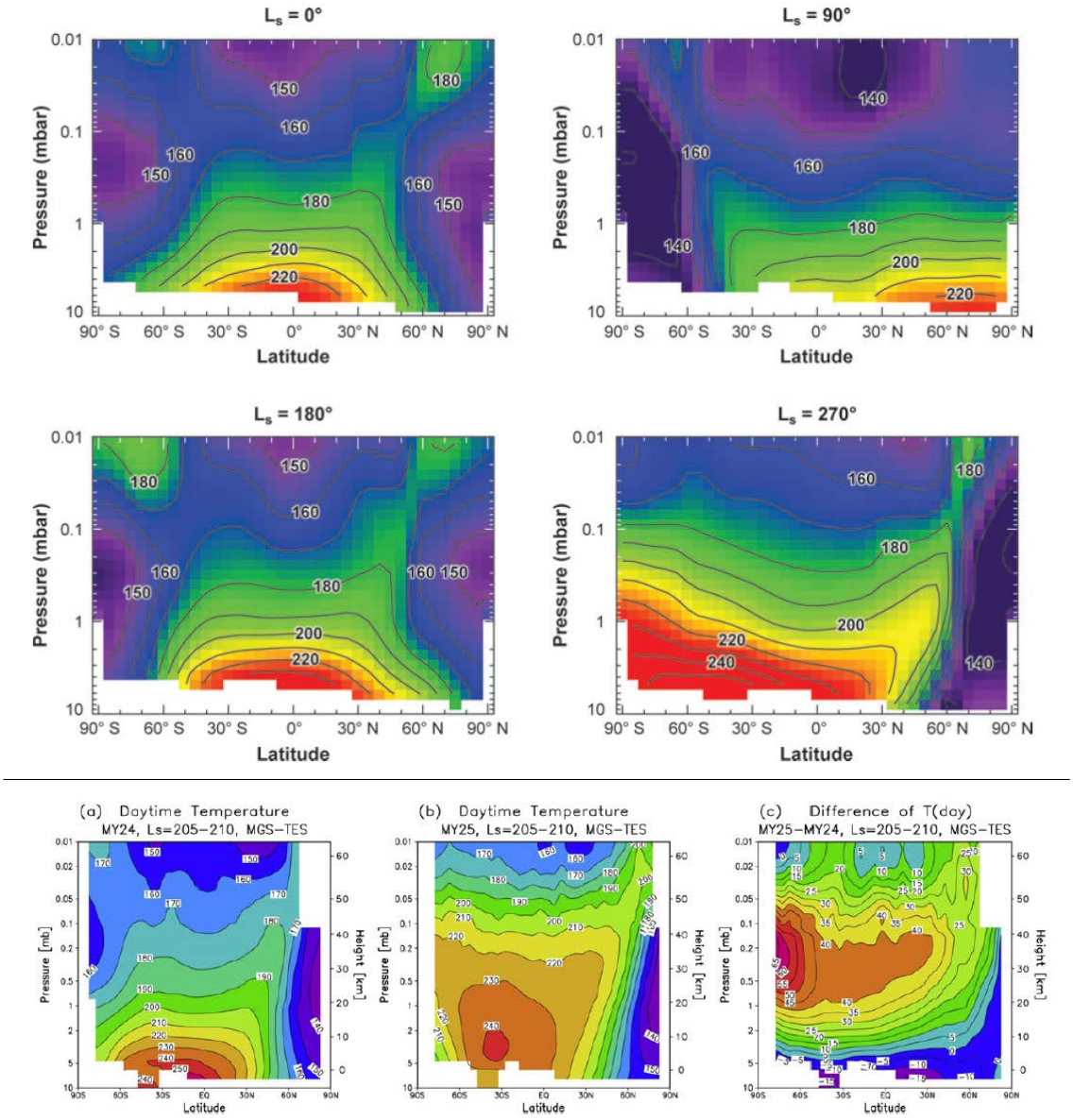

Figure 1.6. Atmosphere temperatures as a function of the latitude and pressure. These graphs show the mean daytime (LTST 14:00) temperatures (in degrees K) measured by MGS-TES (Smith, 2004), as a function of the latitude and pressure or height above the surface, being the top boundary value of 0.01 mbar approximately 65 km above the surface. *Top*: Latitude-height cross sections derived for the four seasons showing the thermal structure under solstice (L_S = 90º, 270º) and equinox (L_S = 0º, 180º) conditions. Source: Smith (2008). *Bottom*: Dust storm effects on the atmospheric temperatures. Mean daytime (LTST 14:00) temperature measured by MGS-TES between LS = 205º to 210º during (a) MY 24, (b) MY 25, and (c) the corresponding temperature differences. A major dust storm occurred around this time in MY 25. Source: Medvedev et al. (2011).

1.2. Atmospheric dust observations and missions

Observations of dust in Mars' atmosphere date back to the early 18th century when obscuration of surface features were noted; however, the concept of "yellow clouds or hazes" was introduced later in the 19th century (McKim, 1999).

Starting around the 1950s, Earth-based telescopic observations in the visible wavelength range were coordinated in order to ensure the adequate and continuous coverage of Mars. After those systematic observations and the monitoring of planet-encircling dust storms, the study of dust has been a major objective of many spacecraft missions to Mars during the last 4 to 5 decades (James et al., 2017; Kahre et al., 2017).

Images retrieved by Mariners 6 and 7 during their Mars fly-by in 1969 (MY 8) showed a relatively clear atmosphere. The lack of surface details suggested the presence of atmospheric dust in the southern impact basin *Hellas* region (e.g., Kahre et al., 2017). Mariner 9 was the first spacecraft that obtained measurements from Mars orbit (November 1971, MY 9), observing a surface obscured by a fully developed global dust storm (Leovy et al., 1972; Conrath, 1975). In 1976 (MY 12), the Viking program orbiter and landers (*Viking Lander 1*, 1976-1980; and *Viking Lander 2*, 1976-1982) arrived to Mars carrying instruments that provided measurements specific to dust. They monitored the temporal and spatial variations of 1977 dust storm and derived the dust column opacity (Colburn et al., 1989). Built upon the success of Mariner and Viking missions, numerous exploration missions have been sent to Mars and have examined its atmosphere in great detail, using orbiting spacecrafts, surface landers and remotely controlled surface exploration vehicles (*rovers*).

The list of spacecraft performing in-orbit atmospheric observations include: Phobos 2 (1988-1989), Mars Global Surveyor (MGS, 1996-2006), Mars Odyssey (2001-present), Mars Express (MEx, 2003-present), Mars Reconnaissance Orbiter (MRO, 2005-present), MAVEN (2013-present), and the ExoMars Trace Gas Orbiter (2016-present).

In addition to the Viking landers, surface-based observations have been retrieved by (Table 1.2; Figure 1.7): Pathfinder (1997), Mars Exploration Rovers (MER), with rovers *Spirit* (2004-2010) and *Opportunity* (2004-mid 2018), Phoenix (2008), Mars Science Laboratory (MSL) rover *Curiosity* (2012-present) and InSight (2018-present).

For in-orbit missions, the main instruments used for atmospheric observation and dust characterisation have been based on thermal infrared sounding, visible imaging of aerosols, radio and UV occultation, and near-infrared spectroscopy. Surface-based observations tools have consisted of Sun and sky imaging, thermal infrared sounding, and meteorological instrument suites featured with sensors for measuring the near-surface temperature, pressure, temperature and wind velocity; in addition to accelerometers and sensor for retrieving the density and temperature during the entry, descent and landing phase of surface landers and rovers (Smith, 2008; James et al., 2017). Although orbital observations provide a more

complete spatial and temporal coverage, more modelling and retrieval assumptions are required as they cannot provide the observed “ground-truth” (Lemmon et al., 2015).

For full descriptions of the spacecraft and instrumentation involved in the robotic exploration missions of Mars, the reader is referred to James et al. (2017) and references therein. Detailed reviews on the observations of the Martian atmosphere retrieved by those missions can be found in, e.g., Dlugach et al. (2003), Korablev et al. (2005), Smith (2008), and Kahre et al. (2017).

Spacecraft	*Landing site*	*Dates of operation*	*Entry season (L_S, in deg.)*	*Entry local time (nearest hour)*
Viking Lander 1	22.7ºN, 48.2ºW	July, 1976 – Nov., 1982	97	16:00
Viking Lander 2	48.3ºN, 226.0ºW	Sep., 1976 – Apr., 1980	118	10:00
Pathfinder	19.1ºN, 33.2ºW	July, 1997 – Sep., 1997	143	03:00
MER-A “Spirit”	14.6ºS, 184.5ºW	Jan., 2004 – Mar., 2010	328	14:00
MER-B “Opportunity”	2.0ºS, 5.5ºW	Jan., 2004 – June, 2018	339	13:00
Phoenix	68.2ºN, 125.7ºW	May, 2008 – Nov., 2008	77	16:00
MSL “Curiosity”	4.6ºS, 222.6ºW	Aug., 2012 – present	151	15:00
InSight	4.5ºN, 224.4ºW	Nov., 2018 – present	295	14:00

Table 1.2. Summary of lander and rover missions. Successful spacecraft missions landed on the surface of Mars with locations, dates of operation, and the seasonal date and local time of entry, descent and landing (Smith et al., 2017).

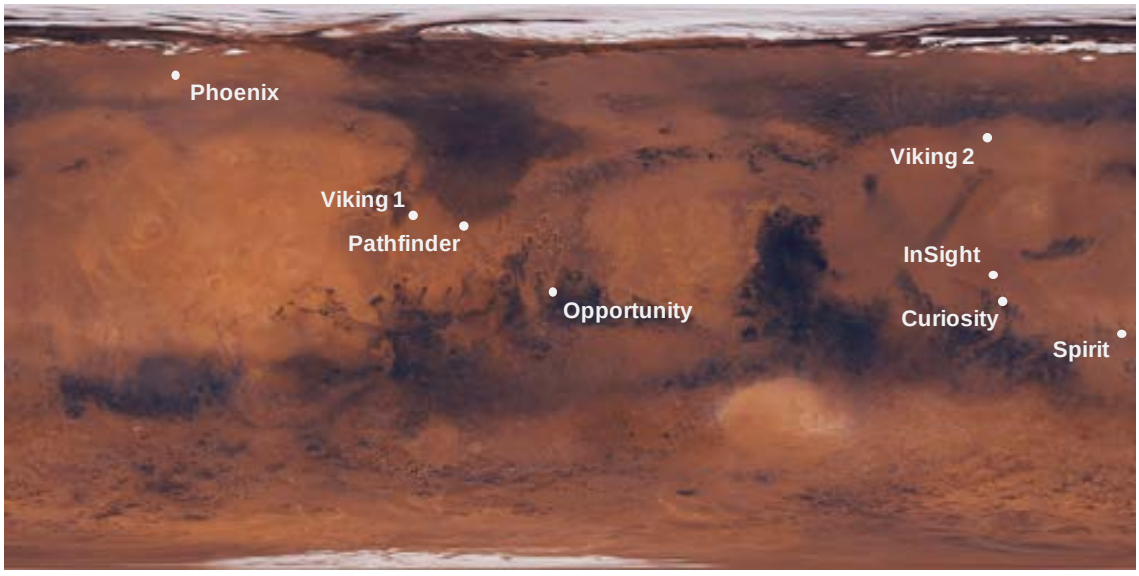

Figure 1.7. Mars missions landing sites. Map of Mars with successful missions landing sites. Source: Adapted from https://mars.nasa.gov/insight/timeline/prelaunch/landing-site-selection/, on top of Viking Global Color Mosaic (MDIM), https://astrogeology.usgs.gov/search/map/Mars/Viking/Color/Mars_Viking_ClrMosaic_global_925m.

1.2.1. The Mars Science Laboratory mission

The Mars Science Laboratory (MSL) mission was launched from Cape Canaveral (Florida, United States of America) on November 26, 2011; and landed on Mars near the base of *Aeolis Mons*, informally designated as "Mount Sharp", inside the 150-km diameter Gale Crater (4.6º South, 137.4º East) on the 5th of August, 2012 (JPL, 2012). The main objective of the MSL mission is to study whether the Gale Crater site has evidence of past and present habitable environments, as proofs show that this site may have once filled with sediment and that Mount Sharp is an erosional remnant of that sediment (e.g., Milliken et al., 2010). These studies are part of a broader analysis of the past and present processes in Mars' atmosphere and surface, and their influences in the habitability (Grotzinger et al., 2012).

The core element of the MSL mission system is the rover *Curiosity*. This remotely operated surface exploration vehicle is equipped with a suite of diverse scientific instruments and payload for performing the relevant studies towards the mission objectives, including: cameras (Mastcam, MAHLI, MARDI), spectrometers (APXS, ChemCam, CheMin, SAM), radiation detectors (RAD, DAN) and an environmental station (REMS) (see Figure 1.8). The full details on MSL mission and its scientific payload can be found in Grotzinger et al. (2012) and references therein. Significant research efforts were placed to several MSL instruments for retrieving the atmospheric dust loading and studying the local environmental dust properties in Gale Crater, in order to contribute to the assessment of the atmospheric circulation and mesoscale phenomena near the surface, identify microscale weather systems, and determine whether Gale Crater is a source or sink within the dusty cycle in the current climate. These studies may be representative of what occurs in other regions with significant topographic contrast, commonly found on Mars. The diurnal dust opacity and its seasonal evolution were retrieved by Mastcam (Lemmon, 2014), REMS (Smith et al., 2016) and ChemCam (McConnochie et al., 2017). Dust particle size distribution analysis was performed by REMS (Vicente-Retortillo et al., 2017) and ChemCam (McConnochie et al, 2017).

In addition to the set of science cameras listed above, the MSL rover is also equipped with a set of 12 engineering cameras: 4 Navigation Cameras (Navcam), and 8 Hazard Avoidance Cameras (Hazcam). MSL engineering cameras (or ECAMs) are build-to-print copies of the MER mission engineering cameras (Maki et al., 2003). Navcams are mounted in the rover's mast and are featured with full-range pointing capacity (180º in elevation, 360º in azimuth) and have 45-degree square field of view (FOV); while Hazcams are fixed to the rover chassis in the front and rear of the vehicle, with 124-degree square FOV. All of the cameras are equipped with a 1024×1024 pixel detector and red/near-IR bandpass filters centred at 650 nm. The main objective of these imagers is to support the operation of the rover during its drive across the surface. The tasks assigned to the engineering cameras include: to monitor the terrain surrounding the vehicle, to provide stereo-imaging of the observation, to derive surface range maps for hazard detection and target designation purposes, and to support the operation of the robotic arm (Grotzinger et al., 2012; Maki et al., 2012).

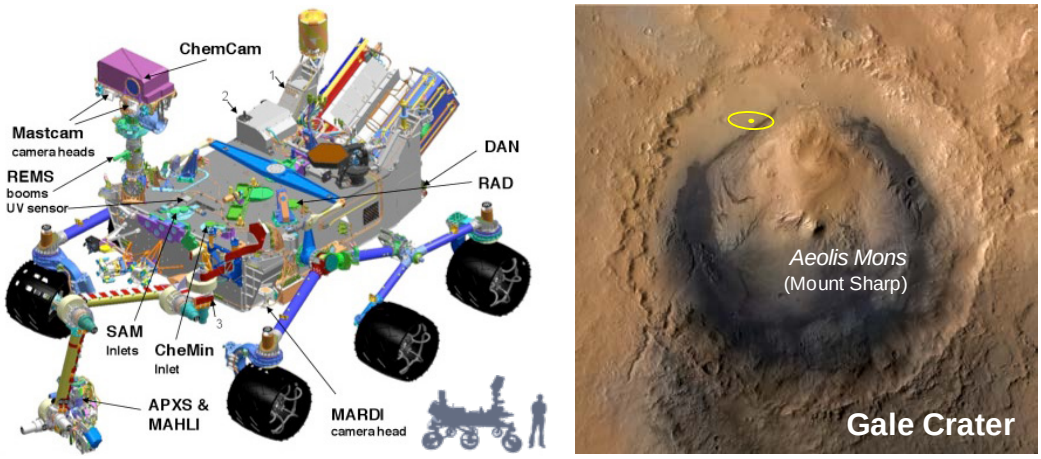

Figure 1.8. Mars Science Laboratory mission. *Left*: Scientific payload onboard MSL rover *Curiosity* (Grotzinger et al., 2012), and size comparison with a 1.75m tall person. *Right*: Gale Crater on Mars and landing ellipse (yellow). Image combines Mars Express, MRO and Viking data. Source: NASA/JPL-Caltech/ESA/DLR/FU Berlin/MSSS.

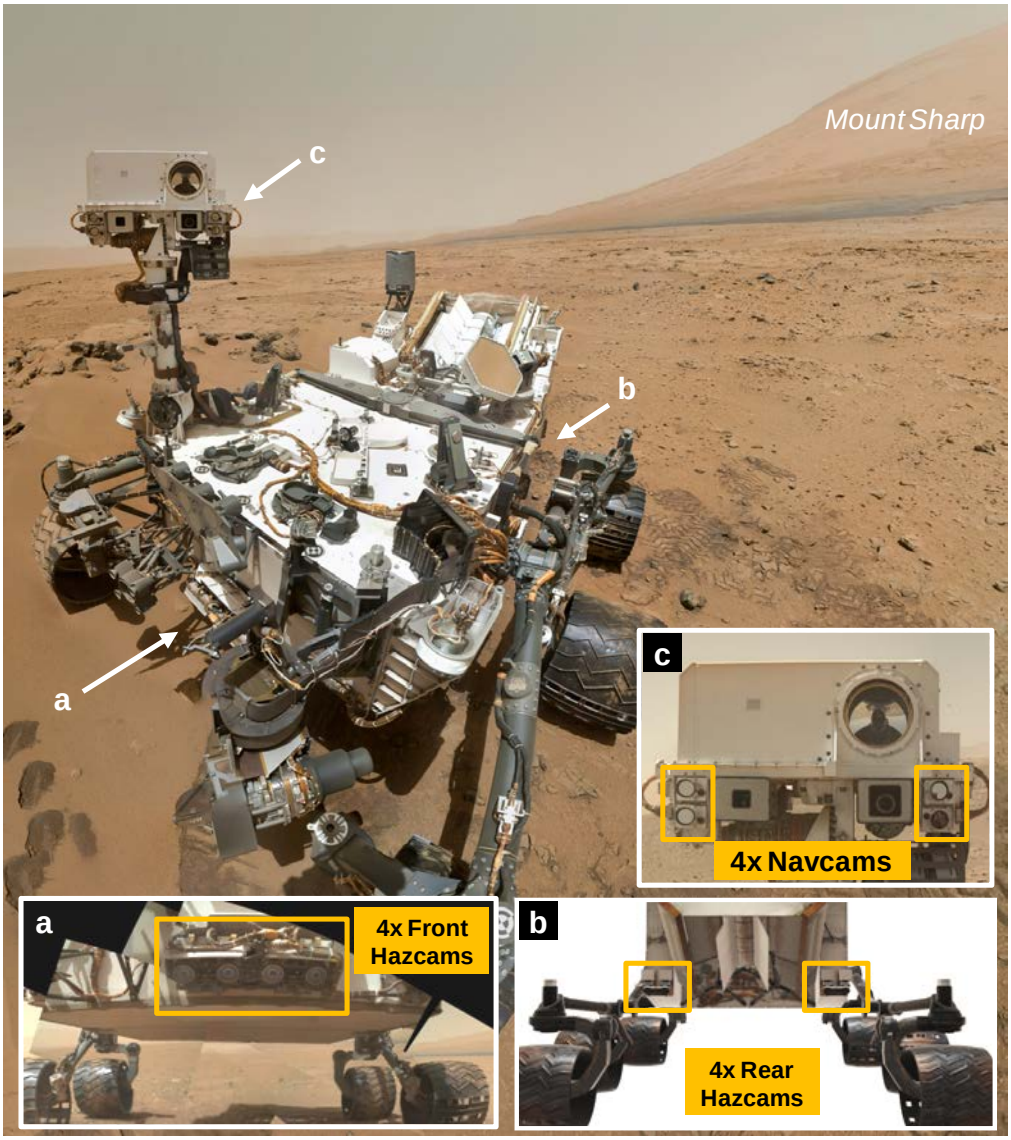

Figure 1.9. MSL rover *Curiosity*. Location of (a) Front Hazcams, (b) Rear Hazcams, and (c) Navcams onboard *Curiosity*. Source: https://photojournal.jpl.nasa.gov/catalog/PIA16239. NASA/JPL-Caltech/Malin Space Science Systems

1.3. Research motivation

The motivation behind this research work is to contribute to Martian dust aerosol particle studies with observations retrieved with surface-based rover engineering cameras; providing an additional source of scientific data, increasing the number of available observations and expanding this way the time and seasonal coverage.

Present and past Mars robotic exploration surface lander and rover missions have been equipped with science cameras with the ability of imaging the Sun, as they were featured with multispectral filter wheels (see review by Gunn and Cousins, 2016); and the retrieved observations were used to measure the atmospheric extinction and characterise the aerosol particle properties. However, in a cost-constrained future scenario for Mars and planetary exploration missions (Kicza and Vorder Bruegge, 1995; Whitcomb, 2003), imaging instrumentation with such technical specifications may be downgraded, or even not included; e.g., the recent Mars InSight mission as part of NASA'S Discovery Program low-cost missions to explore the solar system (Wolfe and Lemmon, 2015; Banerdt et al., 2013).

Although not initially designed as a scientific instrument, images retrieved by Mars surface exploration missions' engineering cameras may be used for atmospheric studies and characterising the dust environment. In addition to their nominal use for local site characterisation for navigation, hazard detection and avoidance, and the monitoring of other payload surface operations; it is possible to take advantage of the large number of retrieved images for the previous purposes and use them as an alternative source of scientific data ("opportunistic observations") for the study of Martian aerosol properties and its atmospheric loading (e.g., Soderblom et al., 2008; Smith and Wolff, 2014; Moores et al., 2015; Moore et al., 2016; Wolfe and Lemmon, 2015; Kloos et al., 2018).

1.4. Aim and objectives

The aim of this work is to retrieve and study the physical and radiative properties of Martian atmospheric dust aerosol, and characterising its seasonal and interannual variability using MSL engineering camera observations. Four specific objectives were identified that shaped the overall research methodology followed in this thesis:

1.4.1. Observational data review and image processing

To review the observation database accumulated by MSL navigation (Navcam) and hazard avoidance (Hazcam) cameras and identify the image files and sequences that can be used for studying the atmospheric dust particles. To generate the set of image processing routines, procedures and tools required for the retrieval of the angular distribution of Martian sky brightness, including the radiometric calibration, geometric reduction and validation of the instruments.

1.4.2. Radiative transfer model of Mars' atmosphere

Development and implementation of a multiple scattering plane-parallel radiative transfer model of the Martian atmosphere, and using the discrete ordinates algorithm for solving the equation. Definition of a parameterisation scheme for characterising airborne dust in Mars' atmosphere using aerosol models for non-spherical particles. Implementation of a retrieval procedure based on the comparison of observations with sky radiance models.

1.4.3. Retrieval of atmospheric dust loading and aerosol particle properties

Retrieval of the column dust optical depth. Characterisation and constraint of dust aerosol particle physical and radiative properties, including: size distribution, shape of the particles and single scattering phase function. Analysis of the seasonal behaviour and inter-annual variation of the outcomes. Comparison of results with previous studies. To identify the capabilities, uncertainties and limitations of the observation dataset, instruments and the implemented retrieval methodology.

1.4.4. Preparation of outcomes, procedures and tools for future studies

Implementation of the developed radiative transfer scheme and the derived dust aerosol properties for Martian mesoscale model simulations. Customisation of the developed framework for the eventual processing and analysis of observation data retrieved by future missions, (e.g.: InSight, Mars 2020, and ExoMars 2020).

1.5. Structure of the thesis

In this first Chapter, the research interests behind the comparative studies of planetary atmospheres and the relevant role played by Mars have been introduced. The main characteristics of Mars' atmosphere and its climate elements have been reviewed; with special emphasis on the airborne dust particles, which is the research subject of this dissertation. Next, a brief summary of the multiple exploration missions and research efforts placed on atmospheric studies have been performed, followed by an introduction to the Mars Science Laboratory (MSL) mission. Finally, the research motivations have been discussed and the aim and objectives of this research work have been stated.

In Chapter 2, the theoretical background of this research study is provided, covering the fundamentals of radiative transfer in planetary atmospheres and light scattering by aerosol particles.

Chapter 3 characterises Mars' atmospheric dust aerosol properties and describes atmosphere model used in this research. First, a literature review of contributions from previous studies regarding the multiple instrumentation and associated observational data, the retrieval methods, technical implementations and selected modelling approach is presented. Subsequently, the

radiative transfer model of Mars atmosphere implemented for this current research is described covering: structure, atmospheric constituents considered, source of input data, and the computation codes used for modelling aerosol particles and solving the radiative transfer problem.

In Chapter 4 the observational data used in this study is shown. First, the technical specifications and capabilities of MSL rover engineering cameras are overviewed. Next, the retrieved observational data are evaluated. Finally, the image processing details for the calibration of MSL Navcam and Hazcam observations and their validation are provided.

Once all the aspects concerning the observation data, image processing and the radiative transfer modelling of Mars atmosphere have been covered, the observation-model comparison, retrieval results and analysis are treated in the following chapters.

Chapter 5 covers the retrieval of atmospheric dust loading and dust aerosol sizes, whereas in Chapter 6 the retrieval of dust single scattering phase function and constraint of the shape of the particles is performed. These chapters share a similar structure. First, a brief introduction is provided covering the fundamentals of the retrieval techniques and the contributions from previous studies. Next, the observational data are described and following this, details of the Martian atmosphere model and the implemented methodology are provided. Finally, the results of the retrieval are presented and discussed, together with the uncertainties and sensitivity of the methodology. Both chapters have been published as independent studies in Icarus, the international peer-reviewed journal of solar system studies (Chen-Chen et al., 2019 a, b).

Finally, in Chapter 7, a summary of the main findings of this research and future prospects are provided.

2. RADIATIVE TRANSFER AND LIGHT SCATTERING

In the theory of the interaction of an electromagnetic wave with small particles, the problem of determining the scattering pattern produced by one particle given its size, shape and composition is called a “direct problem”. Conversely, the “inverse problem” consists in the analysis of the scattered radiation in order to describe the properties of the particles that are responsible for that pattern (Bohren and Huffman, 1983).

The use of photometric observations for studying a planetary atmosphere such as that of the Earth or Mars requires the solution of the inverse radiative transfer problem: in order to interpret the observations, the radiative transfer equation needs to be solved taking into account the unknown radiative properties of atmospheric components (e.g., Yang and Gordon, 1998; Vermeulen et al, 2000).

The radiative properties of the scattering particles describe the way atmospheric particles interact with the incoming radiation and are also required for calculating the aerosol radiative forcing in the atmosphere in climate models. However, their retrieval is not a trivial problem, since the radiative properties of aerosols are defined by the microphysical properties of the particles (size, shape, composition) which are often unknown. In addition, analytical solutions in the derivation of the radiative properties from the physical parameters only exist for homogeneous particles with specific geometries and for particular sizes when compared to the wavelength of illuminating source of radiation (e.g., Mie theory for spherical particles). For the rest of the cases, different assumptions are required regarding the particle properties, the physics involved, and the use of simplifications and computational methods. A complete review of light scattering theories and different computer codes can be found in Wriedt and Hellmers (2008), and Wriedt (2009).

In this Chapter, first the formulation of the fundamental equations governing the radiative transfer in plane-parallel atmospheres is reviewed, together with the solution of the problem using the discrete ordinates method and its implementation in the DISORT code (Stamnes et al., 1988). Reference works on the solution of the radiative transfer equations can be found in, Chandrasekhar (1960), Thomas and Stamnes (1999), and Liou (2002). DISORT code details are provided in Stamnes et al. (2000) and Laszlo et al. (2016).

Next, a brief summary of the theoretical background of light scattering by aerosols and the calculation and modelling of aerosol radiative properties is provided. The detailed formulation and derivation is beyond the scope of this dissertation, for further information the reader is referred to excellent monographs by, e.g., van de Hulst (1957), Hansen and Travis (1974), Bohren and Huffman (1983), Mishchenko (2000), and Liou (2002).

2.1. Radiative transfer in planetary atmospheres

2.1.1. Definitions and equation of radiative transfer

Let's assume a planetary atmosphere considered as a plane-parallel horizontally homogeneous stratified semi-infinite medium. The location in this medium is specified by one vertical coordinate: the optical depth, τ. This variable is measured from top-down: τ at the top of the atmosphere (TOA) is equal to 0, and τ at surface is the column optical depth or total opacity.

Directions are described by two angular coordinates: the cosine of the polar or zenith angle (μ), and the azimuth angle (ϕ). Polar or zenith angles are measured from the upward direction, therefore, all upward directions have positive polar angle cosines $(+\mu)$, while downward intensities have negative polar angle cosines $(-\mu)$. For historical reasons, the cosine of the incident beam polar angle (μ_0) is taken positive (Stamnes et al., 2000). Azimuth angles (ϕ) are measured in an absolute frame of reference, from 0º to 360º.

The optical properties of each layer are characterised by its optical thickness (difference of the bottom- and top-layer optical depth), the single scattering albedo (ω_0), which gives the fraction of an incident beam which is scattered by an infinitesimal volume inside the medium (the remainder being absorbed), and the single scattering phase function (P), which describes how much radiation incident from a given direction (μ, ϕ) is scattered by that volume into another direction (μ', ϕ'), i.e., the angular scattering pattern. (Figure 2.1).

The equation describing the transfer of monochromatic radiation at wavelength λ through the medium, subject to internal emission in local thermodynamic equilibrium and illuminated at the top boundary by a parallel beam in the direction μ_0, ϕ_0 is described with:

$$I_{direct}(\tau) = F_0 \mathrm{e}^{-\tau/\mu_0} \delta(\mu - \mu_0)\delta(\phi - \phi_0) \tag{2.1}$$

$$\mu \frac{\mathrm{d}I(\tau, \mu, \phi)}{\mathrm{d}\tau} = I(\tau, \mu, \phi) - S(\tau, \mu, \phi) \tag{2.2}$$

I_{direct} is the intensity of the direct beam at vertical optical depth τ, F_0 is the flux (irradiance) of the parallel beam normal to the direction of incidence at the top boundary, and δ is the delta function. I is the *diffuse* specific intensity at τ in a cone of unit solid angle along direction μ, ϕ, and S is the "source function".

The source function S is the sum of the radiation scattered into the direction μ, ϕ from all other directions μ', ϕ'; the "pseudobeam" source term $Q^{(beam)}$, and the internal thermal source $Q^{(thermal)}$, characterised by the Planck function $B(T)$ at temperature T at optical depth τ (*cf.* Stamnes et al., 2000; Liou, 2002):

$$S(\tau,\mu,\phi) = \frac{\omega_0(\tau)}{4\pi}\int_0^{2\pi} \mathrm{d}\phi' \int_{-1}^{1} P(\tau,\mu,\phi;\mu',\phi') I(\tau,\mu',\phi') \mathrm{d}\mu' + Q^{(beam)}(\tau,\mu,\phi) + Q^{(thermal)}(\tau) \quad (2.3)$$

with

$$Q^{(beam)}(\tau,\mu,\phi) = \frac{\omega_0(\tau)}{4\pi} P(\tau,\mu,\phi;-\mu_0,\phi_0) F_0 e^{-\tau/\mu_0}$$
$$Q^{(thermal)}(\tau) = \{1-\omega_0(\tau)\} B[T(\tau)] \quad (2.4)$$

Except for the angular quantities, all the terms presented in equations (2.1) to (2.4) depend on the wavelength of radiation, λ, which is omitted from the equations for simplicity. In particular, DISORT code makes no explicit use of wavelength except in the calculation of the Planck function, which requires a wavelength interval (Stamnes et al., 2000).

The term "diffuse" radiation or intensity is associated with multiple scattering processes, described by the first term of the source function in eq. (2.3), and is differentiated from the "direct" solar radiation or intensity (Liou, 2002).

Equation (2.1) gives the solution for the transfer of the direct beam radiation, while the solution of (2.2) provides the diffuse radiation propagating in the direction μ, ϕ at the optical depth τ.

The solution of (2.2) using the discrete ordinates method implemented in the DISORT code (Stamnes et al., 2000) is comprised of three main steps: 1) transforming the equation (2.2) into a system of equations which are functions of the vertical coordinate τ and the angular μ coordinate only (i.e., separation of azimuthal ϕ-dependence); 2) transforming the resulting integro-differential equations into a system of ordinary differential equations; and 3) solving the system of ordinary differential equations using robust linear algebra solvers.

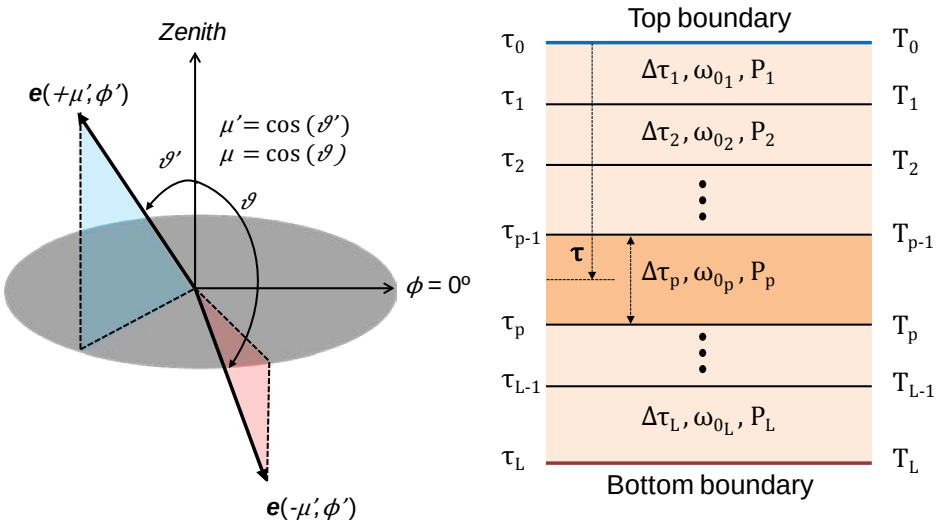

Figure 2.1. Radiative transfer calculations references in DISORT. *Left*: definition of upward and downward directions. *Right*: schematics of the multilayered medium. Source: Adapted from Stamnes et al. (2000), Laszlo et al. (2016).

2.1.2. Separation of azimuthal dependence

The scatterers in the medium are assumed to have random orientations; therefore, ω does not explicitly depend on the direction of the incident beam, and the phase function P depends only on the angle between the incident and scattered beam, not on the incident and scattered directions separately:

$$P(\tau, \mu, \phi; \mu', \phi') = P(\tau, \cos\theta) \tag{2.5}$$

where θ is the scattering angle. Using the cosine law of spherical trigonometry:

$$\cos\theta = \mu\mu' + \sqrt{(1-\mu^2)(1-\mu'^2)} \cdot \cos(\phi - \phi') \tag{2.6}$$

This fact can be used to factor out the azimuthal dependence in expressions (2.2) and (2.3). The phase function is expanded in a series Legendre polynomials, P_l with *2M* terms ($l = 0,1,\ldots,2M-1$):

$$P(\tau, \cos\theta) = \sum_{l=0}^{2M-1} (2l+1) g_l(\tau) P_l(\cos\theta) \tag{2.7}$$

where the expansion coefficients g_l are given by:

$$g_l(\tau) = \frac{1}{2} \int_{-1}^{+1} P_l(\cos\theta) P(\tau, \cos\theta) \mathrm{d}(\cos\theta) \tag{2.8}$$

Considering phase functions as probability distributions, these are normalised to unity so $g_0 = 1$; g_1 is the "asymmetry factor" and usually ranges from 0.6 to 0.9 for aerosols in the solar spectrum (Stamnes et al., 2000). The g terms generally decrease monotonically, so a finite number of terms *2M* in the Legendre expansion are expected to be sufficient.

Next, the addition theorem for spherical harmonics (Chandrasekhar, 1960, Chap. 6, Eq. 86; Thomas and Stamnes, 1999, Eq. 6.30) is applied to (2.7) resulting in:

$$P(\tau, \mu, \phi; \mu', \phi') = \sum_{m=0}^{2M-1} (2 - \delta_{0m}) \left\{ \sum_{l=m}^{2M-1} (2l+1) g_l(\tau) \Lambda_l^m(\mu) \Lambda_l^m(\mu') \right\} \cos m(\phi - \phi') \tag{2.9}$$

The Λ_l^m are the normalised associated Legendre polynomials related to the associated Legendre polynomials P_l^m:

$$\Lambda_l^m(\mu) = \sqrt{\frac{(l-m)!}{(l+m)!}} P_l^m(\mu) \tag{2.10}$$

Since expression (2.9) is essentially a Fourier expansion of the phase function P in azimuth (ϕ), the final step in factoring out the ϕ –dependence is to similarly expand the intensity in a Fourier cosine series:

$$I(\tau,\mu,\phi) = \sum_{m=0}^{2M-1} I^m(\tau,\mu)\cos m(\phi_0 - \phi) \tag{2.11}$$

The substitution of this equation (2.11), as well as expressions (2.3) and (2.11) into the radiative transfer equation (2.2), splits it into *2M* independent integro-differential equations, one for each azimuthal intensity component I^m:

$$\mu\frac{\mathrm{d}I^m(\tau,\mu)}{\mathrm{d}\tau} = I^m(\tau,\mu) - S^m(\tau,\mu), \qquad (m = 0, 1, \dots, 2M-1) \tag{2.12}$$

where the source function S is defined by:

$$S^m(\tau,\mu) = \int_{-1}^{+1} D^m(\tau,\mu,\mu')I^m(\tau,\mu')\mathrm{d}\mu' + Q^m(\tau,\mu) \tag{2.13}$$

and D^m and Q^m are:

$$D^m(\tau,\mu,\mu') = \frac{\omega_0(\tau)}{2}\sum_{l=m}^{2M-1}(2l+1)g_l(\tau)\Lambda_l^m(\mu)\Lambda_l^m(\mu') \tag{2.14}$$

$$Q^m(\tau,\mu) = X_0^m(\tau,\mu)e^{-\tau/\mu_0} + \delta_{0m}Q^{(thermal)}(\tau) \tag{2.15}$$

with:

$$X_0^m(\tau,\mu) = \frac{\omega_0(\tau)F_0}{2}(2-\delta_{0m})\sum_{l=m}^{2M-1}(-1)^{l+m}(2l+1)g_l(\tau)\Lambda_l^m(\mu)\Lambda_l^m(\mu_0) \tag{2.16}$$

and δ_{0m} is the Kronecker delta: $\delta_{0m} = 1$ for $m = 0$; and otherwise $\delta_{0m} = 0$.

In summary, this procedure transforms (2.2) into a set of equations (2.12) which do not depend on the azimuth angle (ϕ). In addition, it uncouples the various Fourier components I^m in (2.12); i.e., I^m does not depend on any I^{m+k} for $k \neq 0$. In particular, the only place where the azimuthal angles are used in the discrete ordinates method code is in reconstructing the intensity from equation (2.11) at the end of the computations (Stamnes et al., 2000).

2.1.3. Discrete Ordinate Approximation: Matrix formulation

The steps presented so far are common to multiple approaches used to solve the radiative transfer equation (2.2). In the discrete ordinates method, the integral in (2.13) is approximated by a quadrature sum. For convenience purposes, an even-number of quadrature angles 2N in the quadrature sum are chosen in order to have the same number of polar angle cosines for $+\mu$ as for $-\mu$. Therefore, the substitution of the integral with a quadrature sum transforms the integro-differential equations in (2.12) into the following system of ordinary differential equations:

$$\mu_i \frac{\mathrm{d}I^m(\tau,\mu_i)}{\mathrm{d}\tau} = I^m(\tau,\mu_i) - S^m(\tau,\mu_i), \qquad (i = \pm 1, \dots, \pm N) \tag{2.17}$$

Each μ_i is called a "stream" and (2.17) represents a "2N stream approximation". When equation (2.13) is written in quadrature form, S^m becomes a linear combination of I^m values at all quadrature angles μ_j $(j = \pm 1, \dots, \pm N)$,

$$S^m(\tau,\mu_i) = \sum_{\substack{j=-N \\ j\neq 0}}^{N} w_j D^m(\tau,\mu_i,\mu_j) I^m(\tau,\mu_j) + Q^m(\tau,\mu_i) \tag{2.18}$$

which makes the system (2.17) coupled in i, but not in m. The discretes ordinates method code (DISORT, Stamnes et al., 2000) draws the μ_i from a Gaussain quadrature rule for [0, 1] and has them mirror symmetric ($\mu_{-i} = -\mu_i$, where $\mu_i > 0$) with weights $w_{-i} = w_i$ (Double-Gauss quadrature).

When applying the discrete ordinate equations to the previously defined plane-parallel vertical inhomogeneous medium, the coefficients D^m in (2.18) are functions of τ; this τ -dependence makes (2.17) a system of *2N* coupled differential equations with non-constant coefficients, with no closed-form analytic solution. To obtain analytic solutions, DISORT assumes that the medium consists of *L* adjacent homogeneous layers (layered medium); the single scattering albedo (ω) and phase function (P) are assumed to be constant within each layer, but allowed to vary from layer to layer (horizontally homogeneous, vertically inhomogeneous) (Figure 2.1)

For better understanding purposes, prior to the presentation of the multi-stream case, the equations system in (2.17) particularised for a four-stream case (*N = 2*) is first provided. Although for the two-stream case (*N = 1*) the resulting system are simpler, the real structure can be better appreciated in the four-stream case (Laszlo et al., 2016). See Stamnes et al. (2000) for the two-stream version. For comprehensive discussion of the two-stream method the reader is referred to, e.g., Meador and Weaver (1980), Toon et al. (1989), and Thomas and Stamnes (1999).

Four-stream approximation (N = 2)

The four-stream approximation is obtained by setting *N = 2* in (2.17) and (2.18), obtaining four coupled differential equations, one for each stream. Recalling the Gaussian quadrature rule applied, dividing both sides by the μ's, rearranging the terms and ordering them according to the directions μ_1, μ_2, $-\mu_1$, and $-\mu_2$, the corresponding equations can be expressed as:

$$\frac{\mathrm{d}}{\mathrm{d}\tau}\begin{bmatrix} I^m(\tau,\mu_1) \\ I^m(\tau,\mu_2) \\ I^m(\tau,-\mu_1) \\ I^m(\tau,-\mu_2) \end{bmatrix} = \begin{bmatrix} -\alpha_{11} & -\alpha_{12} & -\beta_{11} & -\beta_{12} \\ -\alpha_{21} & -\alpha_{22} & -\beta_{21} & -\beta_{22} \\ \beta_{11} & \beta_{12} & \alpha_{11} & \alpha_{12} \\ \beta_{21} & \beta_{22} & \alpha_{21} & \alpha_{22} \end{bmatrix} \begin{bmatrix} I^m(\tau,\mu_1) \\ I^m(\tau,\mu_2) \\ I^m(\tau,-\mu_1) \\ I^m(\tau,-\mu_2) \end{bmatrix} - \begin{bmatrix} Q'^m(\tau,\mu_1) \\ Q'^m(\tau,\mu_2) \\ Q'^m(\tau,-\mu_1) \\ Q'^m(\tau,-\mu_2) \end{bmatrix} \tag{2.19}$$

where the quantities are defined as (dependence of I^m and Q^m with τ has been omitted for clarification purposes):

$$Q'^m(\pm\mu_i) = \pm\mu_i^{-1} Q^m(\pm\mu_i), \qquad (i = 1,2); \tag{2.20}$$

$$\begin{aligned}
\alpha_{11} &= \mu_1^{-1}[w_1 D^m(\mu_1,\mu_1) - 1] = \mu_1^{-1}[w_1 D^m(-\mu_1,-\mu_1) - 1],\\
\alpha_{22} &= \mu_2^{-1}[w_2 D^m(\mu_2,\mu_2) - 1] = \mu_2^{-1}[w_2 D^m(-\mu_2,-\mu_2) - 1],\\
\alpha_{12} &= \mu_1^{-1} w_2 D^m(\mu_1,\mu_2) = \mu_1^{-1} w_2 D^m(-\mu_1,-\mu_2),\\
\alpha_{21} &= \mu_2^{-1} w_1 D^m(\mu_2,\mu_1) = \mu_1^{-1} w_2 D^m(-\mu_2,-\mu_1),
\end{aligned} \tag{2.21}$$

$$\begin{aligned}
\beta_{11} &= \mu_1^{-1} w_1 D^m(\mu_1,-\mu_1) = \mu_1^{-1} w_1 D^m(-\mu_1,\mu_1),\\
\beta_{22} &= \mu_2^{-1} w_2 D^m(\mu_2,-\mu_2) = \mu_2^{-1} w_2 D^m(-\mu_2,\mu_2),\\
\beta_{12} &= \mu_1^{-1} w_2 D^m(\mu_1,-\mu_2) = \mu_1^{-1} w_2 D^m(-\mu_1,\mu_2),\\
\beta_{21} &= \mu_2^{-1} w_1 D^m(\mu_2,-\mu_1) = \mu_2^{-1} w_1 D^m(-\mu_2,\mu_1),
\end{aligned} \tag{2.22}$$

The symmetry properties of D^m, such that $D^m(\mu,\mu') = D^m(-\mu,-\mu')$, as a consequence of equation (2.14), and the fact that $\Lambda_l^m(-\mu) = (-1)^{l+m}\Lambda_l^m(\mu)$, are used for deriving the expressions (2.21) and (2.22).

By introducing the following vectors

$$\mathbf{I}^{\pm} = \{I^m(\tau,\pm\mu_i)\}, \qquad \mathbf{Q}'^{\pm} = \{Q'(\tau,\pm\mu_i)\}, \qquad (i = 1,2), \tag{2.23}$$

and the matrices

$$\boldsymbol{\alpha} = \begin{bmatrix}\alpha_{11} & \alpha_{12}\\ \alpha_{21} & \alpha_{22}\end{bmatrix}, \qquad \boldsymbol{\beta} = \begin{bmatrix}\beta_{11} & \beta_{12}\\ \beta_{21} & \beta_{22}\end{bmatrix}, \tag{2.24}$$

The equation (2.19) can be written in a more compact form as:

$$\frac{\mathrm{d}}{\mathrm{d}\tau}\begin{bmatrix}\mathbf{I}^+\\ \mathbf{I}^-\end{bmatrix} = \begin{bmatrix}-\boldsymbol{\alpha} & -\boldsymbol{\beta}\\ \boldsymbol{\beta} & \boldsymbol{\alpha}\end{bmatrix}\begin{bmatrix}\mathbf{I}^+\\ \mathbf{I}^-\end{bmatrix} - \begin{bmatrix}\mathbf{Q}'^+\\ \mathbf{Q}'^-\end{bmatrix} \tag{2.25}$$

In addition, using the equations in (2.21) and (2.22) the matrices $\boldsymbol{\alpha}$ and $\boldsymbol{\beta}$ can be expressed as:

$$\begin{aligned}
\boldsymbol{\alpha} &= \begin{bmatrix}\mu_1^{-1} & 0\\ 0 & \mu_2^{-1}\end{bmatrix}\left\{\begin{bmatrix}D(\mu_1,\mu_1) & D(\mu_1,\mu_2)\\ D(\mu_2,\mu_1) & D(\mu_2,\mu_2)\end{bmatrix}\begin{bmatrix}w_1 & 0\\ 0 & w_2\end{bmatrix} - \begin{bmatrix}1 & 0\\ 0 & 1\end{bmatrix}\right\}\\
&= \begin{bmatrix}\mu_1^{-1} & 0\\ 0 & \mu_2^{-1}\end{bmatrix}\left\{\begin{bmatrix}D(-\mu_1,-\mu_1) & D(-\mu_1,-\mu_2)\\ D(-\mu_2,-\mu_1) & D(-\mu_2,-\mu_2)\end{bmatrix}\begin{bmatrix}w_1 & 0\\ 0 & w_2\end{bmatrix} - \begin{bmatrix}1 & 0\\ 0 & 1\end{bmatrix}\right\}\\
&= \mathbf{M^{-1}}\{\mathbf{D^+W} - \mathbf{1}\}
\end{aligned} \tag{2.26}$$

$$\begin{aligned}
\boldsymbol{\beta} &= \begin{bmatrix}\mu_1^{-1} & 0\\ 0 & \mu_2^{-1}\end{bmatrix}\left\{\begin{bmatrix}D(\mu_1,-\mu_1) & D(\mu_1,-\mu_2)\\ D(\mu_2,-\mu_1) & D(\mu_2,-\mu_2)\end{bmatrix}\begin{bmatrix}w_1 & 0\\ 0 & w_2\end{bmatrix}\right\}\\
&= \begin{bmatrix}\mu_1^{-1} & 0\\ 0 & \mu_2^{-1}\end{bmatrix}\left\{\begin{bmatrix}D(-\mu_1,\mu_1) & D(-\mu_1,\mu_2)\\ D(-\mu_2,\mu_1) & D(-\mu_2,\mu_2)\end{bmatrix}\begin{bmatrix}w_1 & 0\\ 0 & w_2\end{bmatrix}\right\}\\
&= \mathbf{M^{-1}}\{\mathbf{D^-W}\}
\end{aligned} \tag{2.27}$$

where

$$\begin{gathered}\mathbf{M}=\{\mu_i\delta_{ij}\},\qquad \mathbf{W}=\{w_i\delta_{ij}\},\qquad \mathbf{1}=\{\delta_{ij}\},\\ \mathbf{D}^{+}=\{D^m(\mu_i,\mu_j)\}=\{D^m(-\mu_i,-\mu_j)\},\\ \mathbf{D}^{-}=\{D^m(-\mu_i,\mu_j)\}=\{D^m(\mu_i,-\mu_j)\},\\ i,j=1{,}2\end{gathered} \tag{2.28}$$

Multiple stream approximation (N arbitrary)

Based on the preceding sketch of the four-stream case, it should be straightforward the generalisation to 2N streams.

The system of ordinary differential equations (2.17) is written in matrix form identically to (2.25):

$$\frac{\mathrm{d}}{\mathrm{d}\tau}\begin{bmatrix}\mathbf{I}^{+}\\ \mathbf{I}^{-}\end{bmatrix}=\begin{bmatrix}-\boldsymbol{\alpha} & -\boldsymbol{\beta}\\ \boldsymbol{\beta} & \boldsymbol{\alpha}\end{bmatrix}\begin{bmatrix}\mathbf{I}^{+}\\ \mathbf{I}^{-}\end{bmatrix}-\begin{bmatrix}\mathbf{Q}'^{+}\\ \mathbf{Q}'^{-}\end{bmatrix} \tag{2.29}$$

where the matrix elements are now defined in a more general way as:

$$\begin{gathered}\mathbf{I}^{\pm}=\{I^m(\tau,\pm\mu_i)\},\qquad i=1,\dots,N,\\ \mathbf{Q}'^{\pm}=\mathbf{M}^{-1}\mathbf{Q}^{\pm},\\ \mathbf{Q}^{\pm}=\{Q^m(\tau,\pm\mu_i)\},\qquad i=1,\dots,N,\\ \mathbf{M}=\{\mu_i\delta_{ij}\},\qquad i,j=1,\dots,N,\end{gathered} \tag{2.30}$$

$$\begin{gathered}\boldsymbol{\alpha}=\mathbf{M}^{-1}\{\mathbf{D}^{+}\mathbf{W}-\mathbf{1}\},\\ \boldsymbol{\beta}=\mathbf{M}^{-1}\{\mathbf{D}^{-}\mathbf{W}\},\\ \mathbf{W}=\{w_i\delta_{ij}\},\qquad i,j=1,\dots,N,\\ \mathbf{1}=\{\delta_{ij}\},\qquad i,j=1,\dots,N,\\ \mathbf{D}^{+}=\{D^m(\mu_i,\mu_j)\}=\{D^m(-\mu_i,-\mu_j)\},\qquad i,j=1,\dots,N,\\ \mathbf{D}^{-}=\{D^m(-\mu_i,\mu_j)\}=\{D^m(\mu_i,-\mu_j)\},\qquad i,j=1,\dots,N,\end{gathered} \tag{2.31}$$

where $\mathbf{1}$ corresponds to the identity matrix to distinguish it from the intensity vectors.

2.1.4. Discrete Ordinate Approximation: Solution

The ordinary differential equations in (2.17) are linear in the intensity, these problems are solved by finding the general solution, which is the sum of the homogeneous and particular solutions, and is also required to satisfy the boundary conditions.

In the following lines a brief summary of this process is provided, for full formulation details of the mathematical derivation, code implementation and computation of solutions the reader is referred to Stamnes et al. (2000), Laszlo et al. (2016).

Homogeneous solution

Equation (2.29) is a system of *2N* coupled, ordinary differential equations with constant coefficients, these coupled equations are linear and they can be uncoupled. Solutions to the homogeneous version of (2.29) ($\mathbf{Q}' = 0$) are seeked in the usual form of,

$$\mathbf{I}^{\pm} = \mathbf{G}^{\pm}\mathrm{e}^{-k\tau}, \qquad \mathbf{G}^{\pm} = \{G(\pm\mu_i)\}, \qquad (i = 1,..,N), \tag{2.32}$$

inserting (2.34) in (2.29) results in:

$$\begin{bmatrix} \boldsymbol{\alpha} & \boldsymbol{\beta} \\ -\boldsymbol{\beta} & -\boldsymbol{\alpha} \end{bmatrix} \begin{bmatrix} \mathbf{G}^{+} \\ \mathbf{G}^{-} \end{bmatrix} = k \begin{bmatrix} \mathbf{G}^{+} \\ \mathbf{G}^{-} \end{bmatrix} \tag{2.33}$$

Equation (2.33) is a standard algebraic eigenvalue problem of order *2N* × *2N* and its solution determines the eigenvalues k and eigenvectos $\mathbf{G}^{\pm}$.

Because of the special structure of the matrix in (2.29), the eigenvalues result in positive/negative pairs and the order of the algebraic problem is reduced (see, e.g., Stamnes et al., 2000). The resulting homogeneous solution can be written as:

$$I(\tau, \mu_i) = \sum_{\substack{j=-N \\ j\neq 0}}^{N} C_j G_j(\mu_i)\mathrm{e}^{-k_j\tau}, \qquad (i = -N, \dots, -1, 1, \dots, N) \tag{2.34}$$

where k and G_j are the complete set of eigenvalues and eigenvectors, respectively, and C_j are *2N* integration constants.

Particular solution

In order to obtain the particular solution, the inhomogeneous term in the beam and thermal sources in (2.4) are considered separately, and then the solutions are combined. For beam sources with the form of $Q^{(beam)} = X_0(\mu)\mathrm{e}^{-\tau/\mu_0}$ (2.16), the particular solution is (m-superscripts omitted):

$$I(\tau, \mu_i) = Z_0(\mu_i)\mathrm{e}^{-\tau/\mu_0} \tag{2.35}$$

where Z_0 are determined by the following standard system of *2N* linear algebraic equations

$$\sum_{\substack{j=-N \\ j\neq 0}}^{N} \left[\left(1 + \frac{\mu_j}{\mu_i}\right)\delta_{ij} - w_j D(\mu_i, \mu_j)\right] Z_0(\mu_j) = X_0(\mu_i), \qquad (i = \pm 1, \dots, \pm N) \tag{2.36}$$

For thermal sources, the emitted radiation is isotropic, therefore $Q^0(\tau) = (1-\omega)B[T(\tau)]$; and $Q^m(\tau) = 0$ for $m > 0$. The Planck function B is assumed by DISORT to vary linearly in optical depth across each layer, $B[T(\tau)] = b_0 + b_1\tau$, and the two coefficients b_0, b_1 are derived with the

boundary conditions at top and bottom layers τ_{top} and τ_{bottom}, where the temperatures are known. The thermal source term then has the form:

$$Q^{(thermal)}(\tau) = (1-\omega_0)(b_0 + b_1\tau), \tag{2.37}$$

thus leading to expressions for the particular solutions of:

$$I(\tau, \mu_i) = Y_0(\mu_i) + Y_1(\mu_i)\tau \tag{2.38}$$

Substituting (2.38) in (2.17) returns a system of linear algebraic equations for $Y_0(\mu_i)$ and $Y_1(\mu_i)$:

$$\begin{aligned} \sum_{\substack{j=-N \\ j\neq 0}}^{N} \left[\delta_{ij} - w_j D^0(\mu_i, \mu_j)\right] Y_1(\mu_j) &= (1-\omega) b_1 \\ \sum_{\substack{j=-N \\ j\neq 0}}^{N} \left[\delta_{ij} - w_j D^0(\mu_i, \mu_j)\right] Y_0(\mu_j) &= (1-\omega) b_0 + \mu_i Y_1(\mu_i) \end{aligned} \tag{2.39}$$

General solution

The general solution of (2.17) consists of a linear combination of all the homogeneous solutions, plus the particular solutions for beam and thermal emission sources:

$$I(\tau, \mu_i) = \sum_{\substack{j=-N \\ j\neq 0}}^{N} C_j G_j(\mu_i) \mathrm{e}^{-k_j \tau} + Z_0(\mu_i)\mathrm{e}^{-\tau/\mu_0} + \delta_{m0}[Y_0(\mu_i) + Y_1(\mu_i)\tau] \tag{2.40}$$

The k_j and $G_j(\mu_i)$ for $j \neq 0$ are respectively the eigenvalues and eigenvectors, μ_i the cosine of the quadrature angles, and C_j the constants of integration, to be determined by the boundary and layer continuity conditions.

Intensity at arbitrary angles

Equation (2.40) returns intensities at the *2N* quadrature points. Intensities at directions not coinciding with the quadrature points are calculated from the formal solution of (2.12). For a slab of optical thickness τ_L this solution is:

$$\begin{aligned} I(\tau, +\mu) &= I(\tau_L, +\mu)\mathrm{e}^{-(\tau_L - \tau)/\mu} + \int_{\tau}^{\tau_L} S(t, +\mu)\mathrm{e}^{-(t-\tau)/\mu}\frac{\mathrm{d}t}{\mu}, \\ I(\tau, -\mu) &= I(0, -\mu)\mathrm{e}^{-\tau/\mu} + \int_{0}^{\tau} S(t, -\mu)\mathrm{e}^{-(\tau - t)/\mu}\frac{\mathrm{d}t}{\mu}, \end{aligned} \tag{2.41}$$

where $\mu > 0$ and the m–superscript is omitted.If the source function $S(t, \pm\mu)$ is known, the intensity at arbitrary angles can be derived by integrating S. Using (2.15) with (2.38) the source function (2.13) can be written as:

$$S^m(\tau,\mu) = \sum_{\substack{i=-N \\ i\neq 0}}^{N} w_i D(\mu,\mu_i) I(\tau,\mu_i) + X_0(\mu)\mathrm{e}^{-\tau/\mu_0} + \delta_{m0}(1-\omega_0)(b_0 + b_1\tau) \tag{2.42}$$

Substituting the general solution for $I(\tau,\mu_i)$ (2.40) in (2.42) returns (m-superscripts are omitted):

$$S(\tau,\mu) = \sum_{j=-N}^{N} C_j G_j(\mu)\mathrm{e}^{-k_j\tau} + \delta_{m0}[V_0(\mu) + V_1(\mu)\tau], \tag{2.43}$$

where

$$\begin{aligned} C_0 G_0(\mu) = Z_0(\mu) &= \sum_{\substack{i=-N \\ i\neq 0}}^{N} w_i D(\mu,\mu_i)\, Z_0(\mu_i) + X_0(\mu), \qquad k_0 = 1/\mu_0 \\ G_j(\mu) &= \sum_{\substack{i=-N \\ i\neq 0}}^{N} w_i D(\mu,\mu_i)\, G_j(\mu_i), \qquad \text{for } j \neq 0, \text{and} \\ V_l(\mu) &= \sum_{\substack{i=-N \\ i\neq 0}}^{N} w_i D^0(\mu,\mu_i)\, Y_l(\mu_i) + (1-\omega_0) b_l, \qquad (l = 1, 0) \end{aligned} \tag{2.44}$$

In the equations above the m-superscript is omitted, however, in $D^0$is explicitly written to remind that thermal emissions contributes only to the azimuth-independent component of the intensity.

In a multilayered medium the integral in (2.41) is evaluated by integrating layer-by-layer as follows, for $\tau_{p-1} \le \tau \le \tau_p$ and $\mu > 0$:

$$\begin{aligned} \int_{\tau}^{\tau_L} S(t,+\mu)\mathrm{e}^{\frac{-(t-\tau)}{\mu}}\frac{\mathrm{d}t}{\mu} &= \int_{\tau}^{\tau_p} S_p(t,+\mu)\mathrm{e}^{\frac{-(t-\tau)}{\mu}}\frac{\mathrm{d}t}{\mu} + \sum_{n=p+1}^{L}\left\{\int_{\tau_{n-1}}^{\tau_n} S_n(t,+\mu)\mathrm{e}^{\frac{-(t-\tau)}{\mu}}\frac{\mathrm{d}t}{\mu}\right\} \\ \int_{0}^{\tau} S(t,-\mu)\mathrm{e}^{\frac{-(\tau-t)}{\mu}}\frac{\mathrm{d}t}{\mu} &= \sum_{n=1}^{p-1}\left\{\int_{\tau_{n-1}}^{\tau_n} S_n(t,-\mu)\mathrm{e}^{\frac{-(\tau-t)}{\mu}}\frac{\mathrm{d}t}{\mu}\right\} + \int_{\tau_{p-1}}^{\tau} S_p(t,-\mu)\mathrm{e}^{\frac{-(\tau-t)}{\mu}}\frac{\mathrm{d}t}{\mu} \end{aligned} \tag{2.45}$$

Using the $S_n(t,\mu)$ expression given in (2.43) and substituting in (2.45), the intensities at τ in layer p are:

$$I(\tau,+\mu) = I(\tau_L,+\mu)\mathrm{e}^{\frac{-(\tau_L-\tau)}{\mu}} + \sum_{n=p}^{L}\left\{\begin{array}{l} \displaystyle\sum_{j=-N}^{N} C_{jn}\frac{G_{jn}(+\mu)}{1+k_{jn}\mu}E_{jn}(\tau,+\mu) \\ +\delta_{m0}[V_{0n}(+\mu)F_{0n}(\tau,+\mu) + V_{1n}(+\mu)F_{1n}(\tau,+\mu)] \end{array}\right\} \tag{2.46}$$

$$I(\tau,-\mu) = I(0,-\mu)\mathrm{e}^{-\tau/\mu} + \sum_{n=1}^{p}\left\{\begin{array}{l} \displaystyle\sum_{j=-N}^{N} C_{jn}\frac{G_{jn}(-\mu)}{1-k_{jn}\mu}E_{jn}(\tau,-\mu) \\ +\delta_{m0}[V_{0n}(-\mu)F_{0n}(\tau,-\mu) + V_{1n}(-\mu)F_{1n}(\tau,-\mu)] \end{array}\right\} \tag{2.47}$$

where

$$\begin{aligned} E_{jn}(\tau,+\mu) &= \exp\{-k_{jn}\tau_{n-1} - (\tau_{n-1}-\tau)/\mu\} - \exp\{-k_{jn}\tau_n - (\tau_n-\tau)/\mu\}, \\ F_{0n}(\tau,+\mu) &= \exp\{-(\tau_{n-1}-\tau)/\mu\} - \exp\{-(\tau_n-\tau)/\mu\}, \\ F_{1n}(\tau,+\mu) &= (\tau_{n-1}+\mu)\exp\{-(\tau_{n-1}-\tau)/\mu\} - (\tau_n+\mu)\exp\{-(\tau_n-\tau)/\mu\}, \end{aligned} \tag{2.48}$$

with τ_{n-1} replaced by τ for $n = p$, and

$$\begin{aligned} E_{jn}(\tau,-\mu) &= \exp\{-k_{jn}\tau_n - (\tau-\tau_n)/\mu\} - \exp\{-k_{jn}\tau_{n-1} - (\tau-\tau_{n-1})/\mu\}, \\ F_{0n}(\tau,-\mu) &= \exp\{-(\tau-\tau_n)/\mu\} - \exp\{-(\tau-\tau_{n-1})/\mu\}, \\ F_{1n}(\tau,-\mu) &= (\tau_n-\mu)\exp\{-(\tau-\tau_n)/\mu\} - (\tau_{n-1}-\mu)\exp\{-(\tau-\tau_{n-1})/\mu\}, \end{aligned} \tag{2.49}$$

with τ_n replaced by τ for $n = p$.

Boundary conditions

The resulting system of ordinary equations for solving the radiative transfer must be solved subject to multiple boundary conditions. At the top boundary, it is assumed that the medium is illuminated by a combination of known isotropic diffuse radiation and parallel beam treated as a pseudosource. The bottom boundary is characterised with a known bidirectional reflectance distribution function (BRDF) $\rho_d(\mu,\phi;-\mu',\phi')$, and thermal emission specified in terms of the Planck function B and directional emissivity $\varepsilon(\mu)$:

$$\begin{aligned} I(\tau=0,-\mu,\phi) &= I_{top}(\mu,\phi) = I_{diffuse} + F_0\delta(\mu-\mu_0)\delta(\phi-\phi_0), \\ I(\tau=\tau_L,+\mu,\phi) = I_g(\mu,\phi) &= \varepsilon(\mu)B(T_g) + \frac{1}{\pi}\mu_0 F_0 \mathrm{e}^{-\tau_L/\mu_0}\rho_d(\mu,\phi;-\mu',\phi') \\ &\quad + \frac{1}{\pi}\int_0^{2\pi}\mathrm{d}\phi'\int_0^1 \rho_d(\mu,\phi;-\mu',\phi')\, I(\tau_L,-\mu',-\phi')\mu'\mathrm{d}\mu'. \end{aligned} \tag{2.50}$$

where I_{top} and $I_g$are the intensities incident at the top and bottom boundaries, respectively; τ_L is the total optical depth of the entire medium (column optical depth or opacity). F_0 is the flux of incident beam normal to the direction of incidence at the top boundary.

It is also assumed that the lower boundary is totally opaque and has no preferred direction; in other words, the surface BRDF depends only on the difference between incident and reflected radiation azimuthal angles and is symmetric about the principal plane, thus allowing the expansion of $\rho_d(\mu,\phi;-\mu',\phi')$ in a Fourier series of 2M terms, in a similar way to (2.11):

$$\begin{aligned} \rho_d(\mu,\phi;-\mu',\phi') &= \rho_d(\mu,-\mu';\phi-\phi') = \sum_{m=0}^{2M-1}\rho_d^m(\mu,-\mu')\cos m(\phi_0-\phi), \\ \rho_d^m(\mu,-\mu') &= (2-\delta_{m0})\frac{1}{\pi}\int_0^{\pi}\rho_d(\mu,-\mu';\phi-\phi')\cos m(\phi-\phi')\mathrm{d}(\phi-\phi'), \end{aligned} \tag{2.51}$$

Substituting (2.51) into the second equation of (2.50) and using the Fourier expansion of the intensity, the bottom boundary condition results in

$$\begin{aligned} I(\tau_L,+\mu) \equiv I_g^m(\mu) \equiv \delta_{m0}\varepsilon(\mu)B(T_g) &+ \frac{1}{\pi}\mu_0 F_0 e^{-\tau_L/\mu_0}\rho_d^m(\mu,-\mu_0) \\ &+ (1+\delta_{m0})\sum_{j=1}^{N} w_j\mu_j\rho_d^m(\mu,-\mu_j)I^m(\tau_L,-\mu_j). \end{aligned} \tag{2.52}$$

In addition, it is required that in the multilayered medium the intensity must be continuous across layer interfaces. Therefore, the boundary and continuity conditions for equation (2.17) are:

$$\begin{aligned} I_1^m(0,-\mu_i) &= I_{top}^m(\mu_i), && (i=1,\dots,N);\\ I_p^m(\tau_p,\mu_i) &= I_{p+1}^m(\tau_p,\mu_i), && (p=1,\dots,L;\quad i=\pm1,\dots,\pm N);\\ I_L^m(\tau_L,+\mu_i) &= I_g^m(\mu_i), && (i=1,\dots,N); \end{aligned} \tag{2.53}$$

For the discussion of the boundary conditions, the discrete ordinate solution (2.40) for the p-th layer is rewritten below in the following form:

$$I_p(\tau,\mu_i)=\sum_{j=1}^{N}\left\{C_{jp}G_{jp}(\mu_i)\mathrm{e}^{-k_{jp}\tau}+C_{-jp}G_{-jp}(\mu_i)\mathrm{e}^{+k_{jp}\tau}\right\}+U_p(\tau,\mu_i) \tag{2.54}$$

where $k_{jp}>0$ and $k_{-jp}=-k_{jp}$, and the sum contains the homogeneous solution involving the unknown coefficients C_{jp} to be determined, and U_p is the particular solution given by:

$$U_p(\tau,\mu_i)=Z_0(\mu_i)\mathrm{e}^{-\tau/\mu_0}+\delta_{m0}[Y_0(\mu_i)+Y_1(\mu_i)\tau] \tag{2.55}$$

Inserting (2.54) into (2.53) results in:

$$\sum_{j=1}^{N}\left\{C_{j1}G_{j1}(-\mu_i)+C_{-j1}G_{-j1}(-\mu_i)\right\}=I_{top}(-\mu_i)-U_1(0,-\mu_i),\qquad \{i=1,\dots,N\}; \tag{2.56}$$

$$\begin{aligned} \sum_{j=1}^{N}\left\{\begin{matrix} C_{jp}G_{jp}(\mu_i)\mathrm{e}^{-k_{jp}\tau_p}+C_{-jp}G_{-jp}(\mu_i)\mathrm{e}^{k_{jp}\tau_p}\\ -\left[C_{j,p+1}G_{j,p+1}(\mu_i)\mathrm{e}^{-k_{j,p+1}\tau_p}+C_{-j,p+1}G_{-j,p+1}(\mu_i)\mathrm{e}^{k_{j,p+1}\tau_p}\right]\end{matrix}\right\}\\ =U_{p+1}(\tau_p,\mu_i)-U_p(\tau_p,\mu_i),\qquad \{p=1,..,L-1;\ i=\pm1,\dots,\pm N\}; \end{aligned} \tag{2.57}$$

$$\sum_{j=1}^{N}\left\{C_{jL}r_{jL}(\mu_i)G_{jL}(\mu_i)\mathrm{e}^{-k_{jL}\tau_L}+C_{-jL}r_{-jL}(\mu_i)G_{-jL}(\mu_i)\mathrm{e}^{k_{jL}\tau_L}\right\}=\Gamma(\tau_L,\mu_i),\qquad \{i=1,\dots,N\}; \tag{2.58}$$

where

$$r_{jL}(\mu_i)=1-(1+\delta_{m0})\sum_{n=1}^{N}\rho_d(\mu_i,-\mu_n)w_n\mu_nG_{jL}(-\mu_n)/G_{jL}(\mu_i), \tag{2.59}$$

$$\begin{aligned} \Gamma(\tau_L,\mu_i)=\delta_{m0}\varepsilon(\mu_i)B(T_g)-U_L(\tau_L,+\mu_i)+\frac{1}{\pi}\mu_0F_0\mathrm{e}^{-\tau_L/\mu_0}\rho_d(\mu_i,-\mu_0)\\ +(1+\delta_{m0})\sum_{j=1}^{N}\rho_d(\mu_i,-\mu_j)w_j\mu_jU_L(\tau_L,-\mu_j) \end{aligned} \tag{2.60}$$

Equations (2.56)-(2.58) form a $(2N\times L)\times(2n\times L)$ system of linear algebraic equations, from which the $2N\times L$ unknown coefficients C_{jp} $(j=\pm1,\dots,N;\ p=1,..,L)$ must be determined for deriving the complete solution of the radiative transfer within the discrete ordinate approximation.

2.2. Light scattering by aerosol particles

The scattering of light by an arbitrary non-spherical particle located at the origin of a spherical coordinate system can be described with, a plane electromagnetic wave incident in a direction specified by the unit vector $\mathbf{n}_{\mathrm{inc}}$ given by (e.g., Mishchenko et al., 2000; 2006):

$$\mathbf{E}^{\mathrm{inc}}(\mathbf{R}) = \mathbf{E}^{\mathrm{inc}} \exp(ik\mathrm{n}_{\mathrm{inc}}\mathrm{R}) = \left(E_{\vartheta}^{\mathrm{inc}}\boldsymbol{\vartheta}_{\mathrm{inc}} + E_{\varphi}^{\mathrm{inc}}\boldsymbol{\varphi}_{\mathrm{inc}}\right) \exp(ik\mathbf{n}_{\mathrm{inc}}\mathbf{R}), \tag{2.61}$$

where $i = (-1)^{1/2}$, $k = 2\pi/\lambda$ for free-space wavelength λ, $\mathbf{R}$ is the radius vector with its origin at the origin of the coordinate system, and $\boldsymbol{\vartheta}_{\mathrm{inc}}$ and $\boldsymbol{\varphi}_{\mathrm{inc}}$ are the unit vectors in the ϑ- and φ-directions, such that $\mathbf{n}_{\mathrm{inc}} = \boldsymbol{\vartheta}_{\mathrm{inc}} \times \boldsymbol{\varphi}_{\mathrm{inc}}$. The time factor $\exp(-i\omega t)$ is assumed and is suppressed through this text only for simplification. In the far-field region ($kR \gg 1$), the scattered wave becomes spherical and is given by

$$\mathbf{E}^{\mathrm{sca}}(\mathbf{R}) = E_{\vartheta}^{\mathrm{sca}}(R, \mathbf{n}_{\mathrm{sca}})\boldsymbol{\vartheta}_{\mathrm{sca}} + E_{\varphi}^{\mathrm{sca}}(R, \mathbf{n}_{\mathrm{sca}})\boldsymbol{\varphi}_{\mathrm{sca}}, \quad \mathbf{n}_{\mathrm{sca}} = \mathbf{R}/R, \quad kR \gg 1, \tag{2.62}$$

$$\mathbf{R}\mathbf{E}^{\mathrm{sca}}(\mathbf{R}) = 0, \tag{2.63}$$

$$\begin{bmatrix} E_{\vartheta}^{\mathrm{sca}} \\ E_{\varphi}^{\mathrm{sca}} \end{bmatrix} = \frac{\exp(ikR)}{R}\mathbf{S}(\mathbf{n}_{\mathrm{inc}}, \mathbf{n}_{\mathrm{sca}}) \begin{bmatrix} E_{\vartheta}^{\mathrm{inc}} \\ E_{\varphi}^{\mathrm{inc}} \end{bmatrix} \tag{2.64}$$

where $\mathbf{S}$ is the 2×2 amplitude scattering matrix which transforms the electric vector components of the incident wave into the components of the scattered wave.

The amplitude scattering matrix is the primary quantity that defines the scattering law; it depends on the directions of incidence and scattering, as well as on the size, shape, orientation and composition of the scattering particle. If known, it enables to compute any other light scattering characteristic of the particle, i.e., the radiative properties.

The scattering of light by a particle is completely described by the extinction (C_{ext}) and scattering (C_{sca}) cross-sections, and the dimensionless *scattering matrix* $\boldsymbol{P}$ (Bohren and Huffman, 1983; Mishchenko et al., 2000):

$$\boldsymbol{P}(\theta) = \begin{pmatrix} P_{11}(\theta) & P_{12}(\theta) & P_{13}(\theta) & P_{14}(\theta) \\ P_{21}(\theta) & P_{22}(\theta) & P_{23}(\theta) & P_{24}(\theta) \\ P_{31}(\theta) & P_{32}(\theta) & F_{33}(\theta) & P_{34}(\theta) \\ P_{41}(\theta) & P_{42}(\theta) & F_{43}(\theta) & P_{44}(\theta) \end{pmatrix}, \tag{2.65}$$

where θ denotes the scattering angle, i.e. the angle between the incident and scattered directions.

The scattering matrix describes the transformation of the Stokes vector of the incident beam, $\boldsymbol{I}_{\mathbf{inc}}$, into the Stokes vector of the far-field scattered beam, $\boldsymbol{I}_{\mathbf{sca}}$:

$$\boldsymbol{I}_{sca} = \frac{C_{\text{sca}}}{4\pi R^2}\boldsymbol{P}(\theta)\boldsymbol{I}_{\text{inc}} \tag{2.66}$$

where R is the distance in the far-field from the scatterer to the observation point.

The Stokes vector is defined as a (4×1) column containing the Stokes parameters that describe the polarisation state of electromagnetic radiation $I,\ Q,\ U$ and V in the form of:

$$\boldsymbol{I} = \begin{bmatrix} I \\ Q \\ U \\ V \end{bmatrix} \tag{2.67}$$

The definition of the Stokes parameters and their expressions can be found in, e.g., van de Hulst (1957), Hansen and Travis (1974), Bohren and Huffman (1983).

The scattering matrix (2.65) depends on the wavelength of radiation, the directions of incidence and scattering (i.e., the scattering angle), as well as on the microphysical properties of the particle (size, shape and composition) and its orientation with respect to the reference frame

The scattering matrix is reduced to only six independent non-zero elements when an ensemble of randomly oriented rotationally symmetric, independently scattering particles is considered, resulting in (see definitions for each component in, e.g., Mishchenko et al., 2000):

$$\boldsymbol{P}(\theta) = \begin{pmatrix} P_{11}(\theta) & P_{12}(\theta) & 0 & 0 \\ P_{12}(\theta) & P_{22}(\theta) & 0 & 0 \\ 0 & 0 & P_{33}(\theta) & P_{34}(\theta) \\ 0 & 0 & -P_{34}(\theta) & P_{44}(\theta) \end{pmatrix}. \tag{2.68}$$

The (1,1) element in (2.68) is the well-known phase function and describes the angular distribution of intensity for the scattered radiation, and it is normalised such that the integral over the scattering angle θ is:

$$\frac{1}{2}\int_0^{\pi} P_{11}(\theta)\,\sin(\theta)\,\mathrm{d}\theta = 1. \tag{2.69}$$

The rest of the non-zero elements of the matrix relate the polarisation components between the incident and scattered beams. In atmospheric radiative transfer calculations, the polarisation can be neglected without introducing large errors to radiances or fluxes and therefore we will do so during this thesis.

The quantity

$$g = \frac{1}{2}\int_0^{\pi} P_{11}(\theta)\,\cos(\theta)\,\sin(\theta)\,\mathrm{d}\theta \tag{2.70}$$

is called the asymmetry parameter of the phase function and provides a measure for the direction of light scattering, it is positive for particles that scatter predominantly in the forward

direction, negative for backscattering particles, and $g = 0$ for symmetric phase functions, i.e. light is isotropically scattered.

The absorption cross section is defined as the difference between the extinction and scattering cross sections,

$$C_{\mathrm{abs}} = C_{\mathrm{ext}} - C_{\mathrm{sca}}, \tag{2.71}$$

The probability that a photon incident on a small-volume element is not absorbed is equal to the ratio of the scattering and extinction cross sections and it is called the single scattering albedo ω_0:

$$\omega_0 = \frac{C_{\mathrm{sca}}}{C_{\mathrm{ext}}} = \frac{C_{\mathrm{sca}}}{C_{\mathrm{sca}} + C_{\mathrm{abs}}}, \tag{2.72}$$

When the single scattering albedo tends toward zero, scattering plays a negligible role in the radiation extinction, and thus only absorption properties are required.

2.3. Calculation of radiative properties

Several approaches have been considered in this research study for modelling non-spherical dust aerosol particle optical properties for radiative transfer calculations and retrievals, including, e.g.; the use of analytical single scattering phase functions (Gillespie, 1992; Zhang and Li, 2016), or the use of experimental retrievals from laboratory measurements of Martian dust analogues (Muñoz et al., 2012; Dabrowska et al., 2015). The emphasis here is placed on the formulation of the T-matrix theory used for modelling the light scattering by randomly oriented non-spherical dust aerosol particles (e.g., Dubovik et al., 2006; Mishchenko et al., 1997; Wolff et al., 2001; Merikallio et al., 2011).

First, it is convenient to introduce the size parameter. The size parameter x is the ratio of the size of the particle to the wavelength of the radiation being scattered (λ):

$$x = \frac{2\pi r}{\lambda} = kr, \tag{2.73}$$

where r is the radius of the particle. In the case of non-spherical particles, this parameter corresponds to the radius of the volume or area equivalent sphere (e.g., Mishchenko and Travis, 1998).

This quantity is used for evaluating the scattering regime and determining the most appropriate light scattering theory approach. When the particle is very large compared to the wavelength of incident radiation ($x \gg 1$), the geometrical optics theory is often sufficient to model the scattering of that particle and the scattering intensity does not depend on the wavelength. In

case of $x \ll 1$, the Rayleigh scattering theory is more appropriate; within this range, the scattering intensity is proportional to λ^{-4}. As the size parameter approaches to 1 (x ~ 1 to 50), more sophisticated theories are required for the calculation of the scattered intensity, such as Mie theory.

2.3.1. Mie theory

The Lorenz-Mie-Debye, Lorenz-Mie or mostly known simply as Mie theory provides an analytical solution to calculate the scattering and absorption coefficients, including the phase function, of a spherical particle of radius r at a given wavelength λ, given the size parameter $x = 2\pi r/\lambda$, and complex refractive index, m.

Because of spherical particle symmetries, only the elements S_1 and S_2 of the amplitude scattering matrix (2.64) are non-zero, meaning that scattering by such a sphere does not depolarise the incident radiation and are expressed as a function of the scattering angle, size parameter x and complex refractive index m. For the calculation of the rest of scattering coefficients, Bohren and Huffman (1983) first represented the scattered wave as a series of spherical harmonics. The plane wave incident on the particle is then also expanded in spherical harmonics, and by choosing appropriate boundary conditions at the surface of the particle and setting the expansion coefficients equal to each other, the following infinite expansions are obtained:

$$S_1(x,m,\theta) = \sum_{n=1}^{\infty} \frac{2n+1}{n(n+1)} \big(a_n(x,m)\pi_n(\theta) + b_n(x,m)\tau_n(\theta)\big), \tag{2.74}$$

$$S_2(x,m,\theta) = \sum_{n=1}^{\infty} \frac{2n+1}{n(n+1)} \big(a_n(x,m)\tau_n(\theta) + b_n(x,m)\pi_n(\theta)\big), \tag{2.75}$$

where a_n and b_n depend on the size parameter x and complex refractive index m via the Riccati-Bessel functions, and π_n and τ_n are functions involving the Legendre polynomials (e.g., Bohren and Huffman, 1983; Liou, 2002). The extinction and scattering cross-sections are derived from these elements and result in the following expressions:

$$C_{\text{ext}}(x,m) = \frac{2\pi}{k^2} \sum_{n=1}^{\infty} (2n+1)\text{Re}\big(a_n(x,m) + b_n(x,m)\big), \tag{2.76}$$

$$C_{\text{sca}}(x,m) = \frac{2\pi}{k^2} \sum_{n=1}^{\infty} (2n+1)(|a_n(x,m)|^2 + |b_n(x,m)|^2), \tag{2.77}$$

and the Mie scattering phase function can be written:

$$P(x,m,\theta) = \frac{2\pi\,(|S_1(x,m,\theta)|^2 + |S_2(x,m,\theta)|^2)}{k^2\, C_{\text{sca}}(x,m)} = 1 + \sum_{n=1}^{\infty} A_n(x,m) P_n(\cos\theta), \tag{2.78}$$

where P_n are the Legendre polynomials and the coefficients A_n are functions of a_n and b_n. In practice, for the calculation of the radiative properties for Mie scattering spheres a truncation order is selected linked to the size parameter x.

2.3.2. Rayleigh scattering

In the Rayleigh scattering approximation ($x \ll 1$), the arbitrarily shaped particle is considered as a single electric dipole oscillating in phase with the incident electric field, resulting in the following expressions for the elements of the amplitude scattering matrix (Bohren and Huffman, 1983; van de Hulst, 1957):

$$S_1(\theta) = -\frac{ik^3\alpha}{4\pi}, \tag{2.79}$$

$$S_2(\theta) = S_1(\theta)\cos\theta, \tag{2.80}$$

$$C_{\text{sca}} = \frac{8}{3}\pi k^4 |\alpha|^2 \tag{2.81}$$

$$C_{\text{ext}} = k\,\text{Im}(\alpha) \tag{2.82}$$

$$P(\theta) = \frac{3}{4}(1+\cos^2\theta) \tag{2.83}$$

2.3.3. T-matrix method

The use of a matrix approach to derive the light scattering properties was first given by Waterman (1965) and it has become widely used for particle scattering computations within multiple fields. Currently, the T-matrix method is the fastest exact technique for the computation of non-spherical scattering based on the direct solution of Maxwell's equations (see T-matrix thematic database, Mishchenko et al., 2017). The formulation of the scattering problem is based on solutions to the integral formulation of Maxwell's equation: due to the linearity of those equations, it is possible to expand the incident and scattered waves into spherical harmonics, and then relate the scattering coefficients through a transformation matrix (the "T-matrix"). In this section, a brief summary and the main expressions involved in T-matrix method calculations are provided following the notation by Mishchenko et al.; the complete derivation of the method is provided in, e.g., Mishchenko et al., (1996); while the capabilities of the code are reported in Mishchenko and Travis (1998).

Let's consider the scattering of a plane electromagnetic wave by a single non-spherical particle in a fixed orientation with respect to the reference frame. In the T-matrix approach, the incident and scattered fields can be expressed as a series of spherical harmonics:

$$\mathbf{E}^{\mathrm{inc}}(\mathbf{R}) = \sum_{n=1}^{\infty}\sum_{m=-n}^{n}[a_{mn}\mathrm{Rg}\mathbf{M}_{mn}(k\mathbf{R}) + b_{mn}\mathrm{Rg}\mathbf{N}_{mn}(k\mathbf{R})], \tag{2.84}$$

$$\mathbf{E}^{\mathrm{sca}}(\mathbf{R}) = \sum_{n=1}^{\infty}\sum_{m=-n}^{n}[p_{mn}\mathbf{M}_{mn}(k\mathbf{R}) + q_{mn}\mathbf{N}_{mn}(k\mathbf{R})], \tag{2.85}$$

where $\mathbf{M}_{mn}$ and $\mathbf{N}_{mn}$ are proportional to the spherical Hankel functions as described in Mishchenko et al. (1996), and Rg denotes the regular solution. Owing to the linearity of Maxwell's equations and boundary conditions, the relations between the incident field coefficients, a_{mn} and b_{mn}, and the scattered field coeficients, p_{mn} and q_{mn}, are given as follows:

$$p_{mn} = \sum_{n'=1}^{\infty}\sum_{m'=-n'}^{n'}[T^{11}_{mnm'n'}a_{m'n'} + T^{12}_{mnm'n'}b_{m'n'}], \tag{2.86}$$

$$q_{mn} = \sum_{n'=1}^{\infty}\sum_{m'=-n'}^{n'}[T^{21}_{mnm'n'}a_{m'n'} + T^{22}_{mnm'n'}b_{m'n'}], \tag{2.87}$$

or in matrix notation:

$$\begin{bmatrix}\mathbf{p}\\ \mathbf{q}\end{bmatrix} = \mathbf{T}\begin{bmatrix}\mathbf{a}\\ \mathbf{b}\end{bmatrix} = \begin{bmatrix}\mathbf{T}^{11} & \mathbf{T}^{12}\\ \mathbf{T}^{21} & \mathbf{T}^{22}\end{bmatrix}\begin{bmatrix}\mathbf{a}\\ \mathbf{b}\end{bmatrix} \tag{2.88}$$

where **T** is the transformation matrix. If the **T** matrix for a given scatterer is known, it can be used to calculate the scattered field and, thus, the amplitude scattering matrix.

A fundamental feature of this approach is that the elements of the **T** matrix are independent of the incident and scattered fields, they only depend on the physical (particle size, shape and orientation) and optical (refractive index) properties of the scattering particle.

The computation of the **T** matrix is based on the extreme boundary condition method (Waterman, 1965; Mishchenko et al., 1996). In addition to the expansion of the incident and scattered fields given by equations (2.84) and (2.85), the internal field is also expanded in vector spherical functions:

$$\mathbf{E}^{\mathrm{int}}(\mathbf{R}) = \sum_{n=1}^{\infty}\sum_{m=-n}^{n}[c_{mn}\mathrm{Rg}\mathbf{M}_{mn}(m_r k\mathbf{R}) + d_{mn}\mathrm{Rg}\mathbf{N}_{mn}(m_r k\mathbf{R})], \tag{2.89}$$

where m_r is the complex index of refraction of the particle. The expansion coefficients of the internal field can be related to those of the incident and scattered with the following expressions:

$$\begin{bmatrix}\mathbf{a}\\ \mathbf{b}\end{bmatrix} = \begin{bmatrix}\mathbf{Q}^{11} & \mathbf{Q}^{12}\\ \mathbf{Q}^{21} & \mathbf{Q}^{22}\end{bmatrix}\begin{bmatrix}\mathbf{c}\\ \mathbf{d}\end{bmatrix}, \tag{2.90}$$

$$\begin{bmatrix}\mathbf{p}\\ \mathbf{q}\end{bmatrix} = -\begin{bmatrix}\mathrm{Rg}\mathbf{Q}^{11} & \mathrm{Rg}\mathbf{Q}^{12}\\ \mathrm{Rg}\mathbf{Q}^{21} & \mathrm{Rg}\mathbf{Q}^{22}\end{bmatrix}\begin{bmatrix}\mathbf{c}\\ \mathbf{d}\end{bmatrix}, \tag{2.91}$$

where the elements of the $\mathbf{Q}$ matrix are two-dimensional integrals which must be numerically evaluated over the particle surface and depend again on the physical and optical properties of the particle. The combination of expressions (2.88), (2.90) and (2.91) return:

$$\mathbf{T} = -\mathrm{Rg}\mathbf{Q}[\mathbf{Q}]^{-\mathbf{1}} \tag{2.92}$$

In a general case, $\mathbf{T}$ and $\mathbf{Q}$ matrices contain infinite number of elements as denoted in equations (2.84), (2.85) and (2.89); for practical purposes, these summations are truncated following a certain convergence criteria. The calculation of $\mathbf{T}$ is significantly simplified, reducing to a diagonal matrix in the m and m' indices, when assuming an ensemble of randomly oriented particles; which is reasonable assumption when simulating aerosol particles. In addition, the calculations are also greatly simplified when particles with rotational symmetry considered (Mishchenko et al., 1996).

For this research work, T-matrix calculations have been performed using the publicly available FORTRAN code[1] (Mishchenko and Travis, 1998). This code has been extensively used in previous studies to model the light scattering of dust aerosol in both Earth and Mars' atmospheres (e.g., Dubovik et al., 2006, Wolff et al., 2009; Mishchenko et al., 2017). The full scattering matrix and aerosol radiative properties, such as the single scattering albedo and extinction efficiency, are calculated for a randomly oriented distribution of particles for the following input parameters: wavelength of incident solar radiation, the complex refraction index of the particle, particle size distribution parameters and the shape of the particle. The currently available particle shapes in this code are spheroids, cylinders and Chebyshev particles; these shapes can be then particularised with the diameter-to-length (D/L) aspect ratio parameter (Mishchenko and Travis, 1998).

2.3.4. Additional methods

There are many more numerical solution techniques available for performing the scattering calculations for arbitrarily shaped particles, such as the finite-difference time-domain (FDTD), finite-difference frequency-domain (FDFD), discrete dipole approximation (DDA), finite element (FEM), separation of variables (SVM) or fractal aggregates. For instance, in the FDTD method, the electric and magnetic fields are iterated by solving them in a discretised grid in an alternate manner. In the case of DDA, the scattering particle is described by a finite number of individual dipoles, it is used to model light scattering from small particles of arbitrary shape, and it is very powerful for modelling particle clusters or aggregates, such as Titan aerosols. However, its accuracy and potential is greatly constrained by the computational complexity. In contrast to other approaches that solve the wave equation using an expansion of vector spherical wave functions (e.g., Mie or T-matrix), in DDA for each incoming and outgoing light direction incident on the particle the entire calculation must be repeated. An overview of most of them together

[1] https://www.giss.nasa.gov/staff/mmishchenko/t_matrix.html

with their corresponding numerical codes can be found in, e.g., Liou, (2002), Yurkin and Hoekstra (2007), and Wriedt (2009).

2.3.5. Approximate scattering phase functions

Depending on the physical properties of the particles, the scattering phase function may exhibit large oscillatory variations as a function of the scattering angle, although these features may disappear for polydispersed and randomly oriented non-symmetric particles. For both direct and inverse radiative transfer calculations, it is of high convenience to use simple phase functions for modelling non-spherical particles and to approximate the numerical phase functions when these are cumbersome to generate. For instance, the Dirac delta, truncated Legendre polynomial, or Henyey-Greenstein approximations are among the most used for radiative transfer calculations (Liou, 2002). In particular, the Double Henyey-Greenstein function (Gillespie, 1992) is considered in the retrieval of dust aerosol single scattering phase function presented in Chapter 6.

2.3.6. Experimental retrievals of particle's radiative properties

Radiative properties of particles can be retrieved from experiments instead of derived from direct calculations. This approach is followed for the evaluation of theories and numerical methods or for those cases in which the lack of prior knowledge and/or the complex nature of particles make direct predictions impossible or very uncertain. In these experiments, the measured intensities and fluxes can be used to build databases of scattering properties or validate models for the radiative properties of particles (see, Muñoz et al., 2012; Dabrowska et al., 2015)

3. MARS ATMOSPHERE MODEL

In this Chapter, an overview of the retrieval outcomes from previous studies for characterising Martian atmospheric dust aerosol by different exploration missions and techniques is provided. Water ice and CO_2 ice aerosols are out of the scope of this research study as indicated on page 65. Following this, the Mars atmosphere model used in this research work is detailed.

3.1. Martian dust aerosol properties

Numerous studies have used different approaches for modelling the observations retrieved by different missions in order to characterise and constrain various properties of atmospheric dust. As it has been shown in the previous section, in addition to the atmospheric dust loading and its distribution, the main properties of the aerosol particles important for climate studies and radiative transfer modelling are the size distribution of the particles, the particle shape, the single scattering albedo, phase function and imaginary part of the refractive index. A historical review of the work characterising those dust aerosol properties is presented in this section. For comprehensive and detailed reviews, excellent works have been published by Murphy et al. (1993), Dlugach et al. (2003), Smith (2008), Medvedev et al. (2011), and Kahre et al. (2017).

3.1.1. Dust optical depth

The data collected by both in-orbit and surface-based instruments have greatly contributed to characterise the main features of the dust cycle in the current Martian climate. Although orbital observations allow for a more complete characterisation of dust loading over spatial and temporal scales, more modelling or retrieval assumptions are needed. Therefore, surface-based measurements of the column optical depth are required for characterising of the atmosphere at the specific sites and providing ground truth for orbital observations (Smith, 2004, 2009; Wolff et al., 2009; Lemmon et al., 2015)

In the past decades, a number of spacecraft missions contributed to our present knowledge of airborne dust properties. Mariner 9 Infrared Interferometer Spectrometer (IRIS) instrument studied the decay of the 1971 global dust storm (Hanel et al., 1972). The Infrared Thermal Mapper (IRTM) instrument on-board the Viking mission spacecraft monitored dust optical depth by measuring the absorption in the 9 μm silicate band, including retrievals during two planet-encircling dust storms (Martin and Richardson, 1993). The instruments on the Mars Global Surveyor (MGS) spacecraft mapped the spatial and temporal patterns of airborne dust and surface properties with unprecedented coverage starting in 1999 (MY 24). The Thermal Emission Spectrometer (TES) and the Mars Orbiter Camera (MOC) monitored airborne dust in the thermal infrared through nadir and limb observations in the thermal infrared and visible, respectively (Smith, 2004; Cantor et al., 2001). Following this, data acquired with the broadband

infrared Thermal Emission Imaging System (THEMIS) on Mars Odyssey mission (2001) overlapped in time with MGS-TES retrievals, resulting in a continuous record of derived atmospheric dust opacity at 9 μm (see Figure 1.5) from the beginning of the MGS mission to the present day (Mars Odyssey is currently the longest serving spacecraft in Mars) (Smith, 2009; Montabone et al., 2015).

At present, in addition to Mars Odyssey, data acquired by the Planetary Fourier Spectrometer (PFS; Giuranna et al., 2016), the OMEGA infrared mapping spectrometer (Määttänen et al, 2009) and ultraviolet and infrared atmospheric spectrometer SPICAM (Montmessin et al., 2017a) instruments on-board Mars Express (2003), and the Mars Climate Sounder (MCS; e.g., Heavens et al., 2011a, b), Compact Reconnaissance Imaging Spectrometer for Mars (CRISM; Smith et al., 2013) and Mars Color Imager (MARCI; Cantor et al, 2010) instruments on the Mars Reconnaissance Orbiter (MRO) are used to derive the physical properties and distribution of atmospheric dust (Kahre et al., 2017). From Mars' surface, the monitoring of dust optical depth by direct imaging of the Sun at multiple wavelengths has been performed by the following missions and instruments: Viking Lander cameras (Colburn et al., 1989), the Imager for Pathfinder (IMP) (Smith and Lemmon, 1999), MER Pancam (Lemmon et al., 2004), MER Mini-TES (Smith et al., 2006), Phoenix Lander Surface Stereo Imager (Lemmon et al., 2008; Tamppari et al., 2010), MSL Mastcam (Lemmon, 2014), MSL REMS-UV (Smith et al., 2016). The seasonal and interannual variation of dust aerosol column optical depth at 880 nm from MY 26 to 31 retrieved by the MER rovers (Lemmon et al., 2015) has been provided in Figure 3.1, as a complementary to data showed on (Figure 1.5). It can be appreciated that the overall trend of dust optical depth seen by the rovers is similar to the annual and zonal averaged column optical depth at 9 μm retrieved by the orbiters (Smith, 2004; Smith, 2009; Montabone et al., 2015): a gradual decline in dust opacity to L_S ~ 140º, followed by elevated background dust, then atmospheric dust loading is further enhanced by dust storms after L_S ~ 220º, and then the third wave of dust lifting near L_S = 330º (Lemmon et al., 2015)

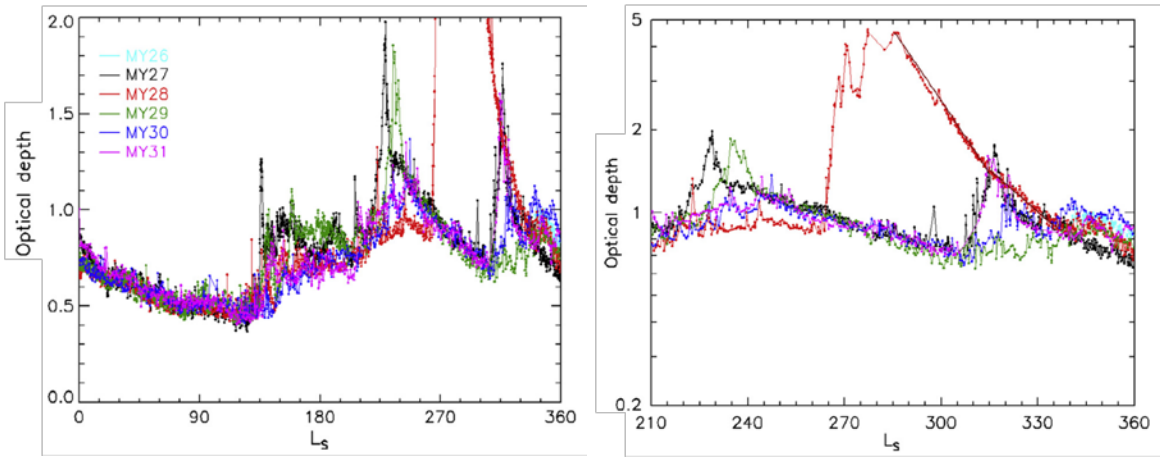

Figure 3.1. Dust optical depth as a function of season. *Left*: Optical depth at 880 nm retrieved by MER-B *Opportunity* Pancam Instrument for Mars Years MY 26 to 31. *Right*: Detailed view corresponding to the dusty season is shown with vertical axis indicating optical depth in logarithmic scale. Source: Adapted from Lemmon et al. (2015).

3.1.2. Vertical distribution

The vertical distribution of dust greatly influences the vertical distribution of solar energy (Pollack et al., 1979) and its characterisation provides insight into the mechanism by which dust enters and leaves the atmosphere. However, the vertical distribution of dust has not been observed as systematically as the column opacity. Observations of line-of-sight dust abundances from the surface looking upwards at different elevations provide information regarding the vertical distribution of dust within the bottom 1-3 scale heights, while limb observations retrieved from orbiting spacecraft provide information on the extent of dust above those altitudes (e.g., Kahre et al., 2017; Guzewich et al., 2017; Sánchez-Lavega et al., 2018). Atmospheric dust vertical profiles retrievals by Mariner 9, Viking Orbiters and Phobos spacecraft (Anderson and Leovy, 1978; Jaquin et al., 1986; Korablev et al., 1993) were approximated by an analytical expression suggested by Conrath (1975), who assumed that the vertical mixing of particles is determined by the effective diffusivity and gravitational settling:

$$q(z) = q_0 \exp\left\{\nu\left[1 - \exp\left(\frac{z}{H}\right)\right]\right\}, \tag{3.1}$$

where q is the dust mass mixing ratio as a function of height, z, q_0 is the mass mixing ratio at the surface; and ν is the ratio between the characteristic dust diffusion time and gravitational sedimentation time (the Conrath parameter), which controls dust cut-off altitude. This expression in pressure coordinates presents the form:

$$\begin{aligned} q(z) &= q_0 \exp\left\{\nu\left[1 - \left(\frac{p_0}{p}\right)\right]\right\}, \qquad p < p_0 \\ q(z) &= q_0, \qquad p \geq p_0, \end{aligned} \tag{3.2}$$

where now q_0 is the dust mixing ratio at surface and p_0 is a reference pressure, e.g., 700 Pa, below which q is taken to be q_0.

These expressions have been extensively used in global circulation models for prescribing dust vertical profiles and calculating the corresponding heating rates (Medvedev et al., 2011). Further analyses of Mariner and Viking data (Anderson and Leovy, 1978; Jaquin et al. 1986) indicated that dust mixing ratios changed in a more complex manner, with aerosol reaching higher altitudes in the equator and decay in a more abrupt manner near the poles. Forget et al. (1999) took into account these findings and modified the Conrath profile to account for the seasonal variability in the height of observable atmospheric dust (Figure 3.2):

$$\begin{aligned} q(z) &= q_0 \exp\left\{0.007\left[1 - \left(\frac{p_0}{p}\right)^{\frac{70}{z_{max}}}\right]\right\}, \qquad p < p_0 \\ z_{max}(\phi, L_S) &= 60 + 18\sin(L_S - 160°) - 22\sin^2\phi \end{aligned} \tag{3.3}$$

where the altitude (km) of the top of the dust layer, z_{max}, varies with latitude (ϕ) and season (L_S)

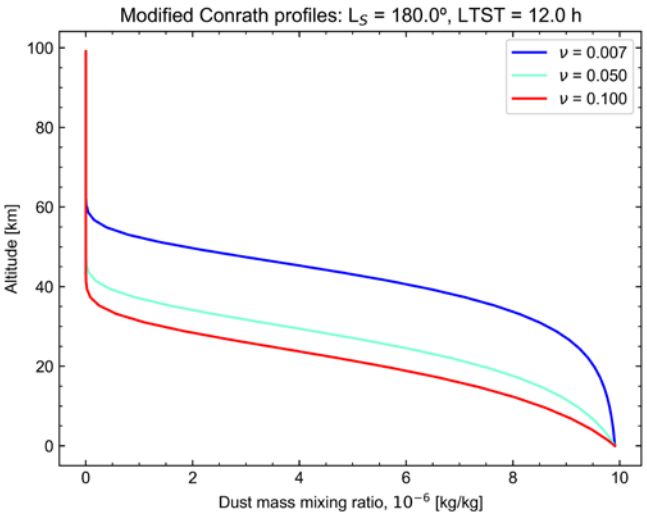

Figure 3.2. Modified Conrath profiles of dust distribution. Dust vertical distribution modified Conrath profiles for different ν parameter values (Forget et al., 1999).

Several observations have indicated that the assumption used in many global circulation models and retrieval algorithms that dust is "well-mixed" with the CO_2 gas is often good. Analysis of limb scans by Viking Landers and near-horizon Sun observations retrieved from the Pathfinder cameras and MER Pancam indicated that the scale height of dust is within 10 to 13 km, consistent with that of the background CO_2. However, although the well-mixed approximation introduced above might be useful for general purpose retrievals, the actual vertical distribution of dust is generally different. Recent Martian limb images retrieved by multiple missions (OMEGA on-board Mars Express, MGS-TES, MRO's CRISM and MCS; see, e.g., Heavens et al., 2011a,b; Medvedev et al., 2011; Guzewich et al., 2014; Kahre et al., 2017) show that dust haze extends much higher above the surface during dust storms than when the atmosphere is less dusty, observing dust reaching altitudes of up to 60 km, whereas during non-dusty conditions the maximum height of dust is about 10 to 20 km (Smith, 2008).

3.1.3. Refractive indices

Dust aerosol refractive indices are another set of optical parameters that are important for radiative transfer calculations. Ockert-Bell et al. (1997) derived the refractive properties in the 0.5 to 0.86 μm wavelength range from the particle size distribution, shape and single scattering properties reported by Pollack et al. (1995). Wolff and Clancy (2003) updated the properties within the 0.2 to 1.35 μm wavelength range using MGS-TES measurements, based on palagonite Mars dust analogue samples (Clancy et al., 1995) and fitting with Tomasko et al. (1999) particle physical properties derived from Pathfinder IMP observations. Further updates in infrared, visible to near-infrared and ultraviolet have been derived by Wolff et al. (2006, 2009). Combined operations of MER (Mini-TES and Pancam) with overflights by MGS-TES and the MRO-CRISM were used to derive several dust physical and radiative properties, including the refractive indices and dust aerosol spatial distribution (Figure 3.3).

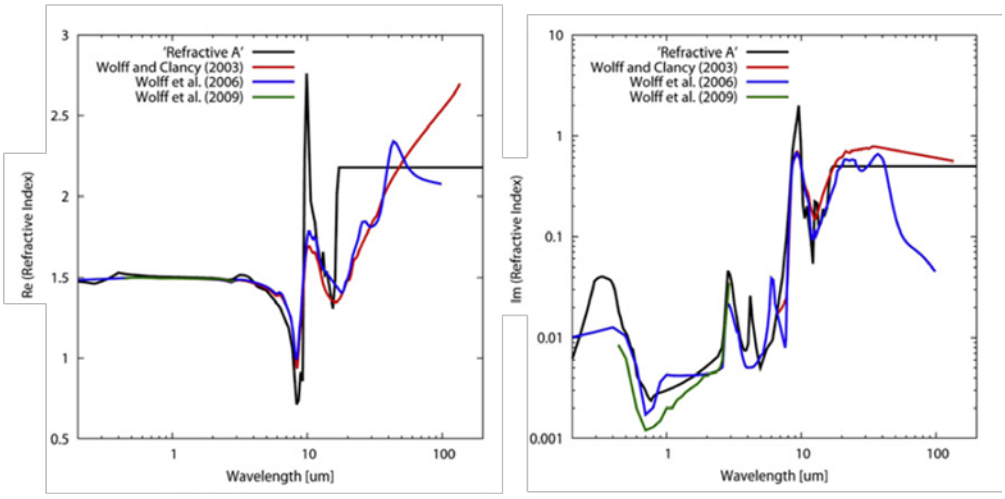

Figure 3.3. Refractive indices of Martian dust aerosol as a function of wavelength. Real (left) and imaginary (right) parts of the refractive indices of Martian dust. "Refractive A" indicates the results derived from Ockert-Bell et al. (2017), Toon et al. (1977) and Forget et al. (1999). Source: Adapted from Medvedev et al. (2011)

3.1.4. Particle size and shape

Information about the size and shape of dust aerosols is most easily obtained by examining the scattering of light by dust and the column dust optical depth ratio at separated wavelengths (e.g., thermal infrared versus visible). Sky observations acquired from surface provide complimentary information to in-orbit retrievals and define strong constraints on the scattering functions. Orbital observations generally include, in addition to radiance scattered from the atmosphere, strong components from light scattered from the surface; whereas for upward looking surface-based observations the sensitivity of derived aerosol properties on the surface properties is less significant (Kaufman et al. 1994; Nakajima et al., 1996; Vermeulen et al., 2000). In this section a summary of main outcomes from previous studies regarding the particle size and shape is provided, with special emphasis on surface-based retrievals. The data presented in the following paragraphs is shown in Table 3.1.

For describing the size of dust particles, the majority of authors within the literature use the nomenclature and definitions provided in Hansen and Travis (1974). The description of dust particle sizes can be expressed in terms of the first two moments of the distribution: the effective radius, r_{eff}, and the dimensionless effective variance, v_{eff}:

$$r_{eff} = \frac{1}{G}\int_{r_1}^{r_2} r\pi r^2 n(r)dr\,, \tag{3.4}$$

$$v_{eff} = \frac{1}{Gr_{eff}^2}\int_{r_1}^{r_2} (r - r_{eff})^2 \pi r^2 n(r)dr\,, \tag{3.5}$$

$$G = \int_{r_1}^{r_2} \pi r^2 n(r)dr\,. \tag{3.6}$$

In these expressions, G is the geometric cross-sectional area of particles, r is the particle equivalent-sphere radius, $n(r)dr$ is the number of particles between r and $r + dr$, and r_1 and r_2 are the minimal and maximal equivalent-sphere radii in the size distribution. Several analytical functions $n(r)$ have been used to approximate the natural particle size (e.g., Mishchenko and Travis, 1998). However, Hansen and Travis (1974) demonstrated that the exact form of the size distribution is not of high relevance for most problems, as long as r_{eff} and v_{eff} parameters are specified.

Toon et al. (1977) analysed Mariner 9 Infrared Interferometer Spectrometer (IRIS) thermal infrared observational data (5 to 50 μm) using plane-parallel atmospheric model to simulate the brightness temperature profiles for different materials in order to compare with IRIS observations. The exploration of the best fitting model to observations was performed by varying a series of parameters: total optical depth, surface temperature, dust particle size distribution, and the wavelength dependent complex refractive indices. For these retrievals, infrared optical constants from known Earth materials were used, with a modified gamma particle size distribution. Best data fits resulted from materials with high SiO_2 content, or clay minerals, such as montmorillonite. However, no single material presented good fit to data. It was highlighted that as Martian dust particles are smaller than the grains of the tested samples and it was not certain that the optical behaviour of the bulk rock was representative of the same rock dispersed. The obtained dust particle distribution size was of r_{eff} = 2.75 μm with v_{eff}= 0.38 and concluded, based on the multiple retrievals during the dust storm event, that the size distribution did not change appreciably with time. Regarding the shape of the particle, Chýlek and Grams (1978) first used a non-spherical randomly oriented particle model (Chýlek et al., 1976) to fit Mariner 9 reflectance data in the UV during the 1971 Mars dust storm.

Pollack et al. (1977) compared the sky brightness at small scattering angles observed by Viking Landers images to results from a multiple-scattering model using the non-spherical semi-empirical theory of Pollack and Cuzzi (1980) and the gamma particle size distribution (Hansen and Travis, 1974), showing best fitting results for r_{eff} = 0.4 μm and v_{eff}= 0.15. Pollack et al. (1979) expanded this study with additional Viking colour data, employing a modified gamma distribution (e.g., Mishchenko and Travis, 1998) that allowed the use of broader distributions (i.e., larger values of v_{eff}), and reported that dust distribution function was best described with r_{eff} = 2.5 μm and v_{eff} = 0.4. However, these studies were limited to scattering angles of 15º due to the vigneting in the Viking Lander observations. Pollack et al. (1995) re-evaluated these data implementing a correction to these images and allowing measurements of the angular distribution of the sky brightness down to approximately 10º. In addition, simultaneous fitting to observations acquired at the 4 available wavelengths were performed, resulting in dust size distributions of $r_{eff} = 1.85 \pm 0.3$ μm and $v_{eff} = 0.5 \pm 0.2$ at the Viking Lander 2 site during northern summer, and $r_{eff} = 1.52 \pm 0.3$ μm for $v_{eff} = 0.5 \pm 0.2$ at the same site during 1977 dust storm. In addition, a modest peak in the backscattering region was retrieved in these

studies, suggesting internal reflections by sharp corners within the particle's geometry associated with fluffy aggregates.

In 1989 the Phobos 2 spacecraft achieved Mars orbit. Although the mission was short, a number of results were obtained. Drossart et al. (1991) evaluated data from the Infrared Spectrometer (ISM) and the solar occultation experiment Auguste, which consisted of three spectrometers sensitive to ultraviolet (UV), visible (VIS) and infrared (IR) light. A poor model fit was reported when using the dust size distribution of Toon et al. (1977) with ISM data, whereas Auguste observations returned superior fits resulting in a dust size distribution with r_{eff} = 1.24 μm and v_{eff} = 0.25. Korablev et al. (1993) derived vertical profiles of volume extinction coefficients from Auguste observations in the IR, and reported average $r_{eff} = 1.26 \pm 0.2$ μm, with $v_{eff} = 0.20 \pm 0.10$. Chassèfiere et al. (1995) analysed data from the different instruments on-board Phobos 2 spacecraft, and derived independent dust size distributions from both Auguste and ISM data obtaining dust distribution function of by$r_{eff} = 1.7 \pm 0.2$ μm and 1.2 ± 0.4 μm, respectively.

Clancy et al. (1995) examined the full spectral range of observations from UV through IR from Mariner 9, Viking and Phobos 2 in order to constrain the Martian atmospheric dust size distribution. Simultaneously fitting both the visible-to-9 μm opacity ratio and the 9 μm-to-30 μm opacity ratio they derived a much broader distribution that previously suggested, with r_{eff} = 1.8 μm and v_{eff} = 0.8. Mars Express has retrieved limb observations using stellar occultations and limb scattering photometric observations at UV wavelengths with the SPICAM instrument (Montmessin et al., 2006). The retrieved results show particle sizes for Martian limb dust hazes above 20 km of r_{eff} from 0.01 to 0.1 μm for v_{eff} 0.1 and 0.5, using the non-spherical aerosol model by Pollack and Cuzzi (1980) with log-normal particle size distribution. Difficulties to separate the ice and dust contribution were reported.

The extensive observational dataset obtained by the Thermal Emission Spectrometer (TES) onboard MGS has greatly contributed in the characterisation of Mars' atmosphere and its dust cycle. Clancy et al. (2003) and Wolff and Clancy (2003) used MGS-TES to derive dust and ice optical depths in the visible and IR band. Visible-to-9 μm opacity ratios returned a r_{eff} of 1.5 ± 0.1 μm for most of the cases (Clancy et al., 2003), although substantial latitudinal and seasonal variations were observed, including large radii during the 2001 dust storm. Their work adopted the v_{eff} = 0.4 from Toon et al. (1977) and the T-matrix code for modelling cylindrical dust aerosol particles; best fits to MGS-TES observed emission phase functions corresponded to disk particles with moderate diameter-to-length aspect ratios of 0.5 and 2.0 (Wolff et al., 2001; Clancy et al., 2003).

Mars Pathfinder imager (IMP) observed angular distribution of sky brightness covering from ~7º to 180º were fitted by Tomasko et al. (1999) with multiple scattering radiative transfer calculations, using the scattering code for modelling non-spherical particles by Pollack and

Cuzzi (1980), to derive dust aerosol size distribution ($r_{eff} = 1.6 \pm 0.15$ μm, v_{eff} from 0.2 to 0.5), and retrieve the single scattering phase function. Markiewicz et al. (1999) conducted independent studies and obtained a r_{eff} varying from 1.45 to 2 μm, with an average value of r_{eff} = 1.70 μm, for v_{eff} = 0.25. The analysis of the obtained phase functions showed good agreements with plate-like particles.

In 2004 the twin MER mission *Spirit* and *Opportunity* rovers began exploring the surface of Mars. Lemmon et al. (2004) used Pancam instrument (Bell et al., 2003; 2006) images (wavelength from 0.4 to 1.0 μm) to constrain the particle properties at the two landing sites. Using the scattering model of Tomasko et al. (1999) with an assumed value of v_{eff} = 0.2; similar dust size distributions of $r_{eff} = 1.47 \pm 0.20$ μm (*Spirit* site) and $r_{eff} = 1.52 \pm 0.18$ μm (*Opportunity* site) were derived. Wolff et al. (2006) used coordinated observations by MER's Miniature Thermal Emission Spectrometer (Mini-TES), MER Pancam, and MGS-TES infrared spectrometer and solar-band bolometer to evaluate vertical and temporal variations in the dust size distribution. Radiative transfer models of these data (T-matrix code for modelling aerosol radiative properties) retrieved r_{eff} values ranging 1.2-1.6 um at the *Spirit* site, and between 1.4-1.8 μm at the *Opportunity* site; with estimated uncertainties of order 0.1-0.2 μm. In addition, a positive correlation was reported between optical depth and r_{eff} (Wolff et al., 2006).

Soderblom et al. (2008) demonstrated the capability of MER Navcams to observe the Martian sky very close to the Sun for evaluating the forward scattering properties of dust aerosol and allowing better constraints on the size distribution. Previous retrievals by Viking Lander cameras (Pollack et al., 1977, 1979, 1995), Mars Pathfinder IMP (Markiewicz et al., 1999; Tomasko et al., 1999) and MER Pancam (Lemmon et al., 2004) were only able to observe the brightness of the Martian sky at scattering angles > 7º (Soderblom et al., 2008). The radiative transfer modelling of the forward scattering was performed using DISORT with Mie code for calculating the single scattering properties of the particles, as the observational data did not sample scattering angles greater than 35º, resulting in r_{eff} around 1.30 μm with v_{eff} of 0.4 to 0.5 (Soderblom et al., 2008).

Smith and Wolff (2014) used MER Navcam and Pancam observations to constrain the size and shape of dust aerosol particles. In this case, they used the radiative transfer model of Wolff et al. (2006, 2009) based in DISORT with T-matrix code for calculating the aerosol particle radiative properties. Navcam Sun pointing observations were used to constrain the particle size, while Pancam sky surveys in the almucantar plane (sky points with same elevation angle as the Sun) reaching high values of scattering angle were used to fit the single scattering phase function and characterise the shape of the particles. This work concluded that cylindrical particles returned better fits than spheres. They also reported a positive correlation between optical depth and dust aerosol size.

At the Arctic region of Mars (68ºN of latitude), the Phoenix Lander used a LIDAR instrument to obtain measurements of atmospheric dust loading and particle size during the late spring

through the middle of summer. Mie scattering calculations performed using the retrieved backscattering ratios were consistent with particle size distributions of r_{eff} in the range of 1.2 to 1.4 μm (Komgem et al., 2013).

Finally, for the ongoing MSL mission, Vicente-Retortillo et al. (2017) calculated the seasonal and interannual variation in the dust aerosol particle size using measurements of the UV radiation retrieved by the Rover Environmental Monitoring Station sensor suite (Gómez-Elvira et al., 2012) in combination with Mastcam instrument opacity measurements (Lemmon, 2014). Results indicated seasonal variations ranging from ~ 0.6 μm during the clear season to 2 μm during the dusty season. McConnochie et al. (2017) used scattered sky light spectra (550 nm to 880 nm) acquired by ChemCam at two different elevation angles and fitted the observations with a discrete ordinates multiple scattering radiative transfer model. Results showed the expected seasonal pattern in dust particle size, with effective radius ranging from about 0.5 to 2.0 μm, and its positive correlation with dust opacity.

3.2. Model

In the following lines, the technical implementation of the radiative transfer base model for this research is presented. The modifications and simplifications made to this base model within the retrieval procedure will be referred and described in the corresponding Section. A schematic overview of the geometry involved in the problem is provided in Figure 3.4.

3.2.1. Radiative transfer code

The radiative transfer problem with multiple scattering in a plane-parallel atmosphere was solved using a Python implementation (*PyDISORT*, Ádámkovics et al., 2016) of version 2.1 of the *DISORT* code (Stamnes et al., 2000), translated from the original FORTRAN based code into C language (*CDISORT*, Buras et al., 2011; Hamre et al., 2013).

3.2.2. Atmosphere model

The Martian atmosphere above Gale Crater is modelled with 30 plane-parallel layers distributed vertically in linearly spaced pressure levels, with a total height of 100 km. For each layer, the corresponding values of atmospheric pressure, temperature, density and composition are retrieved from the *Mars Climate Database*[2] (MCD, version 5.2) (Forget et al., 1999; Millour et al., 2015) and interpolated at each atmospheric layer. These input parameters are loaded for the observation's labelled local true solar time (LTST), solar longitude (L_S) and for the areographic location of Gale Crater (4.6º south; 137.4º east).

[2] http://www-mars.lmd.jussieu.fr/mars/access.html

Reference	Mission (Instrument)	Type	r_{eff} (μm)	v_{eff}	Aerosol model	Comments
Pollack et al., 1977	Viking Landers (Cameras)	Surface	0.40	0.15	Pollack and Cuzzi (1980)	Use of non-spherical particles semiempirical model. Gamma distribution. Superseded by Pollack et al. (1995) due to lack of vigneting correction on observation images.
Toon et al., 1977	Mariner 9 (IRIS)	In-orbit	2.75	0.38	Mie	Thermal IR spectra (5-40 μm). Montmorillonite optical properties. Modified gamma distrib.
Chýlek and Grams, 1978	Mariner 9 (UV sensor)	In-orbit	0.2	0.9	Chýlek et al., (1976)	Ultraviolet (0.27, 0.30 μm) Non-spherical particles model, Log normal distribution: r_g = 0.019 μm; σ_g = 2.26.
Pollack et al., 1979	Viking Landers (Cameras)	Surface	2.5	0.4	Pollack and Cuzzi (1980)	Modified gamma distrib. Superseded by Pollack et al. (1995) due to lack of vigneting correction on observation images.
Drossart et al., 1991	Phobos 2 (Auguste)	In-orbit	1.24	0.25	Drossart (1990)	Photometric profiles of the surface, spectra from 1 to 3 μm. Modified Mie to take into account non-spherical particles. Optical properties of basalt. Modified gamma
Korablev et al., 1993	Phobos 2 (Auguste)	In-orbit	1.26 ± 0.2	0.2	Mie	Limb and solar occultation at 1.9 and 0.37 μm wavelengths. Gamma particle size distrib.
Chassèfiere et al., 1995	Phobos 2 (ISM and Auguste)	In-orbit	Auguste: 1.7 ± 0.2 ISM: 1.2 ± 0.4	0.10-0.40	Drossart (1990)	Combination of ISM and Auguste observations. Modified Mie to take into account particle surface roughness Modified gamma size distrib.
Clancy et al., 1995	Mariner 9, Viking and Phobos	In-orbit	1.80	0.79	Mie	Emission phase function data. Palagonite optical prop. Modified gamma distrib.
Pollack et al., 1995	Viking Landers (Cameras)	Surface	1.52 – 1.85	0.51	Pollack and Cuzzi (1980)	Sky brightness observations. Viking lander results, replacing Pollack et al. 1977; 1979. Log-normal distrib.
Tomasko et al., 1999	Pathfinder (IMP)	Surface	1.45 – 1.75	0.2 - 0.5	Pollack and Cuzzi (1980)	Sky brightness observations in the 0.4 to 0.96 μm range. Gamma distribution.
Markiewicz et al., 1999	Pathfinder (IMP)	Surface	1.45 – 2.00	0.15 - 0.30	Pollack and Cuzzi (1980)	Sky brightness observations in the 0.4 to 0.96 μm range. Modified gamma distrib.
Clancy et al., 2003	MGS (TES)	In-orbit	1.5 ± 0.1; L_S 50º-200º: 1.0 ± 0.2 Dust storm: 1.8 – 2.5	0.4	T-matrix	Visible to IR dust Emission Phase Functions, Spheroidal, D/L = 0.5, and 2.0 Modified gamma distrib.
Wolff and Clancy, 2003	MGS (TES)	In-orbit	1.5 – 1.6	0.4	Mie	Emission Phase Functions, Modified gamma distrib.
Montmessin et al., 2006	Mars Express (SPICAM)	In-orbit	0.01-0.1	0.1, 0.4	Pollack and Cuzzi (1980)	Martian haze limb observations, stellar occultations in UV, above 20 km of altitude. Log-normal distribution
Lemmon et al., 2004	MER (Pancam)	Surface	*Spirit:* 1.47 ± 0.21 *Opportunity*: 1.52 ± 0.18	0.2	Pollack and Cuzzi (1980)	Sky brightness at 0.4 to 1.0 μm wavelengths. Gamma distrib.
Soderblom et al., 2008	MER (Navcam)	Surface	1.25 – 1.35	0.4 – 0.5	Mie	Sun-pointing images, scattering angles from ~ 3º to 30º, Gamma distrib.
Wolff et al., 2006	MGS + MER (TES, Mini-TES, Pancam)	In-orbit and surface	*Spirit:* 1.2 – 1.6 *Opportunity*: 1.4 – 1.8	0.3 – 0.4	T-matrix	Coordinated in-orbit and surface observations campaign. Cylindrical particles of D/L = 2. Gamma distrib.
Wolff et al., 2009	MRO + MER (CRISM & Pancam)	In-orbit and surface	1.8	0.3	T-matrix	Orbit and surface coordinated observations of mission phase functions. Cylindrical particles of D/L = 1. Gamma distrib.
Komguem et al., 2013	Phoenix Lander (LIDAR)	Surface	1.2-1.4	-	Mie	Fits to backscattering opacity ratio at wavelength 0.5 to 1.0 μm Gamma distrib.
Smith and Wolff, 2014	MER (Navcam)	Surface	Seasonal variations, 1.45 – 2.05	0.3	T-matrix	Sun-pointing and sky brightness Cylindrical particles of D/L = 1, Modified gamma distrib.
Vicente-Retortillo et al., 2017	MSL (REMS UV)	Surface	Seasonal variations, 0.60 – 1.75	0.3	T-matrix	Sky radiance with UV sensors, cylindrical particles of D/L = 1, Power law distribution.
McConnochie et al., 2017	MSL (Chemcam)	Surface	Seasonal variations, 0.60 to 1.80	0.3	T-matrix	Spectra of sky brightness, cylindrical particles of D/L = 1, Log-normal distribution.
Chen-Chen et al., 2019a (This research)	MSL (Navcam)	Surface	Seasonal variations, 0.80 to 2.00	0.3	T-matrix	Sun-pointing observations, cylindrical particles, D/L = 1. Log-normal distribution.

Table 3.1. Summary of main retrievals of Martian dust aerosol particle size

The model developed for this thesis has the capacity to initialise the Martian atmosphere loaded with the following constituent species: CO_2, H_2O, O_2, N_2, and O_3. For this general scenario, their abundances (in volume mixing ratio) are retrieved and interpolated at each layer as well from the MCD. The opacity due to the species absorption is calculated using the absorption coefficients derived from the *HITRAN 2012* database (Rothman et al., 2013) for the corresponding pressure and temperature values of each atmospheric level, within the evaluated wavelength range. For the Rayleigh scattering by atmospheric gases, only the contribution of CO_2 has been considered; the model and constants reported in Sneep and Ubachs (2005) was used for calculating the Rayleigh scattering cross section.

However, for the current research scenario in which MSL engineering cameras observations are used, as there are no strong gas absorptions from the atmospheric constituents considered in the model within the cameras wavelength band (600 to 800 nm); the contributions from water ice and CO_2 ice aerosols and the rest of the abovelisted species to the atmospheric opacity is negligible, therefore resulting in a simplification of the radiative transfer problem and an alleviation of the computation time.

3.2.3. Aerosol model

The radiative transfer code requires only 3 parameters at each layer of the discretised Martian atmosphere model for defining the airborne aerosol: the single scattering albedo (ω_0), the single scattering phase function, $P(\theta)$ where θ is the scattering angle; and the optical depth at the specific layer, $\tau(i)$, being i the layer number.

For dust aerosol particles, the computation of the radiative properties was performed using the T-matrix code presented in Section 2.3.3. The refractive indices were retrieved from Wolff et al. (2009) and interpolated for the effective wavelength, which in the case of MSL Navcam and Hazcam is 650 nm (Maki et al., 2012). A well mixed dust situation approach was assumed for this research study, thus the same dust aerosol distribution particle sizes (r_{eff}) and composition are consideded at each atmospheric layer in the model. T-matrix computations were performed for both randomly-oriented cylindrical and spheroidal particles with different diameter-to-length (D/L) aspect ratios (parameter “EPS” within the T-matrix code). The particle size distribution of dust aerosol was modelled for log-normal and power law particle size distributions (Hansen and Travis, 1974; Mishchenko and Travis, 1998)

For the definition of the optical depth at each atmospheric layer due to dust aerosol particles, the vertical distribution of the aerosol mass mixing ratio was modelled using the modified Conrath profile (see Section 3.1.2). When this expression is integrated through the atmosphere height (Heavens et al., 2011a), an expression for the column optical depth at each level can be obtained in the form of:

$$\tau(z) = \tau_0 \cdot \tilde{\sigma}(z) \cdot \exp\left[\nu \cdot (1 - \tilde{\sigma}(z)^{-l})\right] \tag{3.7}$$

where τ_0 is the reference column optical depth at surface, $\tilde{\sigma}(z)$ is the ratio between the pressure at level z, $p(z)$, and a reference pressure level p_0, l is the ratio between the reference height of 70 km and the maximum altitude of observed dust z_{max} given by Equation (3.3) as a function of latitude and solar longitude; and the parameter $\nu = 0.007$, is the ratio between the dust diffusion and surface sedimentation characteristic times (e.g., Forget et al., 1999).

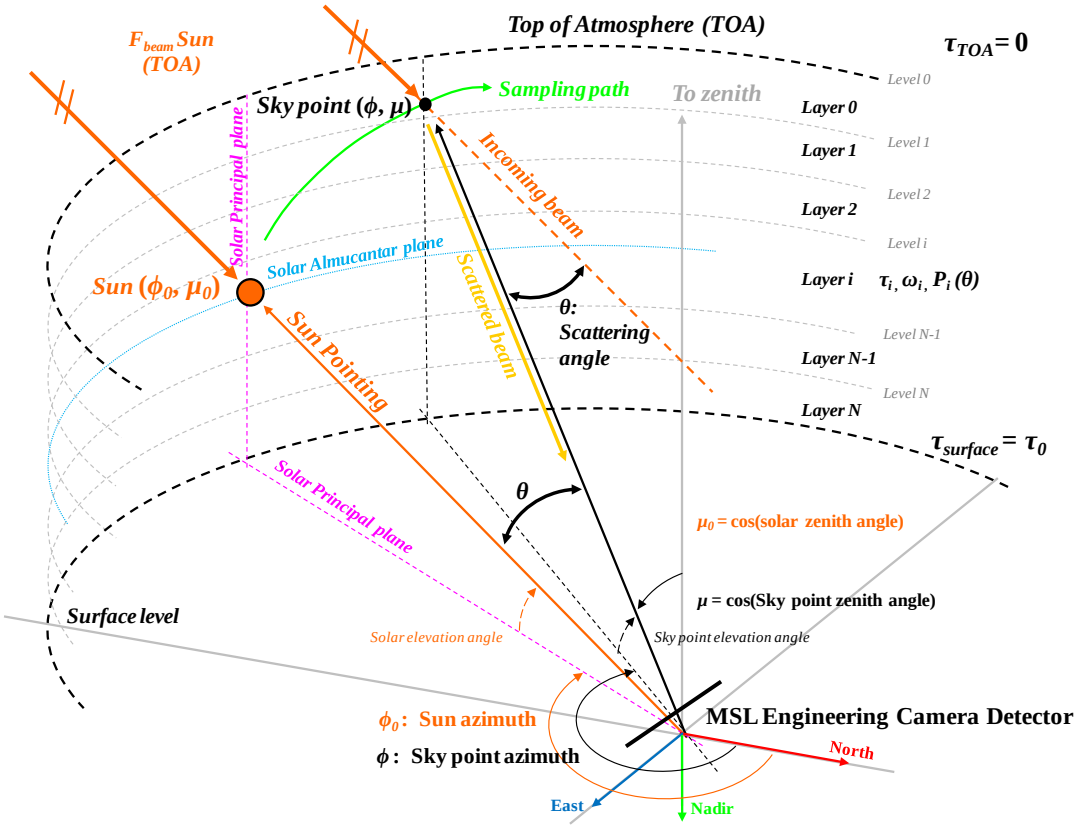

Figure 3.4. Schematic overview of the problem geometry. All the angular quantities are given with respect to the Mars local level reference frame (Maki and Warner, 2013), the frame is fixed relative to the rover and located at the nominal Martian surface, with positive x-axis pointing towards the north, positive y-axis is oriented to the east, and z-axis pointing nadir.

4. OBSERVATIONS

In this Chapter, a comprehensive description of the observation data used in this research is provided. First, MSL Navcam and Hazcam instruments technical properties are introduced, followed by a description of the retrieved observations and the generated image database. Next, the steps involved in the radiometric calibration and geometric reduction of the images are detailed. Finally, the validation of the calibrated data and the evaluation of the associated uncertainties are discussed.

4.1. MSL engineering cameras

4.1.1. Instruments description

The MSL engineering cameras suite is composed of 4 navigation cameras (Navcam) and 8 hazard avoidance cameras (Hazcam). The primary objective of these cameras is to support the navigation and operation of the MSL rover on the Martian surface. The activities include: assessment of terrain's traversability and determining the safe driving directions, characterisation of the vehicle's position and orientation, generation of stereo range maps and derived data for hazard detection, monitoring and avoidance; as well as to support robotic arm operations, target selection and surface imaging activities. Although no science requirements are assigned to the MSL engineering cameras, the returned images may contribute to other instruments by providing contextual data for scientific observations (Maki et al., 2012).

MSL engineering cameras (or ECAMs) are built-to-print copies of the MER engineering cameras (Maki et al., 2003; Maki, 2004). The main difference between these two sets is that MSL engineering cameras are equipped with slightly more powerful heaters to allow operation at colder temperatures (Maki et al., 2012). Each imager is composed of two elements: a detector/optics head and the electronics box (Figure 4.1). The detector head contains the optical lens assembly and a Charged Couple Device (CCD) detector. The camera/rover interface electronics, detector drivers and the heating system in charge of warming up the electronics above the minimum operational temperature are allocated within the electronics box.

The mounting locations of MSL engineering cameras are shown in Figure 4.1. The four Navcams are mounted in the rover's Remote Sensing Mast (RSM), resulting in a configuration that places them at about 1.90 metres above the Martian surface, with a left/right stereo baseline of about 42 cm. A set of four Hazcams (Front Hazcams) are chassis-mounted to the front of the vehicle with a 16.6 cm of stereo baseline, and the four remaining hazard avoidance cameras (Rear Hazcams) are body-mounted on each sides of the rover, with a 10 cm stereo baseline (Maki et al., 2012).

The engineering cameras are controlled by the rover's main computer, referred to as Rover Compute Element (RCE), which is composed of two functionally identical elements, RCE "A" and RCE "B". Each RCE is connected to a dedicated set of 6 engineering cameras (2 Navcams and 4 Hazcams), with only one RCE active at a time, being the second one kept for fault redundancy (Maki et al., 2012). In the case of the Rear Hazcams, the RCE-A and RCE-B Rear Hazcams sets are located at opposite sides of the vehicle (Figure 4.1).

The following list of abbreviations will be used through this text in order to make reference to the imagers. MSL rover's mast mounted Navcams set are labelled as: Navcam Left RCE-A (NLA), Navcam Left RCE-B (NLB), Navcam Right RCE-A (NRA), and Navcam Right RCE-B (NRB). For Hazcams located at the front of the vehicle, these will be: Front Left Hazcam RCE-A (FLA), Front Left Hazcam RCE-B (FLB), Front Right Hazcam RCE-A (FRA), and Front Right Hazcam RCE-B (FRB). Finally, for the Hazcams mounted at the rear of the vehicle, the Rear Left Hazcam RCE-A (RLA) and Rear Right Hazcam RCE-A (RRA) are located on rover's left-side (port); while the Rear Left Hazcam RCE-B (RLB) and Rear Right Hazcam RCE-B (RRB) are on rover's right-side (starboard).

Regarding the optical system, MSL Navcams are equipped with f/12, 14.67 mm fixed-focal length lenses that provide 45 × 45 square-degrees FOV, with a pixel scale at the centre of 0.82 mrad/pixel, the depth of field ranges from 0.5 m to infinity, with a hyperfocal distance of 1.0 m. MSL Hazcam imagers use f/15, 5.58 mm fixed-focal length fisheye lenses with a 124 × 124 square-degrees FOV; the pixel scale at the centre of a Hazcam image is 2.1 mrad/pixel and the depth of field ranges from 0.10 metres to infinity, with a hyperfocal distance of 0.5 metres (Maki, 2004; Maki et al., 2003; 2012).

MSL Navcam and Hazcam detectors are CCD wafers derived from MER spare units (Maki et al., 2012). These consist in frame-transfer devices with an imaging region of 12.3 mm × 12.3 mm containing 1024×1024 pixels (12 microns square pixels). The detector has 3 readout modes: full-frame, 4×1 binned, and windowed. The detector readout time is about 5.4 seconds for a full-frame mode; the full-well capacity of a single pixel is about 170,000 electrons with a gain of 50 electrons/DN.

The components of MSL engineering cameras are shown on Figure 4.1, together with their location and configuration onboard MSL rover. In Figure 4.2 the spectral responsivity curve of MSL engineering cameras is provided. A summary of the configuration of the imagers and the main characteristics and performance of the optics and detectors is provided on Table 4.1.

For the complete description of rover engineering cameras system, see Maki et al. (2003) for MER, and Maki et al. (2012) for MSL. The optical properties of the cameras are discussed in detail in Smith et al. (2001). More details regarding the description of the engineering camera detectors can be found in Maki et al. (2003) and Bell et al. (2003).

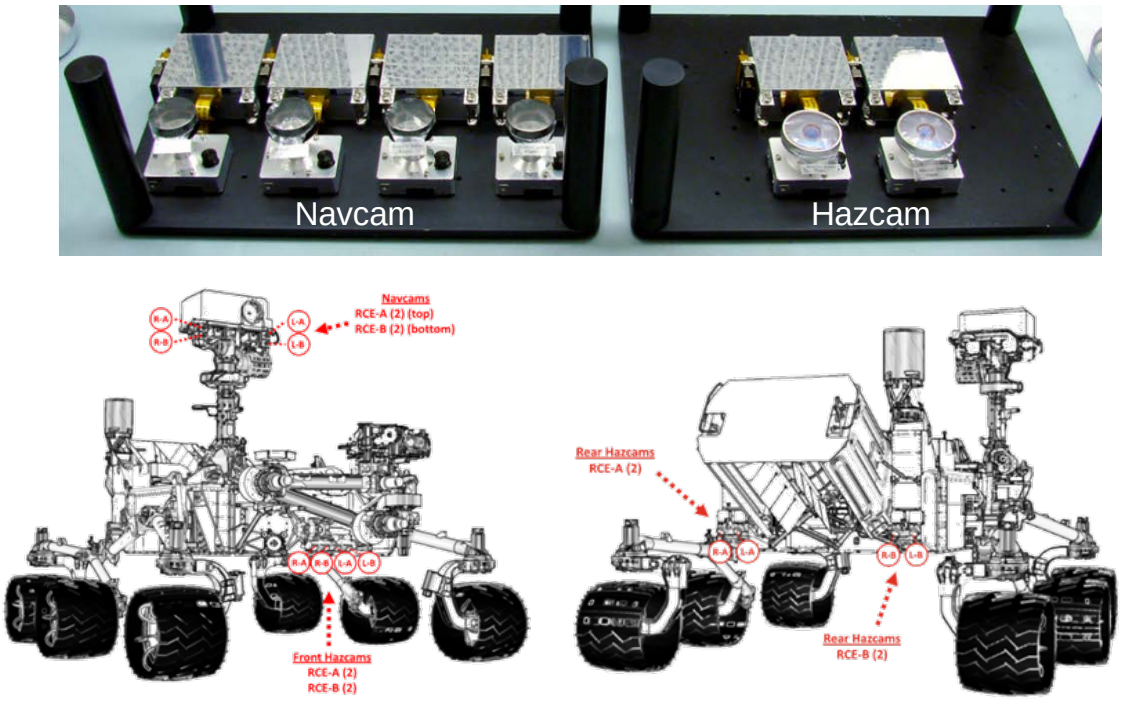

Figure 4.1. MSL engineering cameras: Navcam and Hazcam. Top: Navcams (left) and Hazcam (right) imagers, all of them consist of a detector/optics head connected to an electronics box. Bottom: Location of the cameras on-board MSL Curiosity rover. Source: Adapted from Maki et al. (2012)

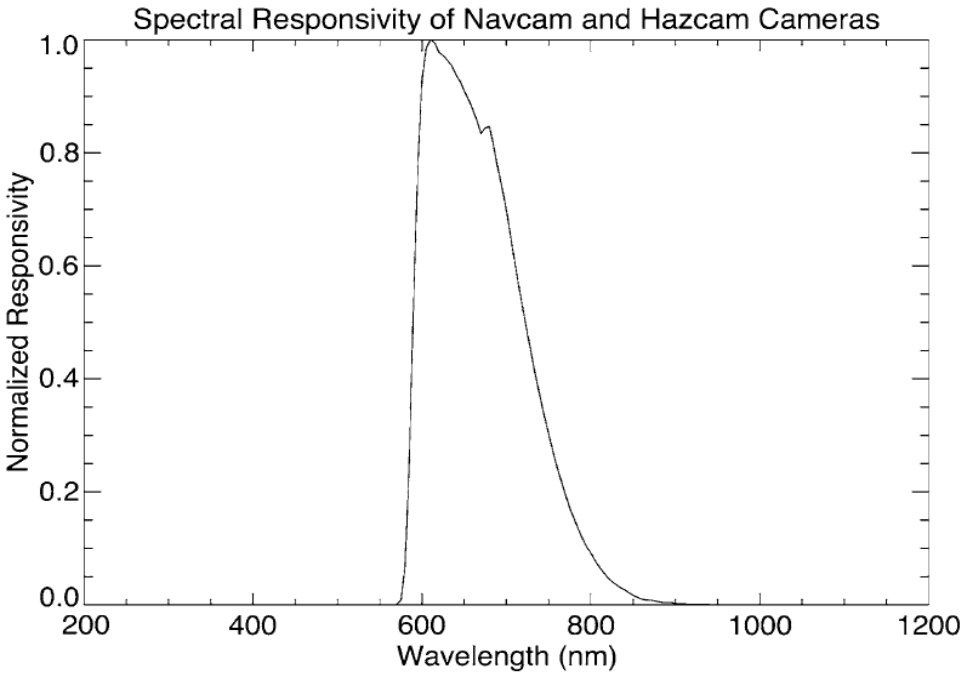

Figure 4.2. Engineering cameras spectral responsivity. Normalised spectral responsivity for Navcam and Hazcam cameras; it incorporates the spectral transmission properties of optics, filters and CCD (Maki et al., 2012). Source: Maki et al. (2012)

	NAVCAM	HAZCAM
Configuration		
Stereo baseline	42.4 cm	16.7 cm (Front Hazcam) 10 cm (Rear Hazcam)
Stereo co-alignment difference	< 1 degree	< 2 degrees
Boresight pointing direction	0º to 360º, in azimuth -87º to +91º, in elevation	45º, below nominal horizon
Height above Martian surface	1.9 m (depends on RSM)	0.68 m (Front Hazcam) 0.78 m (Rear Hazcam)
Mass (per camera)	220 grams	245 grams
Dimensions (per camera)	67 × 69 × 34 mm (electronics) 41 × 51 × 15 mm (detector head)	
Power (per camera)	2.15 Watts	
Optical properties		
Pixel scale at the centre of the FOV	0.82 mrad/pixel	2.1 mrad/pixel
Focal length	14.67 mm	5.58 mm
f/number	12	15
Entrance pupil diameter	1.25 mm	0.37 mm
Field of view (horizontal × vertical)	45º × 45º	124º × 124º
Diagonal FOV	67º	180º
Depth of field	0.5 m – infinity	0.10 m – infinity
Hyperfocal distance	1.0 m	0.5 m
Spectral range	600 – 800 nm	600 – 800 nm
Detector properties		
Average detector full well	170,000 electrons	
Average readout noise (at –55 ºC)	25 electrons	
Average detector gain (at –55 ºC)	50 electrons/DN	
ADC digitization	12 bits/pixel	
Frame transfer time	5.1 msec	
Detector readout time (full-frame mode)	5.4 seconds	
Pixel size	12 × 12 microns	
SNR	> 200:1	
Exposure time	0 – 335.5 seconds, in steps of 5.12 msec	

Table 4.1. MSL engineering camera properties. Summary of camera optics and detector properties of MSL Navcam and Hazcam, together with their onboard configuration. Full technical details regarding MER and MSL engineering cameras can be found in Maki et al., (2003; 2012). Detailed description of the optical properties of the cameras is provided in Smith et al. (2001).

4.1.2. Image files and tools

MSL engineering cameras imaging software systems were also inherited directly from the MER mission (Maki et al., 2012). The onboard flight software capabilities of MSL include: manual and autoexposure, thumbnail generation, 12-to-8 bit companding, spatial downsampling and subframing, image corrections, stereo processing and image metadata collection, among others. Once the imaging commands are received, the flight software automatically powers the camera of interest, the observation is retrieved, read-out from the detectors and transferred to the specific RCE for further processing, then stored and uplinked. Back on Earth, JPL'S

Multimission Image Processing Laboratory (MIPL) (Alexander et al., 2006) performs the ground processing of the engineering camera observations. The downlinked image data is written to Experiment Data Record (EDR) files and, after further processing, the Reduced Data Record (RDR) files are generated for use by the operations team (Maki et al., 2012). The EDR data product corresponds to the raw, uncalibrated, uncorrected image data acquired by the MSL instrument; while RDR data products are limited to MSL rover cameras observation data derived from EDR files or other RDR products (JPL, 2015). Examples of RDRs include: geometrically linearised images, stereo maps, XYZ and range images, surface normal and slope maps, or robotic arm reachability data (Maki et al., 2012; Alexander and Deen, 2017).

The MSL engineering cameras images used in this research study were retrieved from NASA's Planetary Data System (PDS) imaging node archive[3]. In addition to this, the PDS Analyst's Notebook for MSL mission[4] was used to explore the data archive, including the sequence information, operations, science planning and targeting (Stein et al., 2016). For a detailed description of the engineering camera general imaging processing system, see LaVoie et al. (1999) and Alexander et al. (2006). For MSL cameras, the comprehensive description of how image data is acquired, processed, formatted, labelled and how RDR are derived is reported in Alexander and Deen (2017). The format, content and storage of the MSL camera data is provided in the MSL EDR/RDR SIS document (JPL, 2015).

4.1.3. Observation sequences

The RSM is capable of pointing over a range of about 360 degrees in azimuth and 180 degrees in elevation (e.g., Maki et al., 2012; Bell et al., 2017). This pointing capability enables Navcam to acquire compositions and panoramas of the Martian surface and sky. In addition to this, Hazcam's wide field-of-view (about 124-square degrees) and their frequent use have also contributed to accumulate an extensive image database. In a Hazcam's observation, up to 15 degrees of elevation over Mars' local horizon may be reached covering approximately 100 degrees of azimuth. The atmospheric dust loading and characterisation of dust aerosol particles properties is performed by evaluating the angular distribution of the sky brightness along two main directions: the *solar principal plane*, comprised of sky points with same azimuth angle as the Sun; and the *solar almucantar*, with sky points with same zenith angle as the Sun (e.g., Kaufman et al., 1994; Devaux et al., 1998; Dubovik and King, 2000). In particular, the dust size distribution can be derived with measurements of the intensity decay of the solar aureole (Figure 4.3); while the light scattering behaviour at intermediate and large scattering angles can provide relevant information on the aerosol particle shape (Figure 4.4, Figure 4.5).

Although Navcams are not designed to observe the Sun directly (Navcam Sun pointing observations are generally overexposed, even with the minimum exposure time of 5.12 milliseconds), the camera can be safely pointed at the Sun without damage (Maki, 2004; Maki

[3] https://pds-imaging.jpl.nasa.gov/volumes/msl.html
[4] https://an.rsl.wustl.edu/

et al., 2012). On Figure 4.3 and Figure 4.6 (left) Navcam Sun pointing raw observations are provided. In those non-corrected images, due to the presence of the very bright solar disc, the effects of blooming (overflow of charge from a pixel to its neighbours, resulting in white streaks) and frame transfer smear (generated in the pixel data transfer process as the cameras did not have mechanical shutters) can be clearly appreciated. Those clocking effects appearing on the cameras (Peters, 2016) had to be corrected and the resulting pixel-data values had to be converted into physical units; prior to performing the comparisons of the observed sky brightness with radiative transfer models in order to retrieve the dust particle properties. Within the PDS image database, radiometrically corrected RDR files (tagged with "RAD") are available. The applied calibration procedure (named MIPLRAD) is reported in the MSL camera data products software interface specifications document (version 3.5, August 4, 2014) (Alexander and Deen, 2017). MIPLRAD applies the following corrections: flat field, exposure time and temperature-compensated responsivity. After this, the result is calibrated to physical units of radiance (W m^2 nm^{-1} sr^{-1}). However, as it is reported in the same document, the applied calibration consists in a first-order radiometric correction and should be considered approximate. In order to illustrate this, on Figure 4.6 a raw EDR Navcam Sun pointing observation (left) is compared to a radiometrically corrected RDR product (right). It can be observed that the radiometrically corrected data from the PDS archive show a burnt area in the solar disc region, covering up to approximately 15º of scattering angle, thus making these RDR files not suitable for studying the sky brightness angular decay within the forward scattering region. Therefore, the implementation of a radiometric correction for calibrating the EDR files was required for this research study. As these cameras are build-to-print copies of MER engineering cameras (Maki, 2004; Maki et al., 2003, 2012), the in-flight calibration procedure developed by Soderblom et al. (2008) for MER Navcam was adapted to MSL engineering cameras to this purpose.

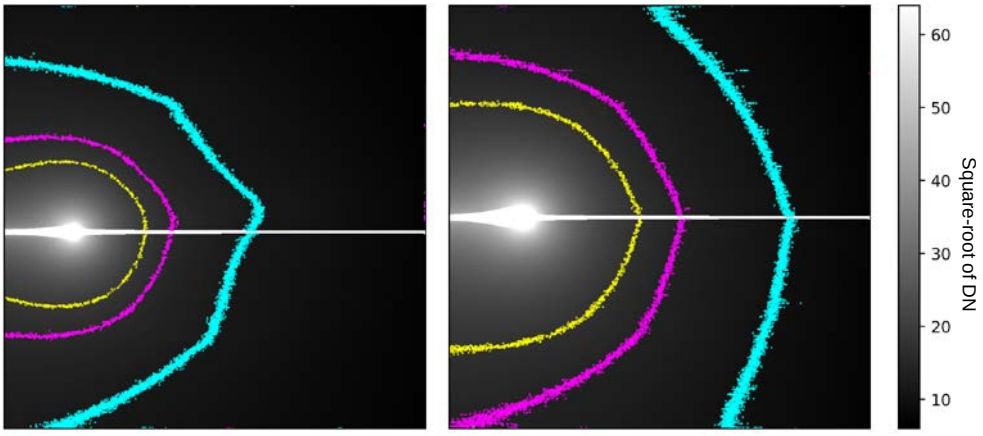

Figure 4.3. MSL Navcam Sun pointing observations. Images generated from EDR files with 12-bit resolution, pixel brightness DN values ranging 0 to 4095. For clarity, images are shown in square root scale. *Left*: sol 637, L_S = 134.4º (non-dusty season), LTST 13:41. *Right*: sol 864, L_S = 269.7º (northern winter solstice, dusty season), LTST 13:48. On both observations, the solar elevation angle above the local horizon was around 56º. The regions with DN values of 100 (cyan), 200 (magenta) and 300 (yellow) contour-lines have been plotted. Image smear and blooming effects can be appreciated on these non-calibrated images due to the presence of the very bright solar disc (Peters, 2016). Source: Adapted from Chen-Chen et al. (2019a)

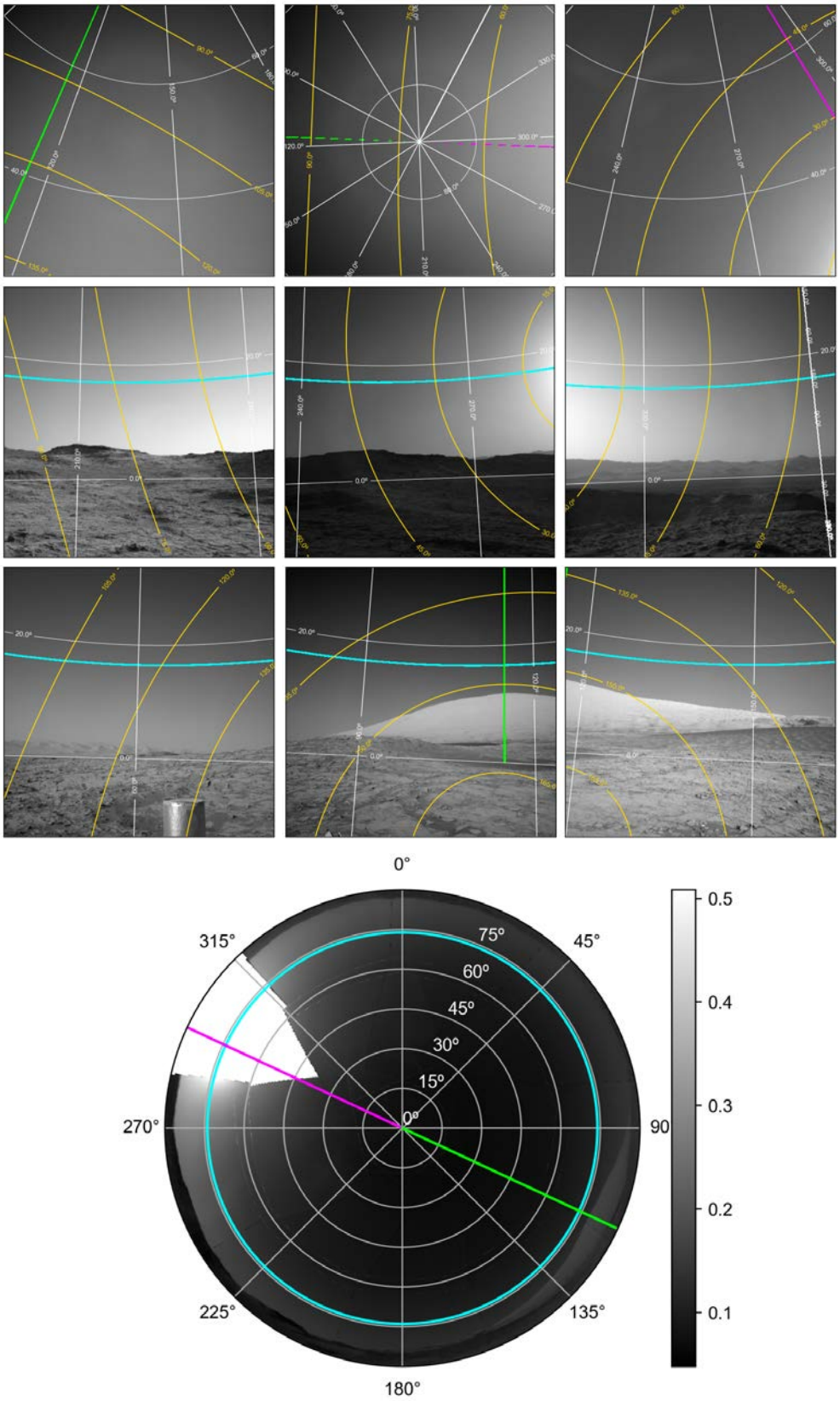

Figure 4.4. MSL Navcam sky-survey observations. Navcam sky-survey sequence retrieved on sol 1268, L_S = 116.1º (MY 33), LTST covering 16:30 to 16:40 (solar elevation angle of 16º to 14º), and the polar-plot composition of the full sequence. For clarity, the square root of the radiance values has been plotted. In all images, the azimuth-elevation grid (white), scattering angles (yellow), solar almucantar (cyan) and principal plane (magenta and green) contours are shown.

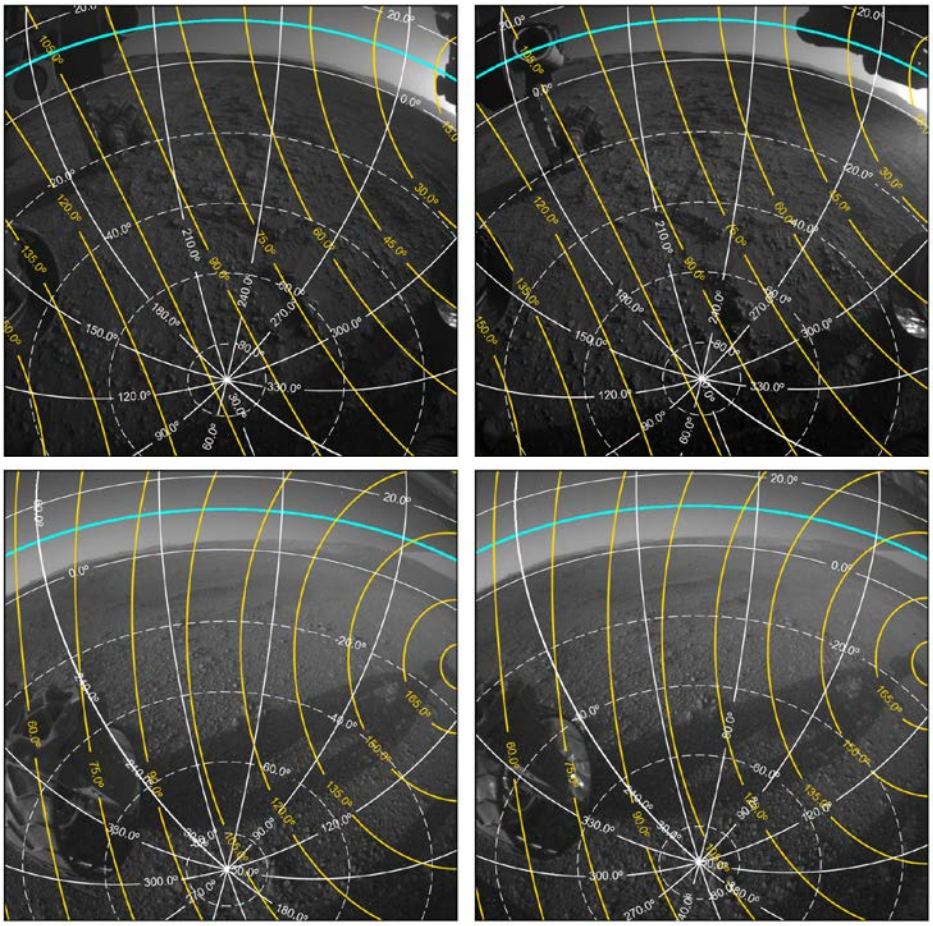

Figure 4.5. MSL Hazcam observations. Hazcam images obtained on sol 1947, L_S = 121.15º (MY 34), LTST ~ 17h and the solar elevation angle is about 11º. From top to bottom, left to right: FLB, FRB, RLB, and RRB. For clarity, the square root of the radiance values has been plotted. The azimuth-elevation grid (white), scattering angles (yellow) and solar almucantar (cyan) contours are shown.

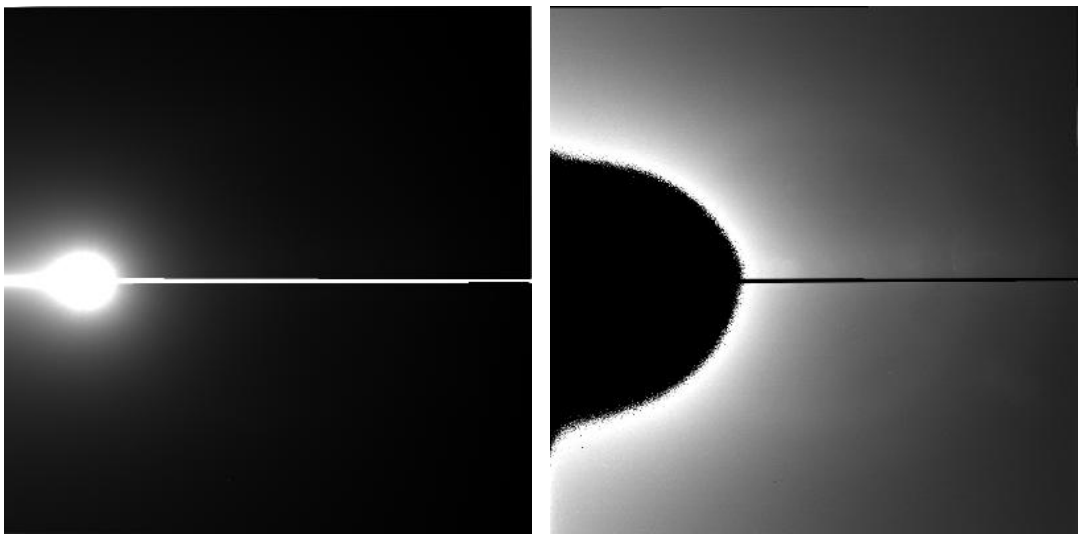

Figure 4.6. Comparison of Sun pointing Navcam observation PDS image products. MSL Navcam SAPP sequence Sun pointing observation file NRB_449782783EDR_F0301366SAPP07612M1.IMG; sol is 589, L_S = 111.15 (MY 32), LTST = 13:22:50, with solar elevation angle of 55.44º. *Left*: Raw EDR image file. *Right*: Current MIPL radiometrically corrected RDR product (RAD) (Alexander and Deen, 2017). Source: Adapted from Chen-Chen et al. (2019a)

4.2. Photometric calibration

The photometric calibration converts the MSL Navcam and Hazcam raw EDR files, with 12-bit pixel DN values, into physical units of absolute radiance (W m^{-2} nm^{-1} sr^{-1}).

For pixel located at row i and column j of an MSL Navcam/Hazcam observation, the following expression summarises the corrections are applied through the calibration procedure:

$$C(i,j)= \frac{\left[R(i,j) - B(j,T_{elec}) - D\left(i,j,T_{CCD},t_{exp}\right) - S(j)\right]}{F(i,j)} \cdot \frac{1}{t_{exp}} \quad (4.1)$$

Where:

- C is the flux value of the calibrated image pixel, in units of DN/s
- R is the raw EDR input value of the pixel, in units of DN
- B is the bias correction, which depends on the imager electronics temperature T_{elec} (ºC), and the pixel position
- D is the dark current correction, depending on the camera CCD temperature T_{CCD} (ºC), and the exposure time t_{exp} (seconds)
- S is the shutter smear removal correction
- F is the flat field image

In the following paragraphs, the stages of the calibration procedure implemented for this research are described. The summary tables with the retrieved calibration parameters are provided on Table 4.2 (MSL Navcam) and Table 4.3 (MSL Hazcam). It is pointed out that not all the Hazcam cameras were used in this study, therefore the resulting calibration parameters are provided only for those cameras which observations were considered (FLB, FRB, RLB, and RRB).

The full description of the in-flight calibration process for MER Navcam can be found in Soderblom et al. (2008). Additional information regarding the calibration of Martian surface cameras may be found in Bell et al. (2003, 2006) for MER Pancam, and Bell et al. (2017) for MSL Mastcam.

4.2.1. Bias removal

MSL engineering cameras CCD vertical serial register line contains an additional set of “prefix” (17) and “suffix” (15) pixels that are masked off from the light and are read out with each image-column (Peters, 2016; Alexander and Deen, 2017). These 32 pixels are called “reference pixels” (labelled as ERP files in the PDS archive) and they record the bias added by the video offset to the signal to prevent it from reaching zero values. Within an ideal scenario, these reference pixel files shall be generated for each observation, so the added bias could be derived and subtracted. For images with a corresponding ERP file, the bias is estimated as the mean of columns 4 through 16 of the reference pixel file. However, due to the mission downlink data-rate

limitations only few MSL engineering cameras observations with reference pixel data were retrieved. For instance, by sol 1648 within Navcam's approximately 70,000 observations there were only 520 ERP files available. Therefore, for those observations with no corresponding ERP file, the added bias needs to be modelled.

Based on the accumulated experience from previous cameras (Bell et al., 2003, 2006, 2017), the bias is modelled with a mean value depending on the device electronics temperature (T_{elec}), and a parameter taking into account the column-to-column variation from the mean bias value (Soderblom et al., 2008).

The bias correction *B* for a column *j* is estimated using the following expression:

$$B(j, T_{elec}) = a_0 + a_1 \cdot \exp(a_2 \cdot T_{elec}) + \text{bias\_offset}(j) \tag{4.2}$$

In this expression, $a_0 + a_1 \cdot \exp(a_2 \cdot T_{elec})$ models the electronics dependence of the column-averaged bias ($\text{bias}_{\text{mean}}$), with constants a_0, a_1 and a_2; while $\text{bias\_offset}(j)$ describes the offset for column *j* from this mean bias.

Mission cruise stage reference pixel data and the limited set of in-flight reference pixel data were combined to derive the parameters a_0, a_1 and a_2, and the $\text{bias\_offset}(j)$ for the bias modelling of Navcam and Hazcam cameras. For each observation and its corresponding ERP file, the bias for each column, $\text{bias}(j)$, was calculated as the mean of rows 4 through 16 of the prefix ERP data; pixel values exceeding more than 2σ from the median were assumed to be spurious data and were not considered in the average.

The $\text{bias}_{\text{mean}}$ was calculated as the mean of bias(j) across all columns:

$$\text{bias}_{\text{mean}} = \frac{\sum_{j=1}^{1024} \text{bias}(j)}{1024} \tag{4.3}$$

The offset bias for each column from the mean bias value, $\text{bias\_offset}(j)$, was calculated by subtracting the $\text{bias}_{\text{mean}}$ from the calculated column bias, $\text{bias}(j)$:

$$\text{bias\_offest}(j) = \text{bias}(j) - \text{bias}_{\text{mean}} \tag{4.4}$$

On Figure 4.7 (Navcams) and Figure 4.8 (Hazcams), the resulting charts from this bias characterisation stage are shown. For each MSL engineering camera, an individual set of parameters (a_0, a_1, a_2) were derived for modelling the mean bias. In the case of the bias offset value as a function of the column index, $\text{bias\_offset}(j)$; as the resulting functions were similar within each set of Navcam and Hazcam imagers, the obtained results were approximated with a logarithmic function for each set.

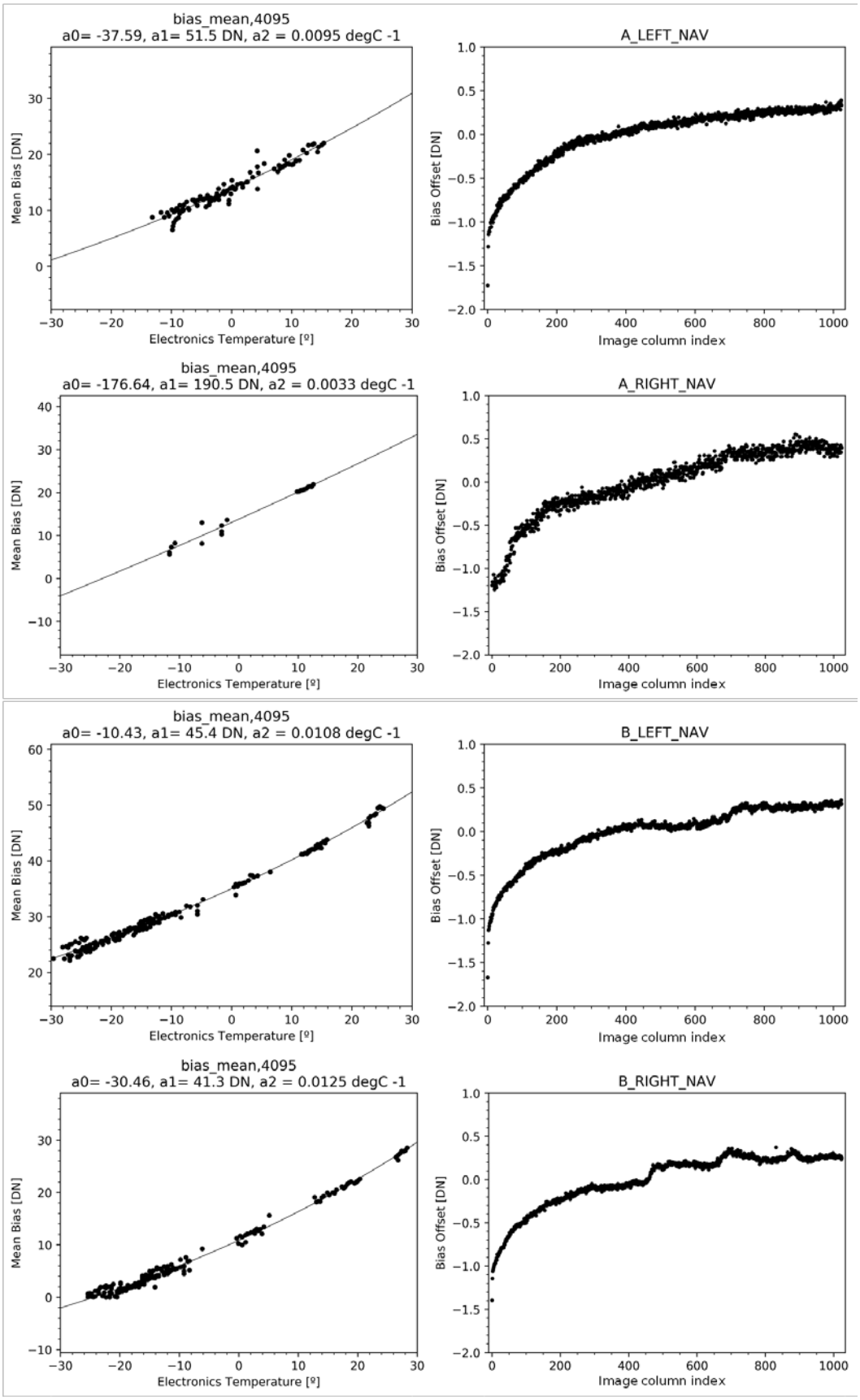

Figure 4.7. MSL Navcam bias correction parameters. *Left*: Mean normalised bias as a function of the electronics temperature for each Navcam, derived from cruise stage and in-flight data. The exponential curve corresponds to the bias model described by equation (4.2). *Right*: Offset bias profiles as a function of the image column index.

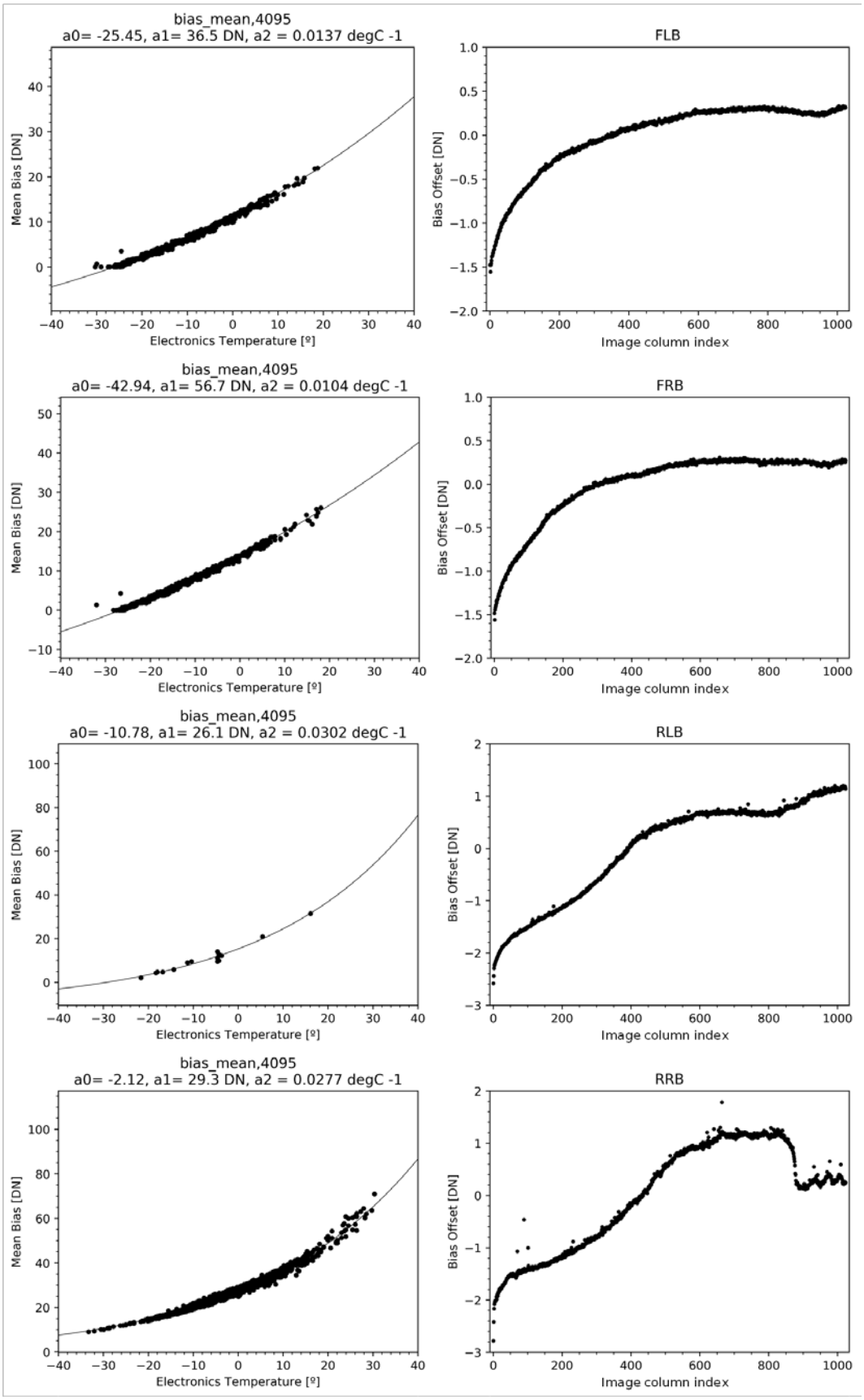

Figure 4.8. MSL Hazcam bias correction parameters. *Left*: Mean normalised bias as a function of the electronics temperature for each Hazcam from data acquired from cruise stage and in-flight data. Exponential curves correspond to the bias model described by equation (4.2). *Right*: Offset bias profiles as a function of the image column index.

4.2.2. Dark current removal

Dark current in an image sensor is the signal generated in a pixel that is not related to the absorption of a photon. Thermally excited electrons freed from the CCD are captured by the pixel, limiting the performance of the imagers and producing false signal (brightening) and noise. As Navcam and Hazcam exposures are not shuttered, it is not possible to measure the amount of dark current that accumulates in a pixel during daytime operations; while at night, temperatures are too low to generate measurable dark current. Therefore, the dark current shall be modelled.

The brightening of the image due to dark current increases significantly at high CCD temperatures and it accumulates during exposure and frame transfer, as image's portions located further from the read-out register are transferred through longer distances, accumulating more dark current (Peters, 2016).

The rate at which dark current accumulates in a pixel located at (i, j) can be approximated by an exponential function of the CCD's temperature (T_{CCD}); and the total dark current accumulated in a pixel, $D(i, j)$, can be then calculated as a product of the this rate and the collection (exposure and read-out) time (t),

$$D\left(i, j, T_{CCD}, t_{exp}\right) = t \cdot \left(b_{0i,j} \cdot \exp(b_{1i,j} \cdot T_{CCD})\right), \quad (4.5)$$

where $b_{0i,j}$ and $b_{1i,j}$ are constants independent of temperature.

The frame transfer read-out method of MSL engineering cameras (Peters, 2016) allows modelling the dark current into two separate components: the active-area and the masked-area dark currents. They correspond to the contributions of the accumulated charge when the detector is exposed to the scene (active-area dark current) and when the CCD is being read out (masked-area dark current)

This way, the dark current correction *D* for a pixel located at row i, column j is,

$$D\left(i, j, T_{CCD}, t_{exp}\right) = D_{Masked}(i, j, T_{CCD}) + D_{Active}\left(i, j, T_{CCD}, t_{exp}\right), \quad (4.6)$$

where t_{exp} is the exposure time.

Masked-area dark current

The read-out time of a full frame Navcam image from the masked region of the CCD is about 5.4 seconds (Maki et al., 2012). During this period, the dark current accumulates and is added to the signal. The image columns located farther from the read-out register take longer time to be read out and therefore accumulate more dark current than columns located closer, therefore the masked area dark current shall be modelled and removed from the image. As the dark

current accumulated in a single pixel depends of the rest of the CCD's pixel through which the signal was propagated during the read-out, for practical reasons the masked area dark current model is separated into two components: the mean dark current of the masked region of the CCD ($\mathrm{dark\_mean}_{\mathrm{Masked}}$), and a scaling factor for each individual pixel, similar to a flat field image, the masked-area dark current flat (DF_{Masked}) (e.g., Bell et al., 2003, 2006). Therefore, the masked-area dark current at a pixel located at row i, column j can be written as:

$$D_{Masked}(i, j, T_{CCD}) = \mathrm{dark\_mean}_{\mathrm{Masked}}(T_{CCD}) \times DF_{Masked}(i, j)\,. \tag{4.7}$$

The mean masked-area dark current can be derived using Equation (4.5): if the coefficients and read-out time within the CCD are assumed to be constant and the time parameter is incorporated into the constant coefficients of the expression, this results in:

$$\mathrm{dark\_mean}_{\mathrm{Masked}}(T_{CCD}) = c_0 \cdot \exp(c_1 \cdot T_{CCD})\,. \tag{4.8}$$

The masked-area dark current was modelled using a set of cruise stage zero-second exposure dark images obtained over a range of temperatures (the list of MSL images used is provided on Table 4.2 and Table 4.3 for Navcam and Hazcam, respectively). On these images, the bias was first removed following the procedure described in Section 4.2.1. Next, hot pixels (pixels with values greater than 5 sigma from the mean value of a 20-pixel box average) were replaced by the mean value; and finally, the mean masked-area dark current for each image was calculated using the centre 1024×256 pixels (Bell et al., 2006; Soderblom et al., 2008). Due to the diverse CCD temperature values existing for each camera, the calculated mean masked-area dark current for each image was modelled with expression (4.8) combining all the data for each set of cameras. The values of the calculated masked-area mean dark current are provided in Figure 4.9 as a function of the CCD temperatures, together with the obtained model fit coefficients described by equation (4.8), with c_0 = 3.734 DN, c_1 = 0.13036 ºC^{-1} for MSL Navcam; and c_0 = 9.976 DN, c_1 = 0.09917 ºC^{-1} for MSL Hazcam.

The modelled masked-area dark current flat image, $DF_{Masked}(i, j)$ in equation (4.7), for each Navcam and Hazcam imager was calculated as the average of the masked-area dark current images normalised by the mean dark current retrieved from the central region (1024×256). Only data retrieved with CCD temperatures > -20 ºC (considered as of high signal-to-noise ratio) were used for deriving the masked-area dark current flats for each camera. The resulting images are provided on Figure A.1 (Navcam) and Figure B.1 (Hazcam) in their corresponding appendix section: APPENDIX A for Navcam, APPENDIX B for Hazcam.

In summary, the masked-area dark current of an MSL engineering camera image is modelled using equation (4.7) using as inputs: the CCD temperature recorded in the image label, the corresponding c_0, c_1 parameters derived for each set of engineering cameras, and the masked-area dark current flat image generated for the specific imager.

Active area dark current

Active area dark current accumulates while an image is integrating on the scene an adding to the total signal (Soderblom et al., 2008). Following a similar approach as for the masked-area dark current, the active-area dark current is modelled as two components: the mean dark current accumulated in the active region of the CCD ($\mathrm{dark\_mean}_{\mathrm{Active}}$), and a scaling factor for each individual pixel (DF_{Active}):

$$D_{Active}(i, j, T_{CCD}, t_{exp}) = t_{exp} \cdot \mathrm{dark\_mean}_{\mathrm{Active}}(T_{CCD}) \times DF_{Active}(i, j). \quad (4.9)$$

The active-area mean dark current can be obtained by dividing equation (4.5) by the exposure time (t_{exp}) and assuming that the corresponding coefficients (in this case: d_0, d_1) are constant across the CCD:

$$\mathrm{dark\_mean}_{\mathrm{Active}}(T_{CCD}) = d_0 \cdot \exp(d_1 \cdot T_{CCD}). \quad (4.10)$$

The active-area dark current for Navcam and Hazcam cameras was modelled using a set of cruise stage dark images acquired at a variety of temperatures with non-zero exposure durations. On these images, the bias was first removed following the procedure described in Section 4.2.1. Next, the masked-area dark current was modelled and removed using equation (4.7), leaving then only the active-area dark current signal. After this, “hot pixels”, with values greater than 5 sigma from the mean value of a 20-pixel box average, were replaced by the mean value; and finally, the mean active-area dark current for each image was calculated by dividing the mean dark current from the central region (256×256) pixels by the exposure duration. In a similar manner as proceeded in the modelling of the masked-area dark current, single active-area dark current rate models were made combining data from each set of Navcams and Hazcams. The obtained mean active-area dark current values are provided in Figure 4.9 as a function of the CCD temperatures, together with the obtained model fit coefficients described by equation (4.10), with d_0 = 12.188 DN s^{-1}, d_1 = 0.10072 $ºC^{-1}$ for MSL Navcam; and d_0 = 17.877 DN s^{-1}, d_1 = 0.09286 $ºC^{-1}$ for MSL Hazcam.

The active-area flat images, $DF_{Active}(i, j)$ in equation (4.9), were derived by normalising the active-area dark current image by the mean dark current from the centre 256×256 pixels. Normalised active-area flat images calculated from images with high signal to noise ratio (CCD temperatures > -20 ºC) were averaged to derive the active-area flat images. The resulting images are shown in Figure A.2 (Navcam) and Figure B.2 (Hazcam) in the corresponding appendix section. In summary, the active-area dark current for MSL Navcam and Hazcam is modelled using equation (4.9) with the following inputs: the CCD temperature record, the d_0, d_1 parameters derived for each sets of cameras, and the active-area dark current flat image generated for the specific imager.

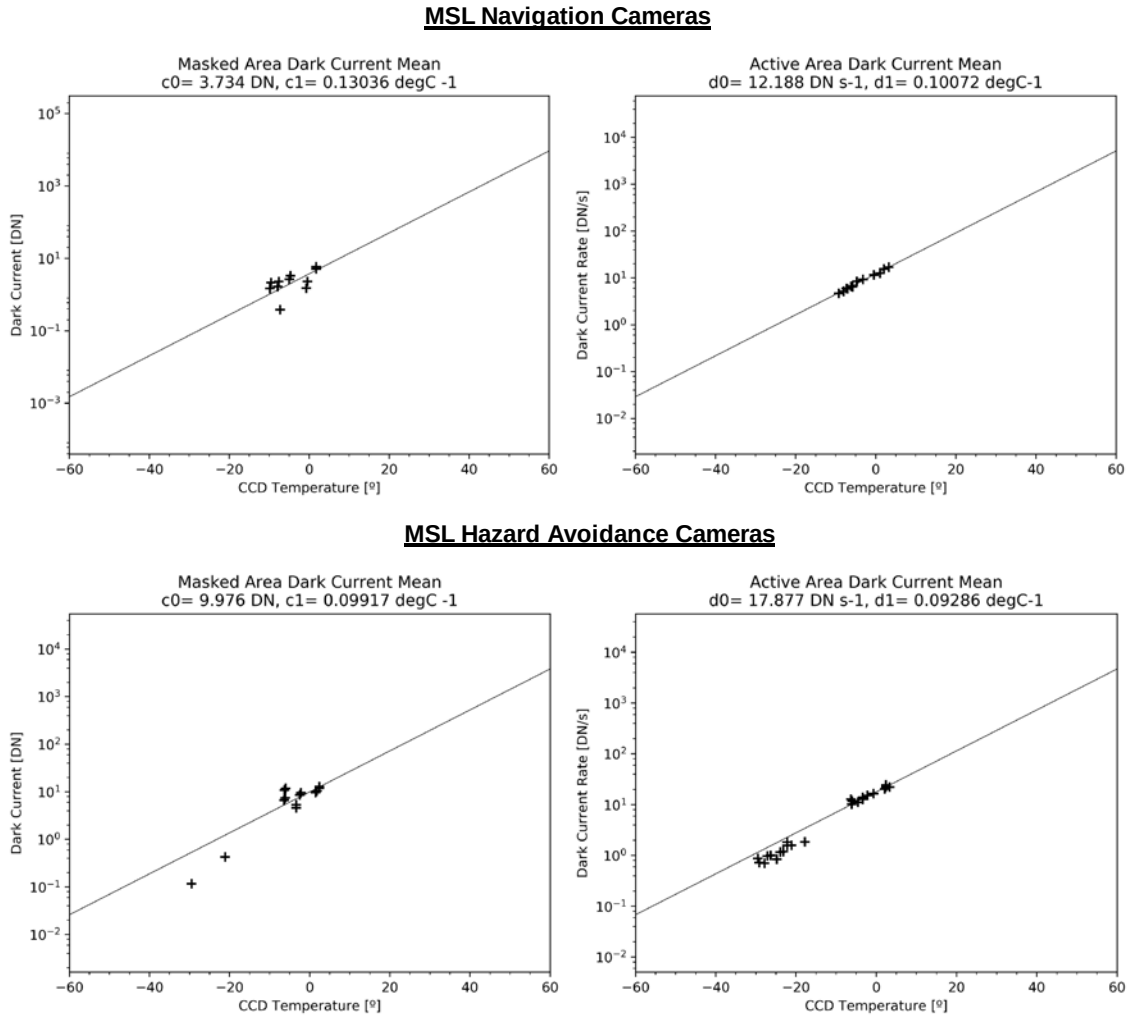

Figure 4.9. MSL Navcam and Hazcam dark current correction parameters. *Left*: Bias-corrected masked-area mean dark current values calculated from averaging central-region pixels (1024×256) as a function of CCD temperature for Navcam (top) and Hazcam (bottom) from cruise stage zero exposure dark images. The exponential curve corresponds to the masked-area dark current model as described by equation (4.8). *Right*: Mean active-area dark current values averaged for the centre 256×256 pixels as a function of the CCD temperature for Navcam (top) and Hazcam (bottom) from cruise stage non-zero exposure dark images. The exponential curve corresponds to the active-area dark current model as defined in equation (4.10). The range of CCD temperatures covered in these graphs is for direct comparison purposes with results for MER Navcam reported in Soderblom et al. (2008).

4.2.3. Shutter smear removal

For frame-transfer CCDs with no mechanical shutters, the exposures are achieved by first removing the accumulated charge from all the pixels in the array, pausing for the selected exposure time and finally shifting the charges column-by-column to neighbouring columns, until they reach the vertical serial register located at the last column, from which they are read-out. During this transfer process, each pixel receives charge from both the scene and its neighbour pixel in its neighbouring column, causing the frame transfer smear effect, being especially significant when a bright feature is present in the image, such as the Sun or its reflection on a surface (Soderblom et al., 2008; Peters, 2016).

The implemented shutter smear removal algorithm was derived from MER Pancam (Bell et al., 2006) and Navcam (Soderblom et al., 2008), and when particularised for MSL the frame transfer direction for each imager, reported in the *MSL Pointing, Positioning, Phasing and Coordinate Systems* document (Peters, 2016), had to be taken into account (*cf.*, Soderblom et al., 2008). The total shutter smear for a row i is recursively calculated and removed for each column j, starting with j = 0, corresponding to the column closest to the masked region (location of the detector's read-out element), using the following expressions:

$$\mathrm{smear}_i(j) = 2\sum_{n=1}^{j-1}\left(\frac{\mathrm{scene}_i(n)}{t}\right)\cdot 5.12\ \mu\mathrm{sec}\,, \tag{4.11}$$

$$\mathrm{scene}_i(j) = \mathrm{signal}_i(j) - \mathrm{smear}_i(j), \tag{4.12}$$

$$\mathrm{smear}_i(0) = 0, \tag{4.13}$$

where t is the exposure duration and signal is the bias and dark corrected DN of pixel (i, j); the 5.12 µsec term corresponds to the clock speed of the CCD. Because the shutter smear for an specific column depends on the observed radiance from all downstream lines, the analytical shutter smear can only be modelled for full-frame images or sub-framed images for which the sub-framed area starts at column j = 0 (Soderblom et al., 2008)

4.2.4. Flat field correction

This step corrects the pixel-to-pixel sensitivity variations due to pixel individual efficiencies and field shading caused by the optical throughput of the camera, resulting in the non-uniform illumination of the CCD. Images (flat fields) of uniformly illuminated targets are used for correcting these effects. Pre-flight flat field images created for each MSL Navcam and Hazcam (Figure A.3 and Figure B.3 in the appendix section, respectively) were downloaded from the PDS imaging node and used in this correction step.

4.2.5. Conversion to physical units

As reported in Soderblom et al. (2008) for MER navigation cameras, the transformation from the resulting calibrated image $C_{i,j}$, with units of DN/s, after performing the operations listed in Equation (4.1) (bias correction, dark current removal, shutter smear removal, and flat fielded) to a calibrated image of the scene with physical units of absolute radiance, $L_{i,j}$ (radiance units: W m^{-2} nm^{-1} sr^{-1}), was modelled following a linear equation dependent on the camera's CCD temperature.

$$L_{i,j} = (K_0 + K_1 \cdot T_{CCD}) \cdot C_{i,j}\,, \tag{4.14}$$

where the coefficients K_0 (units: W m^2 nm^{-1} sr^{-1} (DN s^{-1})$^{-1}$) corresponds to the offset, and K_1 (units: W m^2 nm^{-1} sr^{-1} (DN s^{-1})$^{-1}$ $ºC^{-1}$) is the slope. This assumption was based on the results from pre-flight MER Navcam calibration tests, in which the normalised pixel values (with units of DN/s) of the calibration images of an integrating sphere were compared against the measured radiances, following a similar the approach as described in Bell et al. (2006, 2017).

For MSL engineering cameras these radiometric conversion coefficients where not available, as no pre-flight calibration test were performed on the MSL flight cameras. Therefore, K_0 and K_1 values were estimated from default radiometric conversion coefficients of MER Navcams (e.g., Alexander and Deen, 2017), by averaging the coefficients provided for those cameras in Table 2 of Soderblom et al. (2008). This resulted in K_0 = 9.634e-6 W m^2 nm^{-1} sr^{-1} (DN s^{-1})$^{-1}$, and K_1 = 1.035e-6 W m^2 nm^{-1} sr^{-1} (DN s^{-1})$^{-1}$ $ºC^{-1}$, for both MSL Navcam and Hazcam.

CALIBRATION STAGE	MSL NAVIGATION CAMERAS				SOURCE
	NAV_RIGHT_A: SN_0206	**NAV_RIGHT_B:** SN_0218	**NAV_LEFT_A:** SN_0216	**NAV_LEFT_B**: SN_0215	
Bias removal	a_0 = -176.64 DN a_1 = 190.5 DN a_2 = 0.0033 $ºC^{-1}$	a_0 = -30.46 DN a_1 = 41.3 DN a_2 = 0.0125 $ºC^{-1}$	a_0 = -37.59 DN a_1 = 51.5 DN a_2 = 0.0095 $ºC^{-1}$	a_0 = -10.43 DN a_1 = 45.4 DN a_2 = 0.0108 $ºC^{-1}$	Derived for MSL
Dark current removal: parameters	Masked region mean rate: c_0 = 4.155 DN; c_1 = 0.1112 $ºC^{-1}$ Active region mean rate: d_0 = 12.096 DN, d_1 = 0.1010 $ºC^{-1}$				Derived for MSL, PDS (1)
Masked dark flat image	NRA_384856702EDR_F, NRA_384856709EDR_F	NRB_388221633EDR_F, NRB_388221626EDR_F	NLA_384856702EDR_F, NLA_384856709EDR_F	NLB_388221626EDR_F, NLB_388221633EDR_F	PDS (1)(2)
Active dark flat image	NRA_384856744EDR_F, NRA_384856717EDR_F	NRB_388221640EDR_F, NRB_388221668EDR_F	NLA_384856717EDR_F, NLA_384856744EDR_F	NLB_388221640EDR_F, NLB_388221668EDR_F	PDS (1)(2)
Flat field correction	MSL_FLAT_SN_0206	MSL_FLAT_SN_0218	MSL_FLAT_SN_0216	MSL_FLAT_SN_0215	PDS (3)
Conversion to physical units	K_0 = 9.634e-6 W m^2 nm^{-1} sr^{-1} (DN s^{-1})$^{-1}$; K_1 = 1.035e-8 W m^2 nm^{-1} sr^{-1} (DN s^{-1})$^{-1}$ $ºC^{-1}$				Adapted from MER (4)

(1): https://pds-imaging.jpl.nasa.gov/data/msl/MSLNAV_0XXX/DATA/CRUISE/
(2): Dark masked and active flats are available in this public repository: http://www.ajax.ehu.es/hcc/Icarus2018153/
(3): https://pds-imaging.jpl.nasa.gov/data/msl/MSLNAV_0XXX/CALIB/
(4): Table 2 from Soderblom et al., (2008). A 15% of uncertainty is assumed for K0 and K1 values.

Table 4.2. MSL Navcam calibration parameters

CALIBRATION STAGE	MSL HAZARD AVOIDANCE CAMERAS				SOURCE
	FHAZ_LEFT_B: SN_0208	**FHAZ_RIGHT_B:** SN_0209	**RHAZ_LEFT_B:** SN_0212	**RHAZ_RIGHT_B:** SN_0207	
Bias removal	a_0 = -25.45 DN a_1 = 36.5 DN a_2 = 0.0137 $ºC^{-1}$	a_0 = -42.92 DN a_1 = 56.7 DN a_2 = 0.0104 $ºC^{-1}$	a_0 = -10.78 DN a_1 = 26.1 DN a_2 = 0.0302 $ºC^{-1}$	a_0 = -2.12 DN a_1 = 29.3 DN a_2 = 0.0277 $ºC^{-1}$	Derived for MSL
Dark current removal: parameters	Masked region mean rate: c0 = 9.976 DN; c1 = 0.0992 $ºC^{-1}$ Active region mean rate: d0 = 17.877 DN, d1 = 0.0928 $ºC^{-1}$				Derived for MSL, PDS (1)
Masked dark flat image	FLB_388221706EDR_F, FLB_388221713EDR_F	FRB_388221706EDR_F, FRB_388221713EDR_F	RLB_388221950EDR_F, RLB_388221958EDR_F	RRB_388221950EDR_F, RRB_388221958EDR_F	PDS (1)(2)
Active dark flat image	FLB_388221720EDR_F, FLB_388221830EDR_F	FRB_388221720EDR_F, FRB_388221830EDR_F	RLB_388221965EDR_F, RLB_388221993EDR_F	RRB_388221965EDR_F, RRB_388221993EDR_F	PDS (1)(2)
Flat field correction	MSL_FLAT_SN_0208	MSL_FLAT_SN_0209	MSL_FLAT_SN_0212	MSL_FLAT_SN_0207	PDS (3)
Conversion to physical units	K0 = 9.634e-6 W m^2 nm^{-1} sr^{-1} (DN s^{-1})$^{-1}$; K1 = 1.035e-8 W m^2 nm^{-1} sr^{-1} (DN s^{-1})$^{-1}$ $ºC^{-1}$				Adapted from MER (4)

(1): https://pds-imaging.jpl.nasa.gov/data/msl/MSLHAZ_0XXX/DATA/CRUISE/
(2): Dark masked and active flats are available in this public repository: http://www.ajax.ehu.es/hcc /
(3): https://pds-imaging.jpl.nasa.gov/data/msl/ MSLHAZ _0XXX/CALIB/
(4): Table 2 from Soderblom et al., (2008). A 15% of uncertainty is assumed for K0 and K1 values.

Table 4.3. MSL Hazcam calibration parameters

4.3. Geometric reduction

It is essential to determine the viewing and illumination geometries of the observation prior to the comparison of the observed intensities with model calculations to determine the optical properties of the Martian dust aerosol particles. In the geometric reduction stage (also known as “image navigation”), for each pixel of the image the corresponding values of azimuth, elevation and scattering angles are calculated with respect to a specific reference frame. Derivation of these geometric quantities is straightforward from knowledge of the rover orientation and solar incidence vector in a Martian surface reference frame centred on the rover (Mars Local Level Frame) and the camera pointing vector in the rover’s reference frame (Rover Navigation Frame) (Maki and Warner, 2013).

The geometric reduction of MSL engineering camera images was calculated using the CAHVOR photogrammetric camera model system (Yakimovsky and Cunnningham, 1978; Gennery, 2006). In this camera model, a 3-dimensional point in the scenery is transformed into image pixel row-column coordinates using a system of six vectors: the camera centre position vector (C), perpendicular axis unit vector (A), the horizontal (H) and vertical (V) information vectors, and the optical (O) and radial distortion (R) vectors (Di and Li, 2004; Gennery, 2006). When modelling fish-eye lenses with very large field of view (>100º) such as Hazcams, the CAHVOR model is extend to the CAHVORE model, in which three more parameters are included on the vector (E) for correcting the lens-distortion (Di and Li, 2004).

The component values of these vectors were retrieved from the PDS label of the EDR observation files, where they are designated as MODEL_COMPONENT within the CAMERA_MODEL DATA ELEMENTS section (Alexander and Deen, 2017). These elements can be inverted in order to assign to each image pixel the corresponding values of azimuth and elevation in the a local level coordinate frame system, with positive X, Y, and Z axes pointing at Mars’ north, east, and gravity nadir, respectively (Maki and Warner, 2013; Alexander and Deen, 2017). The derived local azimuth and elevation angles were then used, together with the solar site azimuth and elevation angles, to calculate the scattering angle for each pixel of the image.

When performing the geometric reduction of MSL Navcam Sun pointing image data, it was detected that the coordinates of the Sun centre position recorded in the image label data presented some deviation (generally less than 1º) with respect to the actual solar disc centre observed on these images. This may be caused by uncertainties in the rover’s attitude at the time of the observation, as it has been also reported previously for MER (Soderblom et al., 2008; Lemmon et al., 2015). For such cases, the centre of the bright solar disc was measured, the azimuth and elevation angles were calculated, and compared against the labelled Sun’s position; when there was detected a difference of more than 0.25º between the two values, the position of the Sun was updated, and the scattering angle for each pixel was then re-calculated.

4.4. Validation of calibration

For MSL Navcam images, the uncertainty of the calibration procedure was estimated by comparing the radiance values of the calibrated images with radiometrically calibrated data of MSL Mast Camera (Mastcam).

The Mastcam system is a pair of fixed-focal length, multispectral, colour CCD imagers mounted on the rover's remote sensing mast: Mastcam-Left (M-34) has a 34 mm focal length, FOV of 20º×15º, 1658×1200 pixel CCD; Mastcam-Right (M-100) has 100 mm focal length, FOV of 6.8º× 5.1º. Both of them are equipped with the same 1658×1200 pixels CCD detector; and have an eight-position filter wheel, enabling them to take Bayer "true colour" images, multispectral images in the 400-1100 nm band, and two neutral density-coated Sun filters (Bell et al., 2017). The main objectives of Mastcam are to retrieve landscape observations for studying past and present geologic processes, document atmospheric and meteorological events, and provide support to other science activities and rover operations (Grotzinger et al., 2012; Bell et al., 2017).

For this purpose, the retrievals of Mastcam-Left filter number 4 were used, as the effective wavelength of this filter (674 nm) is the closest one to the effective wavelength of the navigation cameras (~650 nm). Mastcam observation data were retrieved from the PDS and the conversion from the archived 12-bit DN pixel values to physical units of radiance factor (I/F) and absolute radiance (W m^{-2} nm^{-1} sr^{-1}) was performed using the corresponding image-label file recorded conversion values, as described in Section 5.2.7 of Bell et al. (2017).

Martian sky and surface observations retrieved by both cameras, on which the same scene was captured with a similar pointing during the same sol at approximate LTST were selected. Following these criteria, a total of 16 pairs of Navcam and Mastcam observations were identified and used in the comparison (Table 4.4). Several regions of interest appearing on both observations were chosen, and the mean radiance value of these regions was obtained and compared (Figure 4.10); ending up with a total of around 110 different regions of interest.

Comparisons showed that the radiance value differences between the calibrated Navcam images and Mastcam radiometrically corrected data were less than 2%; which is of the same order as the obtained by Soderblom et al. (2008) for MER Navcams when compared to Pancam. As the absolute radiance uncertainty estimated for Mastcam was about 10% (Bell et al., 2017), it was considered for this research study that the absolute radiance uncertainty of the calibrated MSL Navcam images is about 12%.

For the validation of MSL Hazcam calibration parameters, multiple comparisons were performed between Hazcam and Navcam calibrated images. This criterion was selected for these imagers due to the existing significant differences between the cameras FOV ranges (Hazcam 125º square-degrees; Mastcam-Left 20º×15º), and pointing. The comparison procedure was similar to the one followed for Navcam's calibration: observation pairs with similar pointing, and near in

LTST were selected for different sols, and the absolute radiance values for the same scenery features were compared. In this case, results showed average differences of less than 5% between both imagers; as Navcam absolute radiance uncertainty was estimated of about 12%, an absolute radiance uncertainty for Hazcam cameras of about 17% have been then considered.

Navcam file	Sol	LTST	Mastcam file	Sol	LTST	Pointing
NLA_400157480EDR_D0040000NCAM00510M1	30	13:32:28	0030ML0001340020100850D01_DRXX	30	13:36:12	Sky
NLA_400791104EDR_F0040000NCAM00514M1	37	16:51:14	0037ML0001640030101309D01_DRXX	37	16:48:31	Sky
NLA_403614285EDR_D0050104NCAM00524M1	69	12:07:28	0069ML0004860040102539D01_DRXX	69	12:17:19	Ground
NLA_403797280EDR_F0050104NCAM00526M1	71	13:35:47	0071ML0004980040102589D01_DRXX	71	13:32:06	Cal. targ
NLB_421372569EDR_F0060000NCAM00101M1	269	11:33:52	0269ML0011790040106119D01_DRXX	269	11:36:25	Ground
NLB_449260422EDR_M0300786NCAM00505M1	583	16:08:54	0583ML0024390370300420D01_DRXX	583	16:01:10	Sky
NLB_452004100EDR_F0311330NCAM00322M1	614	13:58:01	0614ML0025940050301802D01_DRXX	614	14:02:43	Ground
NRB_452518799EDR_F0311330NCAM00323M1	620	09:07:45	0620ML0026540020302355D01_DRXX	620	09:03:50	Cal. targ
NLB_461944914EDR_F0401378NCAM00390M1	726	13:43:05	0726ML0031010050305083D01_DRXX	726	13:40:12	Ground
NLB_462486418EDR_D0402040NCAM00556M1	732	16:05:57	0732ML0031410080205207D01_DRXX	732	16:00:44	Sky
NLB_468598450EDR_F0441140NCAM02343M1	801	12:15:14	0801ML0034990020400821D01_DRXX	801	12:24:47	Cal. targ
NLB_505708078EDR_F0520936NCAM00203M1	1219	12:35:44	1219ML0055920120503562D01_DRXX	1219	12:33:47	Ground
NLB_508102653EDR_F0521370NCAM00320M1	1246	12:01:32	1246ML0058130120504007D01_DRXX	1246	12:08:05	Ground
NLB_509965530EDR_F0530186NCAM00320M1	1267	11:41:51	1267ML0059320120504318D01_DRXX	1267	11:54:30	Ground
NLB_511122556EDR_F0531182NCAM00320M1	1280	12:31:39	1280ML0060170120504773D01_DRXX	1280	12:36:42	Ground
NLB_521958717EDR_M0052444NCAM00567M1	1402	14:19:41	1402ML0068710030601789D01_DRXX	1402	14:10:13	Sky

Table 4.4. MSL Navcam and Mastcam comparison observation pairs. List of Navcam and Mastcam observation pairs used for the validation of MSL Navcam image calibration procedure. The camera pointing is provided in the last column; "Cal. targ" stands for Mastcam's calibration target, mounted at rover's right-side top deck (Bell et al., 2017).

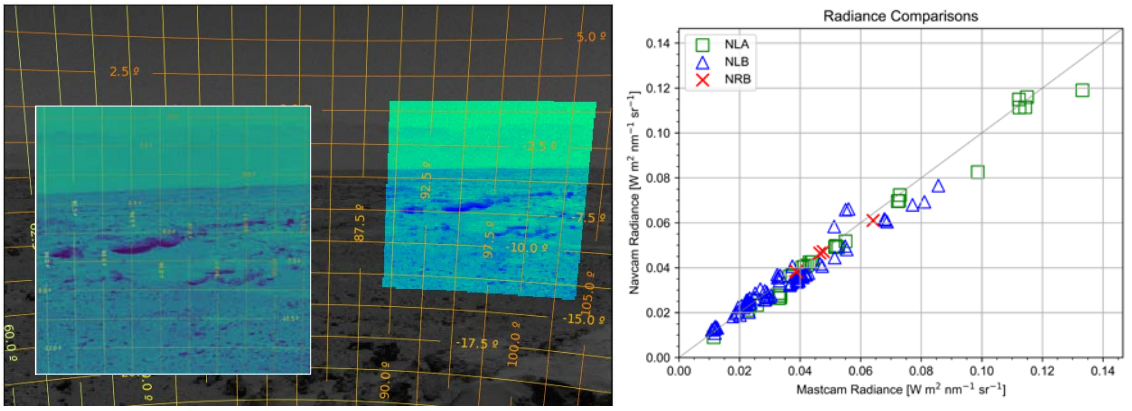

Figure 4.10. MSL Navcam calibration validation. *Left*: Example of a matching-pair of Navcam-Mastcam images used for comparison. Background gray image is Navcam observation raw file NLA_403614285EDR_D0050104NCAM00524M1, obtained on sol 69, L_S = 189.3º, at 12:07:28 LTST. Calibration and geometric reduction were performed on the file; a coordinate grid indicating azimuth and elevation angles with respect to the rover navigation reference frame (RNAV, Peters et al., 2016) is shown. The coloured area at the right of the image shows the scenery captured by the matching Mastcam observation, which is provided on the left-side inset. Mastcam image file is 0069ML0004860040102539D01_DRXX, obtained ten minutes after Navcam's observation (12:17:19 LTST), on the same sol. *Right*: The absolute radiance values were retrieved and compared for several regions of interest (approx. 110) within the 16 pair of Navcam-Mastcam observations, resulting in a mean radiance difference of less than 2%. Source: Adapted from Chen-Chen et al. (2019a).

4.5. Summary

The retrieval and processing of the observation data used in this research study have been discussed in this chapter. The main observation properties and image file types contained in the database have been described. In order to improve the first-order calibration applied to the radiometrically corrected files, the image-processing steps for the implemented photometric calibration and geometric reduction of the MSL engineering cameras raw observations have been detailed; based on the MER Navcam in-flight calibration pipeline developed by Soderblom et al. (2008). The final outcomes of the calibration procedure have been summarised and provided on Table 4.2 (MSL Navcam) and Table 4.3 (MSL Hazcam). Finally, several images of multiple observation-targets retrieved by both MSL engineering cameras and MSL Mastcam (Bell et al., 2017) have been compared in order to validate the implemented calibration, resulting in a total uncertainty in absolute radiance of about 12% for MSL Navcam and 17% for MSL Hazcam.

5. DUST PARTICLE SIZE AND OPTICAL DEPTH

5.1. Introduction

As already discussed in previous chapters, dust aerosol suspended in the Martian atmosphere plays a key role in its climate, as the atmospheric thermal and dynamic structure are mainly governed by the dust seasonal and spatial distribution and its radiative properties (e.g., Gierasch and Goody, 1972). The aerosol radiative properties (i.e., single scattering albedo, phase function, extinction efficiency) depend on the composition and the microphysical characteristics of dust particles. Many improvements have been achieved in the characterisation of dust aerosol particle properties thanks to different exploration missions using both orbital and surface-based observations (e.g., Dlugach et al., 2003; Smith, 2008; Kahre et al., 2017). While remote sensing instruments on-board orbiting spacecraft can provide wider spatial and temporal coverage; when these are compared to ground-based observations, due to the similarity in composition between airborne and surface dust more assumptions are required and more uncertainties arise in the retrieval process (Lemmon et al., 2015).

This research work contributes to the study of Martian atmospheric dust particle physical properties by using MSL rover navigation cameras (Navcams) observations for complementing previous studies with independent retrievals of the particle size distribution effective radius parameters and the column optical depth, together with their seasonal and interannual variations over Gale Crater. The capability of MSL Navcams to obtain Mars' sky images under multiple geometry configurations, including observations very close to the Sun, allows the retrieval of the sky brightness as a function of the angle away from the solar disc centre (scattering angle), which can be evaluated to constrain dust aerosol particle size distribution and its shape. In particular, the sky brightness under a forward scattering scenario (up to 30^{o} away from the Sun), is not sensitive to the aerosol optical properties (the refractive indices, i.e., composition) and shape; as for small scattering angles the intensity is dominated by the aerosol single scattering phase function and differences are negligible for spherical and non-spherical particles (e.g., Pollack et al., 1979; Kaufman et al., 1994; Tomasko et al., 1999; Liou, 2002).

In this study it is presented a methodology for measuring the dust particle size distribution and retrieving its optical depth using MSL Navcam Sun-pointing images. In Section 5.2 the Navcam observations dataset is described. In Section 5.3 the methodology used to retrieve the dust aerosol optical depth and particle size distribution is presented. In Section 5.4 the retrieval outcomes are shown, discussed and validated with retrievals from other instruments; and in Section 5.5 a summary of the findings of this work is provided. The main results of this chapter were published in Chen-Chen et al. (2019a).

5.2. Observations

As discussed in Section 4.1, MSL rover Navcams are used to monitor the terrain surrounding the vehicle, to perform target designation and stereo-observations for supporting the operation of the rover. The four cameras are mounted on the rover's remote sensing mast and are build-to-print copies of MER mission instruments. They count with a 45-by-45 square degree field-of-view, and are featured with a 1024 × 1024 pixel CCD detector with broadband visible filter with an effective wavelength of 650 nm.

The MSL Navcam image database has accumulated more than 70,000 images up to mission sol 1648, covering MY 31 to 33. Within the dataset, 7,000 pictures were obtained with the camera pointing upwards, with an instrument elevation angle greater than 10º, so part of the Martian sky was captured. From these observations, those on which the solar disc was totally contained within the image-frame were selected. In order to reduce the sensitivity to the vertical distribution of dust in the plane-parallel atmosphere approach, the previous sub-set was further reduced by considering only observations with Sun elevation angle greater than 20º (e.g., Lemmon et al., 2015).

This resulted in a final set of 65 Navcam images (Figure 5.1), all of them part of the Surface Attitude Pointing and Positioning (SAPP) observations sequence, which are used to update the rover's position and orientation relative to the local Martian surface (Maki et al., 2012; Peters, 2016). The list of Navcam observations used for this retrieval is provided in Table C.1 in the APPENDIX C.

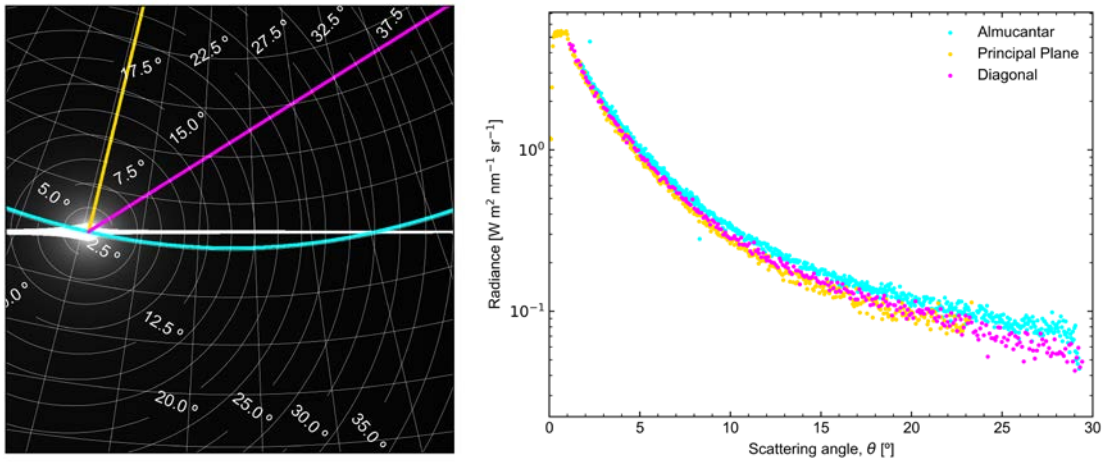

Figure 5.1. Sky brightness curves from Navcam observations. *Left*: Navcam image file NRB_519633718EDR_F0543156SAPP07612M1.IMG, obtained on sol 1376, L_S = 171.85º, LTST 15:08:58. Solar elevation and azimuth angles were respectively 42.11º and 278.92º in Mars local level frame. Radiometric calibration and geometric reduction were performed on the image data. Saturated pixels (white region) were masked off the image and the azimuth-elevation grid and scattering angle contour lines are shown. The sampling paths for different directions are indicated: almucantar (in cyan, along the Sun's elevation angle), principal plane (in yellow, along the solar azimuth angle), and diagonal (in magenta, from the solar disc's centre to the image's top-right corner). *Right*: The sky brightness as a function of the scattering angle for each sampling direction. Source: Adapted from Chen-Chen et al. (2019a)

5.3. Methodology

Mars atmospheric dust aerosol properties were characterised by comparing MSL Navcam observations of near-Sun sky brightness with radiative transfer model computations. The radiative transfer model presented in Section 3.2 was used to simulate the sky radiance (in units of radiance factor, I/F) as a function of the scattering angle (θ) observed by the navigation cameras. Dust aerosol particles radiative properties (single scattering albedo, phase function, etc.) were obtained from T-matrix code calculations for cylindrical particles, with D/L of 1.0 (e.g., Wolff et al., 2009).The retrieval procedure consisted in a brute-force scheme based in the iterative comparison of sky brightness curves observed by Navcams with radiative transfer simulated curves with 2 free parameters: the particle size distribution effective radius (r_{eff}), and the dust column optical depth at surface (τ_0). The output of this retrieval is the pair of (r_{eff}, τ_0) parameters generating the best fitting model-simulation curve under a lowest mean quadratic deviation χ^2 criterion.

For each Navcam observation:

1. The Engineering Data Record (EDR) raw image file was retrieved from NASA's Planetary Data System Imaging Node (PDS), and was calibrated following the guidelines provided in Section 4.2 in order to obtain the observed scene radiance, L_{obs} (W m^2 nm^{-1} sr^{-1}). This radiance was then converted into approximated radiance factor $(I/F)_{obs}$ by dividing each pixel's radiance value by the top of atmosphere (TOA) solar spectral irradiance at the time of the observation convolved to the Navcam filter bandpass (1.524 W m^2 nm^{-1} sr^{-1} at 1 AU), and divided by π (Soderblom et al., 2008; Bell et al., 2017). The solar spectral irradiance data was obtained from Colina et al. (1996).

2. Geometric reduction was performed on the calibrated observation as described in Section 4.3: for each pixel of the image, the corresponding values for the site azimuth and elevation were derived, together with the scattering angles.

3. The Navcam observed sky brightness as a function of the scattering angle curve was generated by sampling the sky radiance factor along a diagonal sampling path (Figure 5.1). This path started at the centre of the solar disc (scattering angle θ = 0º) and finished at the furthest sky point on the image, which due to the observation's geometry for all cases was located at the top right corner of the 1024×1024 pixel image. This sampling direction was selected in order to reduce the relevance of the aerosol vertical distribution by avoiding points with low elevation, and cover as much part of the sky brightness curve as possible (*cf.* Soderblom et al., 2008). The retrieved sky radiance curve was sampled from a scattering angle of $\theta = 4$º to 30º, with steps of 1º. This sample range was selected in order to skip the saturated pixels located near the solar disc region, and to limit possible contributions from instrumental stray and scattered light. Additionally, this also alleviated the computational time requirements related to the number

of streams used in the radiative transfer code for computing the very forward scattering angle region.

4. The modelled curve was generated using the radiative transfer model presented in Section 3.2. For the solar longitude (L_S) and local true solar time (LTST) of the observation, the atmosphere structure model was initiated and the atmospheric parameters at each layer were retrieved from the Mars Climate Database (MCD). Dust aerosol radiative properties (single scattering albedo, phase function) were calculated with the T-matrix code for cylindrical particles with aspect ratio D/L = 1 and leaving the particle size distribution effective radius (r_{eff}) as a free parameter (v_{eff} fixed to 0.3). The vertical distribution of dust opacity $\tau(z)$ was generated using the modified Conrath profile expression (3.7); which depended on the atmospheric pressure, the solar longitude L_S and the dust column optical depth at surface (τ_0), which was left as the second free parameter.

5. Once the model was generated, the radiative transfer problem was solved using the discrete ordinates method (DISORT) for each point in the sky along the defined sampling direction, in order to obtain the modelled sky brightness (in radiance factor, I/F) as a function of the scattering angle. The viewing geometry configuration in the simulation was defined from the position of the Sun and the sky point coordinates retrieved along the sampling path. The number of moments used in the expansion of the aerosol model phase function was set to 250, while the number of streams was fixed to 32 (Buras et al., 2011).

6. The Navcam observed sky brightness as a function of the scattering angle curve, $I/F_{obs}(\theta)$, and the modelled curve, $I/F_{mod}(\theta)$, were compared using a standard χ^2 method:

$$\chi^2 = \sum_{i=1}^{N} \left(\frac{(I/F)_{obs_i} - (I/F)_{mod_i}}{\sigma_i \cdot (I/F)_{obs_i}} \right)^2 \quad (5.1)$$

where for the N sampled points along the curve, the Navcam observed and modelled sky radiance at the specific scattering angle were compared using a least squares quadratic error criterion, with variance σ_i = 0.12 associated with the absolute calibration uncertainty (12%) of MSL Navcam derived in Section 4.4. The reduced χ^2 parameter, χ^2_ν, was then calculated by dividing the obtained χ^2 by the number of degrees of freedom of the problem, $\nu = N - 2$, which was equal to number of sampled points minus the number of free parameters of the retrieval, r_{eff} and τ_0.

The best fitting curve comparison was done in a successive manner, by comparing the observed sky radiance with each of the modelled sky brightness curves generated with combinations of the model free parameters (r_{eff}, τ_0). In order to cover a broad range of possible scenarios, the aerosol particle effective radius was iterated from 0.5 to 2.5 μm, with steps of 0.02 μm; and the dust column opacity at surface was sampled between 0.1 (low dust) and 2.5 (high dust content) with steps of 0.02. The size of the steps were limited due to computational

time requirements; and the limits of the (r_{eff}, τ_0) sampling region were defined based on previous studies at MSL landing site (Lemmon, 2014; Smith et al., 2016; Vicente-Retortillo et al., 2017; McConnochie et al., 2017).

7. The set of parameters (r_{eff}, τ_0) returning the minimum value for the mapped χ^2 were considered the solutions of the retrieval; the uncertainty level associated with each parameter was then calculated from the 68% confidence region (1σ error) (Figure 5.2).

5.4. Results and discussion

In this section, the retrieval outcomes for the aerosol particle size distribution effective radius and dust column optical depth are presented (see Table C.2 in APPENDIX C), the seasonal variation of these parameters along MY 31 to 33 (Figure 5.3 and Figure 5.4) are evaluated, and the outputs and findings are put into context by comparing with results from previous studies. Finally, a discussion is provided regarding the sensitivity of the model and the uncertainties involved in the retrieval procedure.

5.4.1. Dust optical depth

The retrieved seasonal behaviour (Figure 5.3, bottom) shows the gradual decrease corresponding to the low dust opacity season, when optical depth shifts from initial values of τ_0 ~ 0.75 around L_S = 40º, down to its minimum value of τ_0 ~ 0.41 at L_S = 135º (northern hemisphere summer). After this point, a noticeable increase can be appreciated right before L_S = 150º reaching values of τ_0 ~ 0.75; up to maximum opacity values retrieved during this period of τ_0 ~ 1.0 (L_S = 165º). A second period of enhanced dust activity can be observed after L_S = 200º, where there is a steep increase in atmospheric dust loading with opacities scaling from τ_0 close to 0.80 up to τ_0 > 1.25; which corresponds to the maximum optical depth in the retrieved seasonal cycle. The dust column opacity at surface drops back to opacity values of 0.80 (L_S ~ 300º) previous to a third active dust period observed around L_S = 325º, when a subtle increase can be detected reaching τ_0 ~ 1.0, before the final descent at the end of the year down to opacity values of 0.70 (only data for MY 31).

The seasonal behaviour of dust optical depth obtained with MSL Navcam agrees with previous descriptions of long-term dust opacity records retrieved by different missions since MY 12 (Viking Lander 1 and 2; Colburn et al. 1989) for periods without global dust storms (e.g., Figure 10.3 in Kahre et al., 2017). In particular, within the MSL mission context, both interannual and seasonal column optical depth behaviour present an overall good agreement with other MSL instrument opacity results derived by other authors (*cf.*, Lemmon, 2014, Smith et al., 2016, McConnochie et al., 2017).

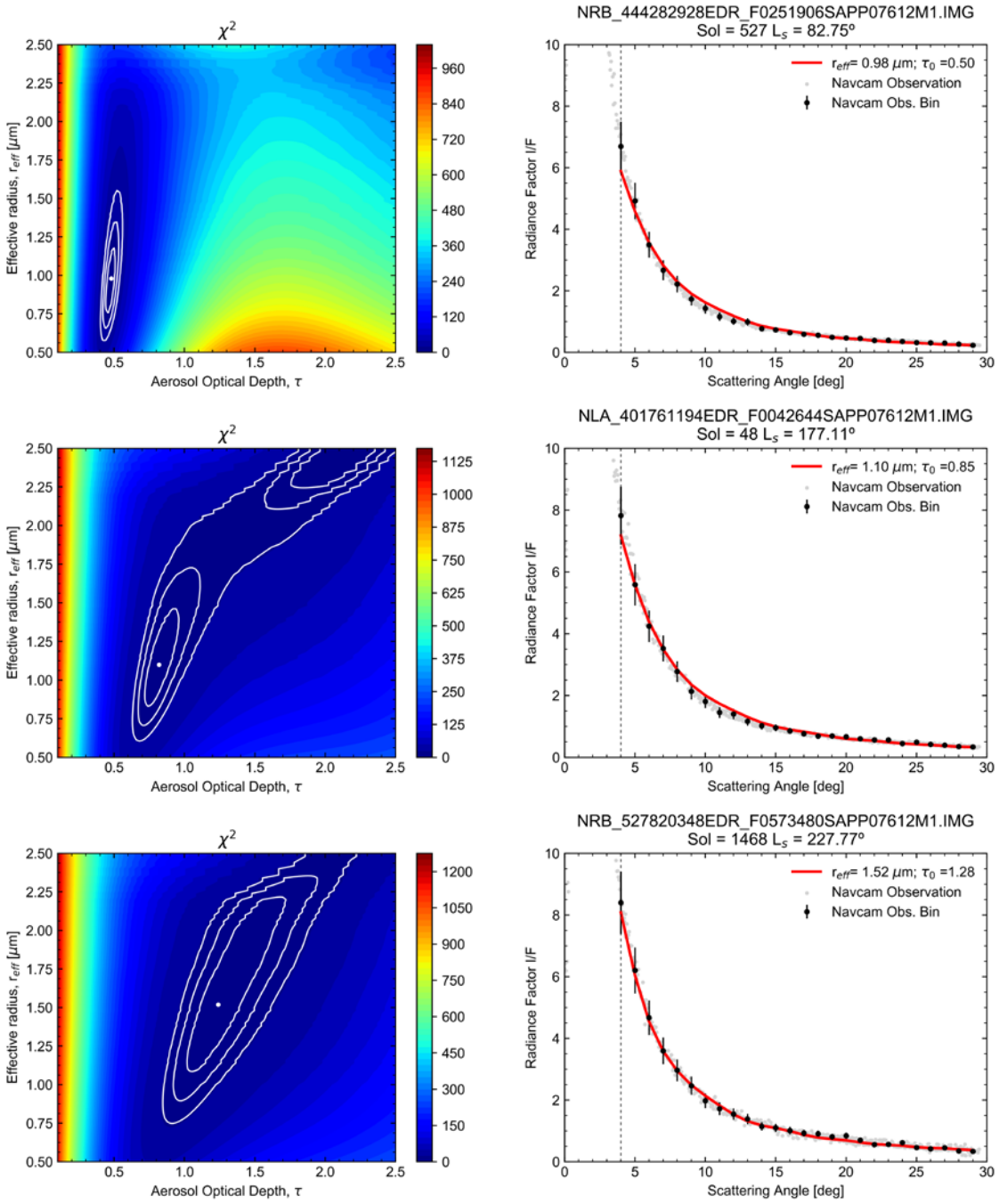

Figure 5.2. Dust optical depth and particle size distribution effective radius results. Results for three scenarios under different atmospheric dust loading conditions are shown on each row: on the left, the χ^2 values of the model-observation curve fitting in the τ_0-r_{eff} parameter space are mapped. The location of the minimum χ^2 and the contours for the 68.3%, 95.4% and 99.7% confidence interval limits are indicated. On the right, the Navcam retrieved sky radiances (gray) and the best fitting model curve (red line) are graphed, together with the binned observation data (black) and the error-bars representing the absolute calibration uncertainty associated with the imager (12%). Source: Adapted from Chen-Chen et al. (2019a).

5.4.2. Dust particle effective radius

The seasonal and interannual variations of dust aerosol particle effective radius are shown in Figure 5.4; these are put into context by comparing with retrievals from other MSL instruments: passive sky spectral observations by ChemCam (McConnochie et al., 2017), and REMS UV photodiodes (Vicente-Retortillo et al., 2017).

The retrieved seasonal behaviour (Figure 5.4, bottom) shows a steady decrease during the first half of the aphelion season (L_S = 0º to 180º), with r_{eff} varying from 1.40 μm down to minimum values of 0.80-0.90 μm (L_S ~ 130º); whereas the second half of the aphelion period it is featured with a gradual increase, reaching an effective radius of 1.50 μm around L_S = 180º, which also corresponds to an enhancement in the dust column opacity. At the beginning of the northern autumn season (L_S = 180º to 270º), the retrieved effective radius decreases to 1.20 μm, before larger particle sizes of r_{eff} ~ 1.50 μm (especially in MY 31) are observed in the proximity of L_S = 230º. At the end of the year, a new decrease can be appreciated with r_{eff} values dropping to 1.00 μm (L_S = 300º, only MY 31 data), prior to a final shift back to 1.30 μm around L_S = 350º.

A discrepancy in the retrieved seasonal behaviour with respect to ChemCam and REMS UV results can be appreciated on the figures, especially during the second half of the year. A possible explanation for this may be found in the analysis of the interannual behaviour (Figure 5.4, top). The lack of ChemCam data for the perihelion season (L_S = 180º to 360º) of MY 33 (sol > 1400) does not make it possible to evaluate the actual level of discrepancy; however, results for the first hall of MY 33 (sols between 1000 and 1400) show that the estimated particle effective radii are smaller when compared to the same period of MY 32, and therefore it might reduce the existing deviation from those studies.

5.4.3. Relationship between dust particle size and optical depth

Retrieval results of dust column optical depth and aerosol particle size distribution effective radius are shown in Figure 5.5. The coefficient of determination (R^2) was calculated for these variables resulting in a value of 0.49, which indicates a low-to-medium correlation. The same R^2 coefficient applied to previous results for MSL site returned values of 0.69 and 0.67 for ChemCam and REMS UV retrievals, respectively (McConnochie et al., 2017; Vicente-Retortillo et al., 2017). However, it is worth highlighting that the temporal range covered by the those instruments are different; being sols 1291, 1150 and 1646 the latest data record for ChemCam REMS UV and Navcam, respectively. If the observational data used in this study were limited to those dates, R^2 correlation coefficients of 0.63 and 0.69 would be then obtained, respectively.

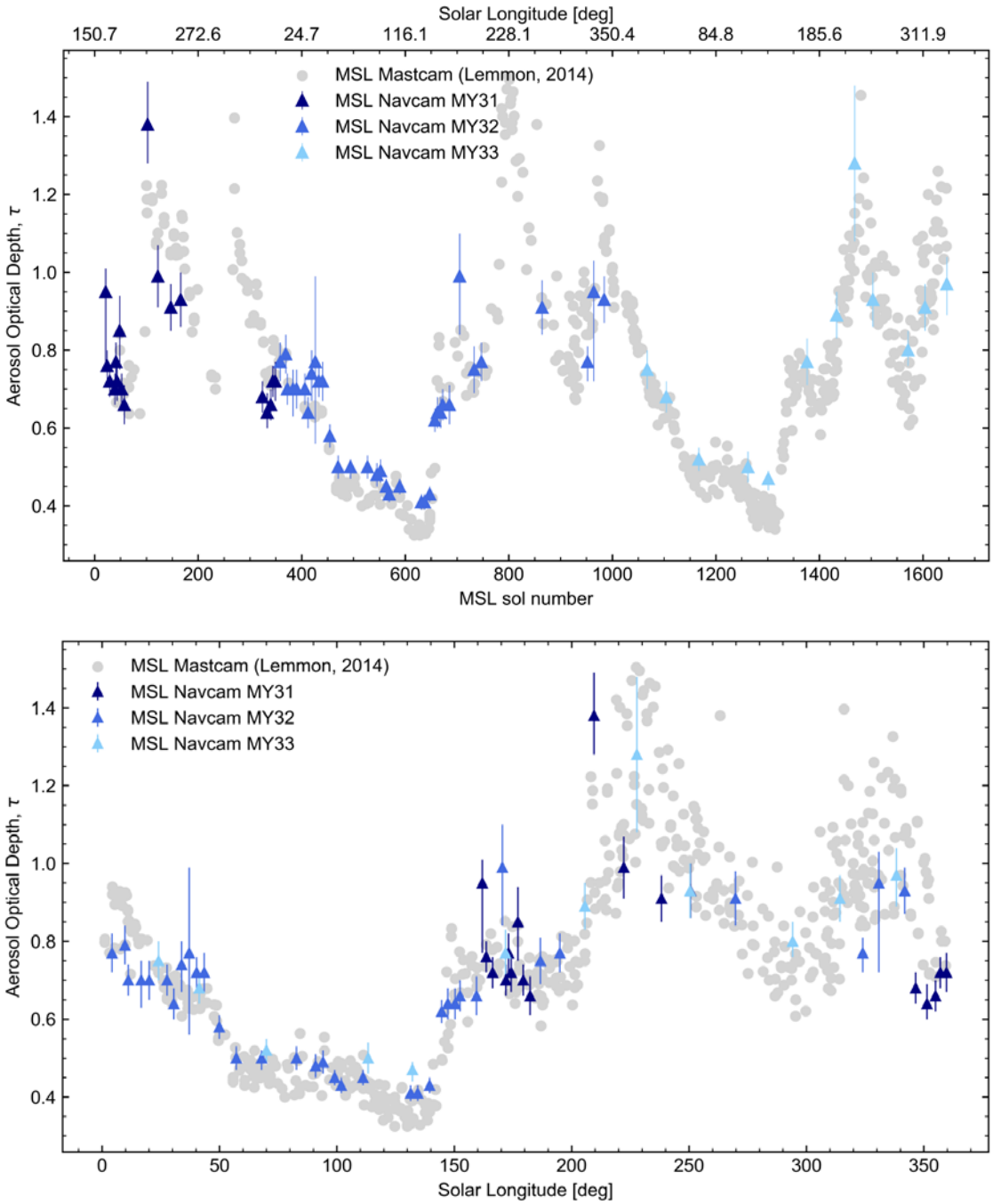

Figure 5.3. Dust aerosol column optical depth at surface derived with Navcam. Results for the interannual (top) and seasonal (bottom) behaviour of dust column optical depth at surface derived from the 65 Navcam observations, covering a period of almost 3 Martian Years, from sol 21 (L_S = 162º, MY 31) to sol 1646 (L_S = 338º, MY 33) are shown. Results are put in context with MSL Mastcam Sun direct imaging optical depth measurements (Lemmon, 2014). For comparison purposes with Mastcam results, the retrieved dust column optical depth by Navcam is referenced to a wavelength of 880 nm. Source: Adapted from Chen-Chen et al. (2019a).

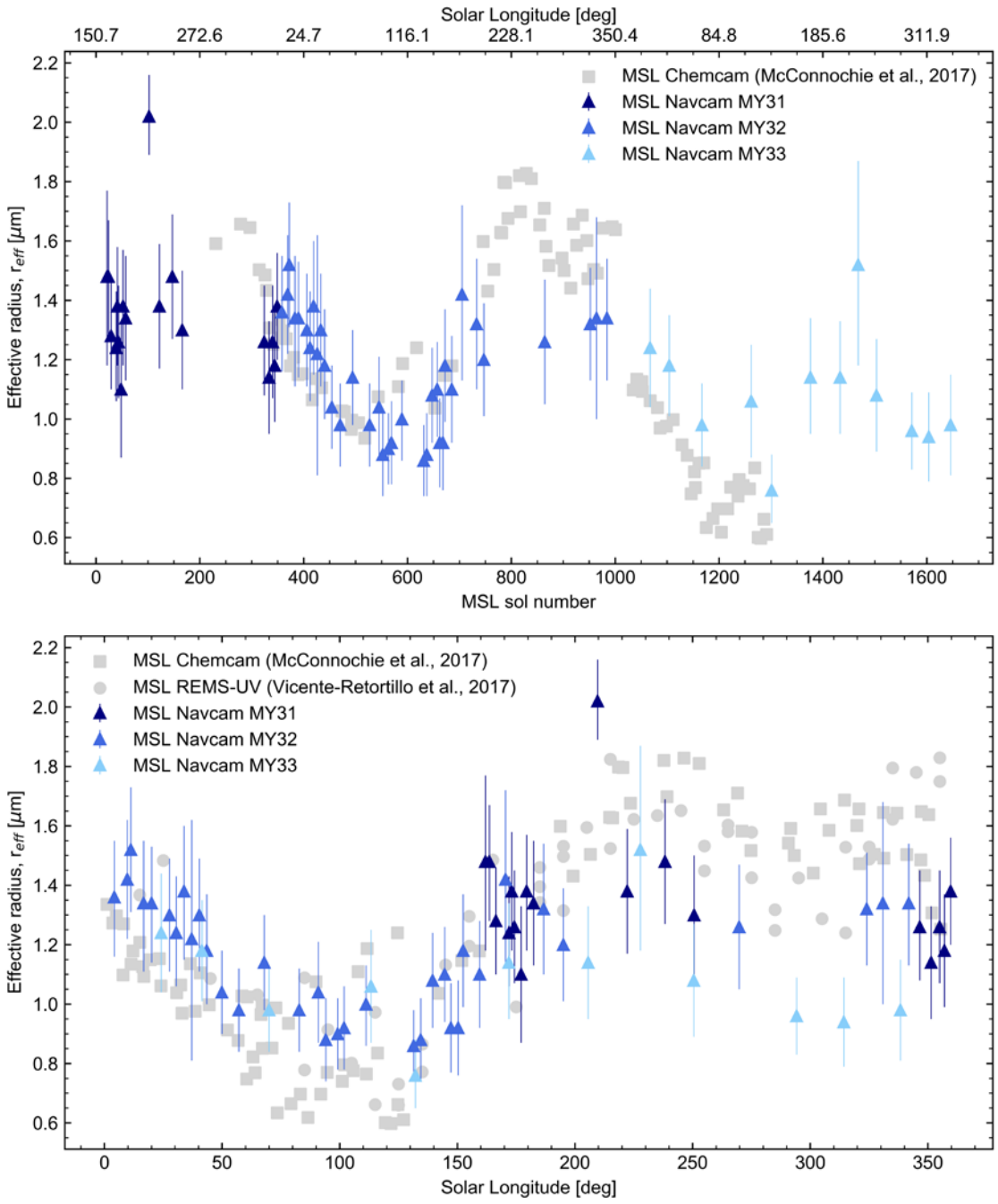

Figure 5.4. Dust aerosol particle size distribution effective radius retrieved with Navcam. Interannual (top) and seasonal (bottom) behaviour of dust particle size distribution effective radius (r_{eff}) parameter derived with Navcam observations for MY 31, 32 and 33. Results from previous studies by MSL ChemCam (squares) (McConnochie et al., 2017) and REMS UV (spheres) (Vicente-Retortillo et al., 2017) are provided for comparison purposes. Source: Adapted from Chen-Chen et al. (2019a).

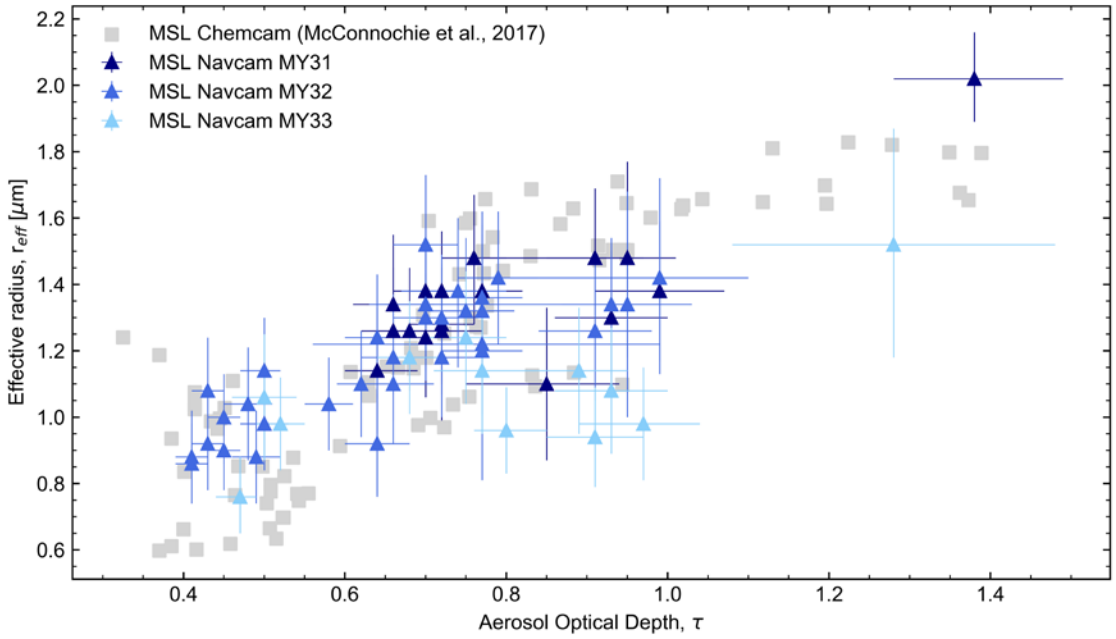

Figure 5.5. Relationship between dust particle effective radius and aerosol optical depth. Dust particle effective radius is plotted as a function of column optical depth. For comparison purposes, retrievals obtained by ChemCam (McConnochie et al., 2017) are included in the figure. Source: Adapted from Chen-Chen et al. (2019a).

5.4.4. Sensitivity study

In the retrieval procedure described above, some assumptions were made on part of the input parameters required in the radiative transfer model for simulating the sky brightness. In the next paragraphs, the robustness of the results of this study is evaluated by evaluating the sensitivity of the outputs to variations in the input parameters.

Parameter retrieval. From the best-fitting regions of the χ^2 maps for the r_{eff}-τ_0 parameter space presented on Figure 5.2, it can be appreciated that the retrieval procedure presents more sensitivity to the column optical depth than to the effective radius. This is mainly due to the different influence that each parameter has on the simulated sky brightness curves: while the column optical depth τ_0 sets the overall radiance factor I/F values of the modelled curves, the effective radius r_{eff} predominantly controls the shape of the curve within the evaluated scattering angles. In order to estimate the effect of τ_0 parameter on the r_{eff} outputs, a simulation run was performed in which the column optical depth inputs were defined in accordance with Mastcam Sun imaging extinction measurements for the nearest sol (Lemmon, 2014); it is reported that the average difference between the opacity values retrieved in this study and Mastcam measurements are of around 10%. When comparing the r_{eff} results derived in the nominal case (2 free parameters) with outputs of fixed-optical depth simulations, a mean difference of about 16% was obtained; being the largest discrepancy values (30% to 45%) located in the L_S = 120º-160º and 300º-330º windows.

Sky radiance sampling path. From the different sky radiance sampling paths presented in Figure 5.1, the diagonal direction was selected, in an analogous way to Soderblom et al. (2008). In order to evaluate the sensitivity of the results to the sampling direction, the retrieval outputs of the base model were compared to simulation results when sampling along the principal plane direction (sky points with same azimuth angle as the Sun). This comparison returned an average difference of 11% for the column optical depth, and 8% for the effective radius parameter. Mean differences for the χ_v^2 parameter were about 5% lower in the principal plane sampling case.

Aerosol particle shape. Regarding the selected shape for dust aerosol particles, previous studies showed that this parameter has negligible influence in the forward scattering region of the brightness curve (scattering angles up to 30º) (Hansen and Travis, 1974; Pollack et al., 1995). The sensitivity of the results to the selected shape of the particle was evaluated by comparing the outputs of two simulations using spherical and cylindrical particle models with diameter-to-length aspect ratio of 1.0. The comparison of the best fitting parameters under these simulations showed average differences of 7% for the optical depth and 13% for the aerosol particle effective radius; both quantities were contained within the uncertainty region of the nominal scenario. The average difference for the χ_v^2 parameter values were approximately less than 2% lower for the spherical particle simulation when compared to the base scenario with cylindrical particles.

Effective variance of the aerosol particle size distribution. Additional retrievals were performed with different particle size distribution effective variance (v_{eff}) in order to characterise the sensitivity of the results to this parameter. Two simulations were run for aerosol particle size distribution v_{eff} set to 0.4 and 0.5 (e.g., Wolff et al., 2006; Tomasko et al., 1999). Results of these retrievals were compared with the base model (v_{eff} = 0.3), obtaining in the v_{eff} = 0.4 case, average differences of 2% and 11% for the best fitting dust optical depth and effective radius, respectively. For v_{eff} = 0.5, these mean variations were about 3% (in τ_0) and 13% (in r_{eff}). When evaluating the χ_v^2 parameter, the resulting values for the 0.4 and 0.5 effective variance models were 4% and 7% lower than the 0.3 case, respectively.

Vertical distribution of the aerosol optical depth. This is related to the dust mass mixing ratio vertical distribution governed by the modified Conrath profile (3.7), which depends on the column optical depth at surface (τ_0), and the l and ν constants, which control the dust layer maximum altitude and the vertical profile shape, respectively. Additional simulations were performed using limit-values of these parameters, for dust layer top altitudes of 40 km (l = 1.75) and 80 km (l = 0.875), and dust profiles with exponential (ν = 0.1) and step (ν = 0.001) shapes. The outputs of these simulations showed that the model had no sensitivity to such variations.

Surface albedo. In the radiative transfer model used in this study the surface albedo parameter was set to an average value of 0.20 for the Gale Crater region (*cf.*, Anderson and Bell, 2010). For surface-based upward looking observations, it is expected that the surface reflectivity has

little impact on the retrieved image intensity; in contrast with in-orbit downward pointing observations, on which the reflection properties of the ground need to be separated from atmospheric dust scattering phase function (Pollack et al., 1995; Tomasko et al., 1999). Several retrievals were performed for different surface albedo values ranging from 0.10 to 0.50, and covering the possible values for the Gale Crater region (Anderson and Bell, 2010). The results of these retrievals showed that the effective radius and dust column opacity had no sensitivity to surface albedo variations.

5.5. Summary

It has been shown that the navigation cameras onboard MSL rover can be used to estimate the atmospheric dust opacity and constrain the aerosol particles size effective radius. For this study, a total of 65 Sun pointing Navcam observations were selected, spanning from sol 21 to sol 1646, covering 2.5 Martian Years. Radiometric calibration and geometric reduction were performed on the images following the calibration process derived in Chapter 4. The observed sky brightness as a function of the scattering angle were compared against modelled curves simulated with a multiple scattering radiative transfer model of Martian atmosphere (Section 3.2), in order to retrieve the optical depth and aerosol effective radius parameters that generate the best fitting curve. The obtained results for atmospheric dust loading showed variations of column optical depth from 0.4 (L_S = 130º) to 1.4 (around L_S = 220º); with aerosol particle effective radius constrained between 0.8 and 2.0 μm. The retrievals presented significant variations in the seasonal behaviour for both variables, showing a positive correlation between high optical depths and large particles. The outcomes of this work were compared with previous studies using different instrumentation onboard MSL rover and presented an overall good agreement (Lemmon, 2014; Smith et al., 2016; McConnochie et al., 2017).

6. DUST SINGLE SCATTERING PHASE FUNCTION

6.1. Introduction

The single scattering phase function describes the angular distribution of the scattered light by aerosols and it is strongly influenced by the size and shape of the particles. In particular, the light scattering behaviour at intermediate and large scattering angles can provide relevant information on the shape (Kaufman et al., 1994). The characterisation of the particle shape is of relevance as it affects the estimates of other parameters, such as the aerosol column opacity and the imaginary part of the complex refractive index (Dlugach et al., 2002; Merikallio et al., 2011). While light scattering calculations for spherical particles are straightforward by using the Lorenz-Mie theory (e.g., Hansen and Travis, 1984), computations considering realistic dispersions of non-spherical particles may result very complex and computationally demanding (Dubovik et al., 2006; Yang et al., 2007; Yurkin and Hoekstra, 2007; Merikallio et al., 2013).

Retrievals of Martian atmospheric dust phase function and constraint of particle shape have been performed by several authors using both orbital and surface-based observations (see Section 3.1). Chýlek and Grams (1978) first used a non-spherical randomly oriented particle model to fit Mariner 9 reflectance data during the 1971 dust storm. Pollack et al. (1995) evaluated Viking Lander sky images using a semi-empirical theory to model scattering properties by non-spherical particles (Pollack and Cuzzi, 1980) for fitting the observations. They retrieved a modest peak in the backscattering region that suggested sharp corners within the particle's geometry. Dust single scattering phase functions derived with radiative transfer simulations to fit sky radiance data observed by Mars Pathfinder IMP camera showed good agreements with plate-like particles (Tomasko et al., 1999; Markiewicz et al., 1999). Wolff et al. (2001) compared MGS-TES dust emission phase function observations to radiative transfer simulations using T-matrix computations for randomly oriented non-spherical aerosols (Mishchenko and Travis, 1998), obtaining best-fits for cylindrical particles with diameter-to-length aspect ratios (D/L) of 2.3 or 0.6. Further comparisons using sky radiance data observed by MER Pancam also derived similar results (Lemmon et al., 2004; Smith and Wolff, 2014). All of these investigations have shown that light scattering by dust aerosol is consistent with non-spherical particles. However, the number of observations and seasonal coverage are limited.

The objective of this study is to characterise Martian atmospheric dust scattering phase function using sky image data retrieved by MSL engineering cameras and to contribute to previous studies by extending the results with observations covering 4 Martian Years (MY 31 to 34). In this case, the large FOV offered by MSL Hazcam, together with their capability to obtain simultaneous observations and their frequent use, make them suitable for studying dust light scattering properties at medium and large scattering angles.

This Chapter 6 is structured as follows. In Section 6.2, the observation dataset used in this work is described. In Section 6.3 the methodology used in this study is detailed, including the description of the aerosol models considered. In Section 6.4 the outcomes of this work are presented and discussed, together with an analysis of the uncertainties and limitations of the method. Finally, Section 6.5 summarises the main findings of this research. Most of the content of this chapter has been reported in Chen-Chen et al., (2019b).

6.2. Observations

MSL Navcam and Hazcam observations were used in this research study. The complete list of Navcam and Hazcam observations used in this retrieval is provided on Table D.1 in the APPENDIX D of this dissertation.

MSL Hazcam opportunistic simultaneous front and rear pointing wide FOV imaging capabilities have been used to retrieve the angular distribution of Martian sky brightness (Figure 6.1, top). The solar elevation angle is about 25º to 5º for observations taken between approximately LTST 16:00 and 17:30, and the solar almucantar plane is contained within Hazcams' FOV. Depending on the rover's orientation and the surrounding topography, it is possible to retrieve the sky radiance as a function of the scattering angle with a 110º-coverage, and reaching up to 160º of scattering angle. The maximum scattering angle in the solar almucantar plane is given by $\theta_{max} = 180^o - 2\varepsilon_{Sun}$, where ε_{Sun} is the solar elevation angle. Therefore, the sampling of sky radiances along the solar almucantar direction was chosen for Hazcam observations.

In addition to those observations, MSL Navcam full sky-survey sequences have been also considered (Figure 6.1, bottom). These datasets consist of multiple observations (usually 17 or 18 images) obtained in the early morning or afternoon in which the complete upper hemisphere was captured. The sky radiance as a function of the scattering angle was retrieved along the solar almucantar, analogously to Hazcams' images.

It is shown on Figure 6.2, for all the observation data retrieved along the solar almucantar, the contour plot of the sky radiance as a function of the scattering angle (θ) and the solar longitude (L_S).

It can be appreciated that the sky brightness intensity and its angular distribution function follows a seasonal variation similar to the one derived for the dust column optical depth (e.g., Lemmon, 2014; Smith et al., 2016). The first part of the year (aphelion season) is characterised for its low dust activity and atmospheric optical depth; which can be also identified in the sky radiance curves, which show a steeper drop in the radiance values during this period (L_S ~ 70º to 140º) in the lateral scattering region (θ = 90º to 120º), when compared to a flatter curve present during the high dust loading season, centred on L_S ~ 200º.

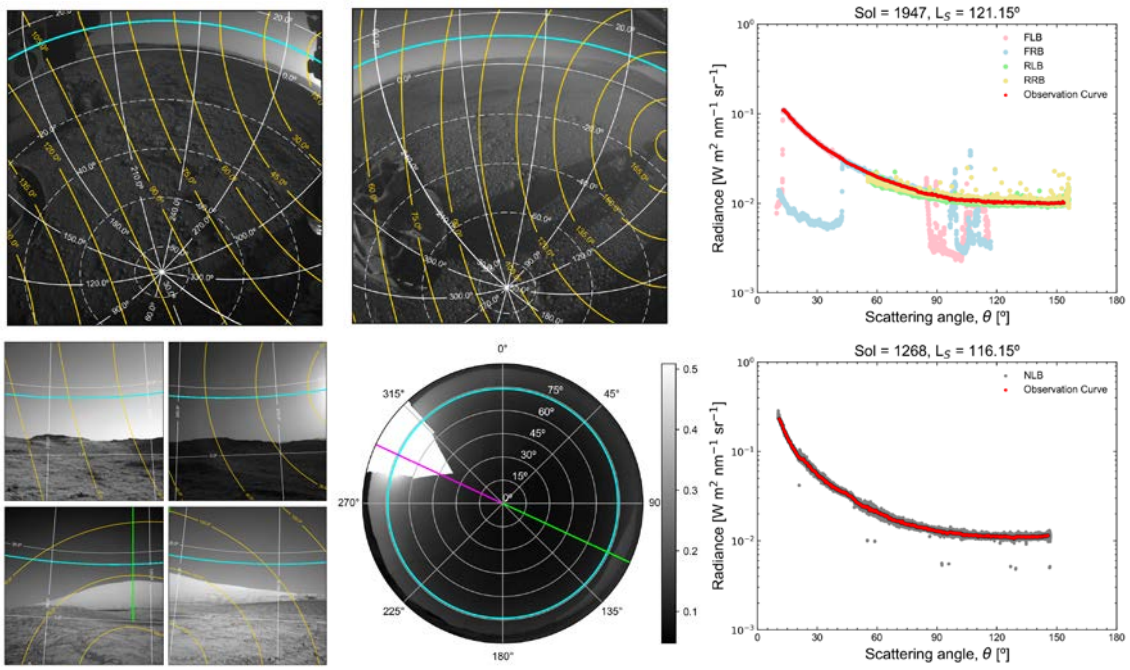

Figure 6.1. MSL engineering cameras observations for evaluating dust phase function. MSL Hazcam (top-row) and Navcam (bottom-row) images used for deriving the sky brightness angular distribution. The azimuth-elevation grid (white) with respect to a local site frame is shown, together with the scattering angles (yellow) and the solar almucantar plane (cyan). *Top-row*: FLB (left) and RLB (centre) Hazcam observations on sol 1947, L_S = 121.15º, LTST ~ 17h, with solar elevation angle of 11º. On the right, the sky radiance retrieved by all Hazcam cameras (FLB, FRB, RLB, RRB) along the solar almucantar plane and the final observation curve derived from these contributions. *Bottom-row*: (Left) Navcam sky-survey observations on sol 1268, L_S =116.1º, LTST from 16:30 to 16:40, solar elevation angle of 16º to 18º. (Centre) Polar-plot of the full sky-survey sequence; for clarity, the square root of radiance values is plotted. The almucantar (cyan) and solar principal plane's forward (magenta) and backward (green) region are also shown. On the right, the sky radiance sampled by each image of the Navcam sky-survey sequence on the solar almucantar (gray) and the final observation curve (red) are plotted. Source: Adapted from Chen-Chen et al. (2019b).

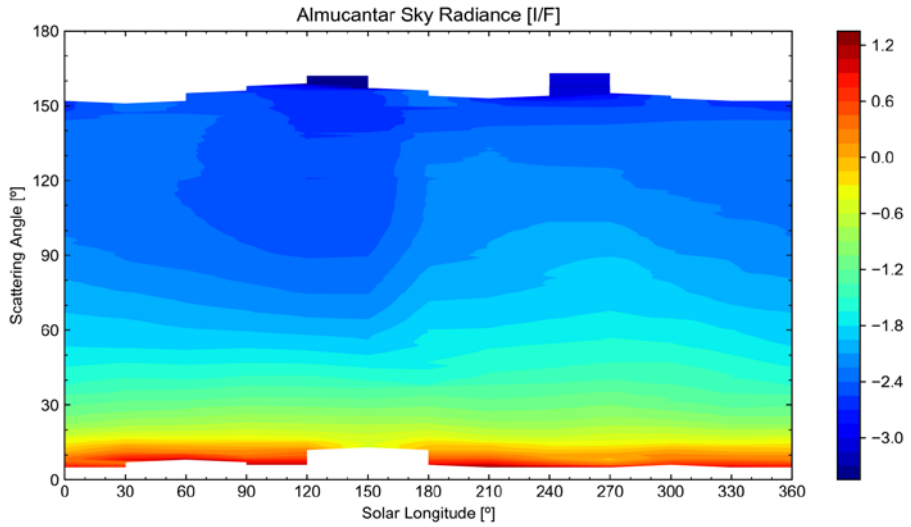

Figure 6.2. Seasonal variation of sky radiance as a function of the scattering angle. MSL engineering cameras observed sky brightness (provided as radiance factor, I/F, in logarithmic scale) along the solar almucantar plane, as a function of the scattering angle (θ) and the solar longitude (L_S). Radiance data is binned every 1º of scattering angle and averaged over a 20º interval in L_S. Source: Adapted from Chen-Chen et al. (2019b).

6.3. Modelling and methodology

In this work the radiative transfer modelled sky brightness curves were iteratively compared to MSL Engineering Camera observations, in order to derive the parameters of the dust single scattering phase function generating the best fitting simulation. In the next paragraphs, the followed methodology to model the angular distribution of sky radiance is described, together with the comparison criterion used.

6.3.1. Radiative transfer model

The radiative transfer scheme presented in 3.2 was used to solve the radiative transfer problem in this scenario. As a summary, the simulations were performed using the discrete ordinates method (Stamnes et al., 1988) for a multiple scattering plane-parallel atmosphere, with pseudo-spherical correction (CDISORT, Buras et al., 2011; Hamre et al., 2013). The atmosphere was modelled with 30 layers distributed in linearly spaced pressure levels with a total height of 100 km. The atmospheric structure parameters were retrieved from the Mars Climate Database (Forget et al., 1999; Millour et al., 2015). Only contributions to the opacity of the atmosphere from dust aerosol and Rayleigh scattering due to the CO_2 were considered.

6.3.2. Aerosol model

The radiative transfer computations required only 3 parameters at each layer of the discretised atmosphere model for the radiance: the aerosol single scattering albedo (ω_0), the single scattering phase function $P(\theta)$, and the vertical distribution of the aerosol optical depth, $\tau(z)$.

The dust optical depth at each layer $\tau(z)$ was modelled following a modified Conrath profile (Forget et al., 1999; Heavens et al., 2011a), and the total column optical depth input value required in these profiles were retrieved from MSL Mastcam direct Sun imaging extinction measurements (Lemmon, 2014) and MSL Navcam retrievals (Chen-Chen et al., 2019a).

For ω_0 and $P(\theta)$, the following 3 modelling approaches were selected for this study:

- *Analytical phase function.* A set of analytical single scattering phase functions were generated using a Double Henyey-Greenstein (DHG) three-parameter analytical expression (Kattawar, 1975; Gillespie, 1992) in the form of:

$$P_{DHG}(\theta) = \alpha \frac{1 - {g_1}^2}{(1 - 2g_1 cos\theta + {g_1}^2)^{3/2}} + (1 - \alpha) \frac{1 - {g_2}^2}{(1 - 2g_2 cos\theta + {g_2}^2)^{3/2}} \quad (6.1)$$

Parameters controlling the forward scattering (g_1), backward scattering (g_2) and the forward-backward ratio (α) were varied in order to simulate different aerosol phase functions (Ignatov, 1997; Zhang and Li, 2016). The g_1 parameter was iterated from 0.50 to 1.00 with steps of 0.01; g_2 was varied between –g1 and +g1 (50 divisions) in order to prevent the backward scattering lobe from being greater than forward lobe and to avoid negative phase function values (Zhang

and Li, 2016). Finally, the parameter controlling the ratio (α) was iterated from 0.50 to 1.00 (fully forward scattering case) with 0.01 steps. Again, this was set in order to control the overall shape of the phase function and use representatives of actual airborne dust phase functions (e.g., Mishchenko et al., 1997; Dubovik et al., 2006). The single scattering albedo was fixed to ω_0 = 0.975 based on results derived from surface-orbit combined observations by Wolff et al. (2009) and particularised for MSL engineering cameras effective wavelength (λ_{eff} ~ 650 nm).

- *T-matrix*. Previous studies have indicated the need to take into account the non-sphericity when modelling the optical properties of Martian dust (e.g., Pollack et al., 1977; Chýlek and Grams, 1978). Although there are available multiple models for calculating the scattering properties of non-spherical particles, software codes for simulating particle shapes with complex and irregular geometry or large ensembles of particles are very computationally demanding (Yurkin and Hoekstra, 2007; Wriedt, 2009). For this study, the T-matrix code was selected (Mishchenko and Travis, 1998) to calculate the radiative properties of randomly oriented cylindrical and spheroidal particles with different diameter-to-length (D/L) aspect ratios and sizes.

For cylindrical particles, the calculated phase functions do simulate well the usual airborne dust phase function in the lateral scattering region (θ approximately from 90º to 120º) (Mishchenko et al., 1997). This way, single aspect ratio cylinders were considered (e.g., Wolff et al., 2009) and the D/L parameter was varied from 0.5 to 2.5 with steps of 0.1.

In the case of spheroidal particles, the computed phase functions for single D/L spheroids present several features, such as peaks and function minimums, within that same scattering region (e.g., Figure 3 in Dubovik et al., 2006), being especially significant when D/L is near 1.0 (spheres); therefore requiring the use of a distribution of aspect ratios and introducing then additional parameters to the retrieval (selected type of aspect ratio distribution and the associated variables) (Dubovik et al., 2006; Merikallio et al., 2011). In order to limit the number of free parameters and control the required computational time of the retrieval, as a first approach, a standard distribution of aspect ratios was implemented for spheroidal particles: the mean aspect ratio (D/L_{mean}) was varied from 0.5 to 2.5 with steps of 0.1, and the variance was fixed to 0.1. The values of the single scattering albedo and phase function were calculated assuming a power law particle size distribution for volume equivalent effective radius (r_{eff}) varying from 0.10 to 1.70 µm in 0.02 µm steps (e.g., Chen-Chen et al., 2019a), with effective variance v_{eff} = 0.3 (e.g. Mishchenko et al., 1997; Dubovik et al., 2006); the refractive complex index was derived from Wolff et al. (2009).

- *Laboratory measurements of Martian dust analogues*. Experimental measurements of single scattering phase functions for different Martian dust analogue samples were retrieved from the Amsterdam-Granada Light Scattering database[5] (Muñoz et al., 2012). The scattering phase

[5] https://www.iaa.csic.es/scattering/

functions at 647 nm for basalt, JSC0, JSC200, JSC-1A and palagonite samples were evaluated in this study. For a comprehensive description of the sample's properties, experimental set up and retrieval of the scattering matrices the reader is referred to the corresponding publications: basalt, JSC0 and JSC200 (Dabrowska et al., 2015); JSC-1A (Escobar-Cerezo et al., 2018) and palagonite (Laan et al., 2009). The single scattering albedo for each sample was approximated using the Lorenz-Mie theory (Mishchenko et al., 1995). For these computations, the particle size distribution parameters (r_{eff}, v_{eff}) and complex refractive index (m) of each sample were derived from the database (Table 6.1).

It is summarised on Table 6.2 the dust aerosol models used in this work and their related parameters.

Sample	$r_{eff}(\mu m)$	v_{eff}	m	ω_0	**Source**
Basalt	6.9	7.0	$1.52 + i\ 0.001$	0.892	Dabrowska et al., 2015
JSC0	29.5	1.1	$1.5 + i\ 0.001$	0.701	Dabrowska et al., 2015
JSC200	28.1	1.2	$1.5 + i\ 0.001$	0.633	Dabrowska et al., 2015
JSC-1A	15.85	2.28	$1.65 + i\ 0.003$	0.708	Escobar-Cerezo et al., 2018
Palagonite	4.5	7.3	$1.52 + i\ 0.0005$	0.960	Laan et al., 2009

Table 6.1. Martian dust analogues properties

Aerosol model	**ω_0**	**Phase function, $P(\theta)$**		
		Parameters	**Range**	**Reference**
Double Henyey-Greenstein	0.975	Forward scattering (g_1), backward scattering (g_2), and ratio (α)	g_1: 0.50 to 1.00, step of 0.01 g_2: - g_1 to +g_1, 50 divisions α: 0.50 to 1.00, step of 0.01	Zhang and Li, 2016
T-matrix	Calculated	*Cylindrical particles:* diameter-to-length aspect ratio (D/L), size distribution effective radius (r_{eff})	D/L: 0.5 to 2.5, step of 0.1 r_{eff}: 0.10 to 1.70 µm, step of 0.02	Mishchenko and Travis, 1998; Wolff et al., 2001
	Calculated	*Spheroidal particles:* Standard shape distrib. Mean diameter-to-length aspect ratio (D/L_{mean}), size distribution effective radius (r_{eff})	D/L_{mean}: 0.5 to 2.5, step of 0.1 r_{eff}: 0.10 to 1.70 µm, step of 0.02	Mishchenko and Travis, 1998; Dubovik et al., 2006
Laboratory measurements	Calculated (Lorenz-Mie)	Martian dust analogue sample experimental phase functions at 647 nm.	*Samples:* Basalt, JSC0, JSC200, JSC-1A, Palagonite	Muñoz et al., 2012; Dabrowska et al. 2015; Escobar-Cerezo et al., 2018; Laan et al., 2009

Table 6.2. Aerosol model parameters for radiative transfer simulations

6.3.3. Retrieval procedure

An iterative retrieval scheme was implemented based on the comparison of radiative transfer simulations and MSL engineering camera observations of Martian sky brightness as a function of the scattering angle. A lowest mean quadratic deviation χ^2 criterion was considered for determining the best fitting curve.

For each Hazcam/Navcam observation:

1. Radiometric calibration and geometric reduction were performed as described in Chapter 4: for each image-pixel the corresponding values of absolute radiance, azimuth/elevation angles with respect to a Mars' local site reference system and the resulting scattering angle were calculated. The absolute radiance was then converted into approximated radiance factor (I/F) units by dividing each pixel's radiance value by the solar spectral irradiance at the top of the atmosphere at the time of the observation convolved to the Hazcam/Navcam bandpass (same for both imagers, 1.524 W m^2 nm^{-1} sr^{-1} at 1 AU) and divided by π (e.g., Soderblom et al., 2008). The solar spectral irradiance data was obtained from Colina et al. (1996).

2. Retrieval of the observed sky brightness as a function of the scattering angle was performed by sampling radiance values along the solar almucantar plane.

3. The simulated sky brightness curves were generated using the radiative transfer model for different combinations of aerosol modelling parameters (Table 6.2) and allocated in a look-up-table (LUT).

5. The observed sky radiance angular distribution function, $I/F_{obs}(\theta)$, and the modelled, $I/F_{obs}(\theta)$, curves contained in the LUT were compared using a standard χ^2 least squares quadratic error criterion:

$$\chi^2 = \sum_{i=1}^{N} \left(\frac{(I/F)_{obs_i} - (I/F)_{mod_i}}{\sigma_i \cdot (I/F)_{obs_i}} \right)^2 \quad (6.2)$$

For the N sampled points along the curve a variance of σ_i = 0.20 was used as a conservative value associated with the absolute calibration uncertainty for MSL engineering cameras considered in Section 4.4. The reduced χ^2 values, χ^2_ν, were calculated by dividing the obtained χ^2 by the number of degrees of freedom $\nu = N - f$, where N is the number of sampled points and f the number of free parameters in the retrieval ($f = 3$ for DHG; $f = 2$ for T-matrix and 1 for laboratory measurements) (Table 6.2)

6. The set of input parameters for each aerosol model generating the simulated sky brightness angular distribution with the minimum χ^{2^2} value was considered the solution of the retrieval (Figure 6.3). The uncertainty level of the solution was estimated from the 68% confidence region (1σ error).

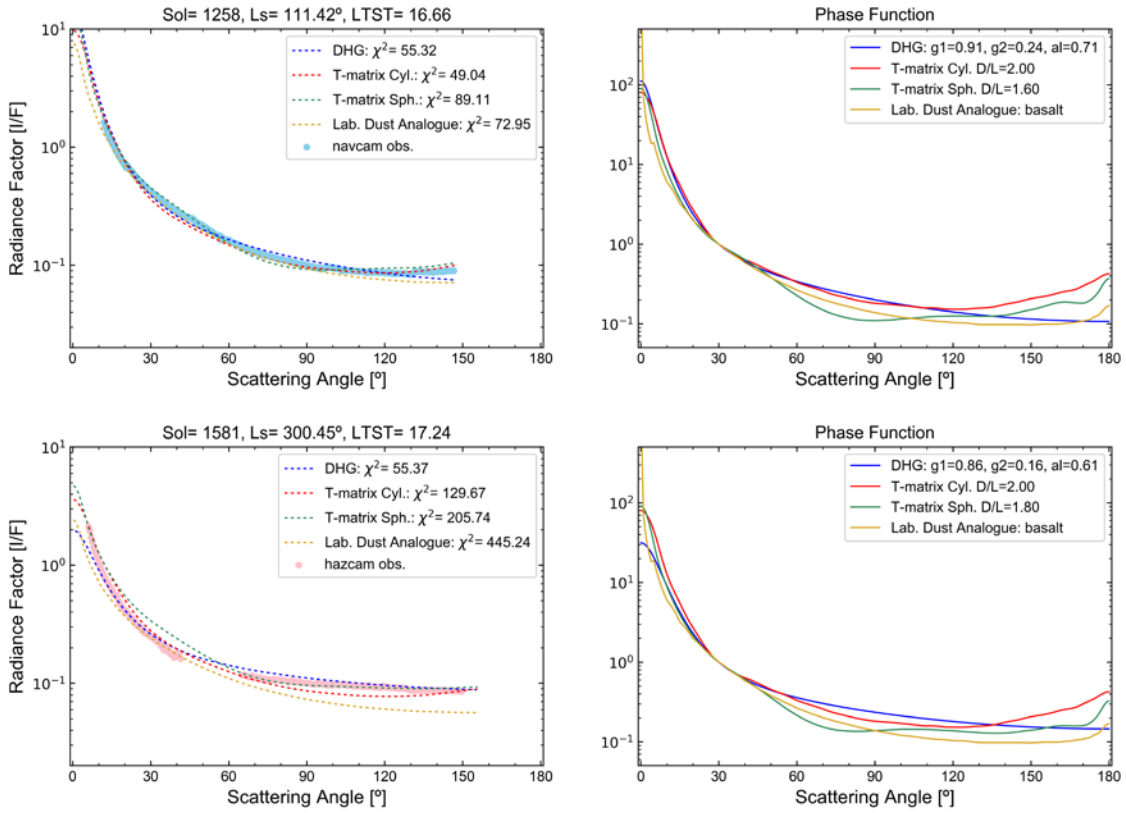

Figure 6.3. Comparison of observed and modelled sky brightness curves. Results of MSL Navcam (top) and Hazcam (bottom) observation comparisons to radiative transfer models: (left) the best fitting sky brightness as a function of the scattering angle simulations for the different aerosol models are provided; (right) the aerosol single scattering phase functions generating those best fitting curves. Phase functions are normalised to 1 at 30 degrees of scattering angle. Source: Adapted from Chen-Chen et al. (2019b).

6.4. Results and discussion

The methodology described in the previous Section 6.3 was followed to retrieve the aerosol model parameters generating the best fitting sky radiance simulations. In this section, the results of the parameterisation scheme are presented. A discussion is provided for studying the seasonal behaviour and the interrelationships of the resulting parameters and the uncertainties of the retrieval are evaluated. A summary table with the complete results of this study is provided in Table D.2 in the APPENDIX D of this dissertation.

6.4.1. Double Henyey-Greenstein phase function parameters

The seasonal and interannual behaviour of the DHG analytical phase function parameters (g_1, g_2, α), and their interrelationships are shown on the left and right columns on Figure 6.4, respectively. The average values retrieved for each parameter are: $g1 = 0.889 \pm 0.098$, $g2 = 0.094 \pm 0.250$ and $\alpha = 0.743 \pm 0.106$. When recurring to the expressions provided on Zhang and Li (2016), these parameter values generate a single scattering phase function with an asymmetry factor of $g = 0.687 \pm 0.081$, which is in good agreement with previous results by

Wolff et al. (2009) at the 650 nm effective wavelength of MSL engineering cameras. It can be appreciated on Figure 6.4 that results for Hazcam observations (red) show a greater dispersion and larger uncertainties than Navcam dataset outcomes (blue). This is mainly related to the pointing particularities of each set of cameras; while mast-mounted free pointing Navcam sky-surveys are capable of retrieving sky radiance curves covering scattering angles from approximately 10º to 150º, rover chassis fixed Hazcam observations are highly dependent on the geometry configuration at the specific LTST and location, thus retrieving image-sets with very different scattering angle coverage.

Regarding the seasonal variability of the DHG parameters, the results obtained during the low opacity aphelion season (L_S ~ 40º to 130º) show noticeable differences when compared to the rest of the year. The sensitivity to possible contribution from the aphelion cloud belt water-ice clouds in the retrieved sky radiance data during this particular season will be discussed below. In particular, the forward scattering parameter (g_1) values tend to be lower within this time. As phase function values in the forward scattering region (θ ~ 5º to 30º) are related to the size of the particle (e.g., Kaufman, 1994; Tomasko et al., 1999), this may suggest the detection of smaller dust particles during this season. However, due to the differences in the scattering angle coverage by each observation, the lack of data in the forward scattering region may originate part of the dispersion in the results, therefore not providing strong evidences for identifying any particular seasonal behaviour. Seasonal differences can be also appreciated in the backward scattering parameter g_2. In this case, the retrieved negative values are mostly located within the same aphelion period (L_S ~ 40º to 130º). DHG analytical phase functions with a $g_2 < 0$ are featured with a positive slope at the end of the backscattering region (minimum of phase function is at θ < 180º, existence of a peak). However, as in the previous case, the existing dispersion in the retrieved data does not allow to identify a clear seasonal behaviour for this parameter.

The interrelationships between the DHG parameters are shown at the right column of Figure 6.4. In this case, output charts tend to be clearer and results show a positive correlation for (g_1, g_2) parameters, and negative correlations for (g_1, α) and (g_2, α); being more evident in the latter case. The obtained negative correlations points out the role of the parameter α as weighting factor for controlling the overall shape of the DHG phase function; when large lobes in the function are obtained at the forward scattering area (g_1 close to 1) or at the backscattering (negative g_2), the parameter α tends to balance the counterpart region by shifting to 0.5 or 1.0, respectively.

Finally, regarding the interannual variability analysis, the different number of available observation data per MY and its seasonal distribution, sums up to the abovementioned dispersion of the retrieval results. Therefore it is not possible to conclude that any particular interannual behaviour was derived from the evaluated data.

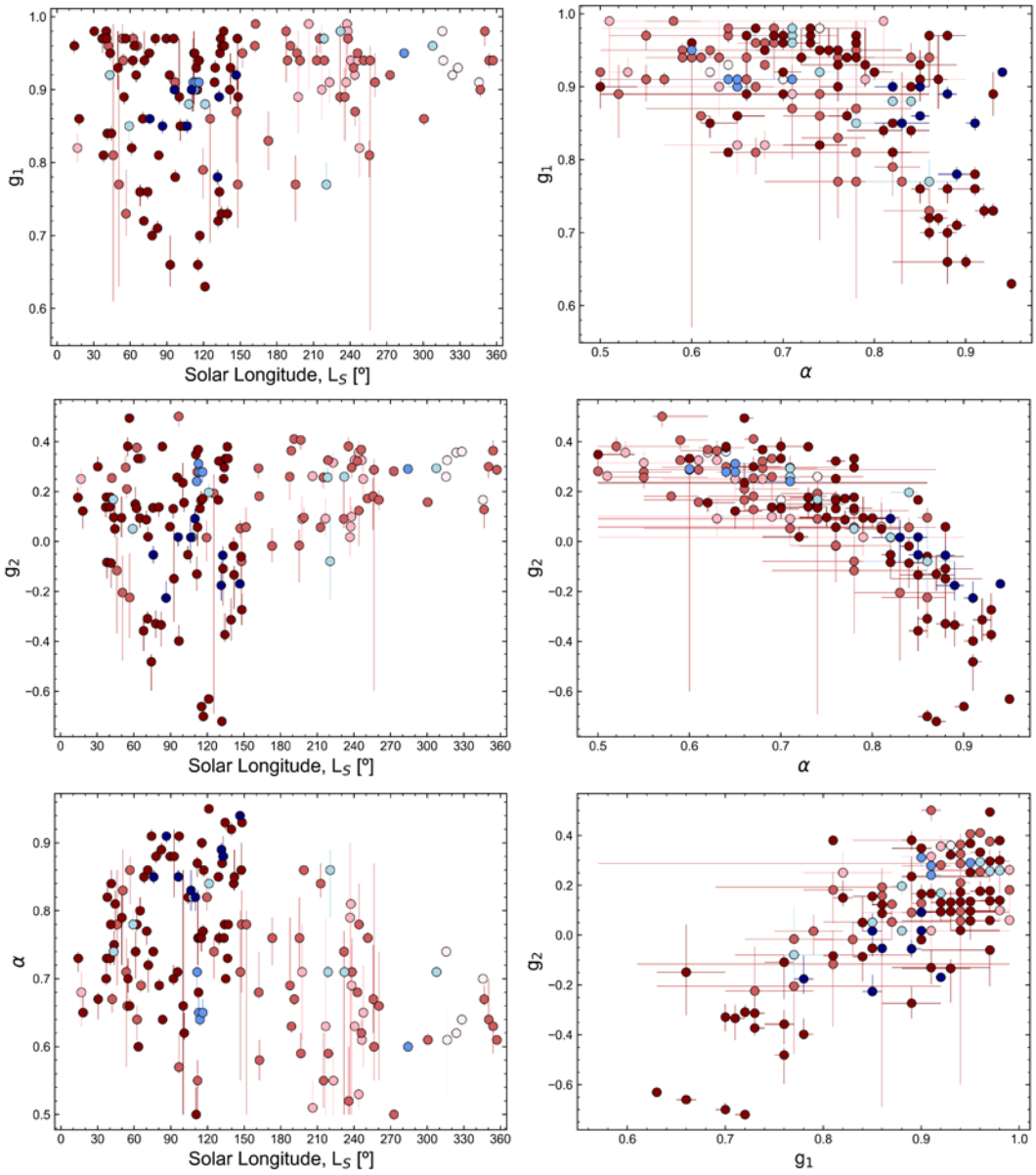

Figure 6.4. Double Henyey-Greenstein parameters seasonal variation and relationships. The seasonal behaviour (left column) and the existing interrelationships (right column) for DHG phase function parameters (g_1, g_2, α) generating the best-fitting sky radiance model to MSL Navcam (blue) and Hazcam (red) observations. Colour shades indicate MY 31 (clearest) to MY 34 (darkest). No data for Navcam MY 31. Source: Adapted from Chen-Chen et al. (2019b).

6.4.2. Dust shape

The retrieval results for the diameter-to-length aspect ratio parameter for randomly oriented cylindrical and spheroidal particles calculated with T-matrix are shown on the top and bottom of Figure 6.5, respectively.

For the cylindrical particles case, the frequency of aspect ratio counts returned average D/L values of 0.70 and 1.90 with an uncertainty of about 0.20, when differentiating D/L values larger and smaller than 1.0. These results present a good agreement with previous studies, e.g.: 0.60 or 2.30 by Wolff et al. (2001). Regarding the seasonal evolution of the diameter-to-length aspect

ratio of cylindrical particles, it is not possible to conclude that the retrieved results show any clear seasonal variability, although average values tend to be slightly larger for the low opacity aphelion season (L_S ~ 0º to 150º).

When evaluating the results for spheroidal particles, on the bottom graph of Figure 6.5 it can appreciated that there is a clear trend for oblate spheroids or "disks" (diameter-to-length aspect ratio D/L > 1). The average of the standard shape distribution mean D/L when only considering the oblate spheroids was about 2.00, with an uncertainty of 0.40. This trend for disk-shaped particles is in agreement with previous studies; for instance, Murphy et al. (1993) concluded that the use of non-spherical disk-shaped particles (in that case, D/L ratio was around 10.0) resulted in an improved maintenance in suspension of the particles at subtropical latitudes in their model-observation comparisons, as well as in their retrieved visible-to-9 μm opacity ratios.

Regarding the seasonal evolution of the aspect ratio parameter, larger D/L values are found in the spheroidal case concentrated within the L_S 150º to 360º. However, it is not possible to conclude that the retrieved results show any clear seasonal variability in both cases.

6.4.3. Martian dust analogue samples

The results of the observation-model comparison retrieval showed that only two models generated the best fitting model curve: basalt (78% of the cases) and palagonite (22%). This outcome is mainly related to the significant differences that exist in the particle size distribution of the available dust analogue samples ($r_{eff,palagonite}$ = 4.5 μm, $r_{eff,basalt}$ = 6.9 μm, $r_{eff,JSC1A}$ = 15.85 μm, $r_{eff,JSC200}$ = 28.1 μm, $r_{eff,JSC0}$ = 29.5 μm), where it can be appreciated that the effective radius parameter for the remaining analogues are about an order of magnitude larger than the usual values reported for Martian atmospheric dust aerosol (r_{eff} order of ~ 1 μm) (e.g., Korablev et al., 2005; Smith, 2008; McConnochie et al., 2017; Chen-Chen et al., 2019a). Previous studies comparing Martian airborne dust with experimental analogue measurements resulted in best fits to samples of palagonite (Clancy et al., 1995; Merikallio et al., 2013) and basalt (Dabrowksa et al., 2015). No relevant seasonal or interannual variability in the best fitting basalt or palagonite dust samples were found.

6.4.4. Sensitivity study of DHG results

The sensitivity of the retrieved DHG parameters to variations of the input values for the single scattering albedo, dust column optical depth and possible presence of water-ice clouds during the aphelion season was evaluated by performing several simulations for these scenarios (Figure 6.6).

Sensitivity to aerosol optical depth. The atmospheric column optical depth is a required input parameter for radiative transfer simulations. Regular measurements from MSL Mastcam afternoon direct Sun-imaging (Lemmon, 2014) and MSL Navcam near Sun-pointing observations (Chen-Chen, et al., 2019a) were used. Dust column optical depth values were

interpolated at the observation's sol (or L_S if there were no data available within a range of 20 sols), which could introduce some uncertainty in our retrieval procedure. The sensitivity of the results to uncertainties in column optical depth measurements was evaluated by simulating two scenarios containing 15% more and less dust atmospheric loading with respect to the nominal case. When the column optical depth was decreased, the analytical DHG phase function parameters g_1, g_2 and α showed a difference of about 4%, 5% and 2.5% respectively with respect to the base scenario; whereas in the case of an increment of the dust extinction the resulting differences were of the order of 2%, 9% and 3%.

Sensitivity to single scattering albedo. The simulated sky brightness also depended on the input value of dust single scattering albedo (ω_0). As it has been abovementioned, for the case of analytical DHG phase functions the single scattering albedo was fixed to 0.975, which is a representative value for Martian dust (Wolff et al., 2009) at the effective wavelength of the cameras. The sensitivity of our retrieval procedure to variations in this parameter was evaluated by comparing the obtained results when the input ω_0 was set to of 0.940 (e.g., Tomasko et al., 1999). The resulting output g_1, g_2 and α parameters varied in the order of 4%, 25% and 2%, respectively, with respect to the nominal scenario.

Sensitivity to presence of water-ice clouds. Part of the observations used in this study were obtained during the aphelion season (centred on L_S ~ 70º) and the possible presence of water-ice clouds from the aphelion cloud belt, developing around L_S = 40º - 60º and dissipating near L_S ~ 150º (e.g., Clancy et al., 1996, 2003; Madeleine et al., 2012) might introduce deviations in the dust phase function parameters retrieval. Although the majority of the observations were taken before 7h or after 16h (LTST), when detections of water-ice clouds are very low and the reported optical depth is almost negligible (Kloos et al., 2018), the sensitivity of the results to this phenomenon was evaluated. For an observation retrieved on sol 1132 (L_S = 54.2º) corresponding to MY 33 (high cloud detection at Gale Crater, e.g. McConnochie et al., 2017; Kloos et al., 2018), a simulation was performed in which a water-ice cloud was added to the base model: the optical depth of the cloud was set to τ_{cloud} = 0.15 as a representative value of afternoon retrievals (Kloos et al., 2018), water-ice scattering properties Q_{ext} and ω_0 were derived from Warren (1984) and the single scattering phase function was modelled with an analytical DHG using water-ice representative parameters from Zhang and Li (2016). Differences between the simulated sky radiance as a function of the scattering angle for the base scenario and the water-ice cloud scenario were about 12% (lower than assumed uncertainty of 15%). When comparing with the observation for retrieving the parameters generating the best fitting curve, variations of the output g_1, g_2 and α parameters of the DHG analytical phase function were of about 4%, 4.5% and 15.0%, respectively. The resulting simulated sky radiance curve including a water-ice cloud model and dust phase function are provided in Figure 6.6.

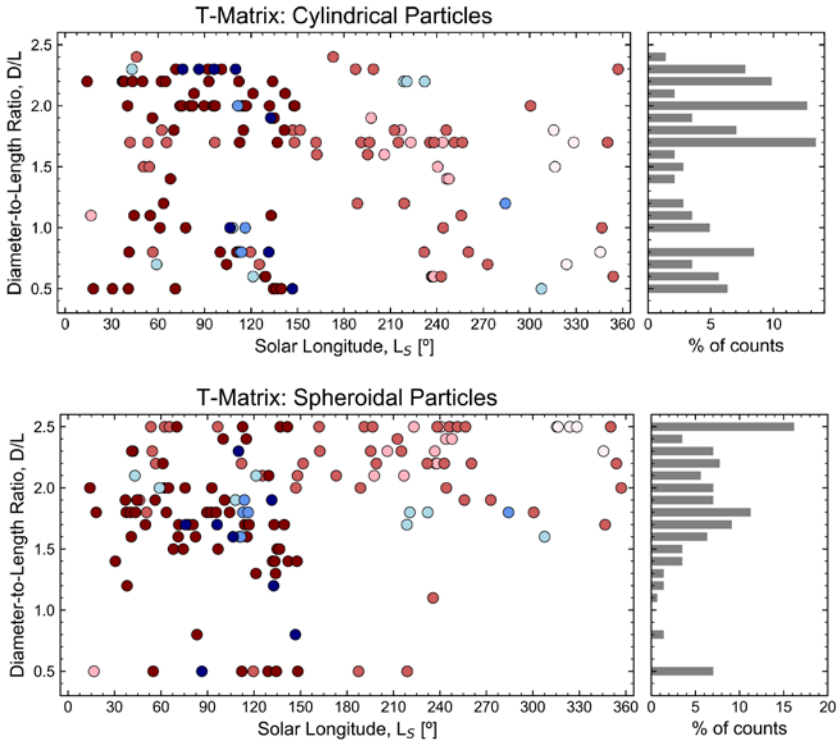

Figure 6.5. Seasonal and interannual behaviour of T-matrix particles aspect ratio. On the left, results of T-matrix cylindrical (top) and spheroidal (bottom) particles diameter-to-length (D/L) aspect ratio parameter generating the best-fitting sky radiance curve model to MSL Navcam (blue) and Hazcam (red) observations, as a function of the solar longitude and Martian Year (MY). Colour shades indicate MY 31 (clearest) to MY 34 (darkest). No data for Navcam MY 32. On the right, the bar chart shows the percentage of counts (frequency) for each D/L value. Source: Adapted from Chen-Chen et al. (2019b)

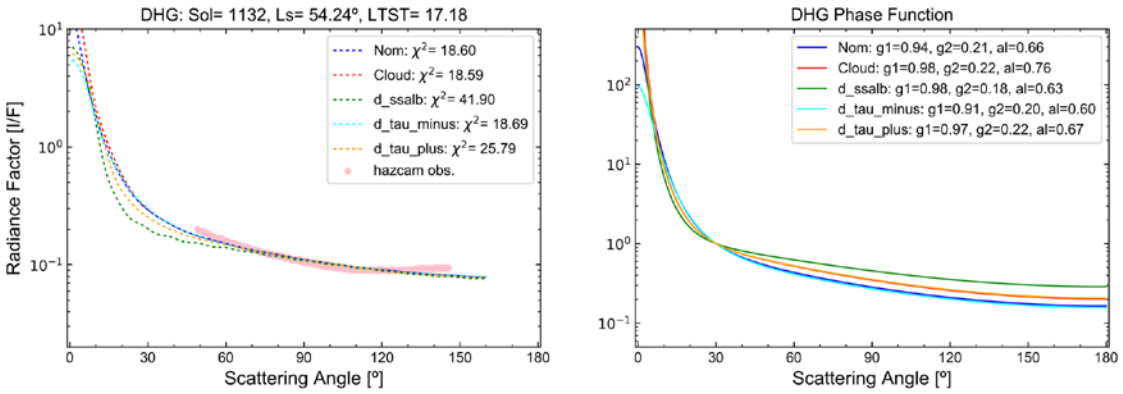

Figure 6.6. Sensitivity analysis of sky radiance model with DHG phase functions. Outputs of DHG analytical phase function parameters (g_1, g_2, α) generating the best fitting sky brightness curve to MSL Hazcam observation corresponding to Sol 1132 (L_S = 54.24º, MY 33), under different simulation cases: nominal scenario (blue), presence of ice-water cloud (red), single scattering albedo set to ω_0 = 0.94 (green), nominal dust column optical depth input value decreased 25% (cyan) and increased 25% (yellow). On the right, modelled sky radiance angular distribution compared to observation: left, DHG single scattering phase function curves generating those simulations. Phase functions are normalised at 1 at 30 degrees of scattering angle. Source: Adapted from Chen-Chen et al. (2019b).

6.5. Summary

In this study sky radiance measurements in the almucantar plane obtained by the MSL Engineering Cameras have been used to constrain the Martian dust single scattering phase function. Hazcam simultaneous forward-rear pointing opportunistic afternoon observations and Navcam sky-survey image sequences were selected and photometric calibration and geometric reduction were performed on the raw images. The angular distribution of sky radiance was retrieved for different seasons and Martian Years. These observations contained data for the intermediate and large scattering angle region, from 30º up to about 160º, where the light scattering due to the aerosol is dominated by the shape of the particle.

The observed sky brightness curves were iteratively compared with radiative transfer sky radiance simulations. The modelled sky radiance as a function of the scattering angle were calculated following a parameterisation scheme for defining the dust single scattering phase function using 3 different aerosol modelling approaches: a three term Double Henyey-Greenstein analytical function, T-matrix code calculations for cylindrical and spheroidal particles, and experimental laboratory retrievals of Martian dust analogues.

Results retrieved from the comparison procedure show average Double Henyey-Greenstein parameter values of g_1 = 0.889±0.098, g_2 = 0.094±0.250, α = 0.743±0.106, which are related to a phase function with an asymmetry parameter of g = 0.673±0.081 (similar to, e.g., Wolff et al., 2009). Existing seasonal differences for the low dust opacity aphelion season (L_S 30º to 150º) were observed for g_1 and g_2, although it was not possible to derive a clear seasonal or interannual behaviour, due mainly to the dispersion in the results and the different seasonal distribution of the data. Best fitting diameter-to-length aspect ratios for T-matrix cylindrical particles were of 0.70±0.20 and 1.90±0.20, presenting a good agreement with previous studies (Wolff et al., 2001). For T-matrix spheroidal particles, the best fitting aspect ratio corresponded to oblate spheroids with standard shape distribution mean value of D/L = 2.00 (oblate spheroids); in agreement with conclusions by Murphy et al. (1993) regarding the use of non-spherical disk shaped particles for extending their suspension times. Comparisons with experimental single scattering phase functions of dust analogues returned only two different best fitting samples, basalt (78%) and palagonite (22%), in line with Dabrowska et al. (2015).

7. SUMMARY AND FUTURE WORK

7.1. Summary and conclusions

The motivation behind this research work is to provide an additional source of observational data in order to contribute to previous dust aerosol studies by expanding the time and seasonal coverage. In this dissertation it has been shown that, although not initially designed as a scientific instrument, MSL rover engineering cameras can be used to evaluate the atmospheric column dust optical depth and to constrain the physical properties of dust aerosol particles, taking advantage of their versatility and frequent use ("opportunistic observations").

The overall context is first defined by introducing the main properties of Mars' atmosphere and pointing out the significant role played by airborne dust aerosols in the thermal structure and atmospheric dynamics. In order to illustrate the level of relevancy, we have introduced the research efforts placed on multiple robotic exploration missions for characterising dust properties and the Mars Science Laboratory (MSL) mission has been introduced.

The objectives defined for this research study consisted in the review and calibration of MSL engineering camera image data, the development of a radiative transfer model of Mars' atmosphere for simulating the observed sky radiances, the implementation of a retrieval procedure for deriving the atmospheric dust loading and characterising aerosol particle properties, and the preparation of the relevant tools and procedures for future studies.

On the modelling side, first the theoretical backgrounds of radiative transfer and light scattering by planetary atmospheres have been discussed. Following this, the results retrieved by previous authors on the characterisation of dust aerosol properties following different modelling approaches have been reviewed. It can be pointed out that T-matrix code is the most extended method for deriving dust aerosol radiative properties within recent studies. Finally, the atmosphere model used throughout this research has been presented, which corresponded to a multiple scattering radiative transfer model for a plane-parallel Martian atmosphere model using the discrete ordinates method.

Regarding the observational data used, the technical specifications of MSL rover engineering cameras (Navcam and Hazcam) have been provided, and the main types of image data retrieved by these cameras have been shown, together with the different existing data files. Next, the calibration procedure implemented for the radiometric calibration and geometric reduction of engineering cameras image-files have been detailed. The calibrated data were validated against multispectral MSL Mastcam instrument, resulting in an absolute radiance uncertainty around 12% in the case of Navcams, and about 17% for Hazcams.

For the retrieval of dust particle size and the column optical depth, we have used 65 Sun-pointing images covering a period of almost three Martian years, from MSL mission sol 21 to sol 1646 (MY 31 to 33). Modelled sky brightness curves were generated as a function of two parameters: the aerosol particle size distribution effective radius and the dust column optical depth at the surface. These were compared with calibrated observations that showed the sky radiance as a function of the scattering angle for the near-Sun region (scattering angle from 4º to 30º). A retrieval scheme was implemented for deriving the parameters that generated the best fitting curve under a least-square error criterion. The obtained results present a good agreement with previous work, showing the usual seasonal variation curve of the column dust optical depth; and retrieving a positive correlation between dust aerosol particle size and derived optical depth.

In the second part, the angular distribution of sky brightness observed by Navcam and Hazcam was used to characterise the atmospheric dust single scattering phase function and to constrain the shape of the particles. An iterative radiative transfer based retrieval method was implemented in order to determine the aerosol modelling parameters which best reproduce the observed sky radiance as a function of the scattering angle. The aerosol models considered in this study for calculating dust radiative properties were an analytical three term Double Henyey-Greenstein (DHG) phase function, T-matrix calculations for cylindrical particles with different diameter-to-length (D/L) aspect ratios and experimental phase functions from laboratory measurements of several Martian dust analogue samples. Results of this study returned mean DHG phase function parameter values g_1 = 0.889±0.098, g_2 = 0.094±0.250, α = 0.743±0.106; generating a phase function with an asymmetry parameter of g = 0.673±0.081. Although differences were observed during the low opacity aphelion season (lower forward scattering values, presence of a peak in the backward region) compared to the rest of the year, no clear evidences of seasonal behaviour or interannual variability were derived. The obtained average D/L aspect ratios for T-matrix calculated cylindrical particles were 0.70±0.20 and 1.90±0.20 and the best fitting Martian dust analogue corresponded to the basalt sample.

7.2. Future work

In this section the future research prospects derived from this study are presented. The future research activities and developments are associated to the use of complementary observational data or new retrievals by forthcoming missions and instruments, as well as developments of the aerosol modelling code and overall retrieval methodology.

7.2.1. Continue with MSL dust monitoring

As of writing, the MSL sol is 2409, L_S = 26.3º (northern hemisphere spring) of MY 35, and the rover has driven about 21 km. The latest observational data evaluated for this research work corresponds to sol 2001, L_S = 148.2º, (northern summer) MY 34. Between these dates, Mars'

has gone through several seasonal changes and climate events, being of particular high relevance the global dust storm in May-July 2018 (e.g., Guzewich et al., 2019, Sánchez-Lavega et al., *in press*). During this planetary-scale dust event, column dust optical depth values reaching τ ~ 10 were reported. It is worth mentioning that when dust storm reached MER Opportunity's location, the rover ceased communications and went into hibernation-mode as the solar panels were not generating enough power. After several months of unsuccessful attempts of contact, the end of mission was declared after 5,111 sols of operation[6].

As part of future research work, MSL Navcam and Hazcam observations from sol 2001 onwards shall be evaluated in order to extend the seasonal coverage, and to retrieve dust aerosol particle properties during the 2018 global dust storm in order to contribute to the better understanding of these phenomena and its effects on climate. In particular, the dust properties (size, single scattering phase function, and its best associated particle shape) can be compared for Martian Years with and without such event. According to outcomes from previous studies and as it has been also inferred from this dissertation, dust particle size show a positive correlation with atmospheric optical depth (e.g., Smith and Wolff, 2014; Vicente-Retortillo et al., 2017; McConnochie et al., 2017; Chen-Chen et al., 2019a). However, the evaluated data does not cover scenarios with such high dust opacity values as reported by Guzewich et al. (2019). Therefore, the evaluation of data sets covering 2018 dust events shall provide insight into the boundaries of this correlation.

7.2.2. Mars 2020 mission

The Mars 2020 rover mission is part of NASA's Mars Exploration Program, a long-term effort of robotic exploration of the Red Planet. The mission is designed to advance high-priority science goals for Mars exploration and it will contribute to determine whether life ever existed on Mars, to characterise the Mars' climate and geology, and to gather knowledge and demonstrate technologies to prepare for future human expeditions to the planet. The mission is scheduled to be launch in July/August 2020 and the selected landing site is Jezero Crater (18.85ºN, 282.48ºW). In order to keep mission costs and risks as low as possible, Mars 2020 design is based on MSL mission architecture, including its rover and the landing system.

As part of Mars 2020 scientific payload, the Mars Environmental Dynamics Analyzer (MEDA) is an integrated suite of sensors designed to address the Mars 2020 mission objectives of characterisation of dust size and morphology and surface weather measurements. It is composed of a dust and optical radiation sensor (RDS) that includes a dedicated camera, pressure sensor, relative humidity sensor, wind sensor, air temperature sensors and thermal infrared sensors for retrieving net flux and ground temperature. In particular, MEDA's measurements objectives regarding dust aerosol particles are to study the physical and optical properties of the local atmospheric aerosols: particle abundance, size distribution, shape, phase

[6] https://mars.nasa.gov/news/8413/nasas-opportunity-rover-mission-on-mars-comes-to-end/

function, and how these optical properties relate to the meteorological cycles (diurnal, seasonal, interannual); and the conditions leading to dust lifting and how the aerosol diurnal cycle responds to the local atmospheric wind regions (Rodriguez-Manfredi et al., 2017). The members of the *Grupo de Ciencias Planetarias* research group of the Universisty of the Basque Country (UPV/EHU), A. Sánchez-Lavega (Co-I), S. Pérez-Hoyos, R. Hueso, and T. del Río-Gaztelurrutia (collaborators), are part of the MEDA science team and will have direct access to the data retrieved by the different sensors.

The Radiation and Dust Sensor (RDS) is part of MEDA instruments and its main objective is to characterise Mars dust opacity, size and morphology (Figure 7.1). It will track the solar direct and diffuse radiation in an observation geometry that characterises the prevailing environmental dust properties. RDS consists on a suite of photodetectors with different spectral bands and a dedicated camera pointed to the sky. The camera, named as SkyCam, consists in the re-use and accommodation of one of JPL's engineering cameras already used in MER/MSL: the hazard avoidance camera (Hazcam). In this case, SkyCam's optical system is tailored for MEDA and includes a shadowing mask for low solar zenith angle scenarios and a neutral filter near to the centre of the lens (Apestigue et al., 2015). The SkyCam will be used to measure the dust opacity cycle and its size distribution by retrieving the intensity decay of the solar aureole, while the azimuthal-coverage provided by the geometrical configuration of the photodetectors will sample the sky brightness at intermediate and large scattering angles (Dubovik and King, 2000; Smith and Wolff, 2014; Smith et al., 2009; Apestigue et al., 2015). The application of the model and methodology presented here would be straightforward, in spite of the differences between the observations described in this thesis and the more wavelength and spatially extended data that MEDA will provide.

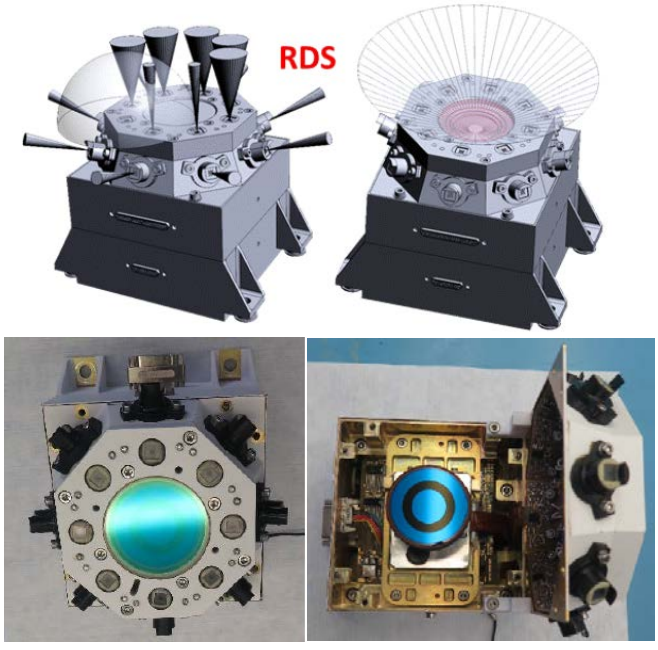

Figure 7.1. MEDA suite Radiation and Dust Sensor (RDS). *Top*: RDS discrete photodetectors (left) and SkyCam (right) field-of-view. *Bottom*: RDS assembly. Source: Rodriguez-Manfredi et al. (2017), Arruego (2018).

In addition, Mars 2020 rover will be equipped with Enhanced Engineering Cameras (EECAM; Maki et al., 2016), an upgrade of the previous rover engineering cameras flown on MER and MSL missions (Maki et al., 2003; 2012). Mars 2020 EECAM utilise a 20 megapixel colour CMOS sensor, in contrast to the 1 megapixel greyscale CCD sensor utilised by the MER/MSL Cameras. The mounting locations of the new engineering cameras are almost similar to current ones on MSL. They have also inherited the same functional requirements from previous missions. Mars 2020 EECAMs significantly improve on the MER/MSL designs by adding the 20 megapixel CMOS sensor with an imaging area of 5120 x 3840 pixels. The field-of-view for EECAMs will be (horizontal x vertical): Navcams, 103º x 77º; Hazcams 156º x 117º. As a result, new Navcams will have more than twice the angular resolution of the MER/MSL Navcam, and Hazcams will have more than 3 times the angular resolution. Both sets will produce colour images, with better antiblooming capability than the MER/MSL designs.

7.2.3. Model developments

In addition to the forthcoming observational data sets, further developments in the methodology shall be performed concerning the aerosol modelling and the retrieval scheme. Aerosol databases with previously computed radiative properties, such as the AERONET network aerosol database (Dubovik et al., 2006), shall be used as an input source for models. This shall be followed by the implementation of supplementary numerical codes for calculating dust aerosol radiative properties for more complex shapes, such as tri-axial ellipsoids (Pitman et al., 2000; Yurkin and Hoekstra, 2007; Meng et al., 2010; Merikallio et al., 2013; Lemmon, 2014). Regarding the retrieval method, it shall be considered the use of optimised inversion algorithms as an alternative to the current iterative brute-force approach, in order to increase the number of parameters evaluated in the radiative transfer problem while keeping reasonable computation times (Dubovik and King, 2000; Yang and Gordon; 1998).

Finally, further comparisons shall be performed for a broader variety of laboratory retrievals of Martian dust analogue single scattering measurements, with adequate particle size distributions, closer to the values retrieved for the atmospheric dust (r_{eff} ranging 1-10 μm).

7.2.4. Mesoscale simulations

Apart from the abovementioned new observational datasets and developments in the model, within the future work it is also planned to take advantage of the derived results and to run mesoscale simulations to model Gale Crater region climatic conditions, in order to assess the impact of using the retrieved dust aerosol properties in these simulations. As it has been highlighted throughout this dissertation, the distribution of dust in the atmosphere is a major driver in determining the thermal structure and dynamics of Mars. Dust is placed into the atmosphere by, among other phenomena, dust storms that are generally considered mesoscale systems. Thus mesoscale atmospheric dynamic is a key element of the Martian dust cycle.

Mesoscale models are comprised of two main modules: the dynamical core integrates the primitive equations for the atmospheric fluid, i.e., Navier-Stokes equations in spherical coordinates, and the physical parameterisation module provides key diabatic forcing in the primitive equations, e.g.: radiative transfer, heat and mass exchanges between surface and atmosphere, etc. (see Rafkin et al., 2017).

For future studies, we have considered the Martian Regional Atmospheric System (MRAMS) mesoscale model (Rafkin et al., 2001), previously used for investigating and interpreting the meteorological environment at Gale Crater region (Pla-Garcia et al., 2016; Rafkin et al., 2016). The physical parameterisations of dust, CO_2 and H_2O cycles implemented in MRAMS are based upon the NASA Ames GCM radiative transfer model (Toon et al., 1989). In particular, regarding the radiative transfer module, current MRAMS scheme is based in a two-stream approach, where only the upward and downward irradiances are considered in the calculations. Monte Carlo methods are also used for solving the radiative transfer problem. In this probability-based approach, photon trajectories are defined individually with random processes. These are very time consuming due to the large quantity of photon trajectories that must be computed. Discrete ordinate methods would allow the user to choose between efficiency and accuracy by selecting the number of discrete ordinates or “streams”.

The motivation behind this research is to evaluate the impact in MRAMS mesoscale simulations results when a DISORT-based multiple streams radiative transfer scheme is implemented (accuracy versus efficiency), together with the derived dust aerosol radiative properties (Figure 7.2).

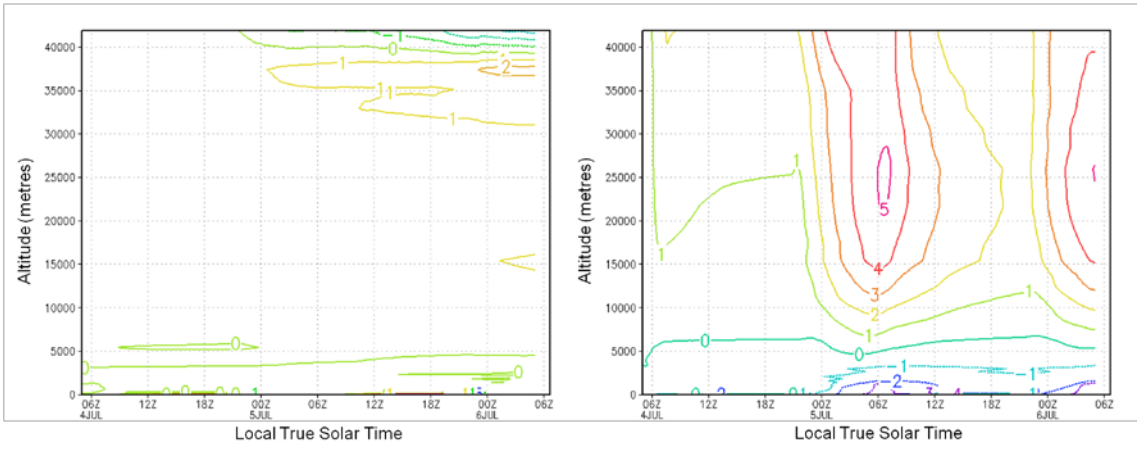

Figure 7.2. PRAMS thermal profile output comparisons. Variations in the temperature (in K) profiles (z = 0 to 40 km) as a function of time (LTST) between PRAMS simulations using DISORT 16-stream code (Stamnes et al., 2000) and the default two-stream code (Toon et al., 1989), for two different column dust optical depth scenarios: τ = 0.10 (*left*) and τ = 2.50 (*right*).

REFERENCES

Ádámkovics, M., Mitchell, J. L., Hayes, A. G., Rojo, P. M., Corlies, P., Barnes, J. W., Ivanov, V. D., Brown, R. H., Baines, K. H., Burrati, B. J., Clark, R. N., Nicholson, P. D., and Sotin, C. Meridional variation in tropospheric methane on Titan observed with AO spectroscopy at Keck and VLT, *Icarus*, 270, 376-388; doi: 10.1016/j.icarus.2015.05.023 (2016)

Alexander, D. A., Deen, R. G., Andres, P. M., Zamani, P., Mortensen, H. B., Chen, A. C., Cayanan, M. K., Hall, J. R., Klochko, V. S., Pariser, O., Stanley, C. L., Thompson, C. K., and Yagi, G. M. Processing of Mars Exploration Rover imagery for science and operations planning, *J. Geophys. Res.*, 111 (E02S02), doi: 10.1029/2005JE002462 (2006)

Alexander, D., and Deen, R. Mars Science Laboratory Project, Software Interface Specification (SIS), *MSL Camera & LIBS EDR/RDR Data Product Software Information Specification*, JPL D-38017, May 31, 2017, Version 4.0 (2017)

Allison, M. Accurate analytic representations of solar time and seasons on Mars with applications to the Pathfinder/Surveyor missions, *Geophys. Res. Lett.*, 24, 1967-1970; doi:10.1029/97GL01950 (1997)

Anderson, E., and Leovy, C. B. Mariner 9 television limb observation of dust and ice hazes on Mars, J. Atmos. Sci, 35, 723-734 (1978)

Anderson, R. B., and Bell III, J. F. Geologic mapping and characterization of Gale Crater and implications for its potential as a Mars Science Laboratory landing Site, *Mars*, 5, 76-128, doi: 10.1555/mars.2010.004 (2010)

Apéstigue, V., Arruego, I., Martínez, J., Jiménez, J.J., Rivas, J., González, M., Álvarez, J., Azcue, J., Martín-Ortega, A., de Mingo, J.R., Álvarez, M.T., Bastide, L., Carretero, A., Santiago, A., Martín, I., Martín, B., Alcacera, M. A., Manzano, J., Belenger, T., López, R., Escribano, D., Manzano, P., Boland, J., Cordoba, E., Sánchez-Lavega, A., Pérez, S., Sainz López, A., Lemmon, M., Smith, M., Newman, C. E., Gómez Elvira, J., Bridges, N., Conrad, P., de la Torre Juárez, M., Urqui, M., and Rodríguez Manfredi, J. A. Radiation and Dust Sensor for MARS2020: technical design and development status overview, European Planetary Science Congress 2015, EPSC Abstracts, vol. 10, EPSC2015-813-2 (2015)

Arruego, I. InMars: a comprehensive program for the development of key-technologies for miniature Martian probes, 15th Annual International Planetary Probe Workshop (2018).

Arvidson, R. E., Guinness, E. A., Moore, H. J., Tillman, J., and Wall, S. D. Three Mars Years: Viking Lander 1 imaging observations, *Science*, 222, issue 4623, 463-468, doi: 10.1126/science.222.4623.463 (1983)

Banerdt, W. B., Smrekar, S., Lognonné, P., Spohn, T., Asmar, S. W., Banfield, D., Boschi, L., Christensen, U., Dehant, V., Folkner, W., and Giardini, D. InSight: A discovery mission to explore the interior of Mars, 44th Lunar Planet. Sci. Conf., held March 18–22, 2013 in the Woodlands, Texas, LPI Contrib. 1719, p.1915. (2013)

Barlow, N. Mars: an introduction to its interior, surface and atmosphere. Cambridge, UK: Cambridge University Press (2008)

Barnes, J. R., Haberle, R. M., Wilson, R. J., Lewis, S. R., Murphy, J. R., and Read, P. L. The Global Circulation. In R. Haberle, R. Clancy, F. Forget, M. Smith and R. Zurek (Eds.), "The Atmosphere and Climate of Mars" (Cambridge Planetary Science, pp. 229-294), Cambridge: Cambridge University Press, doi: 10.1017/9781139060172.009 (2017)

Bell, J. F., III, Squyres, S. W., Herkenhoff, K. E., Maki, J. N., Arneson, H. M., Brown, D., Collins, S. A., Dingizian, A., Elliot, S. T., Hagerott, E. C., Hayes, A. G., Johnson, M. J., Joseph, J., Kinch, K., Lemmon, M. T., Morris, R. V., Scherr, L., Schwochert, M., Shepard, M. K., Smith, G. H., Sohl-Dickstein, J. N., Sullivan, R., Sullivan, W. T., and Wadsworth, M. Mars Exploration Rover Athena Panoramic Camera (Pancam) investigation, *J. Geophys. Res.*, 108 (E12), 8063, doi: 10.1029/2003JE002070 (2003)

Bell, J. F., III, Joseph, J., Sohl-Dickstein, J. N., Arneson, H. M., Johnson, M. J., Lemmon, M. T., and Savransky, D. In-flight calibration and performance of the Mars Exploration Rover Panoramic Camera (Pancam) instruments, *J. Geophys. Res.*, 111, E02S03; doi: 10.1029/2005JE002444 (2006)

Bell, J. F., III, Godber, A., McNair, S., Caplinger, M. A., Maki, J. N., Lemmon, M. T., Van Beek, J., Malin, M. C., Wellington, D., Kinch, K. M., Madsen, M. B., Hardgrove, C., Ravine, M. A., Jensen, E., Harker, D., Anderson, R. B., Herkenhoff, K. E., Morris, R. V., Cisnerios, E., and Deen, R. G. The Mars Science Laboratory *Curiosity* rover Mastcam instruments: Preflight and in-flight calibration, validation, and data archiving, *Earth and Space Science*, 4, 396-452; doi: 10.1002/2016EA000219 (2017)

Bougher S. W. Comparative thermospheres: Venus and Mars, *Adv. Space. Res.*, 15 (4), 21-25 (1995)

Bohren, C. F., and Huffman, D. R. Absorption and scattering of light by small particles, Wiley, New York (1983)

Buras, R., Dowling, T., and Emde, C. New secondary-scattering correction in DISORT with increased efficiency for forward scattering, *J. Quant. Spec. Rad. Trans.*, 112 (12), 2028-2034; doi: 10.1016/j.jqsrt.2011.03.019 (2011)

Cantor, B. A., James, P. B., Caplinger, M., and Wolff, M. J. Martian dust storms: 1999 Mars Orbiter Camera observations, *J. Geophys. Res.*, 106, 23653-26687 (2001)

Cantor, B. A., James, P. B., and Calvin, W. M. MARCI and MOC observations of the atmosphere and surface cap in the north polar region of Mars, *Icarus*, 208, 61-81 (2010)

Chandrasekhar, S. Radiative Transfer, Dover Publications, New York (1960)

Chassèfiere, E., Drossart, P., and Korablev, O. Post-Phobos model for the altitude and size distribution of dust in the low Martian atmosphere, J. Geophys. Res., 100 (E3), 5525-5539, doi: 10.1029/94JE03363 (1995)

Chen-Chen, H., Pérez-Hoyos, S., and Sánchez-Lavega, A. Dust particle size and optical depth on Mars retrieved by the MSL Navigation Cameras, *Icarus*, 319, 43-57, doi: 10.1016/j.icarus.2018.09.010 (2019a)

Chen-Chen, H., Pérez-Hoyos, S., and Sánchez-Lavega, A. Characterisation of Martian dust aerosol phase function from sky radiance measurements by MSL Engineering Cameras, *Icarus*, 330, 16-29, doi: 10.1016/j.icarus.2019.04.004 (2019b)

Chýlek, P., Grams, G. W., and Pinnick, R. G. Light scattering by irregular randomly oriented particles, *Science*, 193 (4252), 480-482, doi: 10.1126/science.193.4252.480 (1976)

Chýlek, P, and Grams, G. W. Scattering by Nonspherical Particles and Optical Properties of Martian Dust, *Icarus*, volume 36, issue 2, 198-203, doi: 10.1016/0019-1035(78)90104-5 (1978)

Clancy, R. T., Lee, S. W., Gladstone, G. R., McMillan, W. W., and Rousch, T. A new model for Mars atmospheric dust based upon analysis of ultraviolet through infrared observations from Mariner 9, Viking, and Phobos, *J. Geophys. Res.*, 100, 5251-5264, doi: 10.1029/94JE01885 (1995)

Clancy, R. T., Grossman, A. W., Wolff, M. J., James, P. B., Rudy, D. J., Billawala, Y. N., Sandor, B. J., Lee, S. W., and Muhleman, D. O. Water vapour saturation at low altitudes around Mars aphelion: a key to Mars climate?, *Icarus*, 122, 36-62, doi: 10.1006/icar.1996.0108 (1996)

Clancy, R. T., Sandor, B. J., Wolff, M. J., Christensen, P. R., Smith, M. D., Pearl, J. C., Conrath, B. J., and Wilson, R. J. An intercomparison of ground-based millimetre, MGS TES, and Viking atmospheric temperature measurements: Seasonal and interannual variability of

temperatures and dust loading in the Mars atmosphere, *J. Geophys. Res.*, 105 (E4), 9553-9571; doi: 10.1029/1999JE001089 (2000)

Clancy, R. T., Wolff, M. J., and Christensen, P. R. Mars aerosol studies with the MGS TES emission phase function observations: Optical depths, particle sizes, and ice cloud types versus latitude and solar longitude, *J. Geophys. Res.*, 108 (E9), 5098, doi: 10.10129/2003JE002058 (2003)

Colburn, D. S., Pollack, J. B., and Haberle, R. M. Diurnal variations in optical depth at Mars, *Icarus*, 79, 159-189 (1989)

Colina, L., Bohlin, R. C., and Castelli, F. The 0.12-2.5 micron absolute flux distribution of the Sun for comparison with solar analogue stars, *Astron. J.*, 112, 307-314, doi: 10.1086/118016 (1996)

Conrath, B. J. Thermal structure of the Martian atmosphere during the dissipation of the dust storm of 1971, *Icarus*, 24, 36-46, doi: 10.1016/0019-1035(75)90156-6 (1975)

Dabrowska, D. D., Muñoz, O., Moreno, F., Ramos, J. L., Martínez-Frías, J., and Wurm, G. Scattering matrices of Martian dust analogs at 488 nm and 647 nm, *Icarus*, 250, 83-94, doi: 10.1016/j.icarus.2014.11.024 (2015)

Des Marais, D. J., Nuth III, J. A., Allamandola, L. J., Boss, A. P., Farmer, J. D., Hoehler, T. M., Jakosky, B. M., Meadows, V. S., Pohorille, A., Runnegar, B., and Spormann, A. M. The NASA Astrobiology Roadmap, *Astrobiology*, 8 (4), doi: 10.1089/ast.2008.0819 (2008)

Devaux, C., Vermeulen, A., Deuzé, J. L., Dubuisson, P., Herman, M., and Santer, R. Retrieval of aerosol single-scattering albedo from ground-based measurements: Application to observational data. *J. Geophys. Res.*, 103 (D8), 8753-8761 (1998)

Di, K., and Li, R. CAHVOR camera model and its photogrammetric conversion for planetary applications, *J. Geophys. Res.*, 109, E04004; doi: 10.1029/2003JE002199 (2004)

Dlugach, Z. M., Mishchenko, M. I., and Morozhenko, A. V. The effect of the shape of dust aerosol particles in the Martian atmosphere on the particle parameters, *Solar System Research*, 36, 367-373, doi: 10.1023/A:1020459320523 (2002)

Dlugach, Z. M., Korablev, O. I., Morozhenko, A. V., Moroz, V. I., Petrova, E. V., and Rodin, A. V. Physical properties of dust in the Martian atmosphere: analysis of contradictions and possible ways of their resolution, *Solar System Research*, 37, 1-19 (2003)

Drossart, P. A statistical model for the scattering by irregular particles, *Astrophys. J.*, 361, L29-L32 (1990)

Drossart, P., Rosenqvist, J., Combes, M., Erard, S., Langevin, Y., and Bibring, J. P. Martian aerosol properties from the Phobos/ISM experiment, *Annales Geophysicae*, 9, 754-760, (1991)

Dubovik, O., and King, M. D. A flexible inversion algorithm for retrieval of aerosol optical properties from Sun and sky radiance measurements*, J. Geophys. Res.*, 105 (D16), 20673-20696 (2000)

Dubovik, O., Sinyuk, A., Lapyonok, T., Holben, B. N., Mishchenko, M., Yang, P. Eck, T. F., Volten, H., Muñoz, O., Veihelmann, B., van der Zande, W. J., Leon, J.-F., Sorokin, M., and Slutsker, I. Application of spheroid models to account for aerosol particle nonsphericity in remote sensing of desert dust, *J. Geophys. Res.*, 111, D11208, doi:10.1029/2005JD006619 (2006)

Ehlmann, B. L., et al. The sustainability of habitability on terrestrial planets: Insights, questions, and needed measurements from Mars for understanding the evolution of Earth-like worlds, *J. Geophys. Res. Planets*, 121, 1927-1961, doi:10.1002/2016JE005134 (2016)

Escobar-Cerezo, J., Muñoz, O., Moreno, F., Guirado, D., Gómez Martín, J. C., Goguen, J. D., Garboczi, E. J., Chiaramonti, A. N., Lafarge, T., and West, R. A. An Experimental Scattering Matrix for Lunar Regolith Simulant JSC-1A at Visible Wavelengths, *The Astrophysical Journal Supplement Series*, 235, 19-27, doi: 10.3847/1538-4365 (2018)

Forget, F., Hourdin, F., Fournier, R., Hourdin, C., and Talagrand, O. Improved general circulation models of the Martian atmosphere from the surface to above 80 km, *J. Geophys. Res.*, 104 (E10), p. 24155-24176, doi: 10.1029/1999JE001025 (1999)

Gennery, D. B. Generalized camera calibration including fish-eye lenses, *Int. J. Comput. Vis.*, 68(3), 239-266; doi: 10.1007/s11263-006-5168-1 (2006)

Gierasch, P. G., and Goody, R. M. The effect of dust on the temperature of the Martian atmosphere, *J. Atmos. Sci.*, 29, 400-402 (1972)

Gillespie, P. An analytic phase function for cylindrical particles, U.S. Army Atmospheric Sciences Laboratory, ASL-TR-0318, U.S. Army Laboratory Command (1992)

Giuranna, M., Grassi, D., Alessandro, A., Scaccabarozzi, D., Saggin, B., Aoki, S., Wolkenberg, P., and Formisano, V. 12 years of atmospheric monitoring by the Planetary Fourier Spectrometer onboard Mars Express, *Geophysical Research Abstracts,* Vol. 18, abstract EGU2016-8609 (2016)

Gómez-Elvira, J., Armiens, C., Castañer, L., Domínguez, M., Genzer, M., Gómez, F., Haberle, R., Harri, A.-M., Jiménez, V., Kahanpää, H., Kowalski, L., Lepinette, A., Martín, J., Martínez-Frías, J., McEwan, I., Mora, L., Moreno, J., Navarro, S., de Pablo, M. A., Peinado, V., Peña, A., Polkko, J., Ramos, M., Renno, N. O., Ricart, J., Richardson, M.,

Rodríguez-Manfredi, J., Romeral, J., Sebastián, E., Serrano, J., de la Torre Juárez, M., Torres, J., Torrero, F., Urquí, R., Vázquez, L., Velasco, T., Verdasca, J., Zorzano, M.-P., and Martín-Torres, J. REMS: The environmental sensor suite for the Mars Science Laboratory rover, *Space Sci. Rev.*, 170, 583-640, doi: 10.1007/s11214-012-9921-1 (2012)

Greeley, R., and Iversen, J. D. Wind as a geological process on Earth, Mars, Venus and Titan, Cambridge Planetary Science Series, Vol. 4. Cambridge University Press, Cambridge (1985)

Greeley R. Geology of Terrestrial Planets with Dynamic Atmospheres. In: Chahine M.T., A'Hearn M.F., Rahe J., Solomon P., Nickle N.L. (eds) Comparative Planetology with an Earth Perspective, Springer, Dordrecht, doi: 10.1007/978-94-017-1092-3_2 (1995)

Grotzinger, J. P., Crisp, J., Vasavada, A. R., Anderson, R. C., Baker, C. J., Barry, R., Blake, D. F., Conrad, P., Edgett, K. S., Ferdowski, B., Gellert, R., Gilbert, J. B., Golombek, M., Gómez-Elvira, J., Hassler, D. M., Jandura, L., Litvak, M., Mahaffy, P., Maki, J., Meyer, M., Malin, M. C., Mitrofanov, I., Simmonds, J. J., Vaniman, D., Welch, R. V., and Wiens, R. C. Mars Science Laboratory mission and science investigation, *Space Sci. Rev.*, 170, 5-56, doi: 10.1007/s11214-012-9892-2 (2012)

Gunn, M. D., and Cousins, C. R. Mars surface context cameras past, present and future, *Earth and Space Science*, 3, doi: 10.1002/2016EA000166 (2016)

Gurwell, M. A., Bergin, E. A., Melnick, G. J., Tolls, V. Mars surface and atmospheric temperature during the 2001 global dust storm, *Icarus*, 175, 23-31, doi: 10.1016/j.icarus.2004.10.009 (2005)

Guzewich, S. D., Smith, M. D., and Wolff, M. J. The vertical distribution of Martian aerosol particle size, *J. Geophys. Res.: Planets*, 119, 2694-2708, doi: 10.1002/2014JE004704 (2014)

Guzewich, S. D., Newman, C. E., Smith, M. D., Moores, J. E., Smith, C. L., Moore, C., Richardson, M. I., Kass, D., Kleinböhl, A., Mischna, M., Martín-Torres, F. J., Zorzano-Mier, M.-P., and Battalio, M. The vertical dust profile over Gale Crater, Mars, J. Geophys. Res.: Planets, 122, 2779-2792, doi: 10.1002/2017JE005420 (2017)

Guzewich, S. D., Lemmon, M., Smith, C. L., Martínez, G., de Vicente-Retortillo, A., Newman, C., et al. Mars Science Laboratory observations of the 2018/Mars year 34 global dust storm, *Geophys. Res. Lett.*, 46, 71–79, doi: 10.1029/2018GL080839 (2019)

Haberle, R. M. Planetary atmospheres: Mars. In J. R. Holton, J. A. Curry, and J. A. Pyle (Eds.), "Encyclopaedia of Atmospheric Sciences" (pp. 1745-1755), Academic Press (2003)

Haberle, R. M., Clancy, R. T., Forget, F., Smith, M. D., and Zurek, R. W. Introduction. In R. Haberle, R. Clancy, F. Forget, M. Smith and R. Zurek (Eds.), "The Atmosphere and Climate of Mars" (Cambridge Planetary Science, pp. 1-2), Cambridge: Cambridge University Press, doi: 10.1017/9781139060172.001 (2017)

Hamre, B., Stamnes, S., Stamnes, K., and Stamnes, J. J. C-disort: A versatile tool for radiative transfer coupled media like the atmosphere-ocean system, AIP Conference Proceedings 1531, 923; doi: 10.1063/1.4804922 (2013)

Hanel, R., Conrath, B., Hovis, W., Kunde, V., Lowman, P., Maguire, W., Pearl, J., Pirraglia, J., Prabhakara, C., Schlachman, B., Levin, G. Straat, P., and Burke, T. Investigation of the Martian environment by infrared spectroscopy on Mariner 9, Icarus, 17, 423-442, doi: 10.1016/0019-1035(72)90009-7 (1972)

Hansen, J. E., and Lacis, A. Sun and dust versus greenhouse gases: an assessment of their relative roles in global climate change, *Nature*, 346, 713-719 (1990)

Hansen, J. E., and Travis, L. D. Light scattering in planetary atmospheres, *Space Sci. Rev.*, 16, 527-610 (1974)

Heavens, N. G., Richardson, M. I., Kleinböhl, A., Kass, D. M., McCleese, D. J., Abdou, W., Benson, J. L., Schofield, J. T., Shirley, J. H., and Wolkenberg, P. M. The vertical distribution of dust in the Martian atmosphere during northern spring and summer: Observations by the Mars Climate Sounder and analysis of zonal average vertical dust profiles, *J. Geophys. Res.*, 116, E04003, doi: 10.1029/2010JE003691 (2011a)

Heavens, N. G., Richardson, M. I., Kleinböhl, A., Kass, D. M., McCleese, D. J., Abdou, W., Benson, J. L., Schofield, J. T., Shirley, J. H., and Wolkenberg, P. M. Vertical distribution of dust in the Martian atmosphere during northern spring and summer: High-altitude tropical dust maximum at northern summer solstice, *J. Geophys. Res.*, 116, E01007, doi: 10.1029/2010JE003692 (2011b)

Ignatov, A. Estimation of the aerosol phase function in backscatter from simultaneous satellite and Sun-photometer measurements, *Journal of applied meteorology*, 36, 688-694, doi: 10.1175/1520-0450(1997)036<0688:EOTAPF>2.0.CO;2 (1997)

Jakosky, B. M., and Farmer, C. B. The seasonal and global behaviour of water vapor in the Mars atmosphere: complete global results of the Viking atmospheric water detector experiment, *J. Geophys. Res.*, 87, 2999-3019 (1982)

James, P. B., Christensen, P. R., Clancy, R. T., Lemmon, M. T., and Withers, P. History of Mars Atmosphere Observations. In R. Haberle, R. Clancy, F. Forget, M. Smith and R. Zurek (Eds.), "The Atmosphere and Climate of Mars" (Cambridge Planetary Science, pp. 20-41), Cambridge: Cambridge University Press, doi: 10.1017/9781139060172.003 (2017)

Jaquin, F., Gierasch, P., and Kahn, R. The vertical structure of limb hazes in the Martian atmosphere, Icarus, 68, 442-461 (1986)

JPL, Mars Science Laboratory Landing Press Kit, July 16, 2012, Jet Propulsion Laboratory, California Institute of Technology, NASA (2012)

JPL, Mars Science Laboratory (MSL) Project, MSL Experiment Data Record (EDR) and Engineering Cameras Reduced Data Record (RDR) Archive Volume Software Interface Specification (SIS), version 1.15, June 23, 2015; JPL D-64995. Jet Propulsion Laboratory, California Institute of Technology (2015)

Kahn, R. Comparative Planetology and the Atmosphere of Earth. A Report to the Solar System Exploration Division, National Aeronautics and Space Administration, NASA (1989)

Kahre, M. A., Murphy, J. R., Newman, C. E., Wilson, R. J., Cantor, B. A., Lemmon, M. T., and Wolff, M. J. The Mars Dust Cycle. In R. Haberle, R. Clancy, F. Forget, M. Smith and R. Zurek (Eds.), "The Atmosphere and Climate of Mars" (Cambridge Planetary Science, pp. 295-337), Cambridge: Cambridge University Press, doi: 10.1017/9781139060172.010 (2017)

Kaufman, Y. J., Gitelson, A. J., Karnieli, A., Ganor, E., Fraser, R. S., Nakajima, T., Mattoo, S., and Holben, B. N. Size distribution and scattering phase function of aerosol particles retrieved from sky brightness measurements, *J. Geophys. Res.*, 99 (D5), 10341-10356, doi: 10.1029/94JD00229 (1994)

Kattawar, G. W. A three-parameter analytic phase function for multiple scattering calculations, *J. Quant. Spec. Rad. Trans.*, 15 (9), 839-849, doi: 10.1016/0022-4073(75)90095-3 (1975)

Kicza, M., and Vorder Bruegge, R. NASA's Discovery Program, *Acta Astronautica*, 35 (1), 41-50, doi: 10.1016/0094-5765(94)00167-K (1995)

Kloos, J. L., Moores, J. E., Whiteway, J. A., and Aggarwal, M. Interannual and diurnal variability in water ice clouds observed from MSL over two Martian Years, *J. Geophys. Res. Planets*, 123, 233-245, doi: 10.1002/2017JE005314 (2018)

Komguem, L., Whiteway, J. A., Dickinson, C., Daly, M., and Lemmon, M. T. Phoenix LIDAR measurements of Mars atmospheric dust, *Icarus*, 223, 649-653, doi: 10.1016/j.icarus.2013.01.020. (2013)

Korablev, O., Krasnopolsky, V. A., Rodin, A. V., and Chassefiére, E. Vertical structure of Martian dust measured by the solar occultation from Phobos spacecraft, *Icarus*, 102, 76-87, doi: 10.1006/icar.1993.1033 (1993)

Korablev, O., Moroz, V. I., Petrova, E. V., and Rodin, A. V. Optical properties of dust and the opacity of the Martian atmosphere, *Adv. Space Res.*, 35, 21-30, doi: 10.1016/j.asr.2003.04.061 (2005)

Laan, E. C., Volten, H., Stam, D. M., Muñoz, O., Hovenier, J. W., and Roush, T. L. Scattering matrices and expansion coefficients of Martian analogue palagonite particles, *Icarus*, 199, 219-230, doi: 10.1016/j.icarus.2008.08.011 (2009)

LaVoie, S. K., Green, W. B., Runkle, A. J., Alexander, D. A., Andres, P. A., DeJong, E. M., Duxbury, E. D., Freda, D. J., Gorjian, Z., Hall, J. R., Hartman, F. R., Levoe, S. R., Lorre, J. L., McAuley, J. M., Suzuki, S., Woncik, P. J., and Wright, J. R. Processing and analysis of Mars Pathfinder science data at the Jet Propulsion Laboratory's Science Data Processing Systems Section, *J. Geophys. Res.*, 104 (E4), 8831 (1999)

Laszlo, I., Stamnes, K., Wiscombe, W. J., and Tsay, S.-C. The Discrete Ordinate Algorithm, DISORT for Radiative transfer. In A. Kokhanovsky (ed.), "Light Scattering Reviews, Volume 11" Springer Praxis Books, doi: 10.1007/978-3-662-49538-4_1 (2016)

Lemmon, M. T., Wolff, M. J., Smith, M. D., Clancy, R. T., Banfield, D., Landis, G. A., Ghosh, A., Smith, P. H., Spanovich, N., Whitney, B., Whelley, P., Greeley, R., Thompson, S., Bell III, J. F., and Squyres, S. W. Atmospheric imaging results from the Mars Exploration Rovers: Spirit and Opportunity, *Science*, 306, 1753-1756, doi: 10.1126/science.1104474 (2004)

Lemmon, M. T., Smith, P. H., Shinohara, C., Tanner, R., Woida, P., Shaw, A., Hughes, J., Reynolds, R., Woida, R., Penegor, J., Oquest, C., Hviid, S. F., Madsen, M. B., Olsen, M., Leer, K., Drube, L., Morris, R. V., and Britt, D. T. The Phoenix Surface Stereo Imager (SSI) Investigation, 39th Lunar and Planetary Science Conference (LPSC), Contribution No. 1391, p. 2156 (2008)

Lemmon, M. T. The Mars Science Laboratory optical depth record, 8th International Conference on Mars, abstract 1338; 2014LPICo1791.1338L (2014)

Lemmon, M. T., Wolff, M. J., Bell III, J. F., Smith, M. D., Cantor, B. A., and Smith, P. H. Dust aerosol, clouds, and the atmospheric optical depth record over 5 Mars years of the Mars Exploration Rover mission, *Icarus*, 251, 96-111, doi: 10.1016/j.icarus.2014.03.029 (2015)

Leovy, C. B., Briggs, G. A., Young, A. T., Smith, B. A., Pollack, J. B., Shipley, E. N., and Wildey, R. L. The Martian atmosphere: Mariner 9 television experiment progress report, *Icarus*, 17 (2), 373-393, doi: 10.1016/0019-1035(72)90006-1 (1972)

Levine, J. S. Dust in the atmosphere of Mars and its impact on human exploration: defining the problems, In J. S. Levine, D. Winterhalter, and R. L. Kerschmann (Eds.), "Dust in the

Atmosphere of Mars and its Impact on Human Exploration" (Cambridge Scholars Publishing, pp. 1-21), Newcastle, UK: Lady Stephenson Library (2018)

Lewis, S. R. Mars: atmosphere: Modelling the Martian atmosphere, *Astronomy & Geophysics*, 44 (4), 4.06-4.14, doi: 10.1046/j.1468-4004.2003.44406.x (2003)

Liou, K. N. An Introduction to Atmospheric Radiation, Volume 84, 2nd Edition, Academic Press (2002)

Lowman, P. "6.1", Exploring Space, Exploring Earth: New Understanding of the Earth from Space Research. Cambridge, UK: Cambridge University Press (2002)

Määttänen, A., Fouchet, T., Forni, O., Forget, F., Savijärvi, H., Gondet, B., Melchiorri, R., Langevin, Y., Formisano, V., Giuranna, M., and Bibring, J.-P. A study of the properties of a local dust storm with Mars Express OMEGA and PFS data, *Icarus*, 201, 504-516, doi: 10.1016/j.icarus.2009.01.024 (2009)

Madeleine, J.-B., Forget, F., Spiga, A., Wolff, M. J., Montmessin, F., Vincendon, M., Jouglet, D., Gondet, B., Bibring, J.-P., Langevin, Y., and Schmitt, B. Aphelion water-ice cloud mapping and property retrieval using the OMEGA imaging spectrometer onboard Mars Express, *J. Geophys. Res. Planets*, 117 (E11), pp. E00J07, doi: 10.1029/2011JE003940 (2012)

Mahaffy, P. R., Webster, C. R., Atreya, S. K., Franz, H., Wong, M., Conrad, P. G., Harpold, D., Jones, J. J., Leshin, L. A., Manning, H., Owen, T., Pepin, R. O., Squyres, S., Trainer, M., and the MSL Science Team. Abundance and isotopic composition of gases in the Martian atmosphere from the Curiosity Rover, *Science*, 341 (6143), 263-266, doi: 10.1126/science.1237966 (2013)

Maki, J. N., Bell III, J. F., Herkenhoff, K. E., Squyres, S. W., Kiely, A., Klimesh, M., Schwochert, M., Litwin, T., Willson, R., Johnson, A., Maimone, M., Baumgartner, E., Collins, A., Wadsworth, M., Elliot, S. T., Dingizian, A., Brown, D., Hagerott, E. C., Scherr, L., Deen, R., Alexander, D., and Lorre, J. Mars Exploration Rover Engineering Cameras, *J. Geophys. Res.*, 108 (E12), 8071; doi: 10.1029/2003JE002077 (2003)

Maki, J. N. Mars Exploration Rover (MER) Project Engineering Camera Calibration Report. MER 420-6-786, JPL D-25540, July 19, 2004. (2004)

Maki, J. N., Thiessen, D., Pourangi, A., Kobzeff, P., Litwin, T., Scherr, L., Elliott, S., Dingizian, A., and Maimone, M. The Mars Science Laboratory Engineering Cameras, *Space Sci. Rev.*, 170, 77-93; doi: 10.1007/s11214-012-9882-4 (2012)

Maki, J. N., and Warner, N. MSL Coordinate Systems for Science Instruments, 3 March 2013, Jet Propulsion Laboratory, California Institute of Technology (2013)

Maki, J. N., McKinney, C. M., Sellar, R. G., Willson, R. G., Copley-Woods, D. S., Gruel, D. C., Nuding, D. L., Valvo, M., Goodsall, T., McGuire, J., Kempenaar, J., and Litwin, T. E. Enhanced Engineering Cameras (EECAMs) for the Mars 2020 rover, 3rd International Workshop on Instrumentation for Planetary Missions, abstract id. 4132 (2016).

Markiewicz, W. J., Sablotny, R. M., Keller, H. U., Thomas, N., Titov, D., Smith, P. H. Optical properties of the Martian aerosols as derived from Imager for Mars Pathfinder midday sky brightness data, *J. Geophys. Res.*, 104 (E4), 9009–9017, doi:10.1029/1998JE900033 (1999)

Martin, T. Z., and Richardson, M. I. New dust opacity mapping from Viking infrared thermal mapper data, *J. Geophys. Res.*, 98 (E6), 10941–10949, doi: 10.1029/93JE01044 (1993)

McConnochie, T. H., Smith, M. D., Wolff, M. J., Bender, S., Lemmon, M., Wiens, R. G., Maurice, S., Gasnault, O., Lasue, J., Meslin, P.-Y., Harri, A.-M., Genzer, M., Kemppinen, O., Martínez, G. M. DeFlores, L., Blaney, D., Johnson, J. R., and Bell III, J. F. Retrieval of water vapour column abundance and aerosol properties from ChemCam passive sky spectroscopy, *Icarus*, 307, 294-326; doi: 10.1016/j.icarus.2017.10.043 (2017)

McKim, R. J. Meeting contribution: recent views of Mars, *Journal of the British Astronomical Association*, 109 (5), 287 (1999)

Meador, W. E., and Weaver, W. R. Two-stream approximations to radiative transfer in planetary atmospheres: a unified description of existing methods and a new improvement, J. Atmos. Sci., 37, 630-643 (1980)

Medvedev, A. S., Kuroda, T., and Hartogh, P. Influence of dust on the dynamics of the Martian atmosphere above the first scale height, *Aeolian Research*, 3, 145-156, doi: 10.1016/j.aeolia.2011.05.001 (2011)

Merikallio, S., Lindqvist, H., Nousiainen, T., and Kahnert, M. Modelling light scattering by mineral dust using spheroids: assessment of applicability, *Atmos. Chem. Phys.*, 11, 5347-5363, doi: 10.5194/acp-11-5347-2011 (2011)

Merikallio, S., Nousiainen, T., Kahnert, M., and Harri, A.-M. Light scattering by the Martian dust analog, palagonite, modeled with ellipsoids, *Opt. Express*, 21, 17972-17985, doi: 10.1364/OE.21.017972 (2013)

Meng, Z., Yang, P., Kattawar, G. W., and Bi, L. Single-scattering properties of tri-axial ellipsoidal mineral dust aerosols: A database for application to radiative transfer calculations, *Journal of Aerosol Science*, 41 (5), 501-512, doi: 10.1016/j.jaerosci.2010.02.008 (2010)

Milliken, R. E., Grotzinger, J. P., and Thompson, B. J. Paleoclimate of Mars as captured by the stratigraphic record in Gale Crater, *Geophys. Res. Lett.*, 37, L04201, doi: 10.1029/2009GL041870 (2010)

Millour, E., Forget, F., Spiga, A., Navarro, T., Madeleine, J. B., Montabone, L., Pottier, A., Lefevre, F., Montmessin, F., Chaufray, J. Y., Lopez-Valverde, M. A., Gonzalez-Galindo, F., Lewis, S. R., Read, P. L., Huout, J.-P., Desjean, M. C., and the MCD/GCM development team. The Mars Climate Database (MCD version 5.2), EPSC Abstracts, Vol. 10, EPSC2015-438 (2015)

Mishchenko, M. I., Lacis, A. A., Carlson, B. E., and Travis, L. D. Nonsphericity of dust-like tropospheric aerosols: implications for aerosol remote sensing and climate modelling, *Geophys. Res. Lett.*, 22 (9), 1077-1080, doi: 10.1029/95GL00798 (1995)

Mishchenko, M. I., Travis, L. D., and Mackowski, D. W. T-matrix computations of light scattering by nonspherical particles: a review, J. Quant. Spec. Rad. Trans., 55, 535-575, doi: 10.1016/0022-4073(96)00002-7 (1996)

Mishchenko, M.I., Travis, L. D., Kahn, R. A., and West, R. A. Modeling phase functions for dustlike tropospheric aerosols using a mixture of randomly oriented polydisperse spheroids, *J. Geophys. Res.*, 102, 16831-16847, doi: 10.1029/96JD02110 (1997)

Mishchenko, M. I., and Travis, L. D. Capabilities and limitations of a current Fortran implementation of the T-matrix method for randomly oriented, rotationally symmetric scatterers*, J. Quant. Spec. Rad. Trans.*, 60 (3), 309-324, doi: 10.1016/S0022-4073(98)00008-9 (1998)

Mishchenko, M. I., Hovenier, J. W., and Travis, L. D., editors. Light Scattering by Nonspherical Particles: Theory, Measurements, and Applications. Academic Press (2000)

Mishchenko, M. I., Travis, L. D., and Lacis, A. A. Multiple scattering of light by particles: radiative transfer and coherent backscattering, Cambridge University Press, Cambridge (2006)

Mishchenko, M. I., Zakharova, N. T., Khlebtsov, N. G., Videen, G., and Wriedt, T. Comprehensive thematic T-matrix reference database: a 2015-2017 update, *J. Quant. Spec. Rad. Trans.*, 202, 240-246, doi: 10.1016/j.jqsrt.2017.08.007 (2017)

Montabone, L., Forget, F., Millour, E., Wilson, R. J., Lewis, S. R., Cantor, B., Kass, D., Kleinböhl, A., Lemmon, M. T., Smith, M. D., and Wolff, M. J. Eight-year climatology of dust optical depth on Mars, *Icarus*, 251, 65-95, doi: 10.1016/j.icarus.2014.12.034 (2015)

Montmessin, F., Rannou, P., and Cabanne, M. New insights into Martian dust distribution and water-ice cloud microphysics, *J. Geophys. Res.: Planets*, 107 (E6), 4-1, doi: 10.1029/2001JE001520 (2002)

Montmessin, F., Quémerais, E., Bertaux, J. L., Korablev, O., Rannou, P., and Lebonnois, S. Stellar occultations at UV wavelengths by the SPICAM instrument: retrieval and

analysis of Martian haze profiles, *J. Geophys. Res.*, 111, E09S09, doi: 10.1029/2005JE002662 (2006)

Montmessin, F., Korablev, O., Lefèvre, F., Bertaux, J.-L., Fedorova, A., Trokhimovskiy, A., Chaufray, J. Y., Lacombe, G., Reberac, A., Maltagliati, L., Willame, Y., Guslyakova, S., Gérard, J.-C., Stiepen, A., Fussen, D., Mateshvili, N., Määttänen, A., Forget, F., Witasse, O., Leblanc, F., Vandaele, A. C., Marcq, E., Sandel, B., Gondet, B., Schneider, N., Chaffin, M., and Chapron, N. SPICAM on Mars Express: a 10 year in-depth survey of the Martian atmosphere, Icarus, 297, 195-216, doi: 10.1016/j.icarus.2017.06.022 (2017a)

Montmessin, F., Smith, M. D., Langevin, Y., Mellon, M. T., and Fedorova, A. The Water Cycle. In R. Haberle, R. Clancy, F. Forget, M. Smith and R. Zurek (Eds.), "The Atmosphere and Climate of Mars" (Cambridge Planetary Science, pp. 338-373), Cambridge: Cambridge University Press, doi: 10.1017/9781139060172.011 (2017b)

Moore, C. A., Moores, J. E., Lemmon, M. T., Rafkin, S. C. R., Francis, R., Pla-García, J., Haberle, R. M., Zorzano, M.-P., Martín-Torres, F. J., Burton, J. R., and the MSL Science Team. A full martian year of line-of-sight extinction within Gale Crater, Mars as acquired by the MSL Navcam through sol 900, *Icarus*, 264, 102-108, doi: 10.1016/j.icarus.2015.09.001 (2016)

Moores, J. E., Lemmon, M. T., Kahanpää, H., Rafkin, S. C. R., Francis, R., Pla-Garcia, J., Bean, K., Haberle, R., Newman, C., Mischna, M., Vasavada, A. R., de la Torre Juárez, M., Rennó, N., Bell, J., Calef, F., Cantor, B., McConnochiet, T. H., Harri, A.-M., Genzer, M., Wong, M. H., Smith, M. D., Martín-Torres, F. J., Zorzano, M.-P., Kemppinen, O., and McCullough, E. Observational evidence of a suppressed planetary boundary layer in northern Gale Crater, Mars as seen by the Navcam instrument onboard the Mars Science Laboratory rover, *Icarus*, 249, 129-142; doi: 10.1016/j.icarus.2014.09.020 (2015)

Muñoz, O., Moreno, F., Guirado, D., Dabrowska, D. D., Volten, H., and Hovenier, J. W. The Amsterdam-Granada Light Scattering Database, *J. Quant. Spec. Rad. Trans.*, 113 (7), 565-574, doi: 10.1016/j.jqsrt.2012.01.014 (2012)

Murphy, J. R., Haberle, R. M., Toon, O. B., and Pollack, J. B. Martian global dust storms: zonally symmetric numerical simulations including size-dependent particle transport, J. Geophys. Res., 98 (E2), 3197-3220 (1993)

Nakajima, T., Tonna, G., Ruizhong, R., Boi, P., Kaufman, Y., and Holben, B. Use of sky brightness measurements from ground for remote sensing of particulate polydispersions, *Appl. Opt.*, 35, 2672-2686 (1996)

Neakrase, L. D. V., and Greeley, R. Dust devil sediment flux on Earth and Mars: laboratory simulations, *Icarus*, 206 (1), 306-318 (2010)

Newman, C. E., Lewis, S. R., Read, P. L., and Forget, F. Modeling the Martian dust cycle 1. Representation of dust transport processes, *J. Geophys. Res.* , 107 (E12), 5123, doi: 10.1029/2002JE001910 (2002)

Ockert-Bell, M. E., Bell, J. F., Pollack, J. B., McKay, C. P., and Forget, F. Absorption and scattering properties of the Martian dust in the solar wavelengths, *J. Geophys. Res.*, 102 (E4), 9039-9050, doi: 10.1029/96JE03991 (1997)

Owen, T. The composition of the Martian atmosphere, *Adv. Space Res.*, 2, 75-80 (1982)

Peters, S. Mars Science Laboratory Pointing, Positioning, Phasing, and Coordinate Systems (PPPCS) Document, Volume 9, Surface Remote Sensing and Navigation., Rev. Public Release, 13 May 2016, JPL, California Institute of Technology (2016)

Pitman, K. M., Wolff, M. J., Clancy, R. T., and Clayton, G. C. On the shape of Martian dust and water ice aerosols, Abstract AAS-DPS Meeting 32, id. 51.09, Bulletin of the American Astronomical Society, Vol. 32, p. 1095 (2000)

Pla-Garcia, J., Rafkin, S. C. R., Kahre, M., Gomez-Elvira, J., Hamilton, V. E., Navarro, S., Torres, J., Marín, M., Vasavada, A. R. The meteorology of Gale Crater as determined from rover environmental monitoring station observations and numerical modeling. Part I: Comparisons of model simulations with observations, Icarus, 280, 103-113, doi: 10.1016/j.icarus.2016.03.013 (2016)

Pollack, J. B. Climatic change on the terrestrial planets, *Icarus*, 37 (3), 479-553 (1979)

Pollack, J. B., Colburn, D. S., Kahn, R., Hunter, J., Van Camp, W., Carlston, C. E., and Wolf, M. R. Properties of aerosols in the Martian atmosphere, as inferred from Viking lander imaging data, *J. Geophys. Res.*, 82, 4479-4496 (1977)

Pollack, J. B., Colburn, D. S., Flasar, F. M., Kahn, R., Carlston, C. E., and Pidek, D. Properties and effects of dust particles suspended in the Martian atmosphere, *J. Geophys. Res.*, 84 (B6), 2929-2945 (1979)

Pollack, J. B., and Cuzzi, J. N. Scattering by nonspherical particles of size comparable to a wavelength: a new semi-empirical theory and its application to tropospheric aerosols*, J. Atmos. Sci.*, 37, 868-881, doi: 10.1175/1520-0469(1980)037<0868:SBNPOS>2.0.CO;2 (1980)

Pollack, J. B., Ockert-Bell, M. E., and Shepard, M. K. Viking Lander image analysis of Martian atmospheric dust, *J. Geophys. Res.*, 100 (E3), 5235-5250, doi: 10.1029/94JE026-40 (1995)

Rafkin, S. C. R., Haberle, R. M., and Michaels, T. I. The Mars Regional Atmospheric Modeling System: model description and selected simulations, *Icarus*, 151 (2), 228-256 (2001)

Rafkin, S. C. R., Pla-Garcia, J., Kahre, M., Gomez-Elvira, J., Hamilton, V. E., Marín, M., Navarro, S., Torres, J., and Vasavada, A. The meteorology of Gale Crater as determined from Rover Environmental Monitoring Station observations and numerical modeling. Part II: Interpretation, Icarus, 280, 114-138, doi: 10.1016/j.icarus. 2016.01.031 (2016)

Rafkin, S. C. R., Spiga, A., and Michaels, T. I. Mesoscale meteorology. In R. Haberle, R. Clancy, F. Forget, M. Smith, and R. Zurek (Eds.), "The Atmosphere and Climate of Mars" (Cambridge Planetary Science, pp. 203-228), Cambridge: Cambridge University Press, doi: 10.1017/9781139060172.008 (2017)

Read, P. L., Lewis, S. R., and Mulholland, D. P. The physics of Martian weather and climate: a review, *Rep. Prog. Phys.*, 78, 125901, 54pp, doi: 10.1088/0034-4885/78/12/125901 (2015)

Rodriguez-Manfredi, J. A., Gomez-Gomez, F., Gomez-Elvira, J., Navarro, S., Prieto-Ballesteros, O., Sebastian, E., de la Torre, M., Schofield, J. T., Tamppari, L. K., Arruego, I., Bridges, N. T., Conrad, P. G., Smith, M., Genzer, M., Harri, A.-M., Lemmon, M., Martinez, G., Newman, C., Sanchez-Lavega, A., Ramos, M., Saiz-Lopez, A., and the MEDA team. Atmospheric science with the MARS 2020 rover - the MEDA instrument, 6th International Workshop on Mars Atmosphere Modelling and Observations Workshop, Granada, Spain, abstract 2017mamo.conf.4408R (2017)

Rossow, W. B. Cloud microphysics – analysis of the clouds of Earth, Venus, Mars, and Jupiter, Icarus, 36, 1-50 (1978)

Rothman, L. S., Gordon, I. E., Babikov, Y., Barbe, A., Benner, D. C., Bernath, P. F., Birk, M., Bizzochi, L., Boudon, V., Brown, L. R., Campargue, A., Chance, K., Cohen, E. A., Coudert, L. H., Devi, V. M., Drouin, B. J., Fayt, A., Flaud, J.-M., Gamache, R. R., Harrison, J. J., Hartmann, J.-M., Hill, C., Hodges, J. T., Jacquemart, D., Jolly, A., Lamouroux, J., Le Roy, R. J., Li, G., Long, D. A., Lyulin, O. M., Mackie, C. J., Massie, S. T., Mikhailenko, S., Müller, H. S. P., Naumenko, O. V., Nikitin, A. V., Orphal, J., Perevalov, V., Perrin, A., Polovtseva, E. R., Richard, C., Smith, M. A. H., Starikova, E., Sung, K., Tashkun, S., Tennyson, J., Toon, G. C., Tyuterev, V. G., and Wagner, G. The HITRAN2012 molecular spectroscopic database, *J. Quant. Spec. Rad. Trans.*, 130, 4-50, doi: 10.1016/j.jqsrt.2013.07.002 (2013)

Sánchez-Lavega, A. An Introduction to Planetary Atmospheres, CRC Press, Taylor & Francis Group (2011)

Sánchez-Lavega, A., Chen-Chen, H., Ordoñez-Etxeberria, I., Hueso, R. del Río-Gaztelurrutia, Garro., A., Cardesín-Moinelo, A., Titov, D., and Wood, S. Limb clouds and dust on Mars

from images obtained by the Visual Monitoring Camera (VMC) onboard Mars Express, *Icarus*, 299, 194-205, doi: 10.1016/j.icarus.2017.07.026 (2018)

Sánchez-Lavega, A., del Río-Gaztelurrutia, T., Hernández-Bernal, J., and Delcroix, M. The onset and growth of the 2018 Martian global dust storm, *Geophys. Res. Lett.*, in press.

Schofield, J. T., Barnes, J. R., Crisp, D., Haberle, R. M., Larsen, S., Magalhães, J. A., Murphy, J. R., Seiff, A., and Wilson, G. The Mars Pathfinder Atmospheric Structure Investigation/Meteorology (ASI/MET) experiment, Science, vol. 278, issue 5344, 1752-1758, doi: 10.1126/science.278.5344.1752 (1997)

Smith, G. H., Hagerott, E. C., Scherr, L. M., Herkenhoff, K. E., and Bell III, J. F. Optical designs for the Mars '03 Rover Cameras, in *Current Developments in Lens Design and Optical Engineering II*, ed. by Fischer, R. E., Johnson, R. B., and Smith, W. J., Proc. SPIE, vol. 4441, p. 118 (2001)

Smith, M. D. Interannual variability in TES atmospheric observations of Mars during 1999-2003, *Icarus*, 167, 148-165, doi: 10.1016/j.icarus.2003.09.010 (2004)

Smith, M. D., Wolff, M. J., Spanovich, N., Ghosh, A., Banfield, D., Christensen, P. R., Landis, G. A., and Squyres, S. W. One Martian year of atmospheric observations using MER Mini-TES, *J. Geophys. Res.*, 111, E12S13, doi: 10.1029/2006JE002770 (2006)

Smith, M. D. Spacecraft observations of the Martian atmosphere, *Annu. Rev. Earth Planet. Sci.*, 191-219, doi: 10.1146/annurev.earth.36.031207.124334 (2008)

Smith, M. D. THEMIS observations of Mars aerosol optical depth from 2002-2008, *Icarus*, 202, 444-452, doi: 10.1016/j.icarus.2009.03.027 (2009)

Smith, M. D., Wolff, M. J., Clancy, R. T., Kleinböhl, A., and Murchie, S., L. Vertical distribution of dust and water ice aerosols from CRISM limb-geometry observations. *J. Geophys. Res.: Planets*, 118 (2), 321-334 (2013)

Smith, M. D., and Wolff, M. J. Dust aerosol particle size and shape using MER NAVCAM and PANCAM sky imaging, The 5th International Workshop on the Mars Atmosphere: Modelling and Observation (MAMO 5th), abstract 2101; 2014mamo.conf.2101S (2014)

Smith, M. D., Zorzano, M.-P., Lemmon, M., Martín-Torres, J., and Mendaza de Cal, T. Aerosol optical depth as observed by the Mars Science Laboratory REMS UV photodiodes, *Icarus*, 280, 234-248; doi: 10.1016/j.icarus.2016.07.012 (2016)

Smith, M. D., Bougher, S. W., Encrenaz, T., Forget, F., and Kleinbhöl. Thermal structure and composition. In R. Haberle, R. Clancy, F. Forget, M. Smith, and R. Zurek (Eds.), "The Atmosphere and Climate of Mars" (Cambridge Planetary Science, pp. 42-75), Cambridge: Cambridge University Press, doi: 10.1017/9781139060172.004 (2017)

Smith, P. H., and Lemmon, M. Opacity of the Martian atmosphere measured by the Imager for Mars Pathfinder, *J. Geophys. Res.*, 1005 (E4), 8975-8985, doi: 10.1029/1998JE900017 (1999)

Sneep, M., and Ubachs, W. Direct measurements of the Rayleigh scattering cross section in various gases, *J. Quant. Spec. Rad. Trans.*, 92 (3), 293-310, doi: 10.1016/j.jqsrt.2004.07.025 (2005)

Snyder, C. W. The Extended Mission of Viking, *J. Geophys. Res.*, 84 (B14), doi: 10.1029/JB084iB14p07917 (1979)

Soderblom, J. M., Bell III, J. F., Johnson, J. R., Joseph, J., and Wolff, M. J. Mars Exploration Rover Navigation Camera in-flight calibration, *J. Geophys. Res.*, 113, E06S19; doi: 10.1029/2007JE003003 (2008)

Stamnes, K., Tsay, S.-C., Wiscombe, W., and Jayaweera, K. Numerically stable algorithm for discrete-ordinate-method radiative transfer in multiple scattering and emitting layered media, *Appl. Opt.*, 27, 2502-2509 (1988)

Stamnes, K., Tsay, S.-C., Wiscombe, W., and Laszlo, I. DISORT, a General-purpose Fortran program for discrete-ordinate-method radiative transfer in scattering and emitting layered media: documentation of methodology, NASA Technical Report, version 1.1 (2000)

Stein, T., Arvidson, R. E., and Zhou, F. PDS Analyst's Notebook for MSL and MER, American Geophysical Union (AGU), Fall Meeting 2016, abstract #IN53C-1912 (2016)

Tamppari, L. K., Bass, D., Cantor, B., Daubar, I., Dickinson, C., et al. Phoenix and MRO coordinated atmospheric measurements, *J. Geophys. Res.*, 115, E00E17, doi: 10.1029/2009JE003415 (2010)

Taylor, F. Comparative planetology, climatology and biology of Venus, Earth and Mars, *Planetary and Space Science*, 59, 889-899, doi: 10.1016/j.pss.2010.11.009 (2011)

Thomas, G. E., and Stamnes, K. Radiative Transfer in the Atmosphere and Ocean, Cambridge University Press, Cambridge (1999)

Tillman, J. E., Johnson, N. C., Guttorp, P., and Percival, D. B. The Martian annual atmospheric pressure cycle – years without great dust storms, *J. Geophys. Res.*, 98, 10963-10971, doi: 10.1029/93JE01084 (1993)

Titus, T. N., Byrne, S., Colaprete, A., Forget, F., Michaels, T. I., and Prettyman, T. H. The CO_2 cycle. In R. Haberle, R. Clancy, F. Forget, M. Smith, and R. Zurek (Eds.), "The Atmosphere and Climate of Mars" (Cambridge Planetary Science, pp. 374-404), Cambridge: Cambridge University Press, doi: 10.1017/9781139060172.012 (2017)

Tomasko, M. G., Doose, L. R., Lemmon, M., Smith, P. H., and Wegryn, E. Properties of dust in the Martian atmosphere from the Imager on Mars Pathfinder, *J. Geophys. Res.*, 104, 8987-9007, doi: 10.1029/1998JE900016 (1999)

Toon, O. B., Pollack, J. B., and Sagan, C. Physical properties of the particles composing the Martian dust storm of 1971-1972, Icarus, 30 (4), doi: 10.1016/0019-1035(77)90088-4 (1977)

Toon, O. B., Pollack, J. B., Ackerman, T. P., Turco, R. P., McKay, C. P., Liu, M. S. Evolution of an impact-generated dust cloud and its effects on the atmosphere, *Geological Society of America*, Special Paper, 190, doi: 10.1130/SPE190-p187 (1982)

Toon, O. B., McKay, C. P., Ackerman, T. P., and Santhanam, K. Rapid calculation of radiative heating rates and photodissociation rates in inhomogeneous multiple scattering atmospheres, *J. Geophys. Res.*, 94 (D13), 16287-16301, doi: 10.1029/JD094iD13p16287 (1989)

van de Hulst, H. C. Light scattering by small particles, New York: John Wiley & Sons, 1957

Vermeulen, A., Devaux, C., and Herman, M. Retrieval of the scattering and microphysical properties of aerosols from ground-based optical measurements including polarization. I. Method, *Applied Optics*, 39, 6207-6220, doi: 10.1364/AO.39.006207 (2000)

Vicente-Retortillo, A., Martínez, G. M., Renno, N. O., Lemmon, M. T., and de la Torre-Juárez, M. Determination of dust aerosol particle size at Gale Crater using REMS UVS and Mastcam measurements, *Geophys. Res. Lett.*, 44, 3502-3508; doi: 10.1002/2017GL0725589 (2017)

Warren, S. G. Optical constants of ice from the ultraviolet to the microwave, *Applied Optics*, 23 (8), 1206 – 1225, doi: 10.1364/AO.23.001206 (1984)

Waterman, P. C. Matrix formulation of electromagnetic scattering, Proc. IEEE, 53, 805-812 (1965)

Whitcomb, G. P. The ESA approach to low-cost planetary missions, *Acta Astronautica*, 52, issues 2-6, 79-86, doi: 10.1016/S0094-5765(02)00141-8 (2003)

Wolfe, C. A., and Lemmon, M. T. Using Engineering Cameras on Mars landers and rovers to retrieve atmospheric dust loading, 46th Lunar and Planetary Science Conference, abstract 2851 (2015)

Wolff, M. J., Clancy, R. T., Pitman, K. M., Bell, J. F., and James, P. B. Constrains on Martian Aerosol Particles Using MGS/TES and HST Data: Shapes, American Geophysical Union (AGU), Fall Meeting 2001, abstract id.P32E-05 (2001)

Wolff, M. J., and Clancy, R. T., Constraints on the size of Martian aerosols from Thermal Emission Spectrometer observations, J. Geophys. Res., 108 (E9), 5097, doi: 10.1029/2003JE002057 (2003)

Wolff, M. J., Smith, M. D., Clancy, R. T., Spanovich, N., Whitney, B. A., Lemmon, M. T., Bandfield, J. L., Banfield, D., Ghosh, A., Landis, G., Christensen, P. R., Bell, J. F., III, and Squyres, S. W. Constraints on dust aerosols from the Mars Exploration Rovers using MGS overflights and Mini-TES, J. Geophys. Res., 111, E12S17, doi: 10.1029/2006JE002786 (2006)

Wolff, M. J., Smith, M. D., Clancy, R. T., Arvidson, R., Kahre, M., Seelos IV, F., Murchie, S., and Savijärvi, H. Wavelength dependence of dust aerosol single scattering albedo as observed by the compact reconnaissance imaging spectrometer, *J. Geophys. Res.*, 114, E00D04, doi:10.1029/2009JE003350 (2009)

Wriedt, T., and Hellmers, J. New scattering information portal for the light-scattering community, J. Quant. Spec. Rad. Trans., 109 (8), 1536-1542, doi: 10.1016/j.jqsrt.2007.11.008 (2008)

Wriedt, T. Light scattering theories and computer codes, *J. Quant. Spec. Rad. Trans.*, 110, 833-843, doi: 10.1016/j.jqsrt.2009.02.023 (2009)

Yakimovsky, Y., and Cunningham, R. A system for extracting three-dimensional measurements from a stereo pair of TV cameras, *Computer Graphics and Image Processing*, 7, 195-210, doi: 10.1016/0146-664X(78)90112-0 (1978)

Yang, H., and Gordon, H. Retrieval of the columnar aerosol phase function and single-scattering albedo from sky radiance over land: simulations, *Applied Optics*, 37, 978-997, doi: 10.1364/AO.37.000978 (1998)

Yang, P., Fent, Q., Hong, G., Kattawar, G. W., Wiscombe, W. J., Mishchenko, M. I., Dubovik, O., Laszlo, I., and Sokolik, I. N. Modeling of the scattering and radiative properties of nonspherical dust-like aerosols, *Journal of Aerosol Science*, 41 (11), 1052-1053, doi: 10.1016/j.aerosci.2007.07.001 (2007)

Yurkin, M. A., and Hoekstra, A. G. The discrete dipole approximation: an overview and recent developments, *J. Quant. Spec. Rad. Trans.*, 106, 558-589, doi: 10.1016/j.jqsrt.2007.01.034 (2007)

Zhang, F., and Li, J. A note on double Henyey-Greenstein phase function, *J. Quant. Spec. Rad. Trans.*, 184, 40-43, doi: 10.1016/j.jqsrt.2016.06.016 (2016)

APPENDIX A

MSL NAVCAM CALIBRATION FILES

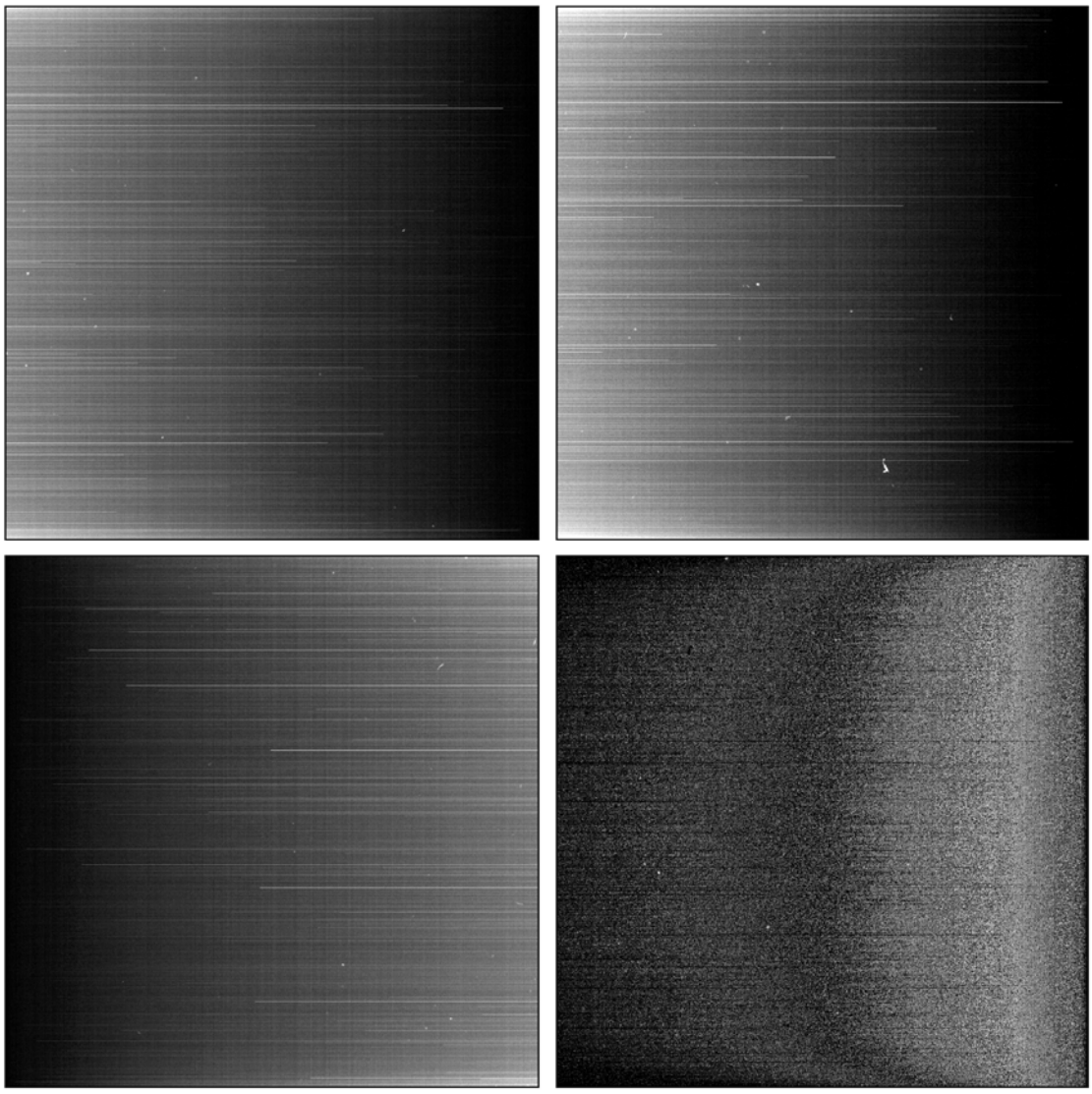

Figure A.1. MSL Navcam masked-area dark current flat image. Masked-area dark current flats for Navcams NLA (top-left), NRA (top-right), NLB (bottom-left) and NRB (bottom-right). The images are linearly stretched between 0.005 and 3.8.

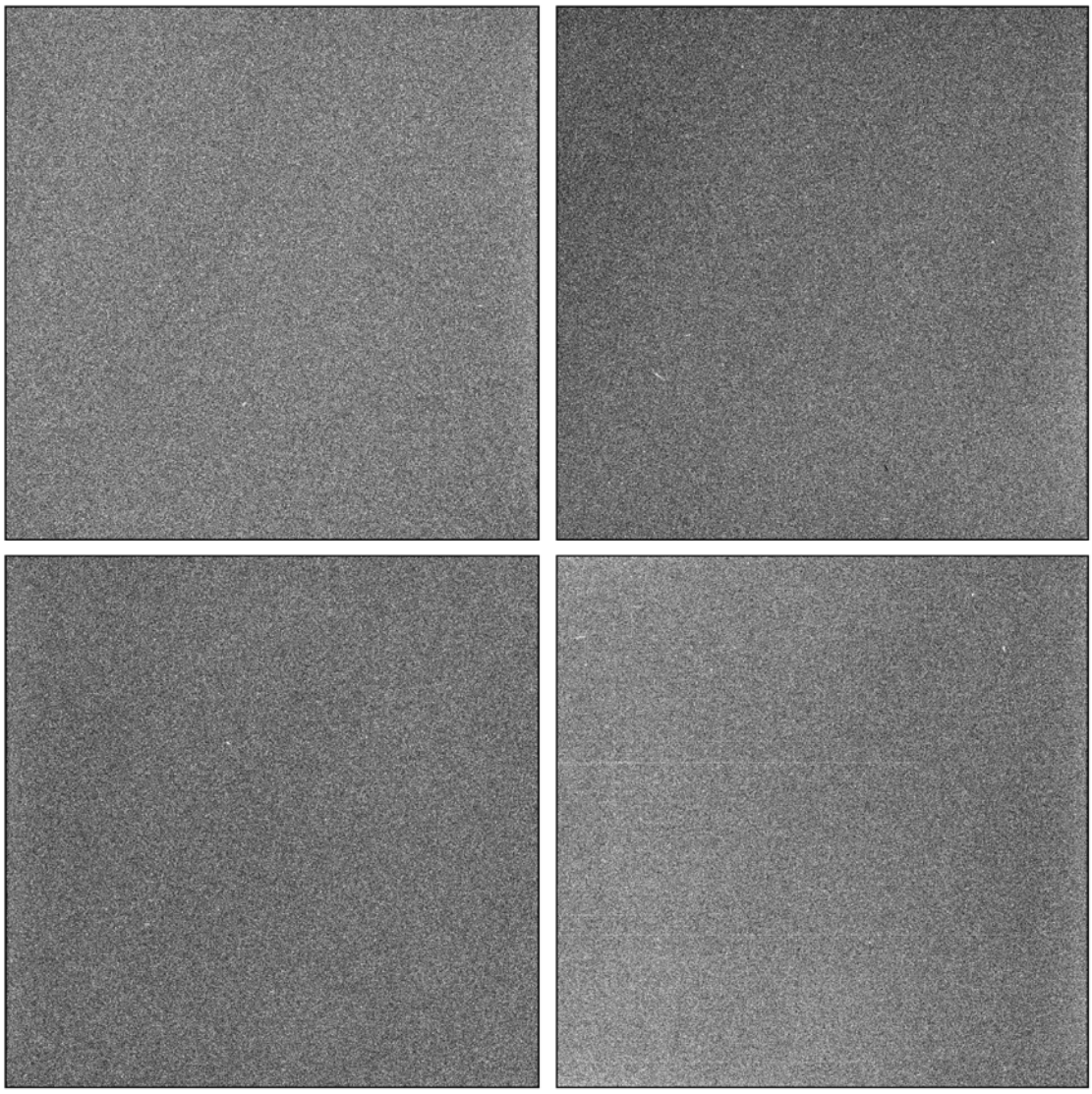

Figure A.2. MSL Navcam active-area dark current flat images. Active-area dark current flats for Navcams NLA (top-left), NRA (top-right), NLB (bottom-left) and NRB (bottom-right). The images are linearly stretched between 0.9 and 1.1.

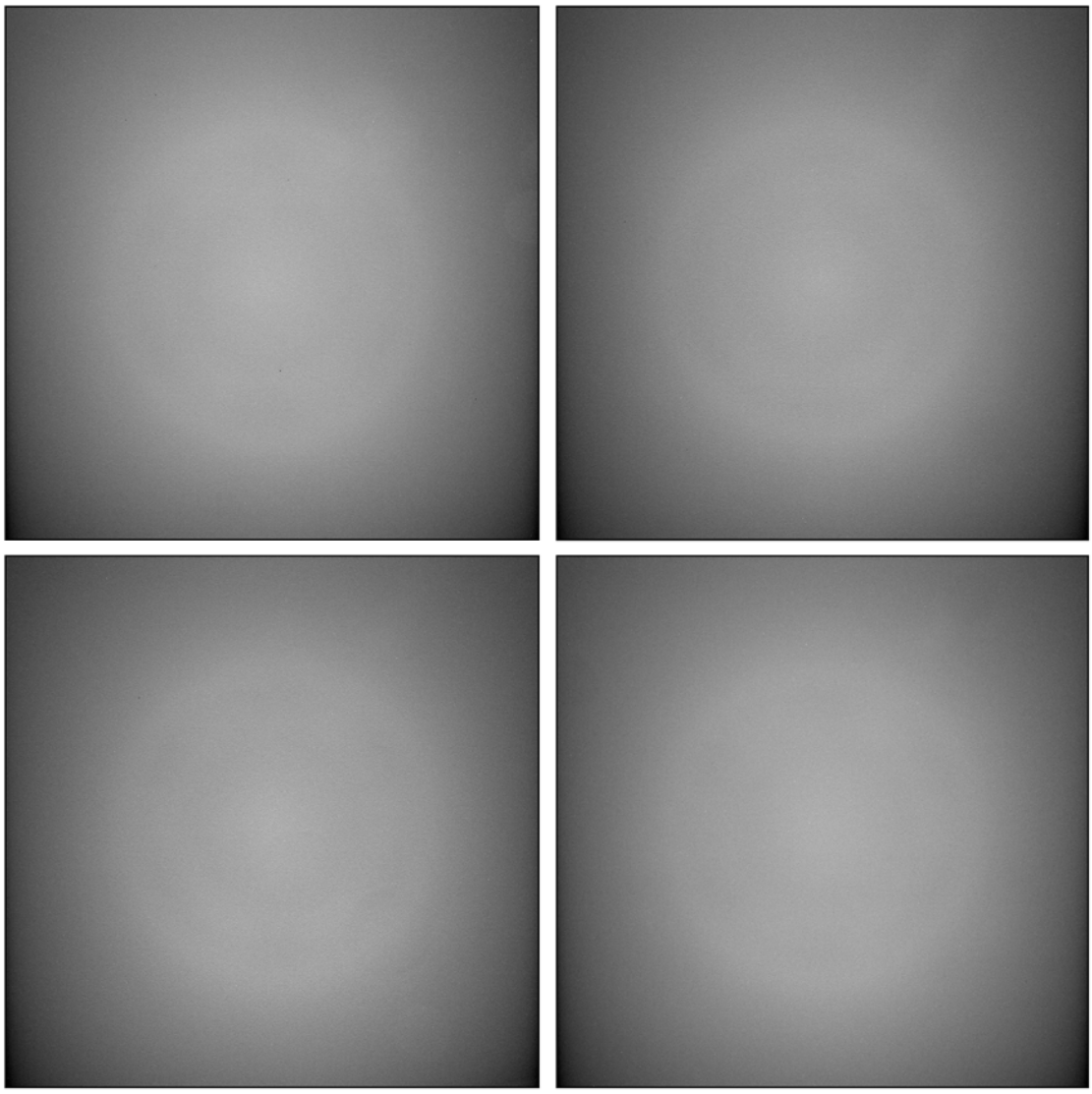

Figure A.3. MSL Navcam pre-flight flat field images. The pre-flight flat field images (Maki et al., 2012) were retrieved from the PDS imaging node database (https://pds-imaging.jpl.nasa.gov/data/msl/MSLNAV_0XXX/CALIB/) and correspond to: NLA (top-left), NRA (top-right), NLB (bottom-left) and NRB (bottom-right). Each image is linearly stretched between 0.5 and 1.25.

APPENDIX B

MSL HAZCAM CALIBRATION FILES

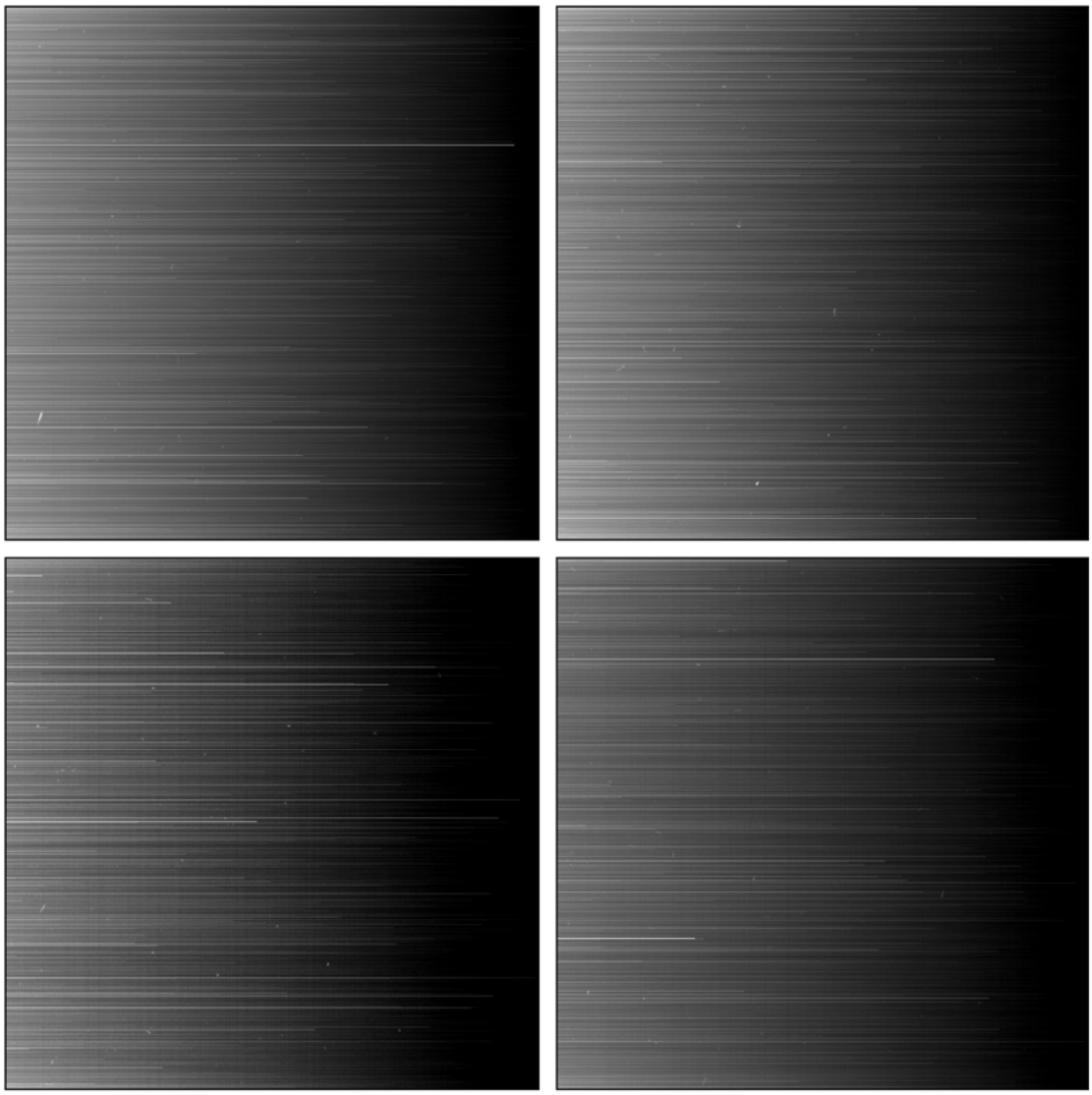

Figure B.1. MSL Hazcam masked-area dark current flat images. Masked-area dark current flats for Hazcams FLB (top-left), FRB (top-right), RLB (bottom-left) and RRB (bottom-right). The images are linearly stretched between 0.005 and 3.8.

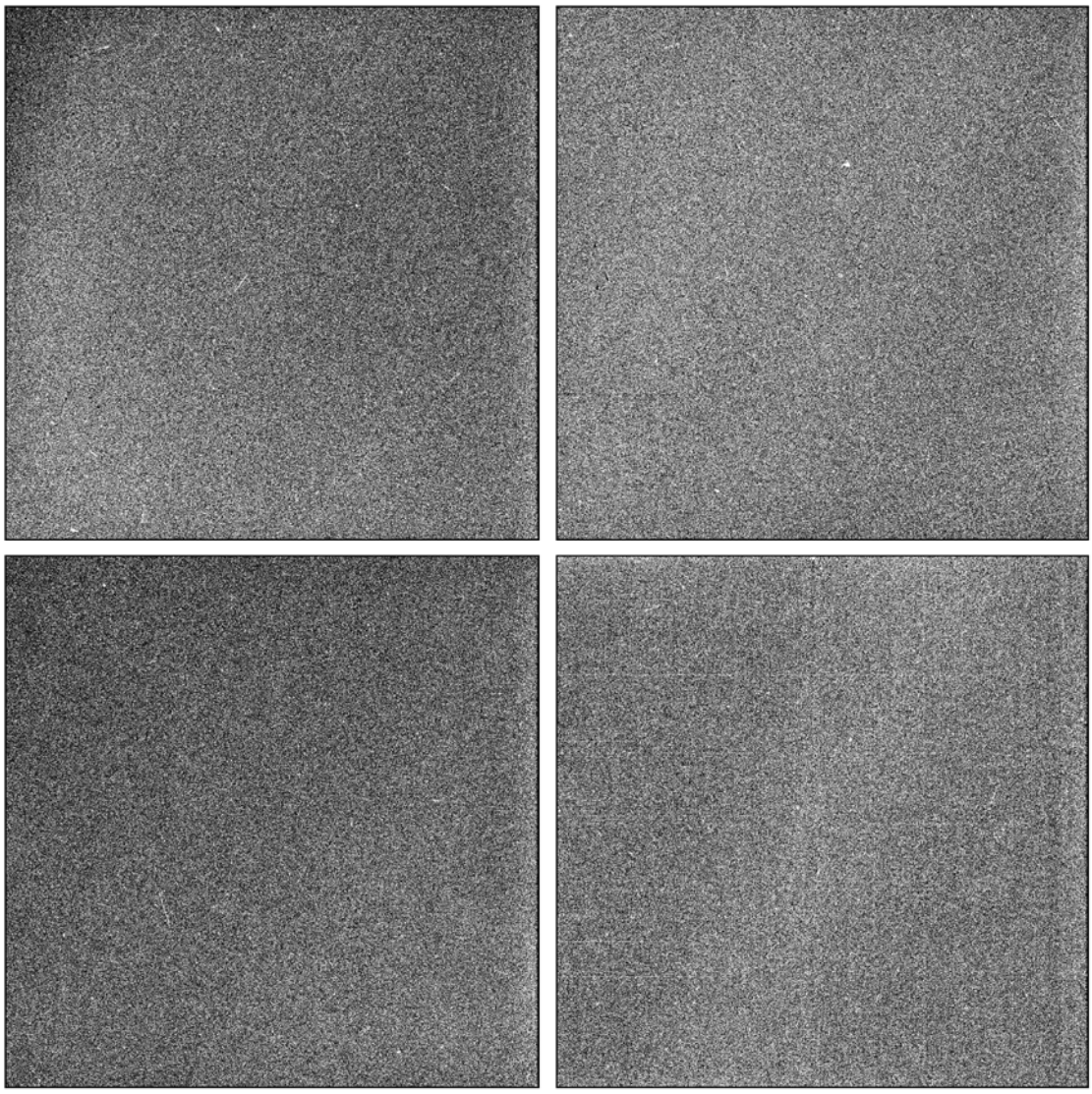

Figure B.2. MSL Hazcam active-area dark current flat images. Active-area dark current flats for Hazcams FLB (top-left), FRB (top-right), RLB (bottom-left) and RRB (bottom-right). The images are linearly stretched between 0.9 and 1.1.

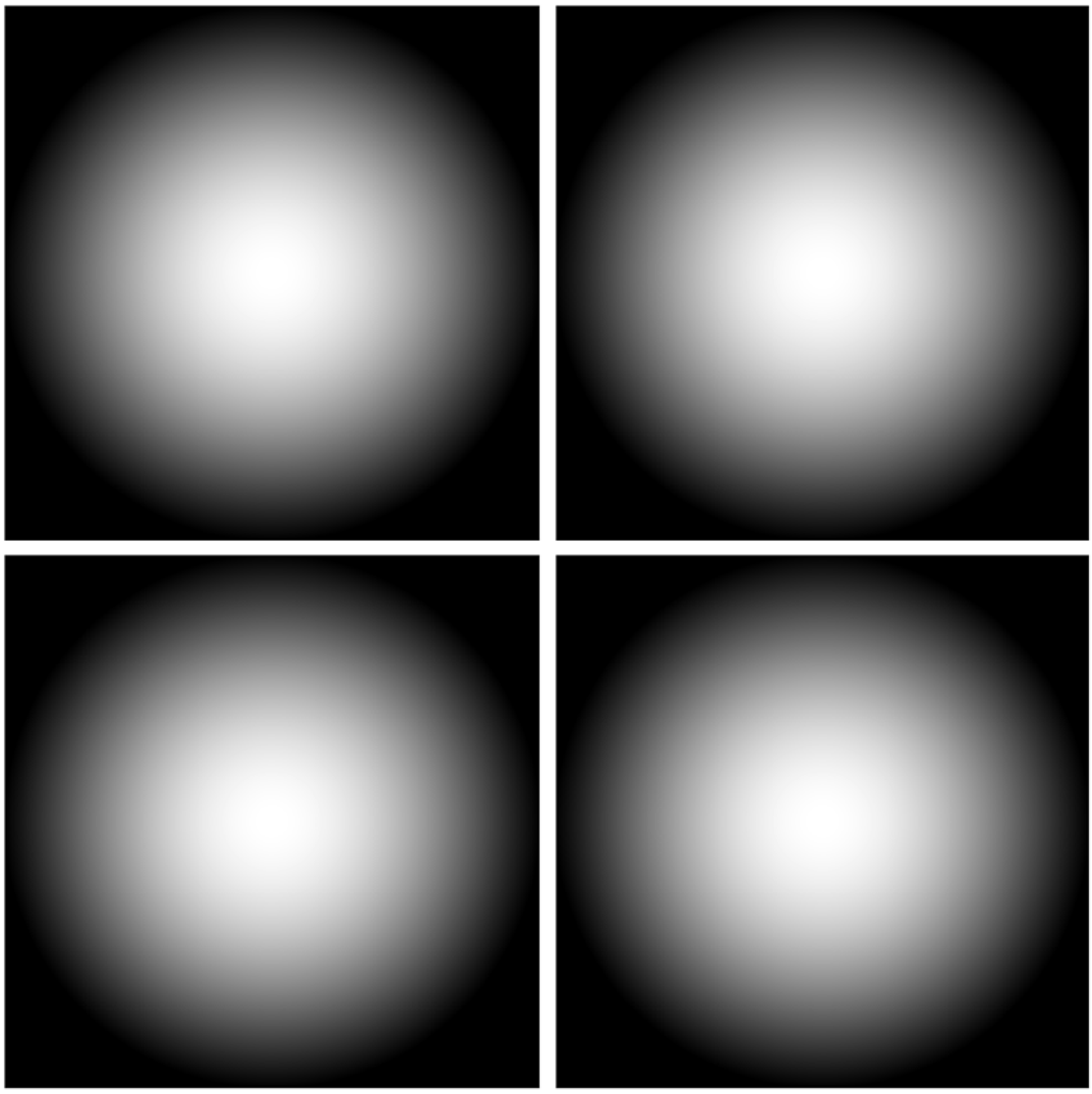

Figure B.3. MSL Hazcam pre-flight flat field images. The pre-flight flat field images (Maki et al., 2012) were retrieved from the PDS imaging node database (https://pds-imaging.jpl.nasa.gov/data/msl/MSLHAZ_0XXX/CALIB/) and correspond to: FLB (top-left), FRB (top-right), RLB (bottom-left) and RRB (bottom-right). Each image is linearly stretched between 0.5 and 1.25.

APPENDIX C

APPENDIX TO CHAPTER 5:

DUST PARTICLE SIZE AND OPTICAL DEPTH

Table C.1. MSL Navcam observations used in Chapter 5. Column values correspond to: MSL mission sol number, solar longitude (L_S, in degrees), Martian Year, local true solar time (LTST), solar azimuth and elevation angles in degrees with respect to the north and the local horizon. These values were used as input parameters for the radiative transfer calculations.

MSL SOL	Solar Longitude [deg]	Martian Year	FILENAME	Local True Solar Time	Sun Azimuth [deg]	Sun Elevation [deg]
21	162.0	31	NLA_399363597EDR_F0030100SAPP07612M1.IMG	14:53:49	285.54	44.95
24	163.6	31	NLA_399626441EDR_F0030372SAPP07712M1.IMG	13:57:47	291.26	58.42
29	166.4	31	NLA_400069880EDR_F0030888SAPP07712M1.IMG	13:51:24	290.26	60.30
39	172.0	31	NLA_400958457EDR_F0040468SAPP07712M1.IMG	14:06:02	283.81	57.50
41	173.1	31	NLA_401136867EDR_F0041238SAPP07712M1.IMG	14:20:13	281.55	54.16
43	174.2	31	NLA_401316500EDR_F0042002SAPP07612M1.IMG	14:54:12	278.36	45.91
48	177.1	31	NLA_401761194EDR_F0042644SAPP07612M1.IMG	15:07:57	275.98	42.69
52	179.4	31	NLA_402115185EDR_F0043200SAPP07612M1.IMG	14:50:16	275.41	47.20
57	182.3	31	NLA_402562341EDR_F0043520SAPP07612M1.IMG	15:43:47	271.94	34.01
102	209.5	31	NLA_406558419EDR_F0050388SAPP07612M1.IMG	16:00:30	258.66	30.16
122	222.2	31	NLA_408330384EDR_F0050938SAPP07612M1.IMG	14:57:39	251.12	44.86
147	238.2	31	NLA_410544820EDR_F0051902SAPP07612M1.IMG	13:26:20	229.73	63.29
166	250.6	31	NLA_412233457EDR_F0052330SAPP07612M1.IMG	13:45:56	230.73	58.16
324	346.5	31	NRB_426264304EDR_F0060864SAPP07612M1.IMG	14:03:12	266.65	59.31
333	351.3	31	NRB_427068209EDR_F0070438SAPP07612M1.IMG	15:25:13	269.00	38.83
340	355.0	31	NRB_427685406EDR_F0081148SAPP07612M1.IMG	14:18:26	272.96	55.36
344	357.0	31	NRB_428038027EDR_F0090770SAPP07612M1.IMG	13:39:20	276.98	64.97
349	359.7	31	NRB_428490085EDR_F0100746SAPP07612M1.IMG	15:53:35	272.68	31.50
358	4.2	32	NRB_429282728EDR_F0110882SAPP07612M1.IMG	14:13:42	280.16	55.99
369	9.7	32	NRB_430259833EDR_F0120982SAPP07612M1.IMG	14:26:51	282.89	52.29
372	11.2	32	NRB_430521464EDR_F0131212SAPP07612M1.IMG	13:11:46	297.40	69.77
383	16.6	32	NRB_431506535EDR_F0141428SAPP07612M1.IMG	15:34:26	281.96	35.24
390	20.0	32	NRB_432125040EDR_F0151762SAPP07612M1.IMG	14:49:40	287.04	45.74
406	27.7	32	NRB_433539267EDR_F0162120SAPP07612M1.IMG	13:15:33	310.60	65.29
412	30.5	32	NRB_434076977EDR_F0171310SAPP07612M1.IMG	14:39:55	293.75	46.74
419	33.8	32	NRB_434700865EDR_F0181406SAPP07612M1.IMG	15:22:30	290.85	36.52
426	37.1	32	NRB_435323449EDR_F0191256SAPP07612M1.IMG	15:43:53	290.91	31.22
433	40.3	32	NRB_435936028EDR_F0201326SAPP07612M1.IMG	13:22:53	315.58	60.92
440	43.5	32	NRB_436559934EDR_F0211648SAPP07612M1.IMG	14:05:36	305.72	52.15
454	49.9	32	NRB_437800741EDR_F0221028SAPP07612M1.IMG	13:37:08	315.40	56.37
470	57.2	32	NRB_439224987EDR_F0231524SAPP07612M1.IMG	14:44:26	303.95	42.25
494	67.9	32	NRB_441349865EDR_F0240562SAPP07612M1.IMG	13:18:00	326.49	56.24
527	82.8	32	NRB_444282928EDR_F0251906SAPP07612M1.IMG	14:21:28	312.50	44.63
545	90.9	32	NRB_445883715EDR_F0261458SAPP07612M1.IMG	15:10:31	305.31	34.98
552	94.1	32	NRB_446499987EDR_F0271500SAPP07612M1.IMG	13:48:00	319.92	50.32
563	99.1	32	NRB_447479279EDR_F0281504SAPP07612M1.IMG	14:34:31	310.06	42.26
569	101.9	32	NRB_448010997EDR_F0291606SAPP07612M1.IMG	14:20:15	312.31	45.07
589	111.2	32	NRB_449782783EDR_F0301366SAPP07612M1.IMG	13:22:50	325.09	55.44
631	131.4	32	NRB_453512631EDR_F0311670SAPP07612M1.IMG	13:50:16	311.36	54.24
637	134.4	32	NRB_454044666EDR_F0321252SAPP07612M1.IMG	13:41:18	312.45	56.48
647	139.5	32	NRB_454932444EDR_F0331334SAPP07612M1.IMG	13:43:25	309.53	57.09
657	144.6	32	NRB_455821590EDR_F0341616SAPP07612M1.IMG	14:07:46	301.35	53.10
662	147.2	32	NRB_456267998EDR_F0351626SAPP07612M1.IMG	14:49:43	293.68	44.20
668	150.3	32	NRB_456799315EDR_F0361708SAPP07612M1.IMG	14:29:06	294.75	49.31
672	152.4	32	NRB_457152376EDR_F0371824SAPP07612M1.IMG	13:56:42	299.06	56.85
685	159.4	32	NRB_458310507EDR_F0381758SAPP07612M1.IMG	15:04:35	285.99	42.12
705	170.5	32	NRB_460084993EDR_F0391930SAPP07612M1.IMG	14:50:54	280.83	46.44
733	186.7	32	NRB_462572793EDR_F0402484SAPP07612M1.IMG	15:27:01	270.07	38.33
747	195.0	32	NRB_463813017EDR_F0412270SAPP07612M1.IMG	14:44:14	265.70	49.10
864	269.8	32	NRB_474199389EDR_F0443000SAPP07612M1.IMG	13:48:01	228.85	56.93
952	323.9	32	NRB_482013079EDR_F0452302SAPP07612M1.IMG	13:35:01	245.47	64.61
964	330.8	32	NRB_483083182EDR_F0462052SAPP07612M1.IMG	14:52:45	257.44	46.69
984	341.9	32	NRB_484852932EDR_F0471818SAPP07612M1.IMG	13:21:25	260.64	69.55
1067	24.1	33	NRB_492221950EDR_F0482954SAPP07612M1.IMG	13:58:10	296.53	57.13

MSL SOL	Solar Longitude [deg]	Martian Year	FILENAME	Local True Solar Time	Sun Azimuth [deg]	Sun Elevation [deg]
1104	41.4	33	NRB_495505377EDR_F0493088SAPP07612M1.IMG	13:51:37	307.87	55.32
1167	69.9	33	NRB_501099548EDR_F0503368SAPP07612M1.IMG	14:32:05	308.98	43.42
1262	113.3	33	NRB_509536696EDR_F0523240SAPP07612M1.IMG	15:45:07	299.38	28.53
1301	132.2	33	NRB_512994632EDR_F0533062SAPP07612M1.IMG	14:41:32	301.25	44.02
1376	171.9	33	NRB_519653718EDR_F0543156SAPP07612M1.IMG	15:08:58	278.92	42.11
1433	205.6	33	NRB_524708540EDR_F0562614SAPP07612M1.IMG	13:42:01	255.24	64.04
1468	227.8	33	NRB_527820348EDR_F0573480SAPP07612M1.IMG	14:47:57	247.96	46.77
1503	250.5	33	NRB_530924083EDR_F0583228SAPP07612M1.IMG	13:33:52	227.71	60.45
1571	294.1	33	NRB_536961350EDR_F0593184SAPP07612M1.IMG	12:59:09	216.75	66.85
1604	314.2	33	NRB_539892888EDR_F0603516SAPP07612M1.IMG	13:19:28	234.43	66.55
1646	338.3	33	NRB_543622726EDR_F0613478SAPP07612M1.IMG	13:39:02	258.44	65.03

Table C.2. Results of dust column optical depth and aerosol effective radius. Column values correspond to: MSL mission sol number, solar longitude (L_S, in degrees), Martian Year, local true solar time (LTST), particle size distribution effective radius (r_{eff}, in μm), dust aerosol column optical depth at surface (τ) referenced to 880nm, and reduced χ^2 parameter (χ^2_ν). The uncertainties of the effective radius and optical depth were calculated for a 68.3% confidence limit (1σ) for a χ^2 type distribution probability density function for each parameter.

MSL SOL	Solar Longitude [deg]	Martian Year	Local True Solar Time	Effective radius, r_{eff} [μm]	Dust Column Optical Depth, τ_0	Reduced χ^2
21	162.0	31	14:53:49	$1.48^{+0.30}_{-0.29}$	$0.95^{+0.06}_{-0.18}$	0.35
24	163.6	31	13:57:47	$1.48^{+0.19}_{-0.20}$	0.76 ± 0.04	0.57
29	166.4	31	13:51:24	1.28 ± 0.18	0.72 ± 0.04	0.10
39	172.0	31	14:06:02	$1.24^{+0.19}_{-0.18}$	0.70 ± 0.04	0.33
41	173.1	31	14:20:13	1.38 ± 0.20	0.77 ± 0.05	0.14
43	174.2	31	14:54:12	1.26 ± 0.19	0.72 ± 0.05	0.40
48	177.1	31	15:07:57	1.10 ± 0.23	$0.85^{+0.09}_{-0.10}$	0.52
52	179.4	31	14:50:16	$1.38^{+0.19}_{-0.20}$	0.70 ± 0.04	0.43
57	182.3	31	15:43:47	1.34 ± 0.21	0.66 ± 0.05	0.13
102	209.5	31	16:00:30	$2.02^{+0.14}_{-0.13}$	$1.38^{+0.11}_{-0.10}$	0.55
122	222.2	31	14:57:39	1.38 ± 0.21	0.99 ± 0.08	0.60
147	238.2	31	13:26:20	1.48 ± 0.21	0.91 ± 0.06	0.34
166	250.6	31	13:45:56	1.30 ± 0.20	0.93 ± 0.07	0.50
324	346.5	31	14:03:12	$1.26^{+0.19}_{-0.18}$	0.68 ± 0.04	0.41
333	351.3	31	15:25:13	1.14 ± 0.19	$0.64^{+0.05}_{-0.04}$	0.54
340	355.0	31	14:18:26	1.26 ± 0.19	0.66 ± 0.04	0.19
344	357.0	31	13:39:20	1.18 ± 0.19	0.72 ± 0.04	0.49
349	359.7	31	15:53:35	1.38 ± 0.18	0.72 ± 0.05	1.01
358	4.2	32	14:13:42	$1.36^{+0.19}_{-0.20}$	0.77 ± 0.05	0.52
369	9.7	32	14:26:51	1.42 ± 0.20	0.79 ± 0.05	0.26
372	11.2	32	13:11:46	1.52 ± 0.21	0.70 ± 0.04	0.28
383	16.6	32	15:34:26	$1.34^{+0.21}_{-0.23}$	$0.70^{+0.05}_{-0.07}$	0.60
390	20.0	32	14:49:40	$1.34^{+0.19}_{-0.20}$	0.70 ± 0.05	0.31
406	27.7	32	13:15:33	1.30 ± 0.19	0.70 ± 0.04	0.36
412	30.5	32	14:39:55	$1.24^{+0.19}_{-0.18}$	0.64 ± 0.04	0.37
419	33.8	32	15:22:30	$1.38^{+0.22}_{-0.23}$	$0.74^{+0.06}_{-0.07}$	0.35
426	37.1	32	15:43:53	$1.22^{+0.40}_{-0.41}$	$0.77^{+0.22}_{-0.21}$	0.16
433	40.3	32	13:22:53	1.30 ± 0.19	0.72 ± 0.04	0.39
440	43.5	32	14:05:36	$1.18^{+0.19}_{-0.18}$	0.72 ± 0.05	0.25
454	49.9	32	13:37:08	1.04 ± 0.14	0.58 ± 0.03	0.25
470	57.2	32	14:44:26	0.98 ± 0.14	0.50 ± 0.03	0.30
494	67.9	32	13:18:00	1.14 ± 0.16	$0.50^{+0.02}_{-0.03}$	0.26
527	82.8	32	14:21:28	0.98 ± 0.14	0.50 ± 0.03	0.62
545	90.9	32	15:10:31	1.04 ± 0.17	0.48 ± 0.03	0.58
552	94.1	32	13:48:00	0.88 ± 0.14	0.49 ± 0.03	0.77
563	99.1	32	14:34:31	0.90 ± 0.12	0.45 ± 0.02	0.45
569	101.9	32	14:20:15	0.92 ± 0.14	0.43 ± 0.02	0.59
589	111.2	32	13:22:50	$1.00^{+0.13}_{-0.14}$	0.45 ± 0.02	0.36
631	131.4	32	13:50:16	0.86 ± 0.12	0.41 ± 0.02	0.44
637	134.4	32	13:41:18	0.88 ± 0.14	0.41 ± 0.02	0.67
647	139.5	32	13:43:25	1.08 ± 0.16	0.43 ± 0.02	0.52
657	144.6	32	14:07:46	1.10 ± 0.16	0.62 ± 0.03	0.32
662	147.2	32	14:49:43	0.92 ± 0.15	0.64 ± 0.04	0.40
668	150.3	32	14:29:06	0.92 ± 0.16	0.64 ± 0.04	0.78
672	152.4	32	13:56:42	1.18 ± 0.19	0.66 ± 0.04	0.59
685	159.4	32	15:04:35	1.10 ± 0.18	0.66 ± 0.05	0.30
705	170.5	32	14:50:54	$1.42^{+0.30}_{-0.29}$	$0.99^{+0.11}_{-0.15}$	0.40
733	186.7	32	15:27:01	1.32 ± 0.22	0.75 ± 0.06	0.37
747	195.0	32	14:44:14	1.20 ± 0.19	0.77 ± 0.05	0.57
864	269.8	32	13:48:01	1.26 ± 0.21	0.91 ± 0.07	0.39
952	323.9	32	13:35:01	1.32 ± 0.19	$0.77^{+0.04}_{-0.05}$	0.34
964	330.8	32	14:52:45	1.34 ± 0.34	$0.95^{+0.08}_{-0.23}$	0.40
984	341.9	32	13:21:25	$1.34^{+0.20}_{-0.21}$	0.93 ± 0.06	0.32
1067	24.1	33	13:58:10	1.24 ± 0.20	0.75 ± 0.05	0.49

MSL SOL	Solar Longitude [deg]	Martian Year	Local True Solar Time	Effective radius, r_{eff} [μm]	Dust Column Optical Depth, τ_0	Reduced χ^2
1104	41.4	33	13:51:37	1.18 ± 0.17	0.68 ± 0.04	0.22
1167	69.9	33	14:32:05	0.98 ± 0.14	0.52 ± 0.03	0.55
1262	113.3	33	15:45:07	1.06 ± 0.19	0.50 ± 0.04	0.65
1301	132.2	33	14:41:32	$0.76^{+0.12}_{-0.11}$	$0.47^{+0.02}_{-0.03}$	0.68
1376	171.9	33	15:08:58	$1.14^{+0.20}_{-0.19}$	0.77 ± 0.06	0.41
1433	205.6	33	13:42:01	1.14 ± 0.19	0.89 ± 0.06	0.42
1468	227.8	33	14:47:57	$1.52^{+0.35}_{-0.34}$	1.28 ± 0.20	0.49
1503	250.5	33	13:33:52	1.08 ± 0.19	0.93 ± 0.07	0.44
1571	294.1	33	12:59:09	0.96 ± 0.13	$0.80^{+0.05}_{-0.04}$	0.23
1604	314.2	33	13:19:28	0.94 ± 0.15	0.91 ± 0.06	0.23
1646	338.3	33	13:39:02	0.98 ± 0.17	$0.97^{+0.07}_{-0.08}$	0.30

APPENDIX D

APPENDIX TO CHAPTER 6:

DUST SINGLE SCATTERING PHASE FUNCTION

Table D.1. MSL Navcam and Hazcam observations used in Chapter 6. Column values correspond to: MSL mission sol number, solar longitude (LS, in degrees), Martian Year, local true solar time (LTST), solar azimuth and elevation angles in degrees with respect to the north and the local horizon, engineering camera (Navcam: NLB; Hazcam: FLB, FRB, RLB, RRB), and spacecraft clock time (Hazcams) or EDR file sequence (Navcams).

Sol	Ls[°]	MY	LTST	Sun Azim. [°]	Sun Elev. [°]	Camera	SCLK/Sequence
269	315.37	31	7:12	106.81	18.60	FLB, FRB,RLB, RRB	421356422, 421356451
270	316.19	31	16:40	253.43	20.31	FLB, FRB	421480269
283	323.77	31	16:56	256.16	16.47	FLB, FRB	422635427
291	328.36	31	17:08	257.82	13.45	FLB, FRB	423346401
322	345.50	31	17:25	264.52	8.92	FRB, FLB, RLB, RRB	426099261, 426099296
383	16.67	32	16:48	278.81	17.12	FRB, FLB, RLB, RRB	431511077, 431511104
439	43.10	32	16:44	289.18	16.55	NLB	ncam00548
474	59.00	32	16:52	293.41	13.90	NLB	ncam00548
582	107.94	32	16:41	296.45	15.83	NLB	ncam00548
610	121.23	32	17:34	291.85	4.25	NLB	ncam00550
751	197.46	32	16:28	264.00	23.24	FRB, FLB	464174522
765	206.07	32	16:49	260.16	18.24	FLB, FRB	465418782
782	216.73	32	16:59	255.97	15.72	FLB, FRB, RLB, RRB	466928832, 466928866
785	218.61	32	16:10	255.03	27.69	NLB	ncam00548
788	220.55	32	17:10	254.56	13.10	NLB	ncam00548
792	223.09	32	16:31	253.61	22.58	FLB, FRB, RLB, RRB	467815011, 467815060
806	232.09	32	16:27	250.61	23.32	NLB	ncam00548
813	236.64	32	17:09	249.67	13.49	FLB, FRB	469682237
814	237.29	32	16:55	249.46	16.70	FLB, FRB	469770196
815	237.93	32	16:46	249.23	18.71	FLB, FRB	469858472
819	240.53	32	16:45	248.58	18.91	FLB, FRB	470213649
824	243.77	32	16:02	246.89	28.79	FLB, FRB	470655026
828	246.40	32	16:46	247.31	18.68	FLB, FRB	471012999
830	247.49	32	16:28	246.77	22.74	FLB, FRB	471189532
924	307.50	32	16:21	250.39	24.74	NLB	ncam00548
1105	41.93	33	17:11	287.74	10.24	FLB, FRB	495606448
1114	46.05	33	16:41	290.29	17.15	FLB, FRB	496403367
1124	50.60	33	16:44	291.54	16.13	FLB, FRB	497291116
1130	53.33	33	17:18	290.95	8.08	FLB, FRB	497825752
1132	54.24	33	17:10	291.47	9.92	FLB, FRB	498002768
1137	56.49	33	16:45	293.10	15.56	FLB, FRB	498445016
1150	62.35	33	17:14	293.29	8.78	FLB, FRB	499600628
1157	65.49	33	17:13	293.95	8.88	FLB, FRB	500221886
1226	96.60	33	16:59	296.75	11.70	FLB, FRB	506345674
1258	111.42	33	16:39	296.01	16.44	NLB	ncam00548
1259	111.90	33	17:02	294.87	11.36	FLB, FRB	509275141
1261	112.82	33	16:01	298.19	25.02	NLB	ncam00548
1263	113.77	33	16:18	296.84	21.38	NLB	ncam00548
1268	116.15	33	16:36	295.27	17.30	NLB	ncam00548
1275	119.51	33	17:12	292.95	9.33	FLB, FRB	510696014
1287	125.30	33	16:30	293.42	19.22	FLB, FRB	511758612
1330	146.96	33	17:16	284.46	9.51	FLB, FRB	515578339
1332	147.99	33	16:40	285.36	18.14	FLB, FRB	515753675
1339	151.68	33	17:09	282.87	11.25	FLB, FRB	516376834
1358	161.91	33	17:35	278.09	5.34	FLB, FRB	518064970
1359	162.44	33	17:03	278.73	13.41	FLB, FRB	518151723
1378	173.02	33	16:46	274.64	18.00	FLB, FRB	519837215
1403	187.49	33	16:15	268.73	26.17	RLB, RRB	522054677
1405	188.69	33	16:38	267.79	20.48	FLB, FRB	522233564
1409	191.09	33	17:24	265.98	9.14	FLB, FRB, RLB, RRB	522591532, 522591583
1416	195.28	33	16:38	264.86	20.72	FLB, FRB	523210121
1418	196.50	33	17:16	263.83	11.31	FLB, FRB	523390041
1422	198.93	33	17:05	262.97	14.10	FLB, FRB, RLB, RRB	523744454, 523744503
1444	212.57	33	17:18	257.39	11.12	FLB, FRB, RLB, RRB	525698534, 525698583
1448	215.07	33	16:53	256.60	17.22	FLB, FRB	526052099
1454	218.88	33	17:04	255.18	14.60	FLB, FRB, RLB, RRB	526585575, 526585624
1474	231.71	33	17:21	250.98	10.57	FLB, FRB	528361546
1480	235.57	33	16:37	249.75	20.95	FLB, FRB	528892687
1484	238.19	33	17:30	249.22	8.64	FLB, FRB, RLB, RRB	529251205, 529251256
1491	242.74	33	17:17	248.23	11.55	FLB, FRB, RLB, RRB	529872102, 529872144
1493	244.04	33	17:11	247.95	13.03	FLB, FRB, RLB, RRB	530049331, 530049373
1496	246.01	33	17:35	247.48	7.38	FLB, FRB, RLB, RRB	530317281, 530317325
1504	251.23	33	17:28	246.64	8.97	FLB, FRB, RLB, RRB	531027377, 531027427
1511	255.78	33	16:42	245.76	19.61	FLB, FRB, RLB, RRB	531646212, 531646260
1512	256.42	33	16:28	245.42	22.63	FLB, FRB	531734165
1518	260.35	33	17:02	245.53	15.07	FLB, FRB	532269165
1537	272.68	33	17:17	245.24	11.64	FLB, FRB, RLB, RRB	533957634, 533957668
1555	284.18	33	16:47	245.83	18.45	NLB	ncam00548
1581	300.45	33	17:14	248.95	12.33	FLB, FRB, RLB, RRB	537865092, 537865126
1661	346.68	33	16:44	265.56	19.20	FLB, FRB	544965612
1668	350.22	33	17:15	266.69	11.29	FLB, FRB, RLB, RRB	545588880, 545588924
1675	353.89	33	16:57	268.62	15.86	FLB, FRB, RLB, RRB	546209039, 546209081
1681	357.01	33	16:46	270.20	18.40	FLB, FRB, RLB, RRB	546740938, 546740972

Sol	Ls[°]	MY	LTST	Sun Azim. [°]	Sun Elev. [°]	Camera	SCLK/Sequence
1715	14.15	34	16:34	278.18	20.70	FLB, FRB	549757840
1723	18.07	34	17:10	278.74	11.63	FLB, FRB, RLB, RRB	550470076, 550470111
1749	30.49	34	16:48	284.46	16.36	FLB, FRB, RLB, RRB	552776265, 552776300
1763	37.03	34	16:16	288.45	23.67	FLB, FRB	554016798
1764	37.50	34	16:46	287.15	16.40	FLB, FRB, RLB, RRB	554107432, 554107474
1765	37.97	34	17:16	286.21	9.12	FLB, FRB, RLB, RRB	554198056, 554198100
1770	40.27	34	16:18	289.50	22.85	FLB, FRB	554638225
1771	40.74	34	16:48	288.20	15.68	FLB, FRB, RLB, RRB	554728843, 554728878
1772	41.21	34	17:19	287.25	8.44	FLB, FRB, RLB, RRB	554819466, 554819510
1777	43.49	34	16:20	290.49	22.06	FLB, FRB	555259647
1779	44.42	34	17:21	288.22	7.71	FLB, FRB, RLB, RRB	555440886, 555440930
1791	49.88	34	16:31	291.98	19.26	FLB, FRB	556502839
1802	54.86	34	16:06	294.89	24.52	FLB, FRB	557477610
1805	56.23	34	16:38	293.36	17.14	FLB, FRB	557745889
1816	61.19	34	17:16	292.96	8.31	FLB, FRB, RLB, RRB	558724543, 558724579
1818	62.08	34	16:49	294.23	14.39	FLB, FRB	558901332
1821	63.42	34	16:28	295.59	19.01	FLB, FRB, RLB, RRB	559165415, 559165450
1824	64.78	34	16:55	294.52	12.89	FLB, FRB, RLB, RRB	559433352, 559433387
1831	67.92	34	17:07	294.62	10.12	FLB, FRB, RLB, RRB	560055379, 560055414
1836	70.17	34	17:18	294.58	7.53	FLB, FRB, RLB, RRB	560499871, 560499907
1838	71.06	34	17:01	295.39	11.49	FLB, FRB, RLB, RRB	560676312, 560676347
1839	71.49	34	16:09	298.29	22.90	FLB, FRB, RLB, RRB	560761909, 560761943
1845	74.19	34	16:41	296.73	15.71	FLB, FRB, RLB, RRB	561296467, 561296488
1848	75.53	34	16:19	298.17	20.55	FLB, FRB, RLB, RRB	561561352, 561561451
1849	75.81	34	07:27	62.56	17.74	NRB	ncam00581
1853	77.79	34	16:54	296.51	12.74	FLB, FRB, RLB, RRB	562007347, 562007382
1859	80.47	34	16:19	298.67	20.44	FLB, FRB, RLB, RRB	562537763, 562537797
1863	82.28	34	16:48	297.18	14.11	FLB, FRB, RLB, RRB	562894592, 562894627
1865	83.18	34	16:42	297.55	15.46	FLB, FRB, RLB, RRB	563071738, 563071766
1872	86.34	34	17:01	296.80	11.25	NRB	ncam00581
1879	89.51	34	17:02	296.76	10.81	FLB, FRB, RLB, RRB	564315716, 564315760
1885	92.21	34	16:05	299.99	23.33	FLB, FRB	564844795
1886	92.68	34	16:59	296.89	11.61	FLB, FRB, RLB, RRB	564936854, 564936898
1892	95.41	34	16:37	297.87	16.48	FLB, FRB, RLB, RRB	565468106, 565468141
1894	96.14	34	07:12	62.66	14.36	NRB	ncam00581
1895	96.78	34	16:37	297.78	16.40	FLB, FRB, RLB, RRB	565734434, 565734468
1902	100.00	34	17:12	295.98	8.73	FLB, FRB	566357944
1904	100.92	34	17:04	296.23	10.62	FLB, FRB, RLB, RRB	566534944, 566534987
1911	104.16	34	17:16	295.43	7.90	FLB, FRB, RLB, RBB	567157071, 567157100
1916	106.47	34	16:27	297.47	19.00	NRB	ncam00582
1924	110.02	34	06:59	64.76	11.59	NRB	ncam00581
1925	110.69	34	17:06	294.91	10.39	FLB, FRB, RLB, RRB	568399163, 568399191
1927	111.62	34	16:53	295.26	13.18	FLB, FRB	568575951
1928	112.08	34	16:20	297.01	20.77	FLB, FRB, RLB, RRB	568662583, 568662679
1929	112.58	34	17:31	293.73	4.75	RLB, RRB	568755797
1932	113.98	34	16:50	294.99	14.01	FLB, FRB, RLB, RRB	569019566, 569019601
1934	114.94	34	17:23	293.52	6.51	RLB, RRB	569199181
1935	115.41	34	16:53	294.59	13.45	FLB, FRB, RLB, RRB	569286026, 569286061
1937	116.36	34	16:53	294.40	13.51	FLB, FRB, RLB, RRB	569463546, 569463588
1938	116.83	34	16:57	294.11	12.56	RLB, RRB	569552596
1947	121.15	34	17:04	292.86	11.12	FLB, FRB, RLB, RRB	570351901, 570351944
1963	128.95	34	17:27	290.05	6.18	FLB, FRB, RLB, RRB	571773544, 571773587
1964	129.44	34	17:18	290.18	8.25	FLB, FRB, RLB, RRB	571861758, 571861809
1968	131.40	34	16:23	292.00	21.03	NRB	ncam00581
1969	131.91	34	17:05	289.92	11.42	FLB, FRB	572304802
1971	132.70	34	07:12	69.62	15.48	NRB	ncam00583
1971	132.91	34	17:14	289.28	9.28	FLB, FRB, RLB, RRB	572482889, 572482940
1972	133.40	34	16:45	290.26	16.04	FLB, FRB, RLB, RRB	572569883, 572569932
1973	133.91	34	17:03	289.36	11.86	FLB, FRB, RLB, RRB	572659745, 572659794
1974	134.41	34	17:12	288.90	9.90	FLB, FRB, RLB, RRB	572749030, 572749080
1975	134.90	34	16:39	290.06	17.55	FLB, FRB, RLB, RRB	572835795, 572835844
1978	136.41	34	16:49	289.11	15.28	FLB, FRB	573102731
1979	136.93	34	17:25	287.67	6.87	FLB, FRB, RLB, RRB	573193678, 573193723
1984	139.46	34	17:10	287.29	10.45	FLB, FRB, RLB, RRB	573636601, 573636651
1988	141.50	34	17:29	286.03	6.15	FLB, FRB, RLB, RRB	573992786, 573992829
1989	142.00	34	16:30	288.08	20.29	FLB, FRB, RLB, RRB	574077879, 574077965
1998	146.66	34	17:03	284.98	12.47	NRB	ncam00581
2000	147.69	34	16:49	285.12	16.02	FLB, FRB, RLB, RRB	575055503, 575055544
2001	148.22	34	17:05	284.32	12.04	FLB, FRB, RLB, RRB	575145295, 575145330

Table D.2. Results for the characterisation of dust aerosol single scattering phase function. Columns correspond to: MSL mission sol number, solar longitude (L_S), Martian Year, local true solar time (LTST), solar elevation angle (º) with respect to the local horizon, camera (Navcam: NAV; Hazcam: HAZ), the best fitting DHG parameters (g_1, g_2, α), diameter-to-length aspect ratio for cylinders and spheroids, Martian dust analogue sample, and the reduced χ^2 (χ^2_ν) value. Uncertainties were calculated for a 68.3% confidence limit (1σ) for a χ^2 distribution probability density function.

Sol	Ls[º]	MY	LTST	Sun elev(º)	Cam	DHG, g_1	DHG, g_2	DHG, α	CYL, D/L	SPH, D/L	Dust Analog.	X^2_ν DHG	X^2_ν CYL	X^2_ν SPH	X^2_ν TAB
269	315.37	31	7:12	18.60	HAZ	$0.98^{+0.00}_{-0.00}$	$0.26^{+0.00}_{-0.00}$	$0.74^{+0.01}_{-0.01}$	1.8	2.5	Palagonite	0.022	0.116	0.041	2.249
270	316.19	31	16:40	20.31	HAZ	$0.94^{+0.03}_{-0.02}$	$0.33^{+0.05}_{-0.04}$	$0.61^{+0.05}_{-0.08}$	1.5	2.5	Palagonite	0.048	0.010	0.026	2.199
283	323.77	31	16:56	16.47	HAZ	$0.92^{+0.02}_{-0.01}$	$0.36^{+0.01}_{-0.00}$	$0.62^{+0.00}_{-0.01}$	0.7	2.5	Basalt	0.013	0.011	0.151	2.784
291	328.36	31	17:08	13.45	HAZ	$0.93^{+0.01}_{-0.00}$	$0.36^{+0.04}_{-0.00}$	$0.64^{+0.00}_{-0.03}$	1.7	2.5	Basalt	0.017	0.044	0.112	4.000
322	345.50	31	17:25	8.92	HAZ	$0.91^{+0.00}_{-0.00}$	$0.17^{+0.00}_{-0.00}$	$0.70^{+0.00}_{-0.00}$	0.8	2.3	Basalt	0.099	0.024	0.154	4.450
383	16.67	32	16:48	17.12	HAZ	$0.82^{+0.02}_{-0.02}$	$0.25^{+0.04}_{-0.04}$	$0.68^{+0.03}_{0.05}$	1.1	0.5	Basalt	0.043	0.144	0.240	1.212
439	43.10	32	16:44	16.55	NAV	$0.92^{+0.00}_{-0.01}$	$0.17^{+0.00}_{-0.04}$	$0.74^{+0.02}_{-0.00}$	2.3	2.1	Basalt	0.049	0.093	0.272	1.163
474	59.00	32	16:52	13.90	NAV	$0.85^{+0.01}_{-0.02}$	$0.05^{+0.00}_{-0.04}$	$0.78^{+0.02}_{-0.00}$	0.7	2.0	Basalt	0.042	0.025	0.181	0.948
582	107.94	32	16:41	15.83	NAV	$0.88^{+0.01}_{-0.00}$	$0.02^{+0.04}_{-0.00}$	$0.82^{+0.00}_{-0.01}$	1.0	1.9	Basalt	0.042	0.077	0.324	0.420
610	121.23	32	17:34	4.25	NAV	$0.88^{+0.00}_{-0.01}$	$0.20^{+0.04}_{-0.04}$	$0.84^{+0.01}_{-0.02}$	0.6	2.1	Palagonite	0.039	0.296	0.658	0.365
751	197.46	32	16:28	23.24	HAZ	$0.89^{+0.09}_{-0.05}$	$0.09^{+0.09}_{-0.11}$	$0.71^{+0.07}_{0.10}$	1.9	2.1	Basalt	0.002	0.026	0.019	1.491
765	206.07	32	16:49	18.24	HAZ	$0.99^{+0.00}_{-0.09}$	$0.26^{+0.00}_{-0.02}$	$0.51^{+0.04}_{-0.01}$	1.6	2.3	Basalt	0.031	0.025	0.077	2.721
782	216.73	32	16:59	15.72	HAZ	$0.90^{+0.09}_{-0.04}$	$0.09^{+0.08}_{-0.07}$	$0.63^{+0.16}_{0.13}$	1.8	2.1	Basalt	0.002	0.010	0.164	4.529
785	218.61	32	16:10	27.69	NAV	$0.97^{+0.00}_{-0.00}$	$0.26^{+0.04}_{-0.00}$	$0.71^{+0.01}_{-0.01}$	2.2	1.7	Basalt	0.036	0.286	1.020	0.601
788	220.55	32	17:10	13.10	NAV	$0.77^{+0.03}_{-0.01}$	$-0.08^{+0.19}_{-0.15}$	$0.86^{+0.03}_{-0.07}$	2.2	1.8	Basalt	0.035	0.113	0.166	3.417
792	223.09	32	16:31	22.58	HAZ	$0.91^{+0.02}_{-0.03}$	$0.32^{+0.04}_{-0.04}$	$0.55^{+0.05}_{-0.05}$	1.7	2.5	Basalt	0.051	0.011	0.163	2.867
806	232.09	32	16:27	23.32	NAV	$0.98^{+0.00}_{-0.00}$	$0.26^{+0.00}_{-0.00}$	$0.71^{+0.01}_{-0.00}$	2.2	1.8	Basalt	0.069	0.364	0.901	1.208
813	236.64	32	17:09	13.49	HAZ	$0.91^{+0.08}_{-0.01}$	$0.02^{+0.16}_{-0.08}$	$0.79^{+0.11}_{0.29}$	0.6	2.3	Palagonite	0.008	0.008	0.185	2.025
814	237.29	32	16:55	16.70	HAZ	$0.99^{+0.00}_{0.07}$	$0.06^{+0.12}_{-0.00}$	$0.81^{+0.00}_{0.31}$	0.6	2.2	Palagonite	0.005	0.014	0.194	3.793
815	237.93	32	16:46	18.71	HAZ	$0.98^{+0.01}_{-0.05}$	$0.10^{+0.04}_{-0.04}$	$0.69^{+0.06}_{0.19}$	0.6	2.2	Palagonite	0.001	0.005	0.228	4.958
819	240.53	32	16:45	18.91	HAZ	$0.94^{+0.01}_{-0.01}$	$0.33^{+0.00}_{-0.00}$	$0.63^{+0.01}_{0.00}$	1.5	2.5	Palagonite	0.090	0.015	0.151	3.112
824	243.77	32	16:02	28.79	HAZ	$0.92^{+0.02}_{-0.00}$	$0.36^{+0.05}_{-0.00}$	$0.53^{+0.01}_{0.02}$	1.7	2.4	Basalt	0.020	0.169	0.645	1.369
828	246.40	32	16:46	18.68	HAZ	$0.94^{+0.01}_{-0.01}$	$0.33^{+0.00}_{-0.04}$	$0.61^{+0.03}_{-0.00}$	1.4	2.5	Basalt	0.073	0.018	0.215	3.225
830	247.49	32	16:28	22.74	HAZ	$0.82^{+0.05}_{-0.04}$	$0.25^{+0.09}_{-0.08}$	$0.96^{+0.00}_{0.00}$	1.4	2.4	Basalt	0.005	0.055	0.337	2.075
924	307.50	32	16:21	24.74	NAV	$0.96^{+0.00}_{-0.00}$	$0.29^{+0.00}_{-0.00}$	$0.71^{+0.00}_{0.00}$	0.5	1.6	Basalt	0.101	0.178	1.197	0.113
1105	41.93	33	17:11	10.24	HAZ	$0.96^{+0.00}_{-0.00}$	$0.25^{+0.00}_{-0.00}$	$0.67^{+0.01}_{-0.02}$	1.7	2.3	Palagonite	0.123	0.008	0.293	2.278
1114	46.05	33	16:41	17.15	HAZ	$0.81^{+0.18}_{-0.20}$	$-0.12^{+0.14}_{-0.25}$	$0.78^{+0.08}_{0.09}$	2.4	1.9	Basalt	0.003	0.012	0.211	2.844
1124	50.60	33	16:44	16.13	HAZ	$0.77^{+0.15}_{-0.14}$	$-0.20^{+0.15}_{-0.27}$	$0.83^{+0.06}_{0.05}$	1.5	1.8	Basalt	0.003	0.021	0.096	2.395
1130	53.33	33	17:18	8.08	HAZ	$0.97^{+0.02}_{-0.00}$	$0.30^{+0.05}_{-0.00}$	$0.71^{+0.05}_{0.14}$	1.7	2.5	Palagonite	0.021	0.168	0.617	1.879
1132	54.24	33	17:10	9.92	HAZ	$0.94^{+0.01}_{-0.00}$	$0.21^{+0.00}_{-0.04}$	$0.66^{+0.06}_{0.01}$	1.5	2.3	Palagonite	0.097	0.005	0.266	2.773
1137	56.49	33	16:45	15.56	HAZ	$0.73^{+0.06}_{-0.03}$	$-0.22^{+0.18}_{-0.16}$	$0.86^{+0.02}_{0.05}$	0.8	2.2	Basalt	0.005	0.007	0.113	1.289
1150	62.35	33	17:14	8.78	HAZ	$0.97^{+0.01}_{-0.00}$	$0.38^{+0.00}_{-0.00}$	$0.64^{+0.02}_{0.03}$	1.8	2.5	Palagonite	0.068	0.073	0.329	1.743
1157	65.49	33	17:13	8.88	HAZ	$0.96^{+0.00}_{-0.01}$	$0.33^{+0.00}_{-0.00}$	$0.69^{+0.01}_{0.01}$	1.7	2.5	Palagonite	0.144	0.074	0.295	2.272
1226	96.60	33	16:59	11.70	HAZ	$0.91^{+0.01}_{-0.01}$	$0.50^{+0.01}_{-0.04}$	$0.57^{+0.05}_{0.01}$	1.7	2.5	Basalt	0.147	0.129	0.368	2.273
1258	111.42	33	16:39	16.44	NAV	$0.91^{+0.01}_{-0.00}$	$0.24^{+0.04}_{-0.00}$	$0.71^{+0.00}_{0.03}$	2.0	1.6	Basalt	0.207	0.183	0.332	0.271
1259	111.90	33	17:02	11.36	HAZ	$0.91^{+0.02}_{-0.03}$	$0.28^{+0.04}_{-0.01}$	$0.55^{+0.03}_{0.05}$	0.8	2.2	Basalt	0.117	0.014	0.204	2.067
1261	112.82	33	16:01	25.02	NAV	$0.90^{+0.00}_{-0.00}$	$0.31^{+0.00}_{-0.04}$	$0.65^{+0.02}_{0.01}$	0.8	1.8	Basalt	0.189	0.108	0.403	0.166
1263	113.77	33	16:18	21.38	NAV	$0.91^{+0.00}_{-0.00}$	$0.28^{+0.00}_{-0.00}$	$0.64^{+0.00}_{0.01}$	0.8	1.9	Basalt	0.194	0.102	0.464	0.239
1268	116.15	33	16:36	17.30	NAV	$0.91^{+0.00}_{-0.01}$	$0.28^{+0.00}_{-0.04}$	$0.65^{+0.02}_{0.01}$	1.0	1.8	Basalt	0.191	0.073	0.446	0.258
1275	119.51	33	17:12	9.33	HAZ	$0.79^{+0.03}_{-0.04}$	$0.02^{+0.07}_{-0.09}$	$0.82^{+0.03}_{0.02}$	0.8	0.5	Basalt	0.055	0.013	0.099	1.154
1287	125.30	33	16:30	19.22	HAZ	$0.86^{+0.02}_{-0.17}$	$0.19^{+0.08}_{-0.88}$	$0.74^{+0.02}_{-0.04}$	0.7	2.1	Basalt	0.015	0.017	0.143	0.198
1330	146.96	33	17:16	9.51	HAZ	$0.87^{+0.06}_{-0.07}$	$0.05^{+0.03}_{-0.04}$	$0.71^{+0.09}_{0.16}$	1.8	2.0	Basalt	0.013	0.026	0.089	3.062
1332	147.99	33	16:40	18.14	HAZ	$0.77^{+0.12}_{-0.06}$	$-0.08^{+0.13}_{-0.11}$	$0.78^{+0.05}_{0.10}$	1.7	2.1	Basalt	0.008	0.016	0.257	2.161
1339	151.68	33	17:09	11.25	HAZ	$0.95^{+0.01}_{-0.02}$	$0.06^{+0.08}_{-0.00}$	$0.78^{+0.02}_{0.28}$	1.8	2.2	Palagonite	0.021	0.027	0.562	3.663
1358	161.91	33	17:35	5.34	HAZ	$0.96^{+0.00}_{-0.01}$	$0.29^{+0.00}_{-0.04}$	$0.68^{+0.06}_{0.01}$	1.7	2.5	Palagonite	0.014	0.592	1.417	1.154
1359	162.44	33	17:03	13.41	HAZ	$0.99^{+0.00}_{-0.00}$	$0.18^{+0.00}_{-0.00}$	$0.58^{+0.03}_{0.03}$	1.6	2.3	Basalt	0.038	0.026	0.370	3.886
1378	173.02	33	16:46	18.00	HAZ	$0.83^{+0.04}_{0.04}$	$-0.02^{+0.07}_{-0.07}$	$0.76^{+0.03}_{0.04}$	2.4	2.1	Basalt	0.010	0.031	0.081	1.861
1403	187.49	33	16:15	26.17	HAZ	$0.98^{+0.01}_{-0.07}$	$0.26^{+0.00}_{-0.09}$	$0.69^{+0.10}_{0.00}$	2.3	0.5	Basalt	0.010	0.042	0.112	0.038
1405	188.69	33	16:38	20.48	HAZ	$0.94^{+0.00}_{-0.00}$	$0.36^{+0.00}_{-0.00}$	$0.63^{+0.00}_{0.01}$	1.2	2.0	Basalt	0.015	0.087	0.502	0.267
1409	191.09	33	17:24	9.14	HAZ	$0.96^{+0.00}_{-0.00}$	$0.41^{+0.00}_{-0.00}$	$0.67^{+0.00}_{0.01}$	1.7	2.5	Palagonite	0.098	0.678	1.042	2.079
1416	195.28	33	16:38	20.72	HAZ	$0.77^{+0.04}_{-0.05}$	$-0.02^{+0.07}_{-0.15}$	$0.76^{+0.06}_{0.05}$	1.6	2.3	Basalt	0.005	0.006	0.255	2.224
1418	196.50	33	17:16	11.31	HAZ	$0.95^{+0.01}_{-0.00}$	$0.41^{+0.00}_{-0.04}$	$0.59^{+0.03}_{0.00}$	1.7	2.5	Basalt	0.052	0.041	0.159	3.629
1422	198.93	33	17:05	14.10	HAZ	$0.94^{+0.01}_{-0.01}$	$0.10^{+0.04}_{-0.00}$	$0.86^{+0.00}_{0.01}$	2.3	2.2	Basalt	0.014	0.121	0.185	1.017
1444	212.57	33	17:18	11.12	HAZ	$0.94^{+0.02}_{0.00}$	$0.06^{+0.04}_{-0.00}$	$0.84^{+0.03}_{0.02}$	1.8	2.4	Palagonite	0.007	0.005	0.261	1.672
1448	215.07	33	16:53	17.22	HAZ	$0.97^{+0.01}_{-0.02}$	$0.26^{+0.00}_{-0.04}$	$0.55^{+0.07}_{0.04}$	1.7	2.3	Palagonite	0.019	0.024	0.046	3.090
1454	218.88	33	17:04	14.60	HAZ	$0.94^{+0.00}_{-0.00}$	$0.33^{+0.00}_{-0.00}$	$0.59^{+0.00}_{0.00}$	1.2	0.5	Basalt	0.077	0.137	0.364	2.266
1474	231.71	33	17:21	10.57	HAZ	$0.89^{+0.10}_{-0.01}$	$0.09^{+0.17}_{-0.04}$	$0.74^{+0.03}_{0.24}$	0.8	2.2	Palagonite	0.007	0.019	0.014	0.803
1480	235.57	33	16:37	20.95	HAZ	$0.89^{+0.04}_{-0.06}$	$0.38^{+0.04}_{-0.03}$	$0.52^{+0.08}_{0.02}$	1.7	1.1	Basalt	0.006	0.143	0.521	2.508
1484	238.19	33	17:30	8.64	HAZ	$0.97^{+0.02}_{-0.01}$	$0.30^{+0.01}_{-0.04}$	$0.71^{+0.05}_{0.03}$	1.7	2.5	Palagonite	0.008	0.367	1.068	3.090
1491	242.74	33	17:17	11.55	HAZ	$0.93^{+0.00}_{-0.00}$	$0.32^{+0.00}_{-0.00}$	$0.68^{+0.00}_{0.00}$	0.6	2.2	Basalt	0.075	0.020	0.013	5.356
1493	244.04	33	17:11	13.03	HAZ	$0.87^{+0.00}_{-0.02}$	$0.12^{+0.00}_{-0.14}$	$0.78^{+0.06}_{0.00}$	1.0	2.0	Basalt	0.196	0.167	0.159	3.394
1496	246.01	33	17:35	7.38	HAZ	$0.95^{+0.00}_{-0.01}$	$0.37^{+0.00}_{-0.00}$	$0.62^{+0.02}_{0.00}$	1.8	2.5	Basalt	0.031	0.645	0.877	7.379
1504	251.23	33	17:28	8.97	HAZ	$0.94^{+0.00}_{-0.00}$	$0.17^{+0.00}_{-0.00}$	$0.76^{+0.01}_{0.00}$	1.7	2.5	Palagonite	0.010	0.078	0.545	1.206
1511	255.78	33	16:42	19.61	HAZ	$0.81^{+0.02}_{-0.03}$	$0.18^{+0.07}_{-0.13}$	$0.67^{+0.08}_{0.05}$	1.1	1.9	Basalt	0.044	0.317	0.642	1.224
1512	256.42	33	16:28	22.63	HAZ	$0.94^{+0.02}_{-0.37}$	$0.29^{+0.05}_{-0.89}$	$0.60^{+0.27}_{0.05}$	1.7	2.5	Basalt	0.007	0.049	0.259	1.229
1518	260.35	33	17:02	15.07	HAZ	$0.91^{+0.04}_{-0.02}$	$0.17^{+0.04}_{-0.04}$	$0.66^{+0.08}_{0.11}$	0.8	2.2	Palagonite	0.005	0.025	0.031	3.046
1537	272.68	33	17:17	11.64	HAZ	$0.92^{+0.00}_{-0.00}$	$0.28^{+0.00}_{-0.00}$	$0.50^{+0.00}_{0.00}$	0.7	1.9	Basalt	0.089	0.015	0.005	2.870

Sol	Ls[°]	MY	LTST	Sun elev(°)	Cam	DHG, g_1	DHG, g_2	DHG, α	CYL, D/L	SPH, D/L	Dust Analog.	X^2_ν DHG	X^2_ν CYL	X^2_ν SPH	X^2_ν TAB
1555	284.18	33	16:47	18.45	NAV	$0.95^{+0.00}_{-0.00}$	$0.29^{+0.00}_{-0.00}$	$0.60^{+0.01}_{-0.00}$	1.2	1.8	Basalt	0.131	0.362	1.159	0.704
1581	300.45	33	17:14	12.33	HAZ	$0.86^{+0.00}_{-0.01}$	$0.16^{+0.00}_{-0.00}$	$0.61^{+0.01}_{-0.00}$	2.0	1.8	Basalt	0.232	0.540	0.857	1.847
1661	346.68	33	16:44	19.20	HAZ	$0.90^{+0.00}_{-0.01}$	$0.13^{+0.00}_{-0.07}$	$0.67^{+0.02}_{-0.01}$	1.0	1.7	Basalt	0.169	0.127	0.199	2.155
1668	350.22	33	17:15	11.29	HAZ	$0.98^{+0.00}_{-0.02}$	$0.30^{+0.00}_{-0.05}$	$0.64^{+0.06}_{-0.00}$	1.7	2.5	Palagonite	0.023	0.098	0.563	1.595
1675	353.89	33	16:57	15.86	HAZ	$0.94^{+0.01}_{-0.01}$	$0.36^{+0.04}_{-0.00}$	$0.63^{+0.01}_{-0.04}$	0.6	2.2	Palagonite	0.020	0.016	0.032	2.803
1681	357.01	33	16:46	18.40	HAZ	$0.94^{+0.00}_{-0.00}$	$0.29^{+0.00}_{-0.00}$	$0.61^{+0.00}_{-0.00}$	2.3	2.0	Basalt	0.109	0.012	0.004	4.206
1715	14.15	34	16:34	20.70	HAZ	$0.96^{+0.01}_{-0.01}$	$0.18^{+0.04}_{-0.00}$	$0.73^{+0.01}_{-0.02}$	2.2	2.0	Basalt	0.021	0.159	0.322	0.787
1723	18.07	34	17:10	11.63	HAZ	$0.86^{+0.00}_{-0.01}$	$0.12^{+0.00}_{-0.07}$	$0.65^{+0.03}_{-0.00}$	0.5	1.8	Basalt	0.228	0.432	0.676	1.943
1749	30.49	34	16:48	16.36	HAZ	$0.98^{+0.00}_{-0.00}$	$0.30^{+0.04}_{-0.00}$	$0.67^{+0.01}_{-0.03}$	0.5	1.4	Basalt	0.389	0.706	1.883	0.791
1763	37.03	34	16:16	23.67	HAZ	$0.97^{+0.01}_{-0.02}$	$0.14^{+0.00}_{-0.04}$	$0.70^{+0.03}_{-0.01}$	2.2	1.9	Basalt	0.012	0.217	0.195	0.577
1764	37.50	34	16:46	16.40	HAZ	$0.97^{+0.00}_{-0.00}$	$0.18^{+0.00}_{-0.00}$	$0.73^{+0.00}_{-0.00}$	2.2	1.8	Basalt	0.140	0.059	0.098	1.046
1765	37.97	34	17:16	9.12	HAZ	$0.81^{+0.00}_{-0.01}$	$-0.08^{+0.00}_{-0.06}$	$0.82^{+0.02}_{-0.00}$	2.2	1.2	Basalt	0.122	0.097	0.136	2.709
1770	40.27	34	16:18	22.85	HAZ	$0.98^{+0.00}_{-0.02}$	$0.14^{+0.00}_{-0.04}$	$0.73^{+0.02}_{-0.01}$	2.2	1.8	Basalt	0.017	0.220	0.451	0.500
1771	40.74	34	16:48	15.68	HAZ	$0.97^{+0.00}_{-0.00}$	$0.18^{+0.00}_{-0.00}$	$0.78^{+0.00}_{-0.00}$	0.5	1.6	Basalt	0.107	0.335	0.694	0.706
1772	41.21	34	17:19	8.44	HAZ	$0.84^{+0.00}_{-0.01}$	$-0.09^{+0.00}_{-0.10}$	$0.84^{+0.02}_{-0.00}$	0.8	2.3	Basalt	0.086	0.008	0.011	3.742
1777	43.49	34	16:20	22.06	HAZ	$0.95^{+0.03}_{-0.01}$	$0.10^{+0.04}_{-0.04}$	$0.75^{+0.02}_{-0.03}$	2.2	1.8	Basalt	0.014	0.136	0.222	0.458
1779	44.42	34	17:21	7.71	HAZ	$0.84^{+0.01}_{-0.01}$	$0.05^{+0.10}_{-0.03}$	$0.81^{+0.02}_{-0.04}$	1.1	1.9	Basalt	0.097	0.032	0.053	3.325
1791	49.88	34	16:31	19.26	HAZ	$0.93^{+0.05}_{-0.03}$	$0.09^{+0.09}_{-0.08}$	$0.79^{+0.04}_{-0.07}$	2.2	1.7	Basalt	0.008	0.023	0.103	0.321
1802	54.86	34	16:06	24.52	HAZ	$0.89^{+0.00}_{-0.01}$	$0.38^{+0.04}_{-0.04}$	$0.70^{+0.03}_{-0.02}$	1.1	0.5	Basalt	0.031	0.174	0.146	0.525
1805	56.23	34	16:38	17.14	HAZ	$0.97^{+0.00}_{-0.00}$	$0.49^{+0.00}_{-0.00}$	$0.66^{+0.01}_{-0.00}$	1.9	1.9	Basalt	0.156	0.211	0.225	0.281
1816	61.19	34	17:16	8.31	HAZ	$0.82^{+0.01}_{-0.01}$	$0.15^{+0.07}_{-0.03}$	$0.74^{+0.03}_{-0.04}$	1.0	2.2	Palagonite	0.014	0.020	0.093	1.437
1818	62.08	34	16:49	14.39	HAZ	$0.94^{+0.00}_{-0.01}$	$0.13^{+0.00}_{-0.04}$	$0.78^{+0.02}_{-0.01}$	2.2	2.0	Basalt	0.025	0.110	0.267	0.771
1821	63.42	34	16:28	19.01	HAZ	$0.96^{+0.00}_{-0.00}$	$0.33^{+0.00}_{-0.00}$	$0.60^{+0.00}_{-0.00}$	1.2	1.8	Basalt	0.102	0.510	1.094	0.585
1824	64.78	34	16:55	12.89	HAZ	$0.92^{+0.00}_{-0.01}$	$0.09^{+0.00}_{-0.04}$	$0.80^{+0.02}_{-0.00}$	2.2	2.0	Basalt	0.035	0.054	0.131	0.889
1831	67.92	34	17:07	10.12	HAZ	$0.76^{+0.01}_{-0.02}$	$-0.36^{+0.06}_{-0.08}$	$0.85^{+0.01}_{-0.01}$	1.4	1.5	Basalt	0.012	0.031	0.006	2.634
1836	70.17	34	17:18	7.53	HAZ	$0.86^{+0.01}_{-0.00}$	$0.09^{+0.04}_{-0.00}$	$0.77^{+0.00}_{-0.02}$	1.8	2.5	Basalt	0.147	0.016	0.146	2.852
1838	71.06	34	17:01	11.49	HAZ	$0.72^{+0.00}_{-0.00}$	$-0.31^{+0.03}_{-0.00}$	$0.86^{+0.00}_{-0.01}$	0.5	1.6	Basalt	0.064	0.398	0.555	1.282
1839	71.49	34	16:09	22.90	HAZ	$0.94^{+0.04}_{-0.01}$	$0.02^{+0.04}_{-0.00}$	$0.72^{+0.01}_{-0.04}$	2.3	1.7	Basalt	0.011	0.012	0.007	0.822
1845	74.19	34	16:41	15.71	HAZ	$0.76^{+0.00}_{-0.01}$	$-0.48^{+0.03}_{-0.12}$	$0.91^{+0.011}_{-0.00}$	2.0	1.5	Basalt	0.087	0.160	0.021	0.970
1848	75.53	34	16:19	20.55	HAZ	$0.95^{+0.00}_{-0.00}$	$0.14^{+0.00}_{-0.00}$	$0.74^{+0.00}_{-0.00}$	2.0	2.0	Basalt	0.021	0.295	0.741	0.782
1849	75.81	34	07:27	17.74	NAV	$0.86^{+0.00}_{-0.00}$	$-0.05^{+0.04}_{-0.04}$	$0.85^{+0.01}_{-0.01}$	2.3	1.7	Basalt	0.050	0.110	0.293	0.231
1853	77.79	34	16:54	12.74	HAZ	$0.70^{+0.01}_{-0.00}$	$-0.33^{+0.05}_{-0.06}$	$0.88^{+0.01}_{-0.01}$	1.0	1.7	Basalt	0.077	0.231	0.239	1.010
1859	80.47	34	16:19	20.44	HAZ	$0.97^{+0.00}_{-0.01}$	$0.14^{+0.00}_{-0.04}$	$0.69^{+0.01}_{-0.00}$	2.0	1.7	Basalt	0.203	0.141	0.239	0.560
1863	82.28	34	16:48	14.11	HAZ	$0.71^{+0.01}_{-0.00}$	$-0.33^{+0.05}_{-0.09}$	$0.89^{+0.01}_{-0.01}$	2.0	1.6	Basalt	0.114	0.360	0.345	0.888
1865	83.18	34	16:42	15.46	HAZ	$0.81^{+0.00}_{-0.00}$	$0.38^{+0.00}_{-0.00}$	$0.64^{+0.00}_{-0.00}$	2.1	0.8	Basalt	0.257	0.060	0.135	0.493
1872	86.34	34	17:01	11.25	NAV	$0.85^{+0.01}_{-0.01}$	$-0.23^{+0.07}_{-0.00}$	$0.91^{+0.00}_{-0.01}$	2.3	0.5	Basalt	0.029	0.037	0.530	0.372
1879	89.51	34	17:02	10.81	HAZ	$0.97^{+0.00}_{-0.00}$	$0.06^{+0.00}_{-0.00}$	$0.88^{+0.00}_{-0.00}$	2.0	1.8	Basalt	0.027	0.101	0.569	0.732
1885	92.21	34	16:05	23.33	HAZ	$0.92^{+0.00}_{-0.01}$	$0.13^{+0.00}_{-0.04}$	$0.70^{+0.02}_{-0.01}$	2.3	1.8	Basalt	0.031	0.047	0.003	0.639
1886	92.68	34	16:59	11.61	HAZ	$0.66^{+0.04}_{-0.03}$	$-0.15^{+0.19}_{-0.17}$	$0.88^{+0.04}_{-0.06}$	2.2	2.0	Basalt	0.021	0.095	0.313	1.239
1892	95.41	34	16:37	16.48	HAZ	$0.97^{+0.00}_{-0.00}$	$0.26^{+0.00}_{-0.00}$	$0.71^{+0.00}_{-0.00}$	2.0	1.8	Basalt	0.069	0.349	1.370	0.497
1894	96.14	34	07:12	14.36	NAV	$0.90^{+0.00}_{-0.00}$	$0.02^{+0.00}_{-0.04}$	$0.85^{+0.01}_{-0.00}$	2.3	1.7	Basalt	0.065	0.023	1.444	0.166
1895	96.78	34	16:37	16.40	HAZ	$0.78^{+0.01}_{-0.00}$	$-0.40^{+0.06}_{-0.00}$	$0.91^{+0.00}_{-0.01}$	2.0	1.5	Basalt	0.101	0.038	0.044	0.874
1902	100.00	34	17:12	8.73	HAZ	$0.89^{+0.08}_{-0.01}$	$0.24^{+0.08}_{-0.10}$	$0.66^{+0.20}_{-0.16}$	0.8	2.4	Palagonite	0.006	0.017	0.048	0.876
1904	100.92	34	17:04	10.62	HAZ	$0.85^{+0.01}_{-0.02}$	$0.16^{+0.00}_{-0.04}$	$0.62^{+0.03}_{-0.01}$	2.3	1.9	Basalt	0.063	0.037	0.066	1.854
1911	104.16	34	17:16	7.90	HAZ	$0.85^{+0.00}_{-0.00}$	$-0.05^{+0.03}_{-0.00}$	$0.82^{+0.00}_{-0.01}$	0.7	1.8	Basalt	0.080	0.040	0.079	2.814
1916	106.47	34	16:27	19.00	NAV	$0.85^{+0.01}_{-0.01}$	$0.02^{+0.07}_{-0.10}$	$0.83^{+0.03}_{-0.03}$	1.0	1.6	Basalt	0.086	0.036	0.413	0.237
1924	110.02	34	06:59	11.59	NAV	$0.90^{+0.01}_{-0.00}$	$0.09^{+0.04}_{-0.00}$	$0.82^{+0.00}_{-0.02}$	2.3	2.3	Basalt	0.034	0.152	0.214	0.439
1925	110.69	34	17:06	10.39	HAZ	$0.90^{+0.01}_{-0.03}$	$0.35^{+0.00}_{-0.05}$	$0.50^{+0.04}_{-0.00}$	0.8	1.6	Basalt	0.296	0.038	0.011	1.505
1927	111.62	34	16:53	13.18	HAZ	$0.91^{+0.06}_{-0.04}$	$-0.13^{+0.07}_{-0.07}$	$0.87^{+0.01}_{-0.02}$	2.0	1.6	Basalt	0.011	0.066	0.029	1.157
1928	112.08	34	16:20	20.77	HAZ	$0.95^{+0.03}_{-0.07}$	$0.06^{+0.04}_{-0.08}$	$0.76^{+0.07}_{-0.04}$	2.2	0.5	Basalt	0.006	0.040	0.050	0.286
1929	112.58	34	17:31	4.75	HAZ	$0.95^{+0.00}_{-0.00}$	$0.37^{+0.00}_{-0.00}$	$0.68^{+0.00}_{-0.01}$	1.7	2.5	Palagonite	0.084	0.673	1.150	2.514
1932	113.98	34	16:50	14.01	HAZ	$0.93^{+0.00}_{-0.00}$	$0.13^{+0.00}_{-0.00}$	$0.76^{+0.00}_{-0.00}$	2.0	1.7	Basalt	0.202	0.114	0.390	0.637
1934	114.94	34	17:23	6.51	HAZ	$0.90^{+0.00}_{-0.00}$	$0.17^{+0.04}_{-0.00}$	$0.76^{+0.00}_{-0.02}$	1.8	2.4	Palagonite	0.083	0.057	0.237	1.790
1935	115.41	34	16:53	13.45	HAZ	$0.66^{+0.01}_{-0.01}$	$-0.66^{+0.01}_{-0.01}$	$0.90^{+0.00}_{-0.01}$	2.0	1.6	Basalt	0.135	0.071	0.273	0.722
1937	116.36	34	16:53	13.51	HAZ	$0.94^{+0.00}_{-0.00}$	$0.17^{+0.00}_{-0.00}$	$0.77^{+0.01}_{-0.00}$	2.0	1.7	Basalt	0.141	0.057	0.458	0.427
1938	116.83	34	16:57	12.56	HAZ	$0.70^{+0.00}_{-0.01}$	$-0.70^{+0.03}_{-0.00}$	$0.86^{+0.00}_{-0.01}$	2.0	1.7	Basalt	0.011	0.077	0.178	0.495
1947	121.15	34	17:04	11.12	HAZ	$0.63^{+0.00}_{-0.00}$	$-0.63^{+0.00}_{-0.00}$	$0.95^{+0.00}_{-0.00}$	2.1	1.3	Basalt	0.268	0.401	0.777	0.275
1963	128.95	34	17:27	6.18	HAZ	$0.91^{+0.00}_{-0.00}$	$0.17^{+0.00}_{-0.00}$	$0.85^{+0.00}_{-0.00}$	0.6	0.5	Palagonite	0.130	0.392	0.586	0.329
1964	129.44	34	17:18	8.25	HAZ	$0.93^{+0.01}_{-0.00}$	$0.32^{+0.00}_{-0.00}$	$0.76^{+0.01}_{-0.01}$	0.6	2.1	Palagonite	0.077	0.123	0.249	0.750
1968	131.40	34	16:23	21.03	NAV	$0.78^{+0.01}_{-0.01}$	$-0.18^{+0.09}_{-0.06}$	$0.89^{+0.01}_{-0.02}$	0.8	1.9	Basalt	0.011	0.013	0.082	0.251
1969	131.91	34	17:05	11.42	HAZ	$0.72^{+0.00}_{-0.01}$	$-0.72^{+0.01}_{-0.00}$	$0.87^{+0.01}_{-0.00}$	2.0	1.4	Basalt	0.100	0.161	0.239	0.246
1971	132.70	34	07:12	15.48	NAV	$0.89^{+0.01}_{-0.00}$	$-0.05^{+0.04}_{-0.04}$	$0.88^{+0.01}_{-0.01}$	1.9	1.7	Palagonite	0.147	0.081	0.112	1.123
1971	132.91	34	17:14	9.28	HAZ	$0.76^{+0.01}_{-0.02}$	$-0.11^{+0.03}_{-0.15}$	$0.88^{+0.03}_{-0.01}$	1.1	1.2	Basalt	0.038	0.043	1.568	0.197
1972	133.40	34	16:45	16.04	HAZ	$0.95^{+0.00}_{-0.00}$	$0.25^{+0.00}_{-0.00}$	$0.76^{+0.00}_{-0.00}$	1.9	1.4	Basalt	0.203	0.190	1.356	0.154
1973	133.91	34	17:03	11.86	HAZ	$0.97^{+0.00}_{-0.00}$	$0.30^{+0.00}_{-0.00}$	$0.78^{+0.00}_{-0.00}$	2.2	1.3	Basalt	0.231	0.178	0.434	0.266
1974	134.41	34	17:12	9.90	HAZ	$0.74^{+0.01}_{-0.00}$	$-0.37^{+0.09}_{-0.03}$	$0.93^{+0.00}_{-0.01}$	0.5	0.5	Basalt	0.007	0.067	0.102	0.982
1975	134.90	34	16:39	17.55	HAZ	$0.96^{+0.00}_{-0.00}$	$0.33^{+0.00}_{-0.00}$	$0.70^{+0.00}_{-0.00}$	1.9	1.5	Basalt	0.292	0.434	1.510	0.228
1978	136.41	34	16:49	15.28	HAZ	$0.98^{+0.00}_{-0.00}$	$0.38^{+0.00}_{-0.00}$	$0.73^{+0.00}_{-0.00}$	0.5	1.5	Basalt	0.140	0.319	1.264	0.166
1979	136.93	34	17:25	6.87	HAZ	$0.96^{+0.00}_{-0.00}$	$0.33^{+0.00}_{-0.00}$	$0.78^{+0.00}_{-0.00}$	1.7	2.5	Palagonite	0.154	0.775	1.314	0.911
1984	139.46	34	17:10	10.45	HAZ	$0.73^{+0.01}_{-0.01}$	$-0.31^{+0.09}_{-0.08}$	$0.92^{+0.01}_{-0.01}$	0.5	1.7	Basalt	0.010	0.118	0.159	1.085
1988	141.50	34	17:29	6.15	HAZ	$0.90^{+0.00}_{-0.00}$	$-0.02^{+0.04}_{-0.00}$	$0.84^{+0.00}_{-0.01}$	1.8	2.5	Palagonite	0.244	0.615	0.928	1.789
1989	142.00	34	16:30	20.29	HAZ	$0.93^{+0.02}_{-0.05}$	$-0.13^{+0.04}_{-0.14}$	$0.85^{+0.04}_{-0.02}$	2.1	1.4	Basalt	0.005	0.165	0.038	0.429
1998	146.66	34	17:03	12.47	NAV	$0.92^{+0.00}_{-0.00}$	$-0.17^{+0.00}_{-0.00}$	$0.94^{+0.00}_{-0.00}$	0.5	0.8	Palagonite	0.032	0.020	0.811	0.442
2000	147.69	34	16:49	16.02	HAZ	$0.97^{+0.00}_{-0.07}$	$-0.06^{+0.00}_{-0.14}$	$0.86^{+0.04}_{-0.00}$	2.0	1.4	Basalt	0.006	0.071	0.022	0.927
2001	148.22	34	17:05	12.04	HAZ	$0.89^{+0.03}_{-0.03}$	$-0.27^{+0.07}_{-0.06}$	$0.93^{+0.00}_{-0.00}$	2.0	0.5	Palagonite	0.006	0.025	0.021	1.197